

Dissertation zur Erlangung des Doktorgrades  
der Fakultät für Chemie und Pharmazie  
der Ludwig-Maximilians-Universität München

Advanced Fluorescence Fluctuation Spectroscopy  
with Pulsed Interleaved Excitation  
Development and Applications

Matthias Höller

aus

Bergisch Gladbach

2011

## **Erklärung**

Diese Dissertation wurde im Sinne von §13 Abs. 3 bzw. 4 der Promotionsordnung vom 29. Januar 1998 von Herrn Professor Lamb betreut.

## **Ehrenwörtliche Versicherung**

Diese Dissertation wurde selbständig, ohne unerlaubte Hilfe erarbeitet.

München, am 07.01.2011

---

(Unterschrift des Autors)

Dissertation eingereicht am: \_\_\_\_\_

1. Gutachter: Prof. Dr. Don C. Lamb

2. Gutachter: Prof. Dr. Christoph Bräuchle

Mündliche Prüfung am: \_\_\_\_\_

# Contents

<b>1</b>	<b>Introduction</b>	<b>1</b>
<b>2</b>	<b>Fluorescence</b>	<b>3</b>
2.1	Fundamentals . . . . .	3
2.2	Fluorescence Anisotropy . . . . .	5
2.3	Förster Resonance Energy Transfer . . . . .	5
<b>3</b>	<b>Optical system</b>	<b>7</b>
3.1	Confocal Microscopy . . . . .	7
3.2	The Confocal Principle . . . . .	7
3.3	Pulsed Interleaved Excitation . . . . .	9
3.4	Confocal setups used for this work . . . . .	9
3.4.1	Two-color PIE multi-parameter setup . . . . .	10
3.4.2	Three-color PIE scanning setup . . . . .	10
<b>4</b>	<b>Fluorescence Fluctuation Spectroscopy</b>	<b>15</b>
4.1	Basic Considerations . . . . .	15
4.2	Number&Brightness Analysis . . . . .	16
4.2.1	Detector noise correction . . . . .	17
4.3	The Photon Counting Histogram . . . . .	19
4.3.1	Theory of photon detection: Mandel's formula . . . . .	19
4.3.2	From Mandel to number and brightness . . . . .	20
4.3.3	Multiple fluorescent species . . . . .	23
4.4	Fluorescence-Intensity Distribution Analysis . . . . .	24
4.4.1	The Point Spread Function in FIDA . . . . .	24
4.4.2	The Generating Function . . . . .	26
4.5	Fluorescence Cumulant Analysis . . . . .	28
4.5.1	Moments . . . . .	28
4.5.2	Factorial moments . . . . .	29
4.5.3	Moment generating function . . . . .	29
4.5.4	Factorial moment generating function . . . . .	30
4.5.5	Cumulants and the CGF . . . . .	31
4.5.6	Factorial Cumulants and the FCGF . . . . .	32
4.5.7	Derivation of FCA . . . . .	32
4.6	Fluorescence Correlation Spectroscopy . . . . .	35
4.6.1	The autocorrelation function . . . . .	35
4.6.2	Fluorescence intensity time dependence . . . . .	37
4.6.3	Model for linear regression . . . . .	37
4.6.4	Triplet states . . . . .	41
4.7	Fluorescence Cross-Correlation Spectroscopy . . . . .	42
4.7.1	The cross-correlation function . . . . .	42

4.8	Scanning FCS . . . . .	44
4.8.1	The Scanning correlation curve . . . . .	45
4.9	Raster Image Correlation Spectroscopy . . . . .	47
4.10	Burst Analysis . . . . .	48
4.10.1	Burst analysis with PIE . . . . .	50
4.11	Photon Distribution Analysis . . . . .	52
4.11.1	PDA theory . . . . .	52
<b>5</b>	<b>Method Development with PIE</b>	<b>56</b>
5.1	Scanning FCS with PIE . . . . .	56
5.2	PIE-Scanning FCS in aqueous solution . . . . .	57
5.3	Raster Image Correlation Spectroscopy with PIE . . . . .	60
5.4	PIE-RICS in aqueous solution . . . . .	61
5.5	PIE-RICS in living cells . . . . .	64
5.6	Application to Ca <sub>v</sub> 1.4 channel domain . . . . .	69
5.7	Application to Ca <sub>v</sub> 1.4 channel ICDI subdomain . . . . .	71
5.8	Discussion . . . . .	73
<b>6</b>	<b>Dnmt1</b>	<b>75</b>
6.1	Introduction . . . . .	75
6.2	Sample preparation . . . . .	76
6.3	Excitation power analysis . . . . .	76
6.4	GFP/GBP . . . . .	78
6.5	Dnmt1:DNA complexes . . . . .	82
6.6	Dnmt1 cross-correlation . . . . .	86
6.7	DNA cross-correlation . . . . .	88
6.8	Further investigation of the Dnmt1:DNA bonds . . . . .	91
6.9	Discussion . . . . .	93
<b>7</b>	<b>Burst Analysis study of conformational changes of BiP</b>	<b>96</b>
7.1	BiP . . . . .	96
7.2	Sample preparation . . . . .	97
7.3	Monitoring BiP conformations . . . . .	99
7.3.1	Inter-domain communication . . . . .	101
7.3.2	Conformation of the lid . . . . .	102
7.4	The co-chaperone ERdj3 . . . . .	105
7.5	Discussion . . . . .	109
<b>8</b>	<b>Summary and Outlook</b>	<b>112</b>
<b>A</b>	<b>Spectra</b>	<b>114</b>
A.1	Two-color PIE multi-parameter setup . . . . .	115
A.2	Three-color PIE scanning setup . . . . .	116
A.2.1	Dnmt1 configuration . . . . .	116
A.2.2	RICS configuration . . . . .	118
<b>B</b>	<b>Computer code</b>	<b>119</b>
B.1	Number & Brightness . . . . .	119
B.2	Fast correlation algorithm [1] . . . . .	120

B.3	Fit algorithm for PCH and FIDA . . . . .	121
B.4	Cumulant Analysis . . . . .	123



# 1 Introduction

Life, in the biophysicist's eye, is governed by the interactions of an enormously complex network of biomolecules, including DNA, RNA, and proteins. All organisms can be regarded as mere accumulations of cells, and the cellular life cycle is maintained by their molecular machinery, constituted, to a large extent, by proteins. The genetic information that encodes this machinery, and therefore life as such, is encoded in DNA. It is then transcribed into messenger RNA by interaction with RNA polymerase and other proteins. Subsequently, it is translated into a vast diversity of proteins suited to perform all different kinds of functions in a cell (and even outside). Therefore, studying proteins, their cellular localizations, their interactions with other biomolecules, and properties such as their conformational states leads to a deeper understanding of how life works on a cellular level.

Today, thanks to the recent decades of technological advances, many biochemical and biophysical methods are available to investigate proteins. For example, their internal structure, formed by the spatial arrangement of peptide chains, can be resolved by X-ray crystallography or nuclear magnetic resonance spectroscopy; electron microscopy or optical super-resolution techniques show their localization within a cell; gel electrophoresis yields information about their abundance and about binding partners; ultracentrifugation or mass spectroscopy can measure their molecular weight; and force spectroscopy probes the strength of intra- or inter-molecular bonds.

Few of these methods, however, allow the scientist to observe a protein in its natural environment, a living cell. Crystallization, for example, alters the energy landscape and therefore the tertiary structure of a protein, and conformational substates are often lost. For super-resolution optical methods or electron microscopy, cells generally have to undergo fixation. It is therefore advantageous to use techniques where the proteins remain in a buffered solution, where they can diffuse freely and their structure is not generally altered by their environment, thus approaching intracellular conditions. A variety of methods summarized under the generic term "Fluorescence Fluctuation Spectroscopy" (FFS) are examples for this approach. Observing proteins within a living cell, however, is an even more ideal approach, since their structure is often influenced by their interaction with a multitude of other proteins and cytosolic molecules. Since cells are generally transparent for light, fluorescence based methods provide a minimally invasive way to observe proteins within a living cell, and are therefore becoming more and more important. It will be part of this work to apply and improve a selection of FFS methods in live-cell measurements.

All FFS methods share a key concept: the noise of the measured fluorescence intensity is not regarded as a perturbation obstructing the actual signal, but as a carrier of valuable information. Since part of the noise is caused by the Brownian diffusion of fluorescent molecules in and out of the observation volume of a confocal microscope, information about these molecules can be extracted from the noise. With correlation-based methods such as Fluorescence Correlation Spectroscopy (FCS), including methods specially adapted to live-cell measurements such as Scanning FCS and Raster Image Correlation Spectroscopy (RICS), the diffusion coefficient

and thus the mobility of a molecule or complex, influenced for example by its size or by interactions with its environment, can be extracted from the signal fluctuations. With Fluorescence Cross-Correlation Spectroscopy and its derivatives, molecular binding can be characterized. Since modern fluorescence detectors count single photons, different approaches to analyze FFS experiments become possible. With the different forms of fluorescence brightness analysis, the number of photons that are detected within fixed time bins are analyzed, yielding information about the molecular brightness of the sample molecules. Thereby, multimer formation or polymerization can be investigated. Very sensitive detectors allow the detection of the fluorescence bursts caused by the diffusion of a single molecule, thus in combination with single pair Förster resonance energy transfer (FRET), the measurement of intramolecular distances becomes possible, shedding light on changes in protein conformation.

Within the scope of this work, methods from all of these categories are implemented and optimized. Some methods, especially the cross-correlation-based techniques, are improved in accuracy by their combination with Pulsed Interleaved Excitation (PIE), a way to remove spectral crosstalk. However, since biophysical methods should never be ends in themselves, the second focus of this work is the application of the most advanced FFS techniques to actual biological and biochemical problems.

Scanning FCS and RICS are fused with PIE to equip them with the ability to unambiguously determine whether two molecular species bind together or not. The binding of Calmodulin to the CaV1.4 calcium channel is then investigated with PIE-RICS, as well as the inhibitory function of its ICDI domain (Chapter 5).

Fluorescence Cross-Correlation Spectroscopy (FCCS) in combination with PIE, and a variety of fluorescence brightness analysis methods are used to study the binding of DNA methyl transferase 1 (Dnmt1) to substrate DNA strands featuring a modified CpG to trap Dnmt1 with a covalent bond during the methylation reaction. Surprisingly, molecular complexes consisting of monomeric Dnmt1, but more than one DNA strand are found with brightness analysis, and confirmed with PIE-FCCS (Chapter 6).

Finally, single molecules Burst Analysis in combination with PIE and FRET are the methods of choice to investigate the changes in the conformation of the Hsp70 chaperone BiP. Different conformational states are found for the ADP-bound and the ATP-bound state. The effects of different substrates as well as of the co-chaperone ERdj3 are identified, yielding a comprehensive picture of the conformational life cycle of BiP (Chapter 7).



## 2 Fluorescence

### 2.1 Fundamentals

*Fluorescence* is the emission of light by molecules of particular species (*fluorophores*), after they were excited into their electronic  $S_1$  state by exposure to light of a different wavelength. A molecule can absorb a photon of wavelength  $\lambda_1$  and energy  $E_1 = \frac{hc}{\lambda_1}$ , shifting one of its electrons into an excited state. After a short time in the nanosecond range, the molecule relaxes and another photon of wavelength  $\lambda_2$  and according energy  $E_2$  is released, where  $\lambda_2 \geq \lambda_1$  and  $E_2 \leq E_1$ . The quantum mechanical processes involved in fluorescence are illustrated by the Jablonski diagram (Figure 2.1).

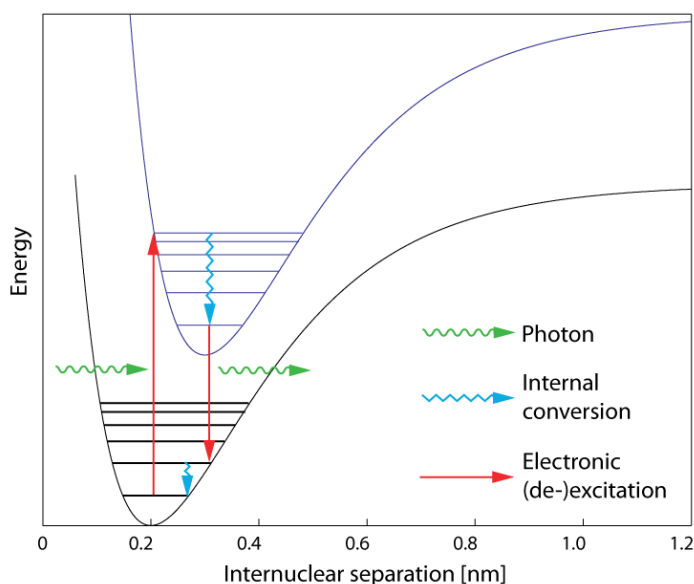


**Figure 2.1:** Jablonski diagram. An incoming photon shifts an electron into an excited state. After internal conversion to the vibrational ground state, the electron returns to the electronic ground state via emission of a fluorescence photon.

When a molecule in the vibrational ground state is electronically excited, the vibrational equilibrium positions of its nuclei change, but according to the *Franck-Condon principle*, the positions of atomic nuclei remain constant during an electronic transition. Hence, the molecule ends up in a vibrationally excited state, and relaxes into its new vibrational ground state before it is electronically deexcited, losing a fraction of its potential energy in the process. The same mechanism applies a second time after electronic relaxation, contributing to the total amount of dissipated energy  $\Delta E = E_1 - E_2$ . This results in the effect that the emitted photons generally have longer wavelengths than the excitation photons and leads to distinct absorption and emission spectra, whose maxima  $\lambda_{1,max}$  and  $\lambda_{2,max}$  are separated by the *Stokes shift*  $\Delta\lambda = \lambda_{2,max} - \lambda_{1,max}$  (Figure 2.2). This is very convenient for fluorescence spectroscopy and

microscopy, because the excitation light – if its wavelength is chosen carefully – can be spectrally separated from the fluorescence emission by optical filters, allowing even the detection of light from a single fluorophore.<sup>1</sup>

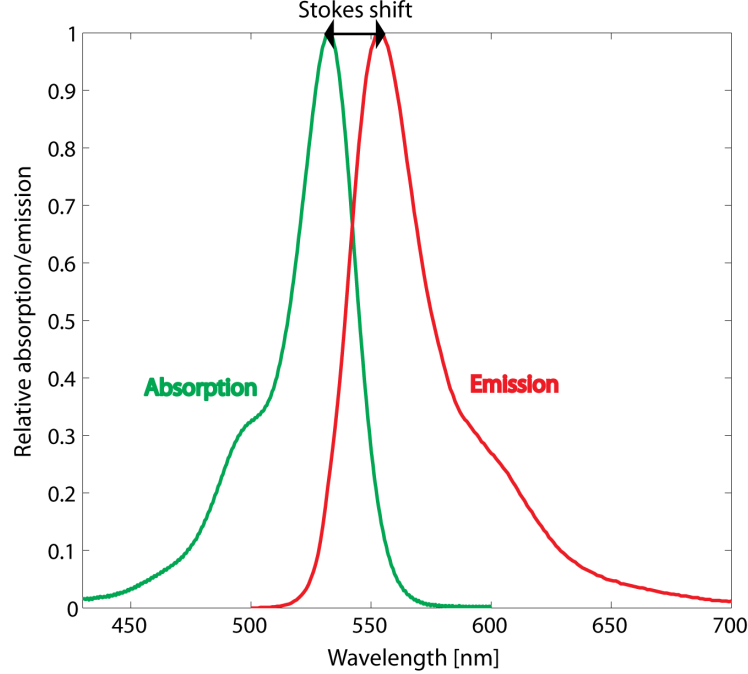


**Figure 2.2:** Stokes shift. The maxima of the absorption and emission spectra of the commercial fluorophore ATTO 532 are separated by a Stokes shift of 21 nm.

Two important attributes of a fluorophore are its *quantum yield*  $\Phi$  and its *fluorescence lifetime*  $\tau$ . Upon excitation, a fluorescence photon can be emitted, or the fluorophore can be de-excited via other pathways, such as nonradiative relaxation or energy transfer to an acceptor fluorophore. The quantum yield is the fraction of absorption processes that actually result in the emission of a fluorescence photon, and can also be expressed in terms of the deexcitation rates  $k$ :

$$\Phi = \frac{\text{Number of emitted photons}}{\text{Number of absorbed photons}} = \frac{k_{\text{fluorescence}}}{k_{\text{fluorescence}} + k_{\text{alternative}}} \quad (2.1)$$

Equation 2.1 bears important consequences. The higher the rate of alternative deexcitation processes  $k_{\text{alternative}}$ , the lower the quantum yield  $\Phi$ . Furthermore, a low quantum yield leads to a decrease in the characteristic time span between excitation and emission, the fluorescence lifetime  $\tau$ , which is experimentally accessible:

$$\tau = \frac{1}{k_{\text{fluorescence}} + k_{\text{alternative}}} \quad (2.2)$$

Since fluorescence is a quantum mechanical process, photon emission times are randomly distributed. The emission probability is constant in time, which results in an exponential fluorescence intensity decay for an ensemble of fluorophores:

<sup>1</sup>Note that the emission spectrum is generally independent of the chosen excitation wavelength.

$$I(t) = I_0 e^{-\frac{t}{\tau}} \quad (2.3)$$

$I_0$  is the emission intensity for  $t = 0$ .

## 2.2 Fluorescence Anisotropy

The absorption of excitation light by a fluorophore and the fluorescence emission are both polarization-dependent processes. The excitation probability is highest when the electric transition moment of a fluorophore is aligned parallel to the electric polarization plane of the incident light, which, in the case of laser excitation, usually has linear polarization<sup>2</sup>. Depending on the speed of molecular rotation relative to the fluorescence lifetime  $\tau$ , the orientation of the electric transition moment at the moment of fluorescence emission can either still be correlated to its position upon excitation, or, if the rotation is very fast, it can be uncorrelated. The magnitude of those correlations influences the polarization of the fluorescence of the sample, which can take any form from linear polarization for a stationary sample to unpolarized for a sample containing rapidly rotating molecules. This phenomenon can be quantified by the *fluorescence anisotropy*  $r$  of the sample:

$$r = \frac{I_{\parallel} - I_{\perp}}{I_{\parallel} + 2I_{\perp}} \quad (2.4)$$

where  $I_{\parallel}$  and  $I_{\perp}$  are the fractions of the fluorescence emission polarized parallel and perpendicular to the excitation light, respectively. Measuring the anisotropy can yield valuable information about the magnitude of a fluorescent molecule and its environment. Synthetic fluorophores are usually fairly small molecules, so in case they are freely diffusing, their anisotropy will be close to zero. However, when they are used to label a macromolecule such as e.g. a protein, their rotational freedom is confined resulting in a larger anisotropy. If there is no rotational freedom of the label itself, the anisotropy is determined by the rotation of the macromolecule, which in turn is based on its size. In reality, however, the label has a certain degree of rotational freedom due to linker flexibility, resulting in a time dependent anisotropy that is high for very short times and then quickly relaxes to a residual value, the anisotropy of the labeled macromolecule. Knowledge of the anisotropy of a molecule is valuable because it yields information about its spatial dimensions.

## 2.3 Förster Resonance Energy Transfer

*Förster Resonance Energy Transfer* (FRET) [2] is the nonradiative transfer of excitation energy between two fluorophores in close proximity. The *donor* fluorophore is excited, and then transfers its energy by dipole–dipole coupling to the *acceptor* fluorophore. The strength of interaction can be characterized by the FRET efficiency  $E$ , which represents the fraction of absorption processes that result in an energy transfer.  $E$  can also be expressed in terms of the deexcitation rates  $k$ :

$$E = \frac{\text{Number of transfers}}{\text{Number of absorbed photons}} = \frac{k_{FRET}}{k_{fluorescence} + k_{nonradiative} + k_{FRET}} \quad (2.5)$$

---

<sup>2</sup>if the polarization of the laser light is imperfect, for example due to depolarization within a fiber, a linear polarization filter can be used to improve the polarization.

The FRET efficiency  $E$  shows a very strong dependence on the distance between donor and acceptor, a fact that makes it a valuable tool to measure distances on the molecular level. Due to the  $\frac{1}{r^3}$  dependence of the near field electric dipole potential [3], both the donor emission and the acceptor excitation probability scales with  $\frac{1}{r^3}$  and therefore  $E$  decays with the product  $\frac{1}{r^6}$ :

$$E(r) = \frac{R_0^6}{R_0^6 + r^6} \quad (2.6)$$

The *Förster radius*  $R_0$  is the donor–acceptor distance at which  $E = 0.5$ , and is typically of the order of 5 nm.  $R_0$  mainly depends on the quantum yield of the donor  $\Phi_D$ , the overlap integral  $J$  between the donor emission spectrum and the acceptor excitation spectrum (hence the term "resonance"), and on the relative orientation of the electric dipole moments of donor and acceptor, characterized by  $\kappa^2$ :\*

$$R_0 = \sqrt[6]{\frac{9000\kappa^2\Phi_D\ln(10)J}{128\pi^5N_A n^4}} \quad (2.7)$$

$N_A$  is Avogadro's number, and  $n$  is the refractive index of the surrounding medium.

---

\*In the case of freely rotating donor and acceptor fluorophores,  $\kappa^2 = \frac{2}{3}$

## 3 Optical system

In this chapter, the theoretical foundations of confocal microscopy are briefly outlined, and the two confocal microscope setups with Pulsed Interleaved Excitation that were used for the experimental work in this thesis are introduced. Both setups are very similar in design but differ in various important details. The two-color PIE multi-parameter setup (Section 3.4.1) is able to resolve the fluorescence anisotropy, but is limited to only two different wavelengths. Knowledge about the anisotropy is important for single molecule Burst Analysis studies (Chapter 7), because it yields information about the rotational freedom of fluorescent labels and thereby aids to determine more accurate FRET results. The three-color PIE scanning setup lacks the anisotropy capabilities, but provides an additional wavelength, thereby allowing to study complex biomolecular reactions with three different binding partners (Chapter 6). Furthermore, with the optical scanner incorporated in this setup, the development and application of advanced fluorescence fluctuation spectroscopy techniques such as Scanning Fluorescence Correlation Spectroscopy and Raster Image Correlation Spectroscopy (Scanning FCS and RICS, Chapter 5) becomes possible.

### 3.1 Confocal Microscopy

The aim of confocal microscopy is to achieve an optimized optical resolution in all three spatial dimensions compared to standard light microscopy. Its basic concept is to observe the fluorescence intensity consecutively in very small pixels of the sample, out of which a complete raster image or even a three dimensional sample reconstruction can be composed. This is achieved by combining a strongly focused illumination with fluorescence detection through a very small aperture, the *confocal pinhole*, with a diameter in the range of  $50\text{ }\mu\text{m}$ . The minimal size that the light can be focused to determines the optical resolution of the system. The focal size and thereby the optical resolution  $R$  is limited by the Abbe limit to a diameter of around  $200\text{ nm}$ , depending on the wavelengths used (Formula 3.1).

### 3.2 The Confocal Principle

Minsky, the inventor of the confocal microscope, used a lamp in combination with a pinhole and a lens to illuminate only a small spot, the projection of the illumination pinhole, in the focal plane of sample [4]. Today, lasers are usually chosen as illumination sources for a confocal microscope, because the coherent light that they produce can be collimated very accurately with a Gaussian beam shape and can therefore also be used to create a diffraction limited illumination spot in the focal plane. Furthermore, their highly monochromatic light can easily be filtered out to separate excitation from emission light. An objective designed to have an immersion medium, typically water or a special immersion oil, between the objective surface and the glass cover slip, is preferably used to focus the light into the sample. That way, interfaces with a high difference in refractive index can be avoided, which increases the numerical aperture  $N_A$ .  $N_A$  is a dimensionless quantity that specifies the maximum angle that the objective can still observe. A high  $N_A$  is preferable to focus the light into the sample, because

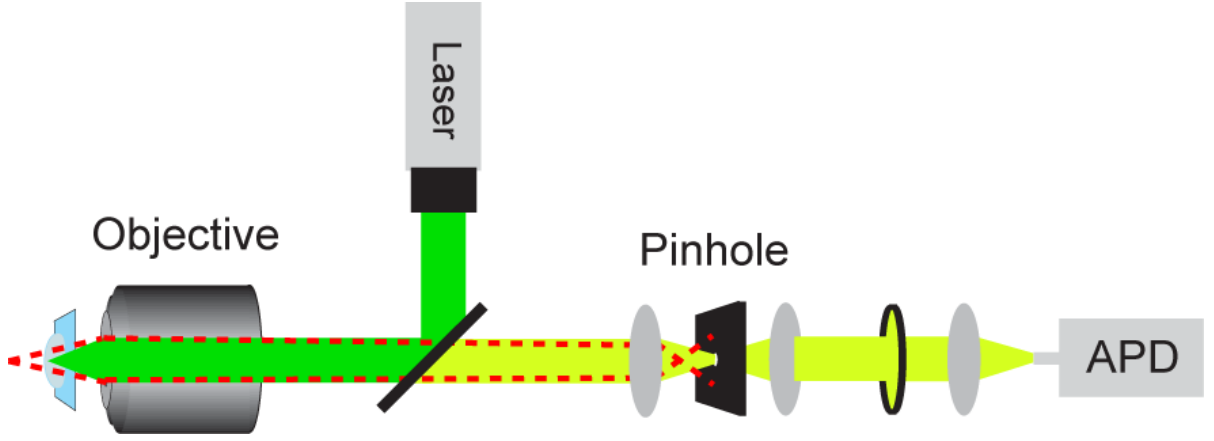


**Figure 3.1:** The confocal principle: A diffraction limited spot in the sample is illuminated by a strongly focused laser (green beam). The fluorescence from that spot is guided through the confocal pinhole (yellow beam). Any fluorescence originating from a plane above or below the focal plane cannot pass the pinhole because it will be focused above or below the conjugated plane where the pinhole resides (red dashed line).

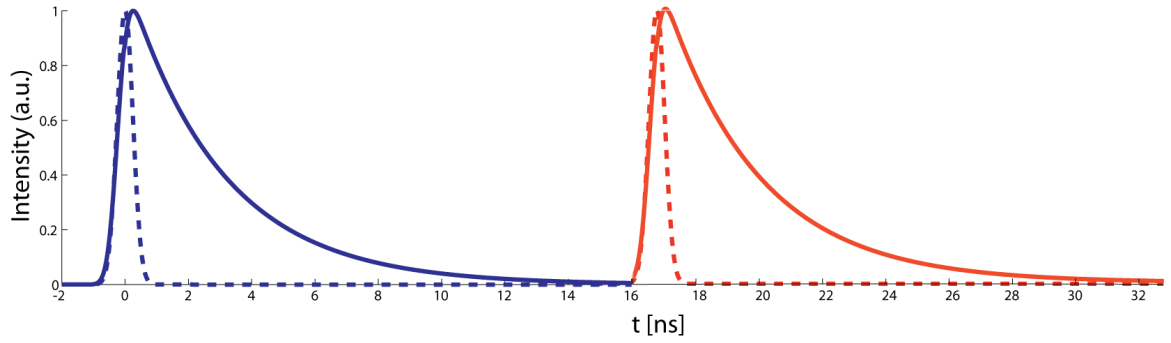


**Figure 3.2:** Pulsed Interleaved Excitation: Pulsed laser sources of different wavelengths (dashed lines) with sub-nanosecond pulse widths are interleaved with each other, generating a pulse train with a spacing sufficiently large to fit the complete fluorescence decays of matching fluorophores (continuous lines) in between.

the size of the focus is reciprocal to  $N_A$  (Formula 3.1). Since above and below the focal plane, increasingly large areas of the sample are also illuminated by the defocused excitation light, a second optical element is necessary to implement confocal microscopy. The *confocal pinhole* is placed into the conjugated plane in the detection pathway, so that any fluorescence originating from points outside the focal plane is strongly attenuated (Figure 3.1) Thus, the strongly focused illumination in combination with the fluorescence detection through a pinhole guarantee that only fluorescence from a very small, diffraction limited spot, described by the *point spread function* (PSF, see Section 4.3.2), is measured. The lateral resolution of a confocal microscope in the theoretical limit of an infinitesimally small pinhole is described by:

$$R_{lateral} = \frac{0.37\lambda_{excitation}}{N_A} \quad (3.1)$$

### 3.3 Pulsed Interleaved Excitation

*Pulsed Interleaved Excitation* (PIE, [5]) is a technique to provide extra information for each detected fluorescence photon in a confocal microscope. In many experimental scenarios, the simultaneous use of two or more lasers with different wavelengths is desirable to excite multiple fluorophores with sufficiently separated excitation and emission spectra. However, in almost all cases, there exists a spectral overlap between those fluorophores. Hence, when the resulting fluorescence photons are optically sorted according to their wavelength, a fraction of typically up to 20 % of the photons can be erroneously assigned as originating from the wrong fluorescent species, depending on the relative position of the spectra with respect to each other and the optical filters used to separate them. This phenomenon is referred to as *spectral crosstalk* or *bleed-through*. To address this problem, pulsed laser sources with pulse lengths in the sub-nanosecond range and high repetition rates of typically  $> 10$  MHz are used in PIE that are interleaved with respect to each other, so that a pulse train with a spacing in the nanosecond range is generated. If these lasers are additionally synchronized with a time correlated single photon counting (TCSPC) system, each fluorescence photon can be assigned to the excitation by one of the laser sources due to the close temporal proximity. Hence, it becomes possible to precisely determine the emitting fluorescent species and remove artifacts due to spectral crosstalk. This is of great advantage especially for *in vivo* measurements, where fluorescent proteins with a large spectral overlap are used, for example the widely used pair of *Green Fluorescent Protein* and *Red Fluorescent Protein* (GFP and RFP). Additionally, in single molecule FRET measurements, the presence of a functioning acceptor fluorophore can be tested simultaneously with the two-channel detection of donor and FRET emission. Also, in a PIE setup, the fluorescent lifetime decay is automatically measured and stored as part of the measurement, further contributing to the wealth of data that is generated from just one measurement.

### 3.4 Confocal setups used for this work

Two experimental setups were used in the scope of this work. The two-color PIE multi-parameter fluorescence detection setup (MFD, [6]) is a confocal microscope designed for the use of synthetic fluorophores with excitation maxima around 532 nm and 635 nm such as ATTO 532 and ATTO 647N. Since there is neither a piezo scanning table nor a galvanometric beam scanner, this setup is used for fluorescence fluctuation spectroscopy measurements where the PSF stays at a stationary point in the sample. In the detection pathway, the fluorescence from each species is separated according to its polarization, allowing the measurement of the fluorescence anisotropy of a sample. This feature, combined with the availability of a very well established FRET pair at the wavelengths present (ATTO 532 and ATTO 647), makes this setup ideally suited for burst analysis measurements with Photon Distribution Analysis (PDA, Sections 4.10 and 4.11).

The three-color PIE scanning setup is a confocal laser scanning microscope with a galvanometric scanner unit designed for the use of a broad spectrum of fluorophores such as for example the fluorescent proteins GFP and RFP, or a combination of synthetic dyes with excitation maxima around 473 nm, 561 nm, 635 nm, and 690 nm such as the according ATTO or Alexa dyes. The fast galvanometric scanner in combination with the wavelengths that match GFP and RFP make this setup ideally suited for live-cell measurements such as imaging, Scanning FCS (Section 4.8), or RICS (Section 4.9). Furthermore, the possibility of observing three different

fluorescent species at the same time allow for studies of complex formation with up to three binding partners.

### 3.4.1 Two-color PIE multi-parameter setup

The internal oscillator of a pulsed laser controller (Sepia: main module PDL 808, oscillator SOM 808, sequencer SSM 808, signal splitter SPM 808, four laser drivers SLM 808, PicoQuant, Berlin, Germany) was used to synchronize two pulsed lasers (PicoTA at 532 nm, LDH-D-C-640 at 635 nm, PicoQuant) such that a pulse train of the two lasers was generated with a close to equal spacing between the different colors. One cycle lasted  $\frac{1}{26.7 \text{ MHz}} = 37.5 \text{ ns}$ , resulting in a time window of  $\sim 18 \text{ ns}$  after each excitation pulse for the fluorescence intensity decay.

Both lasers were coupled into single mode fibers by the manufacturer (laser collimators: 60SMS-1-4-A11-01, 60SMS-1-4-A11-02, Schäfter+Kirchhoff, Hamburg, Germany) and superimposed using a fiber coupled dichroic unit set (WDM-12P-111-532/647-3.5/125-PPP-50-3A3A3A-3-1,1,2:OZ, AMS Technologies, Munich, Germany). The beam was collimated by an achromatic collimator (60FC-4-RGB11-47, Schäfter+Kirchhoff) to ensure a highly conformous collimation for the different colors, an important prerequisite for a good overlap of the three excitation volumes. A  $60\times$  water immersion objective (Plan Apo VC  $60\times$  A/1.20 W, Nikon, Düsseldorf, Germany), mounted in an Eclipse TE300 microscope base (Nikon) was used to focus the beam into the sample. The laser power was usually measured before the final dichroic mirror separating excitation from emission light. 39.2 % of the excitation laser light was transmitted into the sample for 532 nm and 30.7 % for 635 nm.

Fluorescence emission was collected by the same objective, separated from the excitation light by a dichroic mirror (DualLine z532/635, AHF Analysentechnik, München, Germany), and focused onto a pinhole with a diameter of  $50 \mu\text{m}$  (OWIS, Staufen, Germany). The light was collimated again, split into two separate beams according to the two polarizations, and each beam was then further spectrally separated by a dichroic mirror (HC- Beamsplitter BS650, AHF Analysentechnik) according to the emission spectra of the fluorophores used. Each of the resulting beam fractions passed through a carefully chosen bandpass filter (BrightLine HC582/75, ET700/75, AHF Analysentechnik) for further spectral cleanup. An overview over the transmission spectra of the different optical elements is given in the appendix, Figures A.1 and A.2. Each fraction was focused onto the sensitive area of an avalanche photodiode (APD) incorporated in a single photon counting module (SPCM-AQR-14, SPCM-AQR-16, Laser Components, Olching, Germany) with TTL output. All lenses used in this setup were achromatic lens doublets (AC254-xxx-A, xxx is focal length in mm, Thorlabs, Dachau, Germany).

The TTL signal was directly fed into a TCSPC recording system (SPC-154, Becker & Hickl, Berlin, Germany) consisting of four PCI cards, one for each detector. The TCSPC system was synchronized to the Sepia controller so the according excitation laser could be assigned to each detected fluorescence photon.

### 3.4.2 Three-color PIE scanning setup

A pulsed fiber laser with a fixed repetition rate of 27.4 MHz (FFS.SYS-CONT-COMP-TSHG, TOPTICA Photonics, Gräfelfing, Germany) was tuned to a wavelength of 561 nm. An infrared low pass filter (KG5, Schott, Mainz, Germany; transmission spectrum is shown in the appendix, Figure A.3) was used to spectrally clean up the laser light, because an additional



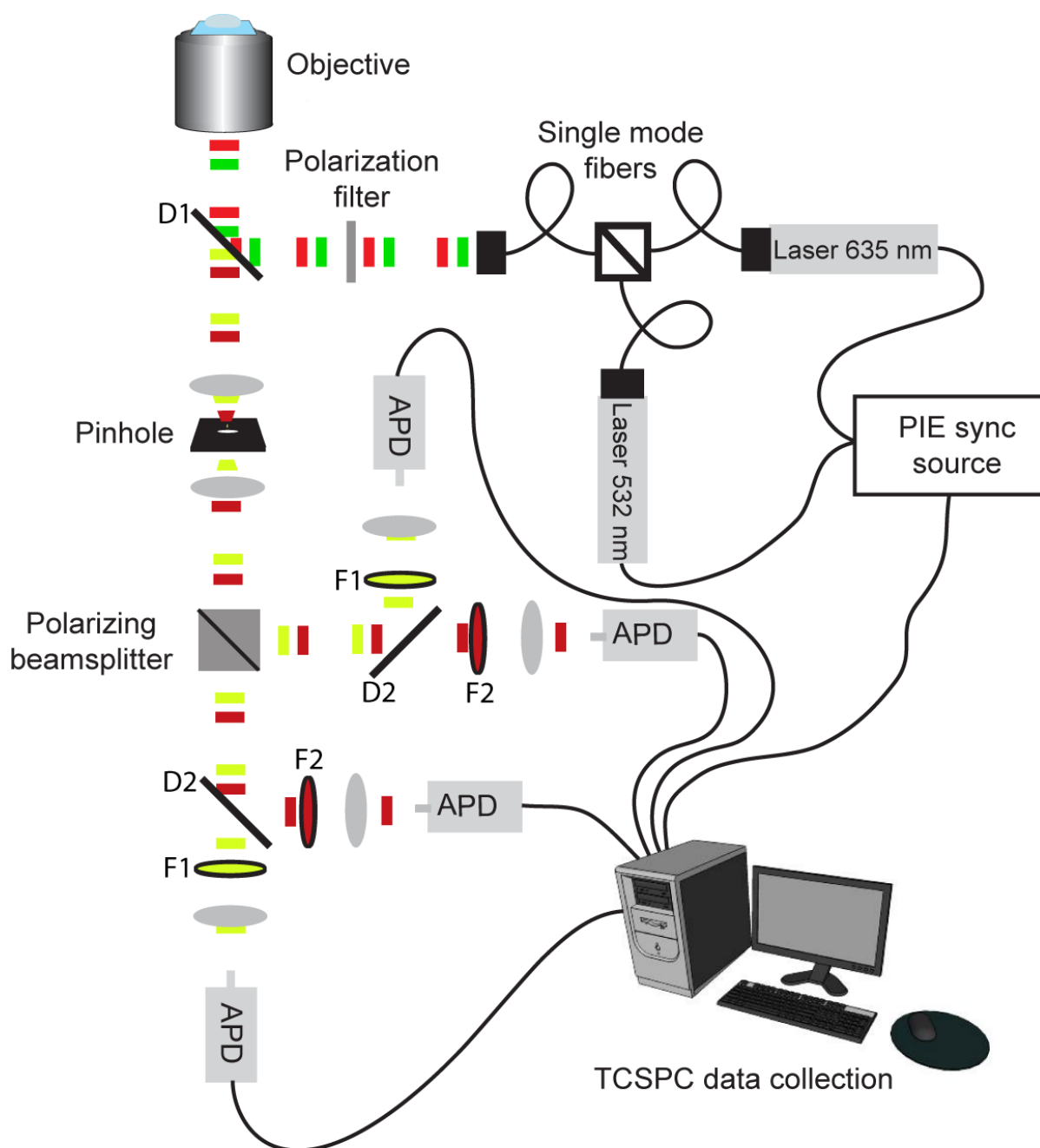


**Figure 3.3:** Schematic of the two-color PIE multi-parameter setup. The fluorescence is divided into two beams with different polarizations by a polarizing beam splitter before separating the two colors from the different fluorophores. Refer to appendix A for spectra of the used filters and dichroic mirrors.

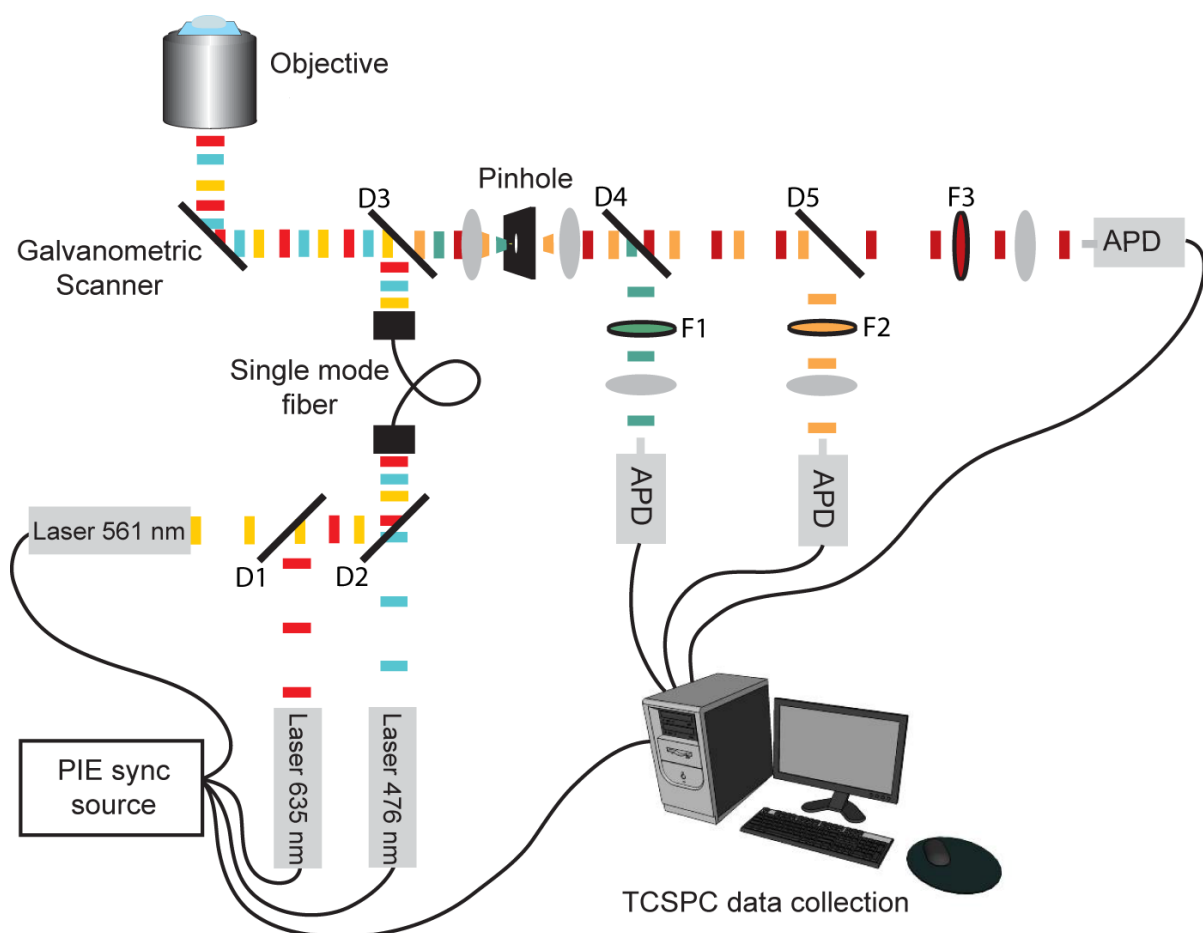


**Figure 3.4:** Schematic of the three-color PIE scanning setup in the configuration used for the RICS and Scanning FCS measurements (Chapter 5). For the Dnmt1 measurements, the 635 nm laser was replaced by a 690 nm laser, and the galvanometric scanner by a mirror. Refer to appendix A for spectra of the used filters and dichroic mirrors.

fraction of infrared light is emitted by this laser due to technical reasons. The laser served as a PIE synchronization source for the whole setup: The laser pulses were converted into electrical ones by a photodiode within the laser. The resulting electrical pulses were broadened to meet the input specifications of the central PIE controller (Sepia II: main module PDL 828, controller SCM 828, oscillator SOM 828, two laser drivers SLM 828, PicoQuant). Two further pulsed lasers (LDH-P-C-470 at 476 nm, LDH-P-C-690 at 690 nm, PicoQuant) were driven by the Sepia II module such that a pulse train of all three lasers was generated with a close to equal spacing between the different colors. One cycle lasted  $\frac{1}{27.4 \text{ MHz}} = 36.5 \text{ ns}$ , resulting in a time window of  $\sim 12 \text{ ns}$  after each excitation pulse for the fluorescence intensity decay. An additional output of the PIE controller was fed into the detection system for synchronization purposes.

The three lasers were superimposed using two dichroic mirrors (500DCXR, 600DCSP, AHF Analysentechnik; transmission spectra are shown in the appendix, Figure A.4) and coupled into a single mode fiber (coupler: HRJC-23AF-400/700-P-20AC, fiber: QPMJ-A3A,3AF-488-3.5/125-3-5-1, OZ Optics, Ottawa, Canada) to achieve a Gaussian beam profile. An achromatic collimator (60FC-4-RGB11-47, Schäfter+Kirchhoff) was used to collimate all three colors.

For the investigations on Dnmt1 (Chapter 6), a  $63\times$  water immersion objective (C-Apochromat  $63\times 1.20 \text{ W}$ , Zeiss MicroImaging, Göttingen, Germany), mounted in a Axiovert 200 microscope base (Zeiss MicroImaging) was used to focus the beam into the sample. For the development of PIE-ScanningFCS and PIE-RICS (Chapter 5), a galvanometric scanner unit with two mirrors for  $x$  and  $y$  (scanner: 6210H, controller: MicroMax 673 Series, Cambridge Technology, Cambridge, USA) in combination with two lenses forming a telescope was installed to scan the beam, and a  $60\times$  water immersion objective (Plan Apo VC  $60\times \text{A}/1.20 \text{ W}$ , Nikon), mounted in an Eclipse TE200 microscope base (Nikon) was used for focusing. The laser power was usually measured before the final dichroic mirror separating excitation from emission light. 39.3 % of the excitation laser light was transmitted into the sample for 476 nm and 41.8 % for 561 nm.

To determine the ideal position for the galvanometric scanner in the beam path, a series of alignment steps were undertaken. First, the two lenses were adjusted so that the two foci overlapped and the telescope was focused at infinity. Then the scanner was placed into one of the outer telescope foci<sup>1</sup> and the back aperture of the objective into the other. For fine adjustment, a laser beam was guided into the setup, the objective lens was removed, a continuous circular scanning pattern was executed by the scanner, and the position of the objective's back aperture was determined to be the point where the laser beam was laterally immobile.

The fluorescence emission was collected by the same objective, separated from the excitation light by a dichroic mirror (Dnmt1: LC-470-568-690TBDR, Laser Components, RICS: R405/488/561/635, AHF Analysentechnik), and focused onto a pinhole with a diameter of  $50 \mu\text{m}$  for the Dnmt1 measurements, or  $80 \mu\text{m}$  for RICS (OWIS). The light was collimated again, then spectrally separated by two subsequent dichroic mirrors (Dnmt1: 565DCXR, 680DCXR, RICS: 565DCXR, FF650-Di01, AHF Analysentechnik) according to the emission spectra of the different fluorophores used. Each of the three resulting beam fractions passed through a carefully chosen bandpass filter (Dnmt1: HQ 525/50 M, HQ 620/80 M, and HQ 715LP custom modified with an extra block from 400 nm to 700 nm, RICS: HQ 525/50 M, ET

<sup>1</sup>Since the scanner consisted of two mirrors with a spatial separation, it was impossible to place both mirrors into the telescope focus at the same time. However, the manufacturer designed them to be so close to each other that placing the central point in between them into the focus caused only negligible deviations.

595/50 M, and ET 700/75 M, AHF Analysentechnik) for further spectral cleanup. An overview over the transmission spectra of the different optical elements is given in the appendix, Figures A.5 and A.6 (Dnmt1 configuration), and Figures A.7 and A.8 (RICS configuration). Each fraction was focused onto the sensitive area of an avalanche photodiode (APD) incorporated in a single photon counting module (SPCM-AQR-13, SPCM-AQR-14, Laser Components) with TTL output. All lenses used in this setup were achromatic lens doublets (AC254-xxx-A, xxx is focal length in mm, Thorlabs).

The TTL signal was conducted through several home built devices (a signal splitter and a 0 – 47 ns pulse delay box) into a TCSPC recording system (SPC-143, Becker & Hickl) consisting of three PCI cards, one for each detector.

## 4 Fluorescence Fluctuation Spectroscopy

### 4.1 Basic Considerations

All of the data evaluation methods that will be described in this chapter are in one way or another making use of the fluctuations in the detected fluorescence signal that arise due to fluorophores diffusing in and out of the confocal volume. Therefore it is important to gain a mental image of how the fluorescence signal is connected to the physical diffusion processes in the confocal volume. For the fluctuations to be visible, the concentration of fluorophores in the sample has to be low enough so that one fluorophore can still change the measured fluorescence intensity significantly enough to be detectable. Typical concentrations for FFS measurements lie within the range of 1 – 100 nM. The limiting factors are the photodetector background noise, which becomes dominant for very low concentrations, and the detector count rate saturation limit yielding an upper boundary.

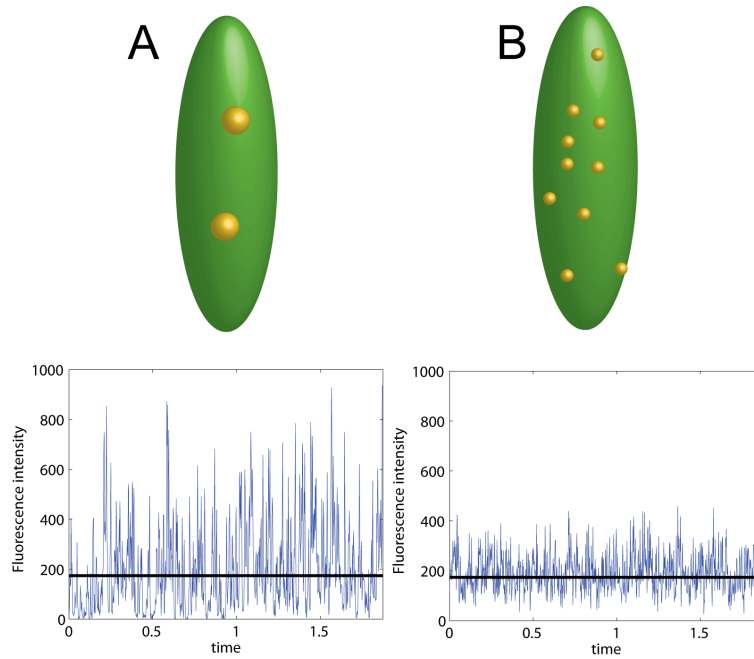


**Figure 4.1:** Two example fluorescence fluctuation measurements: (A) measurement with few large particles of high brightness, (B) measurement with many small particles of low brightness. The average intensity is equal in both cases, whereas the relative size of the fluctuations is larger in case (A) than in case (B).

Consider two solutions of different fluorophores A and B, where A is five times brighter than B under the given experimental conditions, but the concentration of A is five times lower than B, then the mean value  $\langle I \rangle$  of the detected fluorescence intensity will be equal for both solutions. Nevertheless, the fluctuations in the fluorescence signal are much higher for solution A, because the process of a fluorophore A diffusing into or out of the confocal volume will cause a much

larger change in the overall fluorescence intensity than a fluorophore B diffusing in or out. If the hydrodynamic radius of A is also larger than that of B, the fluctuations in case A will also occur on a slower timescale than in case B.

The magnitude of the fluorescence fluctuations can be described by the variance  $\sigma^2$  of the signal. If  $[I_i]$  is a time series of measured fluorescence intensity data points with bin size  $T_{bin}$  and a total of  $N$  bins, then

$$\langle I \rangle = \frac{1}{N} \sum_{i=1}^N I_i \quad \sigma^2 = \frac{1}{N} \sum_{i=1}^N (I_i - \langle I \rangle)^2 \quad *$$
(4.1)

There are numerous ways to analyze the data taken in a fluorescence fluctuation experiment. An overview about the most important methods is given in the following sections. They can be categorized into methods that focus on the analysis of the time independent amplitude of the fluctuations, characterized by probability distributions (Number&Brightness Analysis (N&B), the Photon Counting Histogram (PCH), Fluorescence Intensity Distribution Analysis (FIDA), Fluorescence Cumulant Analysis (FCA)), and methods that focus on the evaluation of the temporal behavior of the fluctuations (Fluorescence Correlation Spectroscopy (FCS), Fluorescence Cross-Correlation Spectroscopy (FCCS), Scanning FCS, Raster Image Correlation Spectroscopy (RICS)), characterized by correlation functions.

## 4.2 Number&Brightness Analysis

N&B [7] is a very straightforward way of interpreting fluorescence intensity fluctuations. It requires no sophisticated theoretical description of the experimental processes; rather, in its most basic form, it requires only two simple assumptions:

1. The detected fluorescence intensity originates from a single species of fluorescent molecules, and its mean value is therefore proportional to both their number and their brightness:  $\langle I \rangle = bn$ , where  $n$  is the average number of molecules in the confocal volume, and  $b$  is the number of photons per molecule and time interval.
2. The variance  $\sigma^2$  of the intensity signal equals  $b\langle I \rangle$ . This reflects the phenomenon shown in the above example with fluorophores A and B: Although in both cases the mean intensity  $\langle I \rangle$  is equal, the variance is larger in case A where  $b$  is bigger.

These two assumptions, transformed into handy equations, already represent a very basic tool to extract the physically meaningful quantities  $b$  and  $n$  from the experimental data:

$$b = \frac{\sigma^2}{\langle I \rangle} \quad n = \frac{\langle I \rangle^2}{\sigma^2} \quad (4.2)$$

---

\* $\sigma^2$  is normalized with  $\frac{1}{N}$  in this work to keep all equations compatible with the definitions of moments and cumulants, in contrast to the more widely used normalization with  $\frac{1}{N-1}$ .

### 4.2.1 Detector noise correction

Although it is possible to estimate an apparent number of molecules and their apparent brightness from Equations 4.2 and to use them to compare measurements relative to each other, they do not yield correct absolute values. The reason is that there is a second source of signal fluctuations that significantly influences the variance  $\sigma^2$ : the photon emission process of the fluorophore, termed *Shot Noise*. Photons are not emitted steadily with a constant time passing between any two emitted photons, but rather according to a Poissonian probability distribution:

$$Poi(n, \lambda) = \frac{\lambda^n e^{-\lambda}}{n!} \quad (4.3)$$

Luckily, for all Poissonian processes,  $\sigma^2$  equals  $\langle I \rangle$  [8], which leads to a corrected version of Assumption 2:

$$\begin{aligned} \sigma^2 &= \sigma_{Diffusion}^2 + \sigma_{Shot\ noise}^2 \\ &= b\langle I \rangle + \langle I \rangle \\ &= (b + 1)\langle I \rangle \end{aligned}$$

Extracting again  $n$  and  $b$  from the assumptions yields corrected versions of Equations 4.2:

$$b = \frac{\sigma^2 - \langle I \rangle}{\langle I \rangle} \quad n = \frac{\langle I \rangle^2}{\sigma^2 - \langle I \rangle} \quad (4.4)$$

A more useful physical quantity than the number of photons per molecule and time interval  $b$  is the *Molecular Brightness*  $\varepsilon$ , defined as the number of photons per second and molecule when the fluorophore is located in the center of the confocal volume.  $b$  can easily be transformed into  $\varepsilon$  by dividing it by the binsize of the time series:

$$\varepsilon = \frac{b}{T_{bin}} \quad (4.5)$$

Note that  $\varepsilon$  is not an intrinsic property of a fluorophore. In addition to the absorption cross section  $\sigma_A$  and quantum yield  $\Phi$  of the fluorophore, it depends on the intensity of the excitation light  $I_0$ , and the detection efficiency  $\kappa$  of the system:

$$\varepsilon = \sigma_A \Phi I_0 \kappa \quad (4.6)$$

N&B provides a very basic way of extracting physical quantities out of fluorescence signals. It is not the most accurate method, but its beauty lies in its simplicity and computationally inexpensive calculations, making it suitable to quickly evaluate a large amount of measurements, as for example in a laser scanning image [7], or for time resolved number and brightness traces in a stationary fluorescence fluctuation experiment (Figure 4.2). In this case, the N&B analysis was performed piecewise for small fragments of the fluorescence intensity trace, yielding temporally resolved traces of both number and brightness. An example algorithm can be found in Appendix B.1.

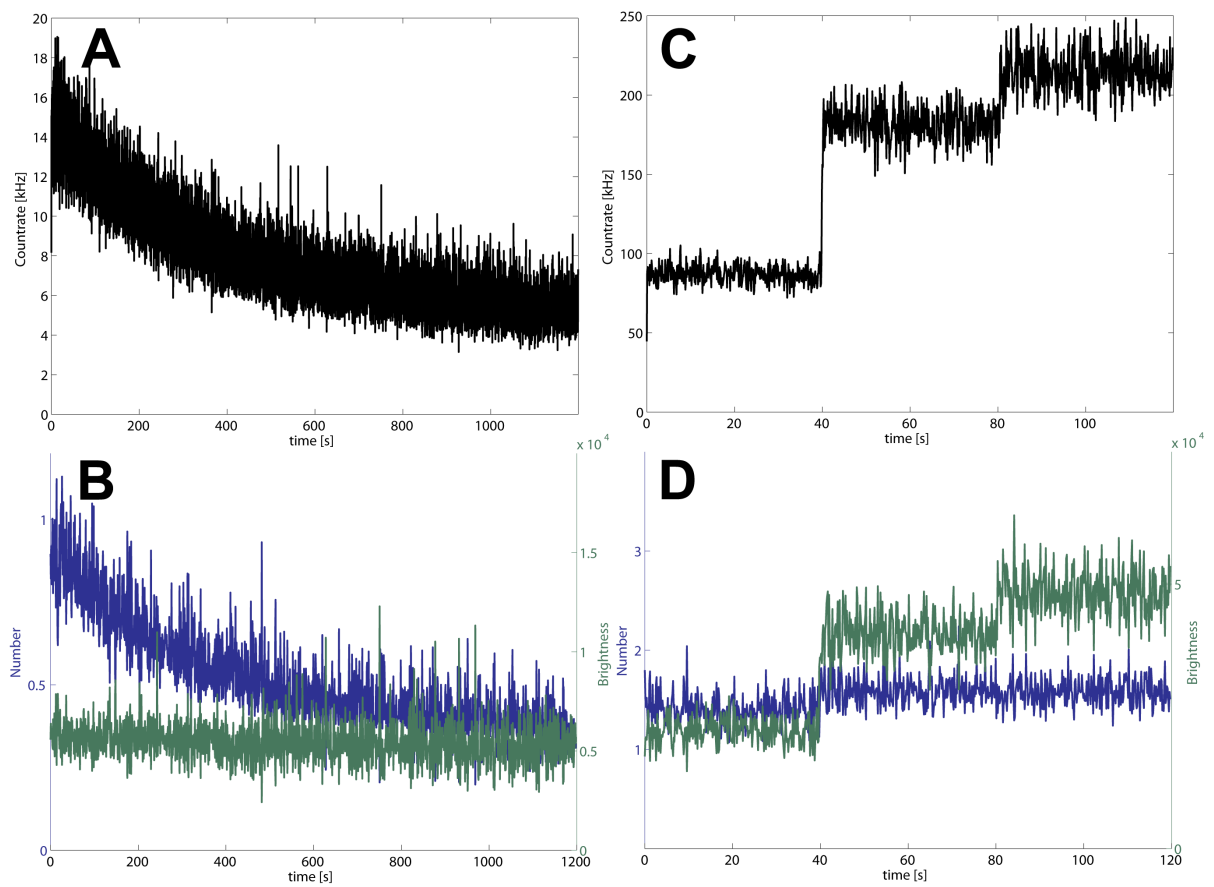


**Figure 4.2:** Number and brightness analysis of two fluorescence fluctuation measurements. (A) Measurement of Dnmt1 (Chapter 6). The average fluorescence intensity is slowly decreasing during the measurement. (B) Number and brightness analysis of (A). Clearly,  $n$  is decreasing while  $\varepsilon$  remains constant. This is caused by an increasing fraction of Dnmt1 molecules adhering to the surfaces of the sample holder, thereby decreasing the number of molecules in solution. (C) Measurement of ATTO 532, where the excitation light intensity was stepwise increased and thus the average fluorescence intensity is also increasing stepwise. (D) Number and brightness analysis of (C).  $n$  remains constant whereas  $\varepsilon$  is stepwise increasing.



### 4.3 The Photon Counting Histogram

In PCH [9], the basic ideas of N&B are placed on a sound theoretical foundation and are further expanded to the case of a mixture of multiple fluorophore species with different molecular brightnesses  $\varepsilon_i$ . The sections on FIDA and FCA (4.4 and 4.5) will be based on the same theoretical concepts. It is therefore necessary to understand them thoroughly.

All these techniques are based on the evaluation of the distribution of detected photon counts, collected in the experimental photon counting histogram (p.c.h., written in lower case to avoid confusion with the name of the method). The p.c.h. is usually normalized to an area of 1 so that it can be identified with and interpreted as the experimental manifestation of a probability distribution.

In order to truly understand the mechanism of PCH, it is necessary to understand what exactly photon counts are, and how the p.c.h. is formed.

#### 4.3.1 Theory of photon detection: Mandel's formula

In a typical fluorescence fluctuation experiment, the confocal volume is placed in a sample solution of fluorescent molecules, creating a location-dependent illumination intensity  $I(\vec{r})$ . The fluorescence emitted by the fluorophores in the confocal volume is collected by the objective, passes through several optical components and is finally focused onto the sensitive area of a photodetector. A time-dependent fluorescence intensity  $W(t)$  is thus measured at the detector surface. The time dependence of  $W(t)$  arises from molecular processes such as Brownian diffusion of fluorophores in and out of the PSF or photobleaching. Depending on the shape of the point spread function and the number and brightness of the fluorophores, this leads to a probability  $p(W)$  that a certain intensity  $W$  reaches the detector at any given time  $t$ .

The detector transforms the incident intensity  $W(t)$  into a series of electrical pulses with a rate which is ideally proportional to  $W(t)$ . The transformation of the continuous intensity  $W(t)$ , described by classical physics, into a series of discrete pulses includes quantum mechanical processes [10] and is therefore of stochastic nature. Hence, the time interval between any two detector pulses will not be equal, but will vary according to Poissonian statistics. If the detected pulses are grouped into sets of  $k$  photon counts within fixed time intervals  $T^1$ , then the values of  $k$  represent the *photon counts during  $T$* , and the probability  $p(k)$  of counting  $k$  photons within  $T$  will follow a Poisson distribution  $Poi(k, W)$  (see Equation 4.3). The broadening of  $p(k)$  compared to  $p(W)$  is referred to as *shot noise*. A mathematical description of the transformation between  $p(W)$  and  $p(k)$  was given by Mandel [11]:<sup>2</sup>

$$p(k) = \int_0^\infty Poi(k, W)p(W)dW = \int_0^\infty \frac{W^k e^{-W}}{k!} p(W)dW \quad (4.7)$$

To understand the formula, it is important to realize that different values of  $W$  can lead to the same number of photon counts  $k$ . Therefore, the probability  $p(k)$  to detect  $k$  photon counts can be written as the summation over all possible values of  $W$  that could lead to  $k$  photon counts, weighted with the probability  $p(W)$  that they occur, and with the Poissonian probability  $\frac{W^k e^{-W}}{k!}$  that they actually lead to exactly  $k$  counts (and not to a different number of counts). The summation is expressed as an integral because of the classical, continuous nature

<sup>1</sup>A prerequisite for PCH is to choose the interval short enough so that during  $T$ , no significant changes in the fluorophore positions occur, so the process can be regarded as stationary

<sup>2</sup>For the moment, a system with a detection efficiency of  $\eta = 1$  is assumed to increase comprehensibility

of  $W$ .

A corollary of Equation 4.7 is the observation that if the light intensity is absolutely constant,  $W(t) = \bar{W}$  and therefore  $p(W) = \delta(W - \bar{W})$ , then the resulting distribution  $p(k)$  will be Poissonian:

$$p(k) = \int_0^\infty \frac{W^k e^{-W}}{k!} \delta(W - \bar{W}) dW = \frac{\bar{W}^k e^{-\bar{W}}}{k!} = Poi(k, \bar{W}) \quad (4.8)$$

The key idea of FCA, PCH, and FIDA is to connect certain properties of the measured p.c.h. with experimental parameters such as the number  $n$  and brightness  $\varepsilon$  of molecules in the PSF. Evidently those parameters will determine  $p(W)$ , so information about them is obviously contained in  $p(W)$  and therefore also in the measurable distribution  $p(k)$ .

### 4.3.2 From Mandel to number and brightness

If the intensity distribution  $p(W)$  can somehow be expressed in terms of the number and brightness of the involved molecules, then it will be possible to extract those parameters also from the measured p.c.h., described by  $p(k)$ , with the help of Mandel's formula (eq. 4.7). Therefore  $p(W)$  will be closely focused upon in this section.

#### The Point Spread Function in PCH

Only fluorescence from molecules within the confocal volume, described by the *Point Spread Function* (PSF), is detected. Therefore, at first, a mathematical description of the PSF will be given. For a confocal microscope with one-photon excitation and detection through a pinhole, the PSF can be described with a three dimensional Gaussian intensity profile  $I(x, y, z)$  [12], normalized by the maximum intensity  $I_0$  at its center:

$$PSF(\vec{r}) = PSF(x, y, z) = \frac{I(x, y, z)}{I_0} = \exp\left(-\frac{2(x^2 + y^2)}{\omega_r^2} - \frac{2z^2}{\omega_z^2}\right) \quad (4.9)$$

$\omega_r^2$  and  $\omega_z^2$  are the distances in radial and axial direction, respectively, where the intensity has decreased to  $\frac{1}{e^2} I_0$ .

#### One single fluorophore

Equation 4.9 can be used to express the fluorescence intensity  $W(\vec{r})$  that reaches the detector for a single fluorophore depending on its position  $\vec{r}$ :

$$W(\vec{r}) = \varepsilon \exp\left(-\frac{2(x^2 + y^2)}{\omega_r^2} - \frac{2z^2}{\omega_z^2}\right) \quad (4.10)$$

$\varepsilon$  is the parameter that transforms the excitation light intensity  $I(\vec{r})$  into the fluorescence intensity  $W$  at the detector - the molecular brightness. Note that  $\varepsilon$  still depends on the binning time  $T_{bin}$ . This can be dealt with according to Equation 4.5. Factors that contribute to  $\varepsilon$  are the excitation probability of the fluorophore, its fluorescence quantum yield, and the detection efficiency of the optical system.

The integration over  $p(W)$  for all possible values of  $W$  in Mandel's Formula (4.7) can now be replaced by an integration over  $p(\vec{r})$  for all possible values of  $\vec{r}$ :

$$p(W) = \int_{\mathbb{R}^3} p(W, r) p(\vec{r}) d\vec{r} \quad (4.11)$$

Equation 4.11, just as Mandel's Equation 4.7, can be understood as a weighted averaging: It has to be realized that different positions  $\vec{r}$  of the fluorophore can lead to the same fluorescence intensity at the detector of  $W$ . The probability  $p(W)$  of creating  $W$  can therefore be expressed as a summation over all possible locations  $\vec{r}$  of the fluorophore that could lead to an intensity of  $W$ , weighted with the probability  $p(\vec{r})$  that the fluorophore assumes that position, and with the probability  $p(W, \vec{r})$  that this position leads to an intensity of  $W$ . This consideration is completely analogous to the one that was proposed to understand Mandel's equation in the previous section.

Here, in contrast to Mandel's equation, the two probabilities  $p(W, r)$  and  $p(r)$  can be expressed analytically in a relatively simple way.  $p(W, \vec{r})$  can be explicitly expressed, since  $W(\vec{r})$  is given by Equation 4.9. Consequently,  $p(W, \vec{r})$  can be expressed as a delta function:  $p(W, r) = 1$  if  $W$  and  $\vec{r}$  meet Equation 4.10, otherwise  $p(W, r) = 0$ .

For a freely diffusing fluorophore, the probability  $p(\vec{r})$  for the fluorophore to be in a particular location  $\vec{r}$  is obviously constant, since there are no preferential locations. The exact value of  $p(\vec{r})$  depends on normalization questions and does not influence the result of this derivation. To keep the equations as comprehensible as possible,  $p(\vec{r}) := p_r$  is defined as a constant value that is independent of  $\vec{r}$ .

$$p(W) = \int_{\mathbb{R}^3} \delta(W - \varepsilon \exp\left(-\frac{2(x^2 + y^2)}{\omega_r^2} - \frac{2z^2}{\omega_z^2}\right)) p_r d\vec{r} \quad (4.12)$$

Inserting Equation 4.12 into Mandel's Equation 4.7 leads to

$$\begin{aligned} p(k) &= \int_{W=0}^{\infty} \frac{W^k e^{-W}}{k!} p(W) dW \\ &= \int_{W=0}^{\infty} \frac{W^k e^{-W}}{k!} \int_{\vec{r} \in \mathbb{R}^3} \delta(W - \varepsilon \exp\left(-\frac{2(x^2 + y^2)}{\omega_r^2} - \frac{2z^2}{\omega_z^2}\right)) p_r d\vec{r} dW \\ &= p_r \int_{\vec{r} \in \mathbb{R}^3} \int_{W=0}^{\infty} \frac{W^k e^{-W}}{k!} \delta(W - \varepsilon \exp\left(-\frac{2(x^2 + y^2)}{\omega_r^2} - \frac{2z^2}{\omega_z^2}\right)) dW d\vec{r} \\ &= p_r \int_{\vec{r} \in \mathbb{R}^3} \frac{\varepsilon \exp\left(-\frac{2(x^2 + y^2)}{\omega_r^2} - \frac{2z^2}{\omega_z^2}\right)^k e^{-\varepsilon \exp\left(-\frac{2(x^2 + y^2)}{\omega_r^2} - \frac{2z^2}{\omega_z^2}\right)}}{k!} d\vec{r} \\ &= p_r \int_{\vec{r} \in \mathbb{R}^3} \text{Poi}(k, W(\vec{r})) d\vec{r} \end{aligned} \quad (4.13)$$

Further evaluation of Equation 4.13 requires a relatively complex analytical integration to simplify the resulting expression. Only the final form of  $p^{(1)}(k; \varepsilon)$  for one fluorophore is shown:

$$p^{(1)}(k; \varepsilon) = \frac{p_r \pi \omega_0^2 \omega_z}{k!} \int_{x=0}^{\infty} \int_{a=0}^{\varepsilon e^{-2x^2}} a^{k-1} e^{-a} da dx \quad (4.14)$$

The inner integral of Equation 4.14 is a ubiquitous mathematical function called *lower incomplete gamma function* and can only be solved numerically.

### Multiple fluorophores

In a fluorescence fluctuation experiment, there is, of course, more than one molecule and, depending on the concentration, multiple fluorophores may be simultaneously present in the confocal volume. For the moment, consider just one molecular species.

To treat the case of  $N$  non-interacting fluorophores, Equation 4.13 has to be integrated not just over the possible coordinates for one molecule, but over the coordinates for  $N$  fluorophores. Therein, the intensity at the detector is the sum of the intensities of each fluorophore  $W_{total} = W(\vec{r}_1) + \dots + W(\vec{r}_N)$ . For comprehensibility, the following equations will only be shown for the case of  $N = 2$  and  $W_{total} = W(\vec{r}_1) + W(\vec{r}_2)$ , but the generalization is straightforward and the result is also valid for  $N$  fluorophores.

$$\begin{aligned}
p^{(2)}(k; \varepsilon) &= p_r^2 \int_{\vec{r}_1 \in \mathbb{R}^3} \int_{\vec{r}_2 \in \mathbb{R}^3} Poi(k, W(\vec{r}_1) + W(\vec{r}_2)) d\vec{r}_1 d\vec{r}_2 \\
&= p_r^2 \int_{\vec{r}_1 \in \mathbb{R}^3} \int_{\vec{r}_2 \in \mathbb{R}^3} Poi(k, W(\vec{r}_1)) \otimes Poi(k, W(\vec{r}_2)) d\vec{r}_1 d\vec{r}_2 \\
&= p_r^2 \int_{\vec{r}_1 \in \mathbb{R}^3} \int_{\vec{r}_2 \in \mathbb{R}^3} \sum_{x=0}^k Poi(k-x, W(\vec{r}_1)) \cdot Poi(x, W(\vec{r}_2)) d\vec{r}_1 d\vec{r}_2 \\
&= p_r^2 \sum_{x=0}^k \int_{\vec{r}_1 \in \mathbb{R}^3} \int_{\vec{r}_2 \in \mathbb{R}^3} Poi(k-x, W(\vec{r}_1)) \cdot Poi(x, W(\vec{r}_2)) d\vec{r}_1 d\vec{r}_2 \\
&= p_r^2 \sum_{x=0}^k \int_{\vec{r}_1 \in \mathbb{R}^3} Poi(k-x, W(\vec{r}_1)) d\vec{r}_1 \int_{\vec{r}_2 \in \mathbb{R}^3} Poi(x, W(\vec{r}_2)) d\vec{r}_2 \\
&= [p^{(1)} \otimes p^{(1)}](k; \varepsilon)
\end{aligned} \tag{4.15}$$

In this derivation a characteristic property of the Poisson distribution was used, namely that the Poisson distribution of a sum of two parameters  $Poi(k, \lambda_1 + \lambda_2)$  equals the *convolution* of two separate Poisson distributions  $Poi(k, \lambda_1) \otimes Poi(k, \lambda_1)$ . The convolution of two distributions, expressed by the operator  $\otimes$ , delivers a new distribution, defined by the sum  $\sum_{x=0}^k Poi(k-x, \lambda_1) Poi(x, \lambda_2)$ .

Equation 4.15 shows that the probability  $p^{(N)}(k; \varepsilon)$  to detect  $k$  photons in the presence of  $N$  molecules is the  $N$ -fold convolution of probabilities  $p^{(1)}(\varepsilon)$ .

The consequential problem to further evaluate Equation 4.15 is the question how many molecules  $N$  there are in the confocal volume. This is an essential step, because this connects  $p(k; \varepsilon)$  with the concentration of fluorophores in the sample, one of the physical quantities of interest.  $N$  is not constant over time, because the process of molecules diffusing in and out of the confocal volume leads to fluctuations. However, the occupation number is governed by Poissonian statistics about the average number of molecules  $\bar{N}$  [13]:

$$p_{number}(N; \bar{N}) = Poi(N, \bar{N}) = \frac{\bar{N}^N e^{-\bar{N}}}{N!} \tag{4.16}$$

Therefore, methodically analogous to Equations 4.7 and 4.11,  $p(k; \varepsilon)$  can be expressed as

$$p(k; \varepsilon) = \int_0^\infty p^{(N)}(k) p_{number; \bar{N}}(N) dN = \sum_{N=0}^\infty p^{(N)}(k) p_{number}(N; \bar{N}) \quad (4.17)$$

As before, the integral can be interpreted as a summation over all possible values of  $N$  that can lead to a photon count of  $k$ , weighted with the probability  $p^{(N)}(k; \varepsilon)$  that  $k$  counts are actually detected in the presence of  $N$  molecules, and with the probability  $p_{number}(N; \bar{N})$  that there are  $N$  molecules in the confocal volume. Due to the discrete nature of the particle number  $N$ , the integration can be explicitly written as a summation in this case. Inserting Equations 4.15 and 4.16 into Equation 4.17 yields

$$p(k; \varepsilon, \bar{N}) = \sum_{N=0}^\infty \left[ \bigotimes_1^N p^{(1)}(k; \varepsilon) \right] \frac{\bar{N}^N e^{-\bar{N}}}{N!} \quad (4.18)$$

where  $p^{(1)}(k; \varepsilon)$  is given by Equation 4.14. Note that while  $N \in \mathbb{N}_0$ ,  $\bar{N}$  is a real number. Since  $\bar{N}$  represents the average number of molecules in the confocal volume, it can be transformed into the concentration  $c$  of molecules in the sample, if the size of the confocal volume is known. Its volume  $V_0$  can be calculated by integrating the point spread function (Equation 4.9) over the complete  $\mathbb{R}^3$ :

$$\begin{aligned} V_0 &= \int_{\mathbb{R}^3} \exp \left( -\frac{2(x^2 + y^2)}{\omega_r^2} - \frac{2z^2}{\omega_z^2} \right) d\vec{r} \\ &= \int_x \exp \left( -\frac{2x^2}{\omega_r^2} \right) dx \int_y \exp \left( -\frac{2y^2}{\omega_r^2} \right) dy \int_z \exp \left( -\frac{2z^2}{\omega_z^2} \right) dz \\ &= \sqrt{\frac{\pi}{2}} \omega_r \cdot \sqrt{\frac{\pi}{2}} \omega_r \cdot \sqrt{\frac{\pi}{2}} \omega_z \\ &= \left( \frac{\pi}{2} \right)^{\frac{3}{2}} \omega_r^2 \omega_z \end{aligned} \quad (4.19)$$

Taking into account Avogadro's constant  $N_A$ , a factor of  $10^3$  to transform between  $m^3$  and  $l$ , and a factor of  $10^9$  to transform between *molar* and *nanomolar* concentrations, Equation 4.19 leads to the desired transformation between  $\bar{N}$  and  $c$ , given in  $nM$  as conventional:

$$c = \frac{10^9}{10^3 N_{Avogadro}} \frac{\bar{N}}{V_0} = \frac{10^6}{N_{Avogadro}} \left( \frac{2}{\pi} \right)^{\frac{3}{2}} \frac{\bar{N}}{\omega_r^2 \omega_z} \quad (4.20)$$

### 4.3.3 Multiple fluorescent species

In many applications, multiple fluorescent species with different molecular brightness are simultaneously present. The incorporation into the PCH formalism works analogous to the derivation presented in Equation 4.15, with one exception. The formula has to be built for an average of  $\bar{N}_1$  molecules of molecular brightness  $\varepsilon_1$ , and of  $\bar{N}_2$  molecules with  $\varepsilon_2$ . Since the only difference between the individual convolution factors are the constants  $\varepsilon_i$  which are contained in  $W$ , the calculation works completely identical and therefore only the result is shown.

$$p(k; \varepsilon_1, \varepsilon_2, \bar{N}_1, \bar{N}_2) = \left( \sum_{N_1=0}^{\infty} \left[ \bigotimes_1^{N_1} p(k; \varepsilon_1) \right] \frac{\bar{N}_1^{N_1} e^{-\bar{N}_1}}{N_1!} \right) \otimes \left( \sum_{N_2=0}^{\infty} \left[ \bigotimes_1^{N_2} p(k; \varepsilon_2) \right] \frac{\bar{N}_2^{N_2} e^{-\bar{N}_2}}{N_2!} \right) \quad (4.21)$$

Of course, Equation 4.21 can easily be extended to any desired number of species. However, since a p.c.h. usually contains only a small number of data points, the possible number of fit parameters is limited and the determination of more than two different fluorescent species with PCH analysis is very difficult and requires exceptional data quality and very large statistics.

Equation 4.21 provides the desired link between the photon distribution  $p(k; \varepsilon_1, \varepsilon_2, \bar{N}_1, \bar{N}_2)$  that can be experimentally measured as the p.c.h., and the physical quantities of interest, one or more molecular brightness and concentrations. Theoretically, all that remains to be done is using the right hand side of the equation as a fit function with parameters  $\varepsilon_i$  and  $\bar{N}_i$  and run a nonlinear regression on the measured data set.

Still, there are a few helpful tricks for the implementation. The calculation of the fit function requires some computationally very expensive operations such as numerical integrations and convolutions. Some of these can be addressed by fitting the *probability generating function* (PGF) instead of the actual data. This is a concept that was first introduced for the implementation of FIDA, but, with some modifications, it can also be applied to PCH. For example computer code, refer to Appendix B.3.

## 4.4 Fluorescence-Intensity Distribution Analysis

FIDA [14] was developed simultaneously with, but independently from PCH. Both techniques share the same theoretical foundations with the aim of connecting an experimentally detected distribution of photon counts (the p.c.h.) with the physical quantities of interest  $\varepsilon$  and  $\bar{N}$ . While the basic ideas of both methods are identical, FIDA differs from PCH in two important technical aspects. First, for FIDA, the PSF is modeled in a different way than in PCH. While for PCH a three dimensional Gaussian shape is assumed, for FIDA a more general, empirical formula is chosen with which a PSF of an arbitrary shape can be modeled. Second, FIDA entirely performs the linear regression in the Fourier transformed space of the *generating function*. The advantage of this technique is that the necessary convolutions are transformed to simple multiplications in Fourier space (which is just a special case of a generating function space), rendering FIDA much more computationally efficient than PCH.

### 4.4.1 The Point Spread Function in FIDA

The key idea in the way the PSF is modeled in FIDA is to dissect it into many subvolumes (*voxels*)  $dV_i$  that are sufficiently small, so that for any voxel an approximately constant excitation intensity  $I_i$  can be assumed so that the brightness at the detector  $W(\vec{r})$  results from the product  $N\varepsilon I_i$  with  $N$  particles of brightness  $\varepsilon_i$  within the voxel  $dV_i$ . This assumption drastically simplifies the derivation of the probability  $p_i(k)$  to detect  $k$  photons from the voxel  $dV_i$ , compared to the probability derived for a complete 3D Gaussian PSF. For one voxel, the new form of  $W(\vec{r})$  (compared to Equation 4.10) reads:

$$W_i(\vec{r}) \begin{cases} N\varepsilon I_i, & \vec{r} \in dV_i \\ 0, & \vec{r} \notin dV_i \end{cases} \quad (4.22)$$

This results in a much simpler expression for  $p(W)$  according to Equation 4.11:

$$p_i(W) = \int_{dV_i} \delta(W - N\varepsilon I_i) p_r d\vec{r} \quad (4.23)$$

Within the defined volume element  $dV_i$ , the probability  $p(\vec{r})$  can be given explicitly:  $p(\vec{r}) = p_r = \frac{1}{dV_i}$ .

Inserting Equation 4.23 into Mandel's Equation (4.7) now yields the probability  $p_i^{(N)}(k)$  to detect  $k$  counts if  $N$  molecules are present:

$$\begin{aligned} p_i^{(N)}(k) &= \int_{W=0}^{\infty} \frac{W^k e^{-W}}{k!} p(W) dW \\ &= \int_{W=0}^{\infty} \frac{W^k e^{-W}}{k!} \int_{\vec{r} \in dV_i} \delta(W - N\varepsilon I_i) \frac{1}{dV_i} d\vec{r} dW \\ &= \frac{1}{dV_i} \int_{\vec{r} \in dV_i} \int_{W=0}^{\infty} \frac{W^k e^{-W}}{k!} \delta(W - N\varepsilon I_i) dW d\vec{r} \\ &= \frac{1}{dV_i} \int_{\vec{r} \in dV_i} \frac{(N\varepsilon I_i)^k e^{-N\varepsilon I_i}}{k!} d\vec{r} \\ &= \frac{dV_i (N\varepsilon I_i)^k e^{-N\varepsilon I_i}}{k!} \end{aligned} \quad (4.24)$$

Note that neither convolutions nor numeric integrations were necessary up to this point. The Poissonian probability of having  $N$  fluorophores in  $dV_i$  is analogous to Equation 4.16:

$$p_{\text{number}}(N; \bar{N}_i) = \text{Poi}(N, \bar{N}_i) = \frac{\bar{N}_i^N e^{-\bar{N}_i}}{N!} \quad (4.25)$$

$\bar{N}_i$  is the average number of fluorophores in  $dV_i$  and depends on the volume of  $dV_i$ . It can therefore be rewritten as  $\bar{N}_i = cdV_i$  where  $c$  is the concentration of fluorophores in the sample. Combining Equations 4.24 and 4.25 according to Equation 4.17 leads to

$$p_i(k; \varepsilon, c, dV_i) = \sum_{N=0}^{\infty} p_i^{(N)}(k) p_{\text{number}}(N; c, dV_i) = \sum_{N=0}^{\infty} \frac{cdV_i^N e^{-cdV_i}}{N!} \frac{(N\varepsilon I_i)^k e^{-N\varepsilon I_i}}{k!} \quad (4.26)$$

The overall p.c.h. for a single molecular species is then the convolution of all contributions of the different subvolumes  $dV_i$  according to Equation 4.26. Furthermore, as in PCH, the case of multiple fluorescent species can also be addressed by convolving their contributions.

$$p(k; \varepsilon, c) = \bigotimes_i p_i(k; \varepsilon, c, dV_i) \quad (4.27)$$

Fitting an experimentally measured p.c.h. with this convolution of a large number of terms would surely be at least as computationally expensive as the PCH equations from the previous section. Fortunately, in the present case, the convolution is the outermost operation of the whole expression. Therefore, a remarkable property of convolutions can be exploited. The PGF of a convolution of distributions simply equals the product of the PGFs of each separate distribution, the *Cauchy product*. So the transformation into the space of generating functions transforms the convolution operation into a plain multiplication.

#### 4.4.2 The Generating Function

The PGF is defined as:

$$G(\xi) = \sum_{k=0}^{\infty} p(k) \xi^k \quad (4.28)$$

$G(\xi)$  is then a power series whose coefficients constitute the original distribution  $p(k)$ . While this is a rather trivial observation, the use of the concept of generating functions lies in the possibility to find a closed form for  $G(\xi)$ , thus allowing analytical operations that would not have been possible on  $p(k)$  itself. Furthermore, if  $\xi = e^{i\varphi}$  is selected, then Equation 4.28 becomes the Fourier transform of  $p(k)$ . This is particularly useful, because fast algorithms are available to transform the experimentally measured photon distributions into the generating function space, allowing to use the final equation of this section (Equation 4.36), that gives a relatively simple expression for  $G(\xi)$ , directly as a data fit model.

Calculating the PGF of the photon distribution  $p_i(k; \varepsilon, c, dV_i)$  from Equation 4.26 yields:

$$\begin{aligned} G(\xi) &= \sum_{k=0}^{\infty} \sum_{N=0}^{\infty} \frac{cdV_i^N e^{-cdV_i}}{N!} \frac{(N\varepsilon I_i)^k e^{-N\varepsilon I_i}}{k!} \xi^k \\ &= e^{-cdV_i} \sum_{N=0}^{\infty} \frac{cdV_i^N}{N!} e^{-N\varepsilon I_i} \sum_{k=0}^{\infty} \frac{(\xi N\varepsilon I_i)^k}{k!} \\ &= e^{-cdV_i} \sum_{N=0}^{\infty} \frac{cdV_i^N}{N!} e^{-N\varepsilon I_i} e^{\xi N\varepsilon I_i} \\ &= e^{-cdV_i} \sum_{N=0}^{\infty} \frac{(cdV_i e^{(\xi-1)\varepsilon I_i})^N}{N!} \\ &= e^{-cdV_i} \exp\left(cdV_i e^{(\xi-1)\varepsilon I_i}\right) \\ &= \exp\left(cdV_i (e^{(\xi-1)\varepsilon I_i} - 1)\right) \end{aligned} \quad (4.29)$$

The definition of the exponential function was used twice in the previous derivation:

$$e^x = \exp(x) := \sum_{k=0}^{\infty} \frac{x^k}{k!} \quad (4.30)$$

With these considerations Equation 4.27 simplifies considerably. :

$$\begin{aligned} p(k; \varepsilon, c) &= \bigotimes_i p_i(k; \varepsilon, c, dV_i) \\ G(p(k; \varepsilon, c)) &= \prod_i G_{p_i}(\xi; \varepsilon, c, dV_i) \\ &= \exp\left(\sum_i cdV_i (e^{(\xi-1)\varepsilon I_i} - 1)\right) \\ &= \exp\left(\int_V c(e^{(\xi-1)\varepsilon I(\vec{r})} - 1) dV\right) \end{aligned} \quad (4.31)$$

The summation over all subvolumes  $dV_i$  converges towards an integration over  $V$  for the limit of infinitely small subvolumes.



The case of  $J$  multiple species can be treated completely analogous to the derivation shown in Equation 4.31. The different  $p_j(k; \varepsilon_j, c_j)$  have to be convoluted, which results in a summation of exponents, as shown above:

$$G(p(k; \varepsilon_1.. \varepsilon_J, c_1..c_J)) = \exp \left( \sum_{j=1}^J c_j \int_V (e^{(\xi-1)\varepsilon_j I(\vec{r})} - 1) dV \right) \quad (4.32)$$

One last step is necessary to allow the integration in Equation 4.32. The PSF  $I(\vec{r})$  is yet undetermined. To avoid a three dimensional integration over  $dV$ ,  $I(\vec{r})$  is substituted according to the following substitution pattern:

$$I(\vec{r}) = e^{-u} \quad (4.33)$$

The substitution of the three dimensional function  $I(\vec{r}) = I(x, y, z)$  by the one dimensional function  $e^{-u}$  is essentially possible because the result of the integration does not depend on actual positions of volume elements but rather on the brightness  $I(\vec{r})$  within them. One could imagine rearranging them from a three dimensional array of volume elements to a one dimensional line, ordered according to their brightness. For a detailed proof of this assumption using the three dimensional Gaussian PSF that is used for PCH as an example case, refer to [15]. In [16], the inventors of FIDA claim to have tested it with a three dimensional Gaussian PSF, but have been unable to obtain satisfying results. They reason that the real excitation light intensity distribution in a confocal instrument is insufficiently well described by this type of function, so they used a slightly different approach. In principle, the transformation between  $dV$  and  $du$  can be derived from Equation 4.33 for any given PSF. For FIDA however, the PSF is not directly described. Instead, the relation between  $dV$  and  $du$  is directly postulated by a relatively arbitrary, empirically determined function (Equation 4.34), that was specifically designed to facilitate solving Equation 4.32. In a later publication [17], a slightly more sophisticated formula (Equation 4.35) was proposed. Note that there is more than one possible description of the PSF that would lead to those expressions:

$$dV = a_1 u + a_2 u^2 + a_3 u^3 du \quad (4.34)$$

$$dV = A_0(1 + a_1 u + a_2 u^2) u^{a_3} du \quad (4.35)$$

$\xi$  is substituted with  $e^{i\varphi}$  as mentioned before, so that the transformation into a PGF according to Equation 4.28 becomes a Fourier transform. If Equation 4.34 is selected to describe the confocal volume, this results then in the final form:

$$G(p(k; \varepsilon_1.. \varepsilon_J, c_1..c_J)) = \exp \left( \sum_{j=1}^J c_j \int_V (e^{(e^{i\varphi}-1)\varepsilon_j e^{-u}} - 1) a_1 u + a_2 u^2 + a_3 u^3 du \right) \quad (4.36)$$

With this equation, the fast Fourier transform of the experimental p.c.h. can be fitted. Alternatively, the fit can be applied the other way round: the result of this equation can be numerically fast Fourier transformed into real space and directly fitted to the experimental p.c.h. This procedure might seem needlessly complicated but has the advantage that the different points of the p.c.h. can be weighted statistically during the fit. For example computer code, refer to Appendix B.3.

## 4.5 Fluorescence Cumulant Analysis

In FCA [18], the concept of FIDA is taken one step further. While in FIDA, the whole PGF is fitted with a sophisticated and complex fit model, FCA makes it possible to calculate the physically interesting quantities  $\bar{N}_i$  and  $\varepsilon_i$  from a set of easily obtainable properties of the distribution, its *factorial cumulants*. No nonlinear regression is necessary, rendering this method very fast and robust.

In order to understand the underlying theory, it is important to introduce a number of mathematical tools to characterize the distribution of detected fluorescence photons.

### 4.5.1 Moments

The *moments* of a distribution are a set of mathematical constructs that present an additional way to describe a distribution  $p(k)$ . The first few moments of a distribution describe its location, width and shape. The first moment corresponds to the mean  $\mu$ , the second moment to the variance  $\sigma^2$ , and the third and fourth moments describe the skewness and kurtosis, respectively (Figure 4.3). Since N&B (Section 4.2) is based on the evaluation of  $\mu$  and  $\sigma^2$ , it can be regarded as one possible form of moment analysis.

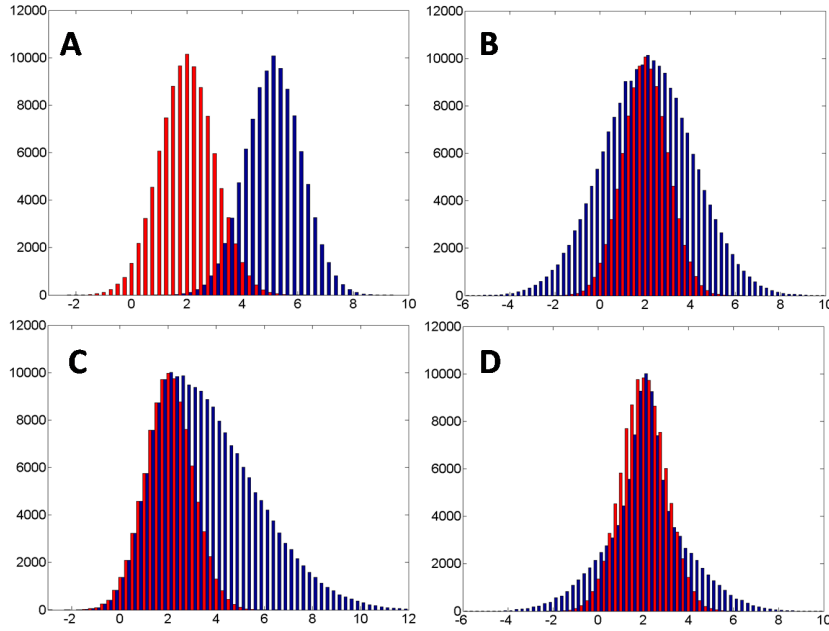


**Figure 4.3:** Variation of the first four moments: mean (A), variance (B), skewness (C), and kurtosis (D)

If  $p(k)$  is a probability distribution<sup>3</sup>, then

$$\mu'_i := \sum_{k=0}^{\infty} (k - c)^i p(k) = \int_{-\infty}^{\infty} (k - c)^i p(k) dk \quad (4.37)$$

<sup>3</sup>A probability distribution is essentially any distribution whose area  $\sum_{k=0}^{\infty} p(k)$  is normalized to 1

is defined as the  $i$ th moment of  $p(k)$  about a value  $c$ , depending on whether  $p(k)$  is a discrete or continuous probability distribution. Below, only the summation will be used, because the probability distributions in this context are discrete.

Two special cases deserve attention:

$$\begin{aligned}\mu_i^* &:= \langle k^i \rangle := \sum_{k=0}^{\infty} k^i p(k) \\ \mu_i &:= \sum_{k=0}^{\infty} (k - \mu)^i p(k)\end{aligned}\tag{4.38}$$

$\mu_i^*$ , the moment about the value 0, is called *raw moment* or *ordinary moment*, and although the use of the nomenclature of moments is often imprecise in literature, chances are if a *moment* is mentioned without further specification, the ordinary moment is meant. Note that there are two different notations prevailing in the literature to refer to ordinary moments.

$\mu_i$ , the moment about the mean  $\mu$  of  $P(n)$ , is called *central moment*.<sup>4</sup> A corollary of Equations 4.38 is that  $\mu_1^* = \mu$  and  $\mu_2 = \sigma^2$ , as mentioned before.

#### 4.5.2 Factorial moments

Besides the moments of a distribution, there is another, slightly more sophisticated construct, the *factorial moments* about zero:<sup>5</sup>

$$\begin{aligned}\mu_{[i]}^* &:= \langle k^{[i]} \rangle := \sum_{k=0}^{\infty} k^{[i]} p(k) \\ \text{where } k^{[i]} &:= k(k-1)(k-2) \cdots (k-i+1)\end{aligned}\tag{4.39}$$

Their use as such is limited and they occur rather rarely; their main use lies within the context of their generating functions.

#### 4.5.3 Moment generating function

The concept of generating functions, introduced in Section 4.4.2, can be extended from the fundamental case of the PGF to generating functions of moments, factorial moments, or cumulants. The *moment generating function* (MGF) is defined as

---

<sup>4</sup>In the literature, the term  $\mu(c)$ , the "mean about  $c$ ", is occasionally observed. This is a relatively exotic construct where  $\mu(c) = \mu - c$ . Here, the "mean" is always the conventional mean, or "mean about zero".

<sup>5</sup>The factorial moments about an arbitrary value  $c$  can be constructed by replacing  $k^{[i]}$  with  $(k - c)^{[i]}$  in the formulas

$$\begin{aligned}
G_k^M(\xi) &:= \langle e^{-\xi k} \rangle = \sum_{k=0}^{\infty} e^{\xi k} p(k) \\
&= \sum_{k=0}^{\infty} \sum_{j=0}^{\infty} \frac{\xi^j k^j}{j!} p(k) \\
&= \sum_{j=0}^{\infty} \frac{1}{j!} \xi^j \sum_{k=0}^{\infty} k^j p(k) \\
&= \sum_{j=0}^{\infty} \frac{1}{j!} \xi^j \langle k^j \rangle
\end{aligned} \tag{4.40}$$

The definition of the exponential function according to Equation 4.30 was used in the second step. The reshaping of Equation 4.40 into the final form was shown to illustrate the benefit of the MGF: The  $i$ th moment of  $p(k)$  can be generated from the MGF by deriving it  $i$  times around zero, which is why it is called moment generating function:

$$\begin{aligned}
\left. \frac{\partial^i}{\partial \xi^i} G_k^M(\xi) \right|_{\xi=0} &= \left. \frac{\partial^i}{\partial \xi^i} \sum_{j=0}^{\infty} \frac{1}{j!} \xi^j \langle k^j \rangle \right|_{\xi=0} \\
&= \sum_{j=0}^{\infty} \frac{1}{j!} \langle k^j \rangle \left. \frac{\partial^i}{\partial \xi^i} \xi^j \right|_{\xi=0} \\
&= \frac{i!}{i!} \langle k^i \rangle \xi^0 + \sum_{j=i+1}^{\infty} \frac{1}{j!} \langle k^j \rangle j \cdot (j-1) \cdots (j-i) \xi^{j-i} \Big|_{\xi=0} = \langle k^i \rangle
\end{aligned} \tag{4.41}$$

#### 4.5.4 Factorial moment generating function

The *factorial moment generating function* (FMGF) can be constructed analogous to the MGF:

$$G_{[k]}^M(\xi) := \langle (\xi + 1)^k \rangle = \sum_{k=0}^{\infty} (\xi + 1)^k p(k) \tag{4.42}$$

Analogous to Equation 4.41, the factorial moments can be generated from the FMGF by deriving it  $i$  times:

$$\begin{aligned}
\left. \frac{\partial^i}{\partial \xi^i} G_{[k]}^M(\xi) \right|_{\xi=0} &= \left. \frac{\partial^i}{\partial \xi^i} \sum_{k=0}^{\infty} (\xi + 1)^k p(k) \right|_{\xi=0} \\
&= \sum_{k=0}^{\infty} p(k) \left. \frac{\partial^i}{\partial \xi^i} (\xi + 1)^k \right|_{\xi=0} \\
&= \sum_{k=0}^{\infty} p(k) k(k-1) \cdots (k-i+1) (\xi + 1)^{(k-i)} \Big|_{\xi=0} \\
&= \sum_{k=0}^{\infty} p(k) k^{[i]} = \mu_{[i]}^*
\end{aligned} \tag{4.43}$$

### 4.5.5 Cumulants and the CGF

The *cumulants*  $\kappa_i$  of a distribution offer an alternative set of values to describe a distribution other than the moments. Their definition is slightly more complex and utilizes moments and MGFs. In exchange, they exhibit some very useful features such as their additivity, which is also responsible for their naming: A cumulant of a convolution of distributions is the sum of the cumulants of each of the original distributions.

Since cumulants are defined by their *cumulant generating function* (CGF), the CGF will be introduced before the actual cumulants. The CGF is defined as the natural logarithm of the MGF (Equation 4.40):

$$G_k^C(\xi) := \ln \left( G_k^M(\xi) \right) = \ln \left( \sum_{j=0}^{\infty} \frac{1}{j!} \xi^j \langle k^j \rangle \right) \quad (4.44)$$

Analogous to the derivation of the moments from the MGF, the  $i$ th cumulant is defined as the  $i$ th derivative around zero of the CGF:

$$\kappa_i := \left. \frac{\partial^i}{\partial \xi^i} G_k^C(\xi) \right|_{\xi=0} \Leftrightarrow G_k^C(\xi) = \sum_{k=1}^{\infty} \frac{\xi^k}{k!} \kappa_i \quad (4.45)$$

By combining Equations 4.44 and 4.45, the cumulants can be calculated from the moments:

$$\sum_{k=1}^{\infty} \frac{\xi^k}{k!} \kappa_i = \ln \left( \sum_{j=0}^{\infty} \frac{\xi^j}{j!} \langle k^j \rangle \right) \quad (4.46)$$

The resolution of Equation 4.46 is tedious and only the final result will be shown here (Equation 4.47). Refer to [8] for a detailed demonstration. A recursion formula (Equation 4.48) may also be given that proves very useful for the actual calculation of the cumulants  $\kappa_i$  from the ordinary moments  $\mu_i^*$ :

$$\kappa_i = i! \sum_{m=1}^i \sum_{\pi, \rho} \prod_{j=1}^m \left( \frac{\mu_{p_j}^*}{p_j!} \right)^{\pi_j} \frac{(-1)^{\rho-1} (\rho-1)!}{\pi_j!} \quad (4.47)$$

$$\begin{aligned} &= \mu_i^* + i! \sum_{m=2}^i \sum_{\pi, \rho} \prod_{j=1}^m \left( \frac{\mu_{p_j}^*}{p_j!} \right)^{\pi_j} \frac{(-1)^{\rho-1} (\rho-1)!}{\pi_j!} \\ &= \mu_i^* - \sum_{k=1}^{i-1} \binom{i-1}{k-1} \kappa_k \mu_{i-k}^* \end{aligned} \quad (4.48)$$

The second summation in Equation 4.47 runs over all non-negative  $\pi_j$  and  $\rho$  subject to  $\sum p_j \pi_j = i$  and  $\sum \pi_j = \rho$ .

For the first few cumulants, relationship 4.47 turns out to be relatively simple:<sup>6</sup>

$$\begin{aligned} \kappa_1 &= \mu_1^* \\ \kappa_2 &= \mu_2^* - (\mu_1^*)^2 \\ \kappa_3 &= \mu_3^* - 3\mu_2^* \mu_1^* + 2(\mu_1^*)^3 \\ \kappa_4 &= \mu_4^* - 4\mu_3^* \mu_1^* - 3(\mu_2^*)^2 + 12\mu_2^* (\mu_1^*)^2 - 6(\mu_1^*)^4 \end{aligned} \quad (4.49)$$

---

<sup>6</sup>Equations for the cumulants up to  $\kappa_{10}$  are given in [8]

It can be shown that for a convolution of distributions, which occurs for example in the theory of fluorescence fluctuation spectroscopy, their cumulants simply add up.

#### 4.5.6 Factorial Cumulants and the FCGF

Analogous to the factorial moments, it is also possible to define *factorial cumulants*. Their definition and connection to factorial moments follows very closely the deduction of the cumulants in the previous section 4.5.5. The factorial cumulants are defined by their *factorial cumulant generating function* (FCGF), which is defined as the natural logarithm of the FMGF:

$$G_{[k]}^C(\xi) := \ln \left( G_{[k]}^M(\xi) \right) = \ln \left( \sum_{k=0}^{\infty} (\xi + 1)^k p(k) \right) \quad (4.50)$$

The  $i$ th factorial cumulant is then defined as the  $i$ th derivative around zero of the FCGF:

$$\kappa_{[i]} := \left. \frac{\partial^i}{\partial \xi^i} G_{[k]}^C(\xi) \right|_{\xi=0} \Leftrightarrow G_{[k]}^C(\xi) = \sum_{k=1}^{\infty} \frac{\xi^k}{k!} \kappa_{[i]} \quad (4.51)$$

The easiest way to actually calculate the factorial cumulants is with the help of the cumulants [8]. The cumulants in turn could then be calculated from the moments according to Equation 4.49. However, the according equations are cumbersome already for  $\kappa_{[3]}$  and  $\kappa_{[4]}$  and become very long for higher  $\kappa_{[i]}$ . It is therefore advantageous to express the factorial cumulants not in terms of the ordinary moments but the central moments and the mean  $\mu$ . The equations become much less complex, and as an additional advantage, the central moments of a distribution can be easily computed in MATLAB with the `moment()` command.

$$\begin{aligned} \kappa_{[1]} &= \kappa_1 & &= \mu \\ \kappa_{[2]} &= \kappa_2 - \kappa_1 & &= \mu_2 - \mu \\ \kappa_{[3]} &= \kappa_3 - 3\kappa_2 + 2\kappa_1 & &= \mu_3 - 3\mu_2 + 2\mu \\ \kappa_{[4]} &= \kappa_4 - 6\kappa_3 + 11\kappa_2 - 6\kappa_1 & &= \mu_4 - 6\mu_3 - 3\mu_2^2 + 11\mu_2 - 6\mu \end{aligned} \quad (4.52)$$

#### 4.5.7 Derivation of FCA

The aim of FCA is to find a simple connection between the cumulants of an experimentally measured p.c.h., which can be computed in a split second, and the physically interesting quantities of number  $N$  and brightness  $\varepsilon$ . Like PCH and FIDA, FCA uses Mandel's Equation 4.7. The first step is to show that the FMGF of the photon counts (experimentally determinable) equals the MGF of the fluorescence intensity  $W$  (to be expressed in terms of  $N$  and  $\varepsilon$ ):

$$\begin{aligned}
G_{[k]}^M(\xi) &= \sum_{k=0}^{\infty} (\xi + 1)^k p(k) \\
&= \sum_{k=0}^{\infty} (\xi + 1)^k \int_0^{\infty} \frac{W^k e^{-W}}{k!} p(W) dW \\
&= \int_0^{\infty} \sum_{k=0}^{\infty} (\xi + 1)^k \frac{W^k e^{-W}}{k!} p(W) dW \\
&= \int_0^{\infty} e^{-W} \sum_{k=0}^{\infty} \frac{[(\xi + 1)W]^k}{k!} p(W) dW \\
&= \int_0^{\infty} e^{-W} e^{(\xi+1)W} p(W) dW \\
&= \int_0^{\infty} e^{-\xi W} p(W) dW = G_W^M(\xi)
\end{aligned} \tag{4.53}$$

Since the CGF and FCGF are defined as the natural logarithms of the MGF and FMGF, respectively, from Equation 4.53 also follows the equality of the CGF with the FCGF, and since the cumulants and factorial cumulants are uniquely defined by the CGF and FCGF, the factorial cumulants of  $p(k)$  equal the cumulants of  $p(W)$ .<sup>7</sup>

Now that a connection has been found between the experimental measurements and the cumulants of  $p(W)$ , the second step is to find a relationship between the cumulants of  $p(W)$  and  $\varepsilon$  and  $N$ . Analogous to the derivation of PCH and FIDA, the case of a single freely diffusing fluorophore is initially considered as a preliminary step. Since the cumulants are based on the moments, at first an expression for the moments of  $p(W)$  is derived. Therein, the definition of  $p(W)$  from Equation 4.12 in the PCH section is used:

$$\begin{aligned}
\mu_i^* &= \langle W^i \rangle = \int_0^{\infty} W^i p(W) dW \\
&= \int_0^{\infty} W^i \int_{\mathbb{R}^3} \delta(W - \varepsilon \exp\left(-\frac{2(x^2 + y^2)}{\omega_r^2} - \frac{2z^2}{\omega_z^2}\right)) p_r d\vec{r} dW \\
&= \int_{\mathbb{R}^3} \left( \varepsilon \exp\left(-\frac{2(x^2 + y^2)}{\omega_r^2} - \frac{2z^2}{\omega_z^2}\right) \right)^i p_r d\vec{r} \\
&= \varepsilon^i p_r \int_{\mathbb{R}^3} \exp\left(-\frac{2i(x^2 + y^2)}{\omega_r^2} - \frac{2iz^2}{\omega_z^2}\right) d\vec{r} \\
&= \left(\frac{\pi}{2i}\right)^{\frac{3}{2}} \omega_r^2 \omega_z \varepsilon^i p_r
\end{aligned} \tag{4.54}$$

Up to this point, the derivation resembles closely the derivation of PCH itself. The key idea lies in the expansion to multiple fluorophores. In PCH, complicated convolutions of probability

---

<sup>7</sup>Furthermore, from Equation 4.53 also follows the equality of the factorial moments of  $p(k)$  with the moments of  $p(W)$ .

distributions were necessary to expand the theory to multiple fluorophores. In contrast, here, a simple addition of cumulants solves the problem. The cumulants of  $p(W)$  can be expressed according to Equation 4.47:

$$\begin{aligned}\kappa_i^{(1)} &= \langle W^i \rangle + i! \sum_{m=2}^i \sum_{\pi, \rho} \prod_{j=1}^m \left( \frac{\langle W_{p_j} \rangle}{p_j!} \right)^{\pi_j} \frac{(-1)^{\rho-1} (\rho-1)!}{\pi_j!} \\ &= \left( \frac{\pi}{2i} \right)^{\frac{3}{2}} \omega_r^2 \omega_z \varepsilon^i p_r + i! \sum_{m=2}^i \sum_{\pi, \rho} \prod_{j=1}^m \left( \frac{\left( \frac{\pi}{2i} \right)^{\frac{3}{2}} \omega_r^2 \omega_z \varepsilon^i p_r}{p_j!} \right)^{\pi_j} \frac{(-1)^{\rho-1} (\rho-1)!}{\pi_j!}\end{aligned}\quad (4.55)$$

Although this equation looks very complex, there is one important point to note. The probability  $p_r$  for a freely diffusing fluorophore to occupy a location  $\vec{r}$  equals  $1/V_{total}$ , where  $V_{total}$  is the total sample volume (not to be confused with the confocal volume!). Therefore, the second term of Equation 4.55 can be schematically written in a simplified way:

$$\kappa_i^{(1)} = \frac{1}{V_{total}} \left( \frac{\pi}{2i} \right)^{\frac{3}{2}} \omega_r^2 \omega_z \varepsilon^i + \sum_{m=2}^i \frac{1}{V^m} f_m \quad (4.56)$$

Here, the factor  $f_m$  summarizes all factors and summands in the second term of Equation 4.55 that belong to the  $m$ th exponent of  $\frac{1}{V}$ . The cumulants of the distribution  $p(W)$  for the total number of molecules in the sample  $N_{total}$  (not to be confused with the number of molecules in the confocal volume,  $N$ ) is simply the summation of all cumulants. Since for each and every molecule,  $\kappa_i^{(1)}$  is the same, the summation simplifies to a multiplication with  $N_{total}$ :

$$\begin{aligned}\kappa_i^{(N_{total})} &= N_{total} \kappa_i^{(1)} \\ &= \frac{N_{total}}{V_{total}} \left( \frac{\pi}{2i} \right)^{\frac{3}{2}} \omega_r^2 \omega_z \varepsilon^i + N_{total} \sum_{m=2}^i \frac{1}{V^m} f_m \\ &= c \left( \frac{\pi}{2i} \right)^{\frac{3}{2}} \omega_r^2 \omega_z \varepsilon^i + c \sum_{m=1}^{i-1} \frac{1}{V^m} f_m \\ &= c \left( \frac{\pi}{2i} \right)^{\frac{3}{2}} \omega_r^2 \omega_z \varepsilon^i \quad \text{for } V \rightarrow \infty\end{aligned}\quad (4.57)$$

where  $c$  is the concentration in the units *molecule per m<sup>3</sup>*. Now it becomes clear why Equation 4.55 was reduced to the form of Equation 4.56: For a large sample volume, the limit  $V \rightarrow \infty$  may be taken, and the right term converges to zero. Only the first term remains, because the concentration of molecules is an intrinsic property and does not scale with the volume. Using Equation 4.19 to calculate the volume of a three dimensional Gaussian PSF, and recalling that the cumulants of  $p(W)$  equal the factorial cumulants of  $p(k)$ , this leads to the final expression for the cumulants:

$$\kappa_{[i]}(p(k)) = \kappa_i(p(W)) = i^{-\frac{3}{2}} \bar{N} \varepsilon^i \quad (4.58)$$

The generalization of Equation 4.58 to the case of multiple fluorescent species is trivial due to the additivity of the cumulants:

$$\kappa_{[i]}(p(k)) = \kappa_i(p(W)) = i^{-\frac{3}{2}} \sum_j \bar{N}_j \varepsilon_j^i \quad (4.59)$$

Example computer code to calculate  $N$  and  $\varepsilon$  with FCA is provided in Appendix B.4.



## 4.6 Fluorescence Correlation Spectroscopy

FCS, introduced in theory and experiment in [19], [20], and [21], is a method that, in contrast to the methods introduced so far, is based on the temporal behavior of the fluorescence fluctuations rather than their amplitude. Consequently, the physical quantity that can be determined with FCS, besides the particle number  $\bar{N}$ , is the diffusion coefficient  $D$  rather than the molecular brightness  $\varepsilon$ .<sup>8</sup>  $D$  is calculated from the average time  $\tau_D$  that a fluorophore takes to traverse the confocal volume, and it is easily understandable that  $\tau_D$  influences the duration of the fluorescence fluctuations rather than their amplitude. Knowledge about the diffusion coefficient of a molecule is valuable because it gives a statement about its hydrodynamic radius, and thereby about its size.

### 4.6.1 The autocorrelation function

Correlation analysis is a concept from signal theory to determine statistically, on what time scales two signals resemble each other. A special case is the autocorrelation analysis, where a signal is compared to itself instead of a different one. The idea behind applying autocorrelation analysis to fluorescence fluctuation signals is simple. As discussed before, the signal fluctuations are caused by the fluctuations of fluorophores into and out of the confocal volume. Therefore, on a statistical basis, the fluorescence signal should exhibit a "self-similarity" on time scales smaller than or equal to the time the fluorophores take to diffuse through the confocal volume. Evaluating the time scale where the self-resemblance disappears therefore yields information about the diffusion time  $\tau_D$  of the molecules in question.

Mathematically, the self-similarity is expressed by the *autocorrelation function*. In this function, the fluorescence signal at a time  $t$  is compared with itself at a later time  $t + \tau$ . The comparison is done by multiplication and then averaging over all available times  $t$ :  $\langle W(t)W(t + \tau) \rangle$ . This construct can be normalized by dividing it by the square average intensity, and brought to a zero baseline by subsequently subtracting 1\*, resulting in the *normalized autocorrelation function*  $G(\tau) = \frac{\langle W(t)W(t + \tau) \rangle}{\langle W(t) \rangle^2} - 1$ .  $G(\tau)$  is expressed in terms of the actual fluctuations  $\delta W(t) := W(t) - \langle W(t) \rangle$  for subsequent calculations:

$$\begin{aligned}
 G(\tau) &= \frac{\langle W(t)W(t + \tau) \rangle}{\langle W(t) \rangle^2} - 1 \\
 &= \frac{\langle W(t)W(t + \tau) \rangle - \langle W(t) \rangle^2 - \langle W(t) \rangle^2 + \langle W(t) \rangle^2}{\langle W(t) \rangle^2} \\
 &= \frac{\langle W(t)W(t + \tau) \rangle - \langle W(t) \rangle \langle W(t) \rangle - \langle W(t + \tau) \rangle \langle W(t) \rangle + \langle W(t) \rangle^2}{\langle W(t) \rangle^2} \\
 &= \frac{\langle W(t)W(t + \tau) - W(t) \langle W(t + \tau) \rangle - W(t + \tau) \langle W(t) \rangle + \langle W(t) \rangle \langle W(t + \tau) \rangle \rangle}{\langle W(t) \rangle^2} \\
 &= \frac{\langle (W(t) - \langle W(t) \rangle) (W(t + \tau) - \langle W(t + \tau) \rangle) \rangle}{\langle W(t) \rangle^2} \\
 &= \frac{\langle \delta W(t) \delta W(t + \tau) \rangle}{\langle W(t) \rangle^2} = \frac{\langle \delta W(0) \delta W(\tau) \rangle}{\langle W(0) \rangle^2}
 \end{aligned} \tag{4.60}$$

Here,  $\delta W(t)$  quantifies the difference between the intensity at a time  $t$  from the average intensity, thus being a measure for the size of the fluctuations. To understand the mechanism of

<sup>8</sup> $\varepsilon$  can however be determined from  $\bar{N}$  and the average measured fluorescence intensity  $\bar{W}$ .

\*This step is sometimes omitted, leading to a baseline value of  $G(\tau) = 1$  for uncorrelated intensity pairs.

Equation 4.60, it is helpful to realize that generally two different things can happen: The first possibility is that for all pairs of time points with a time difference  $\tau$ ,  $W(t)$  and  $W(t + \tau)$  are uncorrelated. Then the products  $\delta W(t)\delta W(t + \tau)$  will yield randomly distributed, uncorrelated results. Therefore the averaging  $\langle \delta W(t)\delta W(t + \tau) \rangle$  over all the products will converge to zero. The second possibility is that for many pairs of time points with a time difference  $\tau$ ,  $W(t)$  and  $W(t + \tau)$  have similar values, e.g. because the fluorophores that  $W(t)$  originates from did not move far enough during  $\tau$  to allow  $W(t + \tau)$  to change to a value completely unrelated to  $W(t)$ . In this case, the products  $\delta W(t)\delta W(t + \tau)$  will generally yield values greater than zero, and their average  $\langle \delta W(t)\delta W(t + \tau) \rangle$  will therefore also be greater than zero.

Figure 4.4 shows an idealized autocorrelation curve  $G(\tau)$  that exhibits a positive autocorrelation for values of  $\tau$  smaller than the diffusion time of the corresponding fluorophores, and zero autocorrelation otherwise.

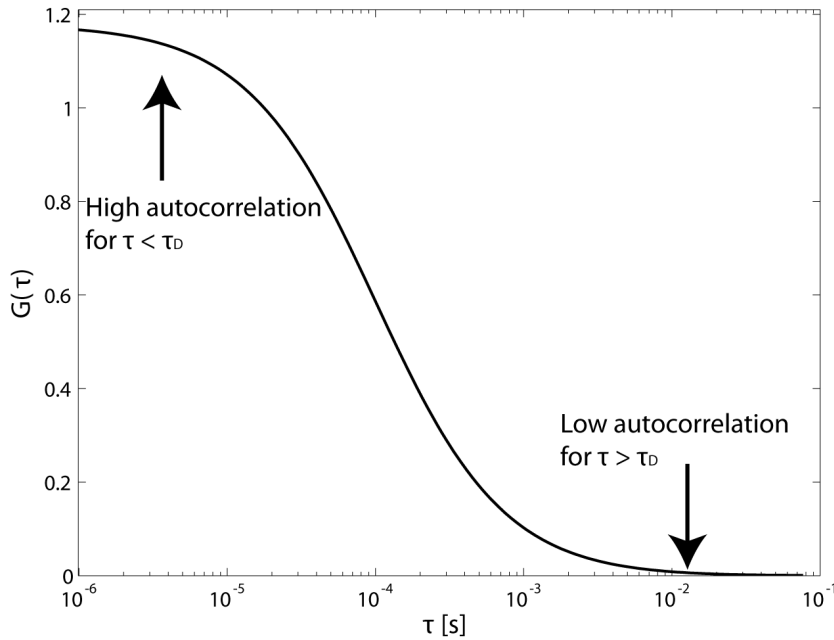


**Figure 4.4:** Typical autocorrelation curve for freely diffusing fluorophores. For short correlation times, the fluorophores are in a position close to their original ones, so the corresponding intensity pairs correlate. For long correlation times, vice versa.

Apart from the diffusion time, another physical quantity of the sample can be extracted from the curve: the concentration  $c$  of fluorophores. This is also easily understandable. If the concentration is comparably high and a relatively large number of molecules is located within the confocal volume, then the change in fluorescence  $\delta W$  due to one fluorophore diffusing in or out of the volume will be small, resulting in a small amplitude  $G(0)$  of the autocorrelation curve. In contrast, if  $c$  is low, then only a few fluorophores are located within the confocal volume and the fluctuations will be large relative to the total fluorescence intensity, resulting in a large amplitude  $G(0)$ .

In order to extract information from the autocorrelation curve, it is necessary to translate the above considerations into a mathematical framework. Here, in contrast to PCH, FIDA, and FCA, it is not necessary to employ Mandel's formula because the shot noise is randomly

distributed and does not contribute to the correlation curve. Therefore only the fluorescence intensity  $W(t)$  at the detector surface is considered. A second difference to the theoretical foundation of PCH, FIDA, and FCA is that for FCS the time dependence of  $W(t)$  is essential and can not be neglected by using the probability  $p(W)$ . Instead, an explicit expression for  $W(t)$  has to be found.

#### 4.6.2 Fluorescence intensity time dependence

For FCS, the fluorescence intensity  $W(\vec{r}, t)$  that originates from a location  $\vec{r}$  in the sample, is expressed as a product of the local concentration  $C(\vec{r}, t)$ , the normalized local excitation brightness  $I(\vec{r})$ , and the molecular brightness  $\varepsilon$ . Therefore the total fluorescence intensity is the spatial integration over the product of the above factors:

$$W(t) = \int_{\mathbb{R}^3} \varepsilon I(\vec{r}) C(\vec{r}, t) d\vec{r} \quad (4.61)$$

The fluorescence intensity fluctuations are caused by fluctuations in the local concentration  $C(\vec{r}, t)$ . In order to resolve the autocorrelation,  $\delta W(t)$  has to be expressed:

$$\begin{aligned} \delta W(t) &= W(t) - \langle W(t) \rangle \\ &= \varepsilon \int_{\mathbb{R}^3} I(\vec{r}) C(\vec{r}, t) d\vec{r} - \langle \varepsilon \int_{\mathbb{R}^3} I(\vec{r}) C(\vec{r}, t) d\vec{r} \rangle \\ &= \varepsilon \int_{\mathbb{R}^3} I(\vec{r}) C(\vec{r}, t) d\vec{r} - \varepsilon \int_{\mathbb{R}^3} I(\vec{r}) \langle C \rangle d\vec{r} \\ &= \varepsilon \int_{\mathbb{R}^3} I(\vec{r}) (C(\vec{r}, t) - \langle C \rangle) d\vec{r}^* \\ &= \varepsilon \int_{\mathbb{R}^3} I(\vec{r}) \delta C(\vec{r}, t) d\vec{r} \end{aligned} \quad (4.62)$$

#### 4.6.3 Model for linear regression

Inserting Equation 4.62 into the autocorrelation function 4.60 yields

$$\begin{aligned} G(\tau) &= \frac{\langle \delta W(\tau) \delta W(0) \rangle}{\langle W(0) \rangle^2} = \frac{\langle \varepsilon \int_{\mathbb{R}^3} I(\vec{r}) \delta C(\vec{r}, \tau) d\vec{r} \cdot \varepsilon \int_{\mathbb{R}^3} I(\vec{r}') \delta C(\vec{r}', 0) d\vec{r}' \rangle}{\left( \varepsilon \int_{\mathbb{R}^3} I(\vec{r}) \langle C \rangle d\vec{r} \right)^2} \\ &= \frac{\int_{\mathbb{R}^3} \int_{\mathbb{R}^3} I(\vec{r}) I(\vec{r}') \langle \delta C(\vec{r}, \tau) \delta C(\vec{r}', 0) \rangle d\vec{r} d\vec{r}'}{\langle C \rangle^2 \left( \int_{\mathbb{R}^3} I(\vec{r}) d\vec{r} \right)^2} \end{aligned} \quad (4.63)$$

---

\*Given a stationary and ergodic sample (ergodic: every sizable subsample is representative of the whole sample),  $\langle C \rangle$  is independent of time and location. Therefore it can also be viewed as an ensemble average over all fluorophores in the sample.

To further develop Equation 4.63, the expression  $\langle \delta C(\vec{r}, \tau) \delta C(\vec{r}', 0) \rangle$  has to be resolved. The fluctuations in the local concentration, caused by molecular diffusion, are governed by Fick's Second Law [22], which not only applies to  $C(\vec{r}, t)$ , but also to  $\delta C(\vec{r}, t)$ :

$$\begin{aligned} \frac{\partial}{\partial t} C(\vec{r}, t) &= D \vec{\nabla}_{\vec{r}}^2 C(\vec{r}, t) \\ \frac{\partial}{\partial t} (\delta C(\vec{r}, t) - \langle C \rangle) &= D \vec{\nabla}_{\vec{r}}^2 (\delta C(\vec{r}, t) - \langle C \rangle) \\ \frac{\partial}{\partial t} \delta C(\vec{r}, t) &= D \vec{\nabla}_{\vec{r}}^2 \delta C(\vec{r}, t) \quad , \text{ because } \frac{\partial}{\partial t} \langle C \rangle = 0 \text{ and } \vec{\nabla}_{\vec{r}}^2 \langle C \rangle = 0 \end{aligned} \quad (4.64)$$

$\vec{\nabla}_{\vec{r}}$  is the *del* operator, defined as  $\vec{\nabla}_{\vec{r}} = \frac{\partial}{\partial x} \vec{x} + \frac{\partial}{\partial y} \vec{y} + \frac{\partial}{\partial z} \vec{z}$ . The index  $\vec{r}$  indicates the variable that the operator works on.

The differential equation 4.64 can be solved by transforming it into Fourier space. Therefore the Fourier expansion  $\delta C(\vec{r}, t) = \int_{\mathbb{R}^3} e^{i\vec{\rho}\vec{r}} \delta \hat{C}(\vec{\rho}, \tau) d\vec{\rho}$  is used here:<sup>9</sup>

$$\begin{aligned} \frac{\partial}{\partial t} \delta C(\vec{r}, t) &= D \vec{\nabla}_{\vec{r}}^2 \delta C(\vec{r}, t) \\ \frac{\partial}{\partial t} \int_{\mathbb{R}^3} e^{i\vec{\rho}\vec{r}} \delta \hat{C}(\vec{\rho}, \tau) d\vec{\rho} &= D \vec{\nabla}_{\vec{r}}^2 \int_{\mathbb{R}^3} e^{i\vec{\rho}\vec{r}} \delta \hat{C}(\vec{\rho}, \tau) d\vec{\rho} \\ \int_{\mathbb{R}^3} e^{i\vec{\rho}\vec{r}} \frac{\partial}{\partial t} \delta \hat{C}(\vec{\rho}, \tau) d\vec{\rho} &= \int_{\mathbb{R}^3} \vec{\nabla}_{\vec{r}}^2 e^{i\vec{\rho}\vec{r}} D \delta \hat{C}(\vec{\rho}, \tau) d\vec{\rho} \end{aligned} \quad (4.65)$$

Because  $\vec{\nabla}_{\vec{r}}$  operates in  $\vec{r}$ -space, but not in  $\vec{\rho}$ -space, it follows that  $\vec{\nabla}_{\vec{r}}^2 \delta \hat{C}(\vec{\rho}, \tau) = 0$ . Therefore, Equation 4.65 simplifies:

$$\int_{\mathbb{R}^3} e^{i\vec{\rho}\vec{r}} \frac{\partial}{\partial t} \delta \hat{C}(\vec{\rho}, \tau) d\vec{\rho} = \int_{\mathbb{R}^3} i^2 \vec{\rho}^2 e^{i\vec{\rho}\vec{r}} D \delta \hat{C}(\vec{\rho}, \tau) d\vec{\rho} \quad (4.66)$$

Because the Fourier transform is a bijection in  $\mathbb{R}^3$ , the integrands in Equation 4.66 are equal, and the resulting differential equation in  $\tau$  for  $\delta \hat{C}(\vec{\rho}, \tau)$  can now be solved. The result can subsequently be Fourier back transformed into  $\vec{r}$ -space:

$$\begin{aligned} \frac{\partial}{\partial t} \delta \hat{C}(\vec{\rho}, \tau) &= -\vec{\rho}^2 D \delta \hat{C}(\vec{\rho}, \tau) \\ \delta \hat{C}(\vec{\rho}, \tau) &= \delta \hat{C}(\vec{\rho}, 0) e^{-\vec{\rho}^2 D \tau} \\ \int_{\mathbb{R}^3} e^{i\vec{\rho}\vec{r}} \delta \hat{C}(\vec{\rho}, \tau) d\vec{\rho} &= \int_{\mathbb{R}^3} e^{i\vec{\rho}\vec{r}} \delta \hat{C}(\vec{\rho}, 0) e^{-\vec{\rho}^2 D \tau} d\vec{\rho} \\ \delta C(\vec{r}, \tau) &= \int_{\mathbb{R}^3} e^{i\vec{\rho}\vec{r}} \frac{1}{(2\pi)^3} \int_{\mathbb{R}^3} e^{-i\vec{\rho}\vec{r}'} \delta C(\vec{r}', 0) d\vec{r}' e^{-\vec{\rho}^2 D \tau} d\vec{\rho} \end{aligned} \quad (4.67)$$

With this, the expression  $\langle \delta C(\vec{r}, \tau) \delta C(\vec{r}', 0) \rangle$  from Equation 4.67 can be constructed:

<sup>9</sup>The convention used in this work for the Fourier transforms is:

$$\begin{aligned} \hat{f}(\vec{\rho}) &= \frac{1}{2\pi} \int_{\mathbb{R}^3} e^{-i\vec{\rho}\vec{r}} f(\vec{r}) d\vec{r} \\ f(\vec{r}) &= \int_{\mathbb{R}^3} e^{i\vec{\rho}\vec{r}} \hat{f}(\vec{\rho}) d\vec{\rho} \end{aligned}$$

$$\begin{aligned}
\langle \delta C(\vec{r}, \tau) \delta C(\vec{r}', 0) \rangle &= \left\langle \int_{\mathbb{R}^3} e^{i\vec{\rho}\vec{r}} \frac{1}{(2\pi)^3} \int_{\mathbb{R}^3} e^{-i\vec{\rho}\vec{r}'} \delta C(\vec{r}', 0) d\vec{r}' e^{-\vec{\rho}^2 D \tau} d\vec{\rho} \delta C(\vec{r}, 0) \right\rangle \\
&= \frac{1}{(2\pi)^3} \int_{\mathbb{R}^3} e^{i\vec{\rho}\vec{r}} \int_{\mathbb{R}^3} e^{-i\vec{\rho}\vec{r}'} \langle \delta C(\vec{r}', 0) \delta C(\vec{r}, 0) \rangle d\vec{r}' e^{-\vec{\rho}^2 D \tau} d\vec{\rho}
\end{aligned} \tag{4.68}$$

The term  $\langle \delta \hat{C}(\vec{r}', 0) \delta C(\vec{r}, 0) \rangle$  describes the average correlation between molecules at positions  $\vec{r}'$  and  $\vec{r}$  at the same time. Obviously no molecule can be simultaneously at two different positions, so the average correlation is zero unless  $\vec{r}' = \vec{r}$ . Therefore the term can be simplified:

$$\begin{aligned}
\langle \delta C(\vec{r}', 0) \delta C(\vec{r}, 0) \rangle &= \langle \delta C(\vec{r}, 0) \delta C(\vec{r}, 0) \rangle \delta(\vec{r}' - \vec{r}) \\
&= \langle \delta C(\vec{r}, 0)^2 \rangle \delta(\vec{r}' - \vec{r}) \\
&= \langle C \rangle \delta(\vec{r}' - \vec{r})
\end{aligned} \tag{4.69}$$

Since the distribution of fluorophores in the sample is governed by Poissonian statistics, in the last step the property of the Poisson distribution was exploited that its variance equals its mean. For a more elaborate explanation refer to [20]. Inserting Equation 4.69 into Equation 4.68 yields

$$\begin{aligned}
\langle \delta C(\vec{r}, \tau) \delta C(\vec{r}, 0) \rangle &= \frac{1}{(2\pi)^3} \int_{\mathbb{R}^3} e^{i\vec{\rho}\vec{r}} \int_{\mathbb{R}^3} e^{-i\vec{\rho}\vec{r}'} \langle C \rangle \delta(\vec{r}' - \vec{r}) d\vec{r}' e^{-\vec{\rho}^2 D \tau} d\vec{\rho} \\
&= \frac{\langle C \rangle}{(2\pi)^3} \int_{\mathbb{R}^3} e^{i\vec{\rho}\vec{r}} e^{-i\vec{\rho}\vec{r}} e^{-\vec{\rho}^2 D \tau} d\vec{\rho} \\
&= \frac{\langle C \rangle}{(2\pi)^3} \int_{\mathbb{R}^3} e^{i\vec{\rho}(\vec{r}-\vec{r}) - \vec{\rho}^2 D \tau} d\vec{\rho} \\
&= \frac{\langle C \rangle}{(4\pi D \tau)^{\frac{3}{2}}} e^{-\frac{(\vec{r}-\vec{r})^2}{4D\tau}}
\end{aligned} \tag{4.70}$$

With this result and with the assumption of a three dimensional Gaussian PSF (Equation 4.9), the autocorrelation function (Equation 4.63) can be further developed and brought to an analytical form that can be used to fit experimentally obtained autocorrelation curves and extract  $D$  and  $\bar{N}$ :

$$\begin{aligned}
G(\tau) &= \frac{\int_{\mathbb{R}^3} \int_{\mathbb{R}^3} I_0 e^{\left(-\frac{2(x^2+y^2)}{\omega_r^2} - \frac{2z^2}{\omega_z^2}\right)} I_0 e^{\left(-\frac{2(x'^2+y'^2)}{\omega_r^2} - \frac{2z'^2}{\omega_z^2}\right)} \frac{\langle C \rangle}{(4\pi D\tau)^{\frac{3}{2}}} e^{-\frac{(\vec{r}-\vec{r}')^2}{4D\tau}} d\vec{r} d\vec{r}'}{\langle C \rangle^2 \left( \int_{\mathbb{R}^3} I(\vec{r}) d\vec{r} \right)^2} \\
&= \frac{1}{\langle C \rangle \omega_r^2 \omega_z \pi^{\frac{3}{2}}} \left( \frac{1}{1 + \frac{4D\tau}{\omega_r^2}} \right) \sqrt{\frac{1}{1 + \frac{4D\tau}{\omega_z^2}}} \\
&= \frac{1}{\langle C \rangle \omega_r^2 \omega_z \pi^{\frac{3}{2}}} \left( \frac{1}{1 + \frac{\tau}{\tau_D}} \right) \sqrt{\frac{1}{1 + \frac{\omega_r^2}{\omega_z^2} \frac{\tau}{\tau_D}}} , \text{ where } \tau_D = \frac{\omega_r^2}{4D} \\
&= \frac{2^{-\frac{3}{2}}}{\bar{N}} \left( \frac{1}{1 + \frac{\tau}{\tau_D}} \right) \sqrt{\frac{1}{1 + \frac{\omega_r^2}{\omega_z^2} \frac{\tau}{\tau_D}}}
\end{aligned} \tag{4.71}$$

In the last step, the volume of the PSF according to Equation 4.19,  $V_0 = (\frac{\pi}{2})^{\frac{3}{2}} \omega_r^2 \omega_z$ , in combination with the trivial relation  $\bar{N} = \langle C \rangle V_0$ , was used to obtain the final form. The *structure parameter*,  $p = \frac{w_z}{w_r}$ , is often substituted in Equation 4.71. An example FCS analysis is shown in Figure 4.5

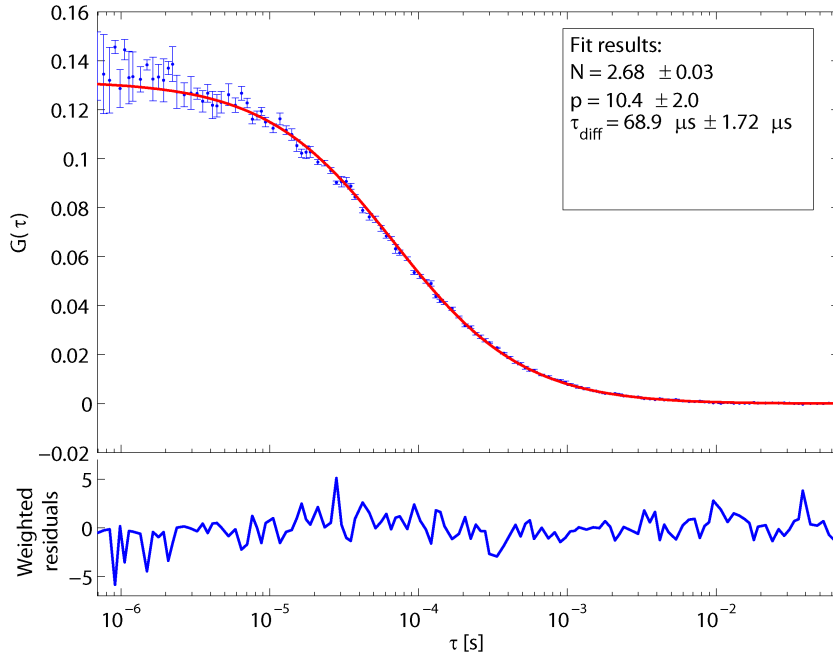


**Figure 4.5:** Autocorrelation analysis of a nanomolar solution of the freely diffusing synthetic fluorophore ATTO 488. Fluorescence fluctuation data was measured for 180 s, and divided into eight partitions. Autocorrelation curves were computed for each partition separately and subsequently averaged to obtain an average autocorrelation curve with error bars. The model from Equation 4.71 was used to fit the data (red line). The weighted residuals are shown at the bottom.

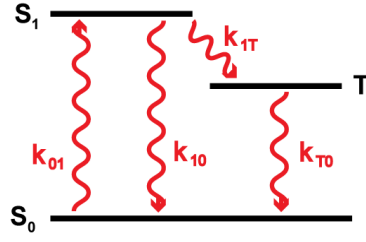


**Figure 4.6:** Schematic of the relevant singlet and triplet states of a typical fluorophore. The fluorescence rate  $k_{10}$  is usually high compared to the intersystem crossing rates  $k_{1T}$  and  $k_{T0}$ , because these transitions are quantum mechanically forbidden. Once in the triplet state, the fluorophore will therefore be nonfluorescent for a comparably long time.

The calculation of the autocorrelation curves from the measurement data was performed using an algorithm optimized for low computation times [23]. The algorithm is given in Appendix B.2

#### 4.6.4 Triplet states

Very often the model introduced in the previous section is insufficient to fit an experimentally obtained curve. The reason is that many fluorophores have a relatively high probability to enter a triplet state at the excitation intensities typically used for FCS. This leads them to be temporary non-fluorescent until they relax back to the singlet ground state. This effect appears in the autocorrelation curve as an additional slope, usually at faster timescales than diffusion. A scheme with rate constants is shown in Figure 4.6.

The transition into and out of triplet states appears as a flickering in the fluorescence of the fluorophore. Therefore, it will become visible in the autocorrelation curves. Since this usually occurs on a microsecond time scale, the fluorophores can be regarded as stationary during this process, because the diffusional motion is much slower. There are fully developed models that describe analytically the influence of triplet state kinetics on the autocorrelation curve [24, 25]:

$$G(\tau) = G_D(\tau) \left( 1 + \frac{T}{1-T} e^{-\lambda\tau} \right) \quad (4.72)$$

There,  $G_D(\tau)$  is the diffusional autocorrelation (Equation 4.71),  $T$  is the fraction of the molecules in the triplet state in the equilibrium, and  $\lambda$  is given by the different rates (Figure 4.6):

$$\lambda = \frac{1}{\tau_{trip}} = -k_{T0} - \frac{k_{01}k_{1T}}{k_{01} + k_{10}} \quad (4.73)$$

Because of the different timescales, the triplet state effect can be easily identified in the autocorrelation curve:

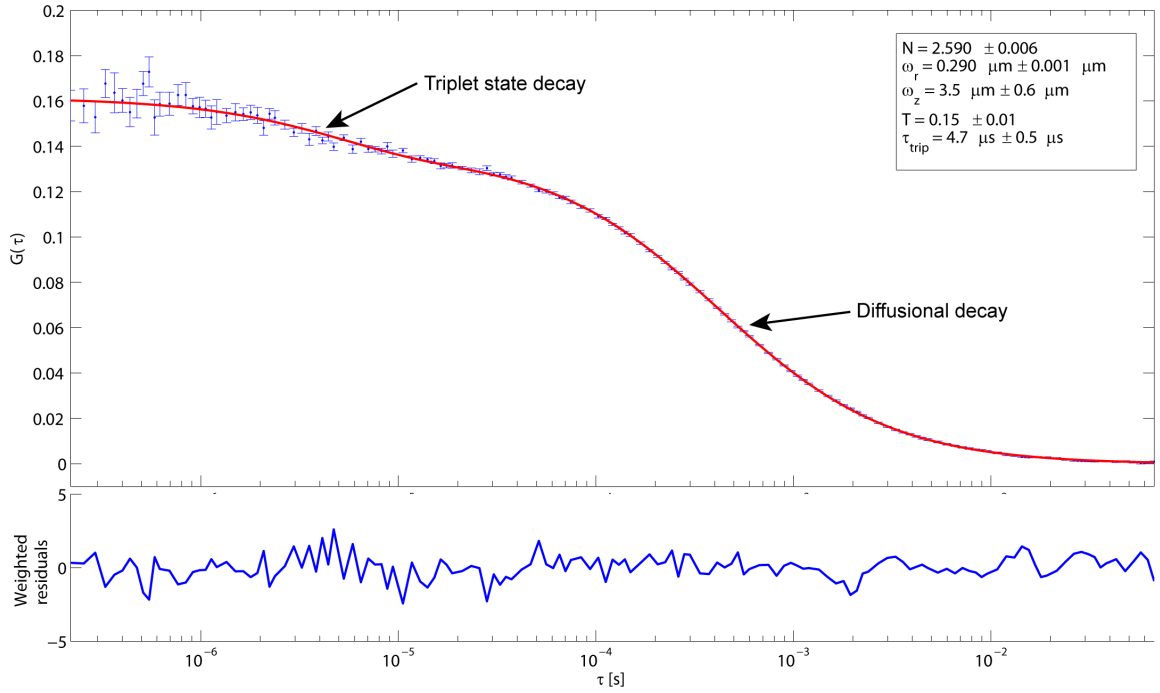


**Figure 4.7:** Autocorrelation analysis of a nanomolar solution of a DNA double strand labeled with ATTO 565. The model from Equation 4.72 was fitted to the data (red line).

## 4.7 Fluorescence Cross-Correlation Spectroscopy

FCCS [26] is a generalization of FCS where a fluorescence fluctuation signal is correlated with a second signal, e.g. originating from a different fluorescent species, rather than to itself. As a result, in FCCS, the cross-correlation is calculated rather than the autocorrelation.

Although FCS and FCCS are methodically similar, their advantages could not be more different. The main result of an FCCS analysis of differently labeled fluorescence species is an assertion about the presence of a dual-labeled species, which can be used as a direct and unambiguous measure for molecular binding. For example, in Chapter 6, the binding of a protein to a DNA strand is assessed under different conditions with FCCS.

The idea of FCCS has been even further extended to a triple correlation [27], where three different signals are used to calculate a two-dimensional correlation function. This concept, however, was not used within the scope of this work.

### 4.7.1 The cross-correlation function

The derivation of the theoretical background of FCCS follows closely that of FCS with the only difference that two different fluorescent species are considered. Hence, the cross-correlation function is defined as:

$$\begin{aligned}
 G_{ij}(\tau) &= \frac{\langle \delta W_i(t) \delta W_j(t + \tau) \rangle}{\langle W_i(t) \rangle \langle W_j(t) \rangle} \\
 &= \frac{\langle \delta W_i(0) \delta W_j(\tau) \rangle}{\langle W_i(0) \rangle \langle W_j(0) \rangle}
 \end{aligned} \tag{4.74}$$

The detected intensities of the detectors  $i$  and  $j$ , respectively, are the sums of the contributions of the respective fluorescence species alone and the dual-labeled fluorescence species  $ij$ :



$$W_i(t) = \varepsilon_i \left( \int_{\mathbb{R}^3} I(\vec{r}) C_i(\vec{r}, t) d\vec{r} + \int_{\mathbb{R}^3} I(\vec{r}) C_{ij}(\vec{r}, t) d\vec{r} \right) \quad (4.75)$$

Inserting Equation 4.75 into Equation 4.74 yields

$$\begin{aligned} G_{ij}(\tau) &= \frac{\varepsilon_i \varepsilon_j \int \int_{\mathbb{R}^3 \mathbb{R}^3} I(\vec{r}) I(\vec{r}') \langle (\delta C_i(\vec{r}, 0) + \delta C_{ij}(\vec{r}, 0)) (\delta C_j(\vec{r}', \tau) + \delta C_{ij}(\vec{r}', \tau)) \rangle d\vec{r} d\vec{r}'}{\varepsilon_i \varepsilon_j \int \int_{\mathbb{R}^3 \mathbb{R}^3} I(\vec{r}) I(\vec{r}') \langle C_i(\vec{r}, 0) + C_{ij}(\vec{r}, 0) \rangle \langle C_j(\vec{r}', 0) + C_{ij}(\vec{r}', 0) \rangle d\vec{r} d\vec{r}'} \\ &= \frac{\int \int_{\mathbb{R}^3 \mathbb{R}^3} I(\vec{r}) I(\vec{r}') \left( \langle \delta C_i(\vec{r}, 0) \delta C_j(\vec{r}', \tau) \rangle + \langle \delta C_i(\vec{r}, 0) \delta C_{ij}(\vec{r}', \tau) \rangle + \langle \delta C_{ij}(\vec{r}, 0) \delta C_j(\vec{r}', \tau) \rangle + \langle \delta C_{ij}(\vec{r}, 0) \delta C_{ij}(\vec{r}', \tau) \rangle \right) d\vec{r} d\vec{r}'}{\langle C_i + C_{ij} \rangle \langle C_j + C_{ij} \rangle \left( \int_{\mathbb{R}^3} I(\vec{r}) d\vec{r} \right)^2} \end{aligned} \quad (4.76)$$

There cannot be a positive average correlation between two fluorophores when they diffuse independently from each other. Therefore,  $\delta C_i(\vec{r}, 0) \delta C_j(\vec{r}', \tau) = \delta_{ij} \langle \delta C_i(\vec{r}, 0) \delta C_i(\vec{r}', \tau) \rangle^*$ , and only the last of the four correlation terms in Equation 4.76 remains:

$$\begin{aligned} G_{ij}(\tau) &= \frac{\int \int_{\mathbb{R}^3 \mathbb{R}^3} I(\vec{r}) I(\vec{r}') \langle \delta C_{ij}(\vec{r}, 0) \delta C_{ij}(\vec{r}', \tau) \rangle d\vec{r} d\vec{r}'}{\left( \langle C_i \rangle + \langle C_{ij} \rangle \right) \left( \langle C_j \rangle + \langle C_{ij} \rangle \right) \left( \int_{\mathbb{R}^3} I(\vec{r}) d\vec{r} \right)^2} \end{aligned} \quad (4.77)$$

From here on, the further development of the equation follows the FCS derivation (Equations 4.63 to 4.71), resulting in

$$G_{ij}(\tau) = \frac{\langle C_{ij} \rangle}{(\langle C_i \rangle + \langle C_{ij} \rangle) (\langle C_j \rangle + \langle C_{ij} \rangle)} \frac{1}{\omega_r^2 \omega_z \pi^{\frac{3}{2}}} \left( \frac{1}{1 + \frac{\tau}{\tau_D}} \right) \sqrt{\frac{1}{1 + \frac{\omega_z^2}{\omega_r^2} \frac{\tau}{\tau_D}}} \quad (4.78)$$

As mentioned in the introduction to this chapter, FFS methods are applicable for concentrations approximately between 1 – 100 nM, restricting the usefulness of FCCS for molecular systems with high dissociation constants. An additional restriction follows from the first term in this equation: the amplitude of the cross-correlation function does not only depend on the concentration of the dual labeled fluorescent species, but rather on its concentration relative to both of the single labeled ones. The sensitivity of FCCS therefore strongly depends on the fraction of dual labeled species (e.g. bound molecules), so a large excess of either single labeled species has to be avoided.

---

\*In this formula,  $\delta_{ij}$  is the Kronecker delta:  $\delta_{ij} = \begin{cases} 0, & i \neq j \\ 1, & i = j \end{cases}$

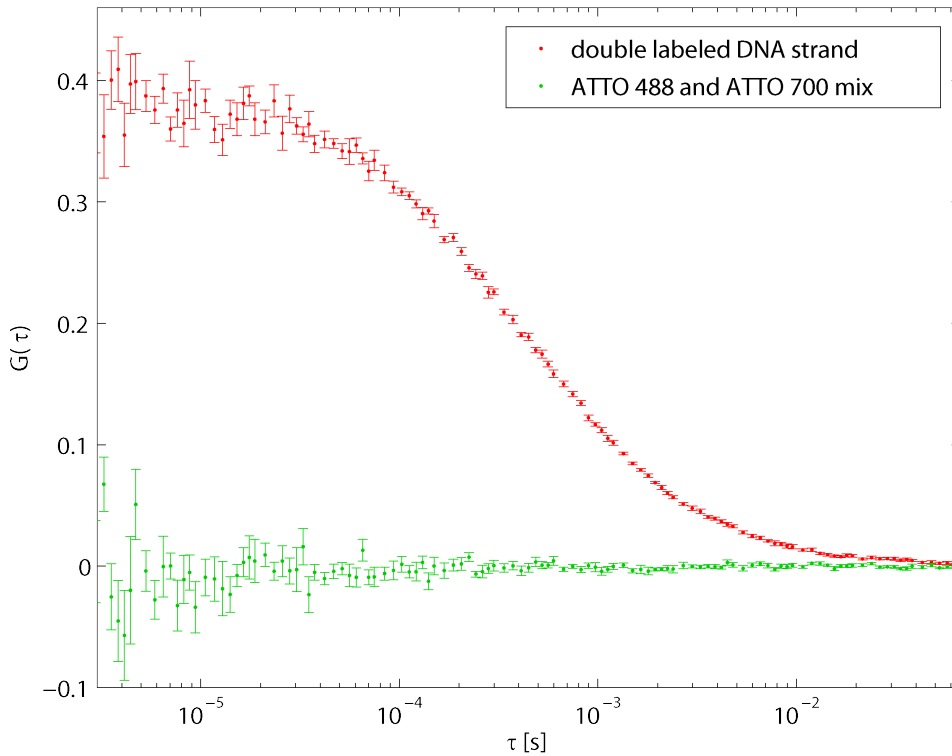


**Figure 4.8:** Two cross-correlation curves. Green: mixture of ATTO 488 and ATTO 700 fluorophores in aqueous solution. All fluorophores diffuse independently from each other, therefore the cross-correlation amplitude is zero. Red: mixture of two complementary DNA strands, one labeled with ATTO 488, and the other with ATTO 700. DNA double strands were subsequently formed by hybridization that thus carried both fluorophores. Hence the cross-correlation clearly has an amplitude larger than zero.

In order to quantify the amount of double labeled molecules in the sample with FCCS, it is necessary to include in the calculation the amount of both single labeled species (Equation 4.78). Therefore, it is advantageous to employ a global fit simultaneously to all three curves, both FCS curves and the FCCS curve.

## 4.8 Scanning FCS

A common issue with FCS and FCCS measurements, especially in a cellular environment, is photobleaching of the fluorophores. Photobleaching is a process where the fluorophore is photochemically destroyed after excitation, thereby permanently losing its ability to fluoresce. Several mechanisms can be responsible for photobleaching. Commonly, a molecule that is converted into an electronically excited state is more likely to interact with surrounding molecules such as oxygen. Therefore, for many fluorophores, a possible way to reduce photobleaching is removing as much of the oxygen in the sample solution as possible by *oxygen scavengers* such as for example glucose oxidase.

Not all fluorophores are equally prone to photobleaching. Fluorescent proteins such as GFP and RFP are generally more likely to bleach than synthetic fluorophores such as the rhodamine or cyanine dyes. Since photobleaching is connected to the fluorophores being in an excited state, the time until photobleaching of a fluorophore (not to be confused with the fluorescent lifetime  $\tau$ , see Equation 2.2) depends on the overall time it spends in the excited state. If the excitation intensity is increased, the fluorophore will be excited more often, and therefore bleach faster.

In a confocal setup, if a molecule diffuses slower, it will, on average, spend more time within the excitation volume before diffusing out. Therefore, it will be exposed to excitation light longer than a quickly diffusing molecule and therefore be more prone to bleaching.

Unfortunately, these considerations have a large impact on FCS and FCCS measurements in cells. For fluorescence measurements in cells, generally only fluorescent proteins are used as markers. Also, due to molecular crowding, diffusion within a cell will usually be very slow compared to diffusion in a free solution, so the fluorophores will be exposed to the excitation light comparably long. Since the use of oxygen scavengers is also impossible in cells, photobleaching becomes a major problem for FCS and especially FCCS measurements in cells.

One possible solution to that problem is to perform the measurements in a non-stationary fashion. In Scanning FCS [28, 29], the confocal volume is constantly moved, typically in a circle or back and forth along a line (Figure 4.9 A). It is irrelevant whether the confocal volume itself is moved through the sample (as is the case when a galvanometric beam scanner is used), or if the sample is moved through a stationary confocal volume (as happens when a piezoelectric microscope scanning stage is employed). In any case, the exposition time of the fluorophores to the excitation light is greatly reduced. However, the correlation curve is strongly affected by the scanning, which effectively superimposes an additional directed movement on the Brownian diffusion of the fluorophores.

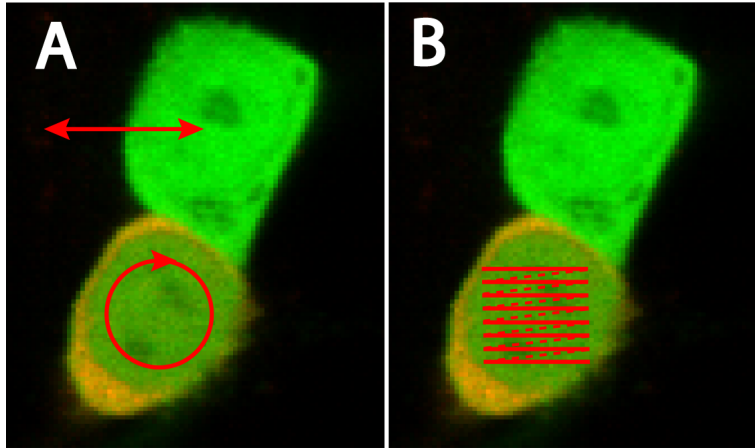


**Figure 4.9:** HEK293 cells transfected with GFP (upper cell), or with both GFP and an mCherry-labeled, cytosolic protein fragment (lower cell), diffusing independently from each other. The mCherry-labeled fragment cannot enter the nucleus due to its size. (A) Scanning FCS. The laser is continuously scanned through the sample with a defined trajectory, e.g. a circle or a line. (B) RICS. A whole area of the sample is raster-scanned.

#### 4.8.1 The Scanning correlation curve

In the case of scanning FCS, the PSF is no longer stationary. For circular scanning in the  $xy$ -plane, it can be described by the following time dependent displacement vector:

$$\vec{r}_{xy}(t) = r \begin{pmatrix} \cos(\Phi_0 + \omega t) \\ \sin(\Phi_0 + \omega t) \end{pmatrix} \quad (4.79)$$

Here,  $r$  is the radius of the scanning circle,  $\omega$  is the angular scanning frequency, and  $\Phi_0$  is the phase offset at the start of the measurement at  $t = 0$ . This results in a time dependent PSF, based on the three dimensional Gaussian PSF from Equation 4.9:

$$PSF(x, y, z, t) = \exp \left( -\frac{2(x - r \cos(\Phi_0 + \omega t))^2 - 2(y - r \sin(\Phi_0 + \omega t))^2}{\omega_r^2} - \frac{2z^2}{\omega_z^2} \right) \quad (4.80)$$

Inserting this Equation into the FCS derivation from Section 4.6 results in the following expression for the correlation function:

$$G(\tau) = G_D(\tau) \cdot G_S(\tau) = \frac{1}{\langle C \rangle \omega_r^2 \omega_z \pi^{\frac{3}{2}}} \left( \frac{1}{1 + \frac{\tau}{\tau_D}} \right) \sqrt{\frac{1}{1 + \frac{\omega_r^2}{\omega_z^2} \frac{\tau}{\tau_D}}} \cdot \exp \left( -\frac{4r^2 \sin^2(\frac{\omega\tau}{2})}{\omega_r^2 \left( 1 + \frac{\tau}{\tau_D} \right)} \right) \quad (4.81)$$

Figure 4.10 shows example Scanning FCS measurements on a solution of freely diffusing ATTO 488 fluorophores. Two Scanning FCS curves with different scanning radii are shown. A stationary FCS measurement is given for comparison, which works as an envelope for the Scanning FCS curves. The Scanning FCS curves show peaks at the correlation times  $\tau$  where the confocal volume has completed one or more cycles and has returned to its original location, thus resulting in a correlation as high as the respective stationary FCS curve. In between, the correlation decreases when there is no spatial overlap between the confocal volumes at different positions of the scanning trajectory. All three curves in Figure 4.10 were globally fitted with the model given in Equation 4.80. The scanning radii and frequency could be determined by the fit as well as the usual FCS fit parameters.

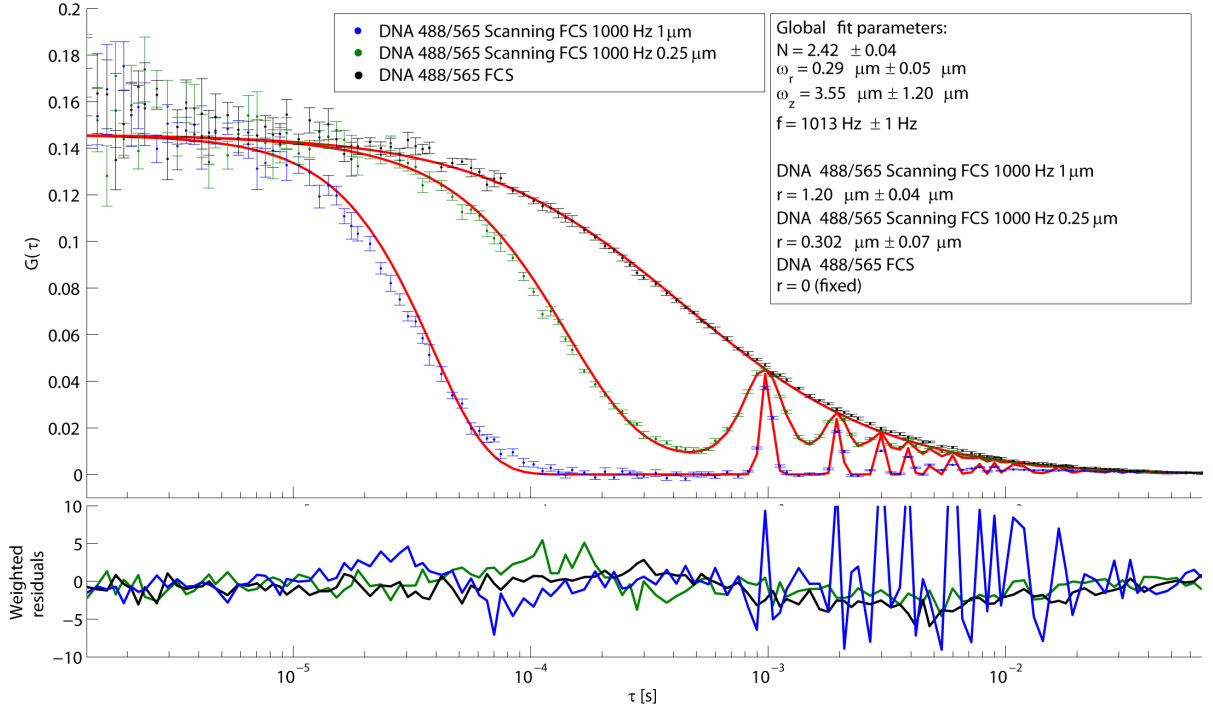


**Figure 4.10:** Scanning FCS curves of a solution of a DNA double strand labeled with ATTO 488. The scanning frequency was set to 1 kHz, with two different radii. A standard FCS measurement of the same sample is shown for comparison. The scanning FCS frequency and radii can be extracted from the fits.

It is of course straightforward to extend Scanning FCS to the case of cross-correlating two different fluorescent species, making the technique versatile to directly study molecular binding in cells.

## 4.9 Raster Image Correlation Spectroscopy

RICS [30, 31, 32] is a way to take the concept of Scanning FCS one step further. The idea of using a non-stationary focus to avoid bleaching is maintained and even extended: Instead of scanning only a circle or line within the sample, a whole region is raster-scanned with a confocal microscope (Figure 4.9 B). Thereby, a maximal amount of statistics is gained with a minimal light exposure of each point in the sample while allowing simultaneous measurements on two different timescales that can be up to two orders of magnitude apart.

Conveniently, RICS can be performed on standard image data acquired with a traditional laser scanning microscope, and does not require a TCSPC system. The image information is spatially correlated in  $x$  and  $y$ , resulting in a two-dimensional correlation pattern (Figure 4.11), that provides the same information about the sample as FCS. To create an image, all photons are binned into pixels according to their arrival time relative to the current position of the confocal volume.  $I(x, y)$  is defined as the number of photons in the pixel with the coordinate  $(x, y)$ . The two dimensional spatial correlation function is defined as:

$$G(\Delta x, \Delta y) = \frac{\langle I(x, y)I(x + \Delta x, y + \Delta y) \rangle}{\langle I(x, y) \rangle^2} \quad (4.82)$$

Note that here, the averaging goes over all spatial coordinates  $(x, y)$  rather than over time, as in FCS.

For free Brownian diffusion, this leads to the following expression:

$$G(\Delta x, \Delta y) = \frac{2^{-\frac{3}{2}}}{\bar{N}} \left( \frac{1}{1 + \frac{4D(\tau_x \Delta x + \tau_y \Delta y)}{\omega_r^2}} \right) \sqrt{\frac{1}{1 + \frac{4D(\tau_x \Delta x + \tau_y \Delta y)}{\omega_z^2}}} \exp \left( -\frac{\frac{1}{2} \left[ \left( \frac{2\Delta x s}{\omega_r} \right)^2 + \left( \frac{2\Delta y s}{\omega_r} \right)^2 \right]}{\left( 1 + \frac{4D(\tau_x \Delta x + \tau_y \Delta y)}{\omega_r^2} \right)} \right) \quad (4.83)$$

In the formula,  $\bar{N}$  is the average number of fluorophores in the confocal volume,  $D$  is their diffusion coefficient,  $\tau_x$  and  $\tau_y$  are the pixel sampling times in  $x$  and  $y$  direction,  $\omega_r$  and  $\omega_z$  are the radial and axial dimensions of the PSF, and  $s$  is the distance between adjacent pixels. Figure 4.11 shows a typical RICS correlation pattern that was recorded in a solution of freely diffusing DNA labeled with ATTO 565. Since the scanning of an image line is fast compared to the molecular diffusion, the  $x$  dimension of the correlation pattern is governed by the size of the confocal volume, because the images were recorded with a certain oversampling<sup>10</sup>. During the time between two lines, however, a significant amount of fluorophores can diffuse away. Therefore, the decay of the correlation pattern is much faster in the  $y$  direction, resulting in a narrower curve in  $y$ . Analogous to FCS, the diffusion coefficient can be determined by fitting Equation 4.83 to the data. Likewise, the concentration of the fluorophores is encoded in the amplitude of the correlation pattern and can be determined by the fit, too. Finally, as was the case with Scanning FCS, a cross-correlation of two different fluorescent species is also possible, allowing the study of molecular binding with RICS.

<sup>10</sup>Oversampling means that the distance between to pixels is smaller than the actual size of the confocal volume.

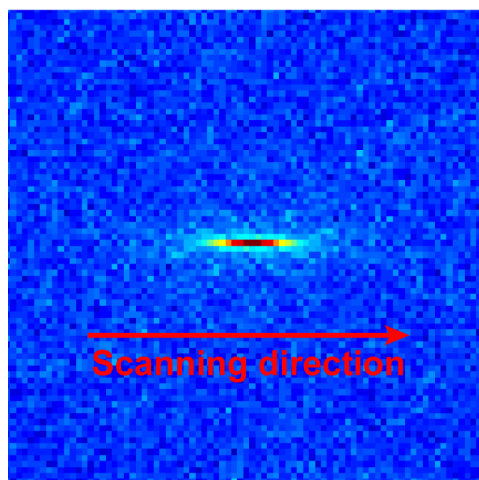


**Figure 4.11:** RICS correlation pattern. 50 images with a size of  $10\ \mu\text{m}$  were recorded in a solution of freely diffusing DNA labeled with ATTO 565 with a recording time of 500 ms per frame or  $7.6\ \mu\text{s}$  per pixel. RICS was performed on each image separately, and the resulting correlation patterns were averaged to reduce noise. A peak can be seen in the center. Its  $x$  dimension results from the size of the confocal volume relative to the image size. The  $y$  dimension gives information about the diffusion time of the fluorophores relative to the image scanning time.

## 4.10 Burst Analysis

Whereas the methods introduced so far yielded information about the molecular brightness and diffusion coefficient of a molecule or molecular complex (and thereby its size), or about the binding of different molecules to each other, the methods discussed in this and the next section, Burst Analysis [33, 34] and PDA [35, 36, 37], address fundamentally different questions. For Burst Analysis, standard stationary FFS measurements are taken according to the principles introduced before, but are applied on a sample with a much lower concentration than usual. All of the quantities mentioned above are in principle still accessible, but additionally and more importantly, single molecule FRET measurements become possible due to the low sample concentration. Even subpopulations with different FRET values (see Chapter 2.3) can be resolved within one sample, yielding e.g. information about multiple conformational states of a molecular species.

The main experimental difference that distinguishes Burst Analysis from the other techniques is the very low concentration of fluorescent molecules in the sample. Whereas in the FFS methods introduced so far, concentrations in the low  $nM$  range are typically used, for Burst Analysis the sample is around  $10 - 100\times$  more dilute, around  $10 - 100\ \text{pM}$ . Under these conditions, most of the time there are no fluorophores in the confocal volume, and only occasionally a single fluorophore diffuses through it. This is reflected in a fluorescence intensity trace that consists of a low background noise, disrupted by single, well separated bursts of fluorescence originating from the process a fluorophore diffusing through the confocal volume (Figure 4.12), hence the name. The fact that each burst can be assigned to a single fluorophore is exploited in the analysis. For FRET measurements, the donor is excited with an adequate wavelength, and donor and acceptor emission are detected with two different detectors separated by a carefully chosen dichroic mirror (see Section 3.4 for details).

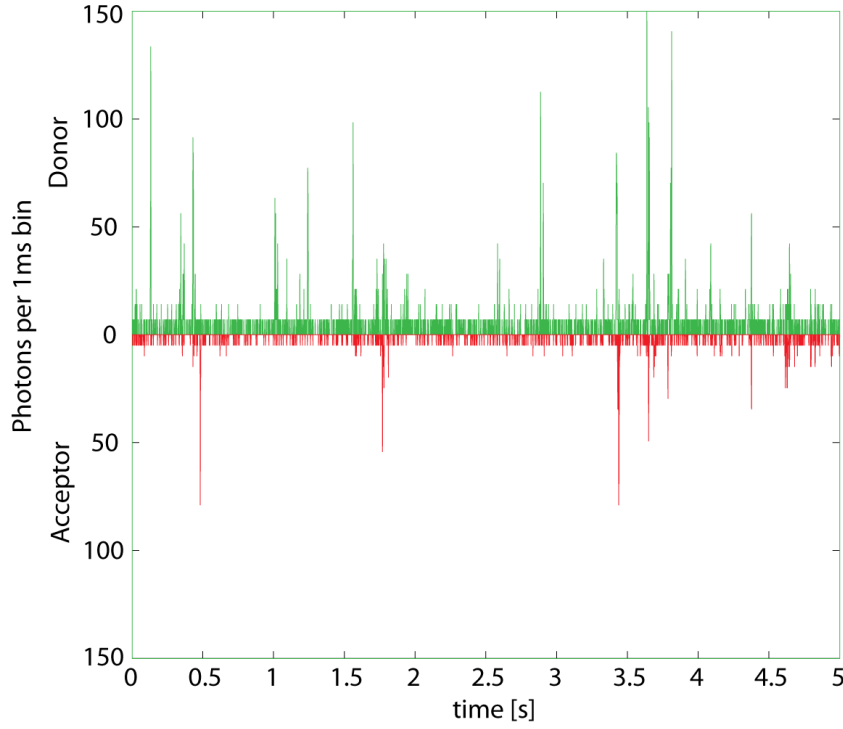


**Figure 4.12:** Typical Burst Analysis fluorescence intensity trace. Single molecules, labeled with FRET donor and acceptor fluorophores, diffuse through the confocal volume where the donor is excited. Donor fluorescence and, in the case of FRET, acceptor fluorescence are detected as fluorescence bursts for each molecule separately.

There are several algorithms available to identify a burst within the trace. The most straightforward idea is to apply a threshold well above the background level. Adjacent bins with a photon count above that threshold are then assigned to a burst, and the total number of photons within the burst can be counted [34]. One problem with this method is that the photon numbers in a burst are systematically underestimated because the border regions of a burst are lost when they fall below the threshold. An improvement can be achieved by introducing a second, lower, threshold value that is applied after a burst was already identified, to extend it to both sides until the photon count numbers have dropped even below the second, lower threshold [38].

The more sophisticated *all-photon-burst-search* (APBS) algorithm [6] has a different principle. In this approach, the photons are not collected in time bins. Rather, the inter-photon times  $\Delta t$  are analyzed.  $\Delta t$  will be large when only background is present compared to its value in the presence of a fluorophore. A burst is identified if a certain number of consecutive  $\Delta t$  values are below a chosen threshold value. This principle significantly improves the separation of the burst from the background.

Using PIE, this approach can be expanded, as will be discussed in the next section.

In order to interpret the data in terms of donor-acceptor distances, FRET efficiencies are calculated for each burst. The most straightforward way to approximate them is by calculating the fraction of acceptor photon counts  $I_{FRET}$  out of the total photon counts  $I_D + I_{FRET}$ :

$$E = \frac{I_{FRET}}{I_{FRET} + \gamma I_D} \quad (4.84)$$

$\gamma$  is a factor that accounts for the difference in quantum yield  $\Phi$  and detection efficiency  $\eta$  between donor and acceptor and can be either calculated according to  $\gamma = \frac{\eta_A \Phi_A}{\eta_D \Phi_D}$  [34] or determined experimentally as shown in the next section. To calculate accurate FRET values, two additional phenomena have to be accounted for. Due to the general characteristics of fluorescence excitation and emission spectra, there is usually a small overlap of the donor emission spectrum with the selected acceptor emission band pass filter (*Spectral crosstalk*, see e.g. Figure A.2). Furthermore, there is usually also a small acceptor excitation probability for the selected donor excitation laser wavelength (*Direct excitation*, see e.g. Figure A.1). The fractions of spectral crosstalk and direct excitation can be determined in separate measurements with the donor-only and acceptor-only species, respectively, or determined via PIE as shown in the following section. The correction for spectral crosstalk is then relatively unproblematic, whereas for the correction of the direct excitation, information about the amount of acceptor-only labeled molecules is required, which is not accessible when only the donor is excited. One possible solution to this dilemma is the combination of Burst Analysis with PIE.

#### 4.10.1 Burst analysis with PIE

There are several improvements that the use of PIE contributes to burst analysis measurements, most importantly the calculation of the *stoichiometry*  $S$ , that is a measure for the fraction of donor to acceptor fluorophores attached to a single molecule. Knowledge of  $S$  allows sorting the molecules according to their labeling. For example, molecules with only a donor fluorophore from can be distinguished from those that have low or zero FRET efficiency, and likewise, molecules with only an acceptor fluorophore can be identified (Figure 4.13). Moreover, with PIE, the *dual-channel-burst-search* (DCBS, [39]) algorithm allows one to filter out acceptor-only and photobleaching events at the earliest possible stage, during burst selection. An advanced nomenclature for the intensities is introduced, since PIE yields both the excitation source and the detector for each photon:  $I_{DD}$  is the fluorescence on the donor detector after excitation with the donor laser (earlier given as  $I_D$ );  $I_{DA}$  is the fluorescence on the acceptor detector after excitation with the donor laser (earlier given as  $I_{FRET}$ ); and  $I_{AA}$  is the fluorescence on the acceptor detector after excitation with the acceptor laser. With the new nomenclature, and corrected for direct excitation  $\alpha$  and crosstalk  $\beta$ , a more accurate formula for  $E$  can be given, compared to Equation 4.84, as well as an expression for  $S$  [40]:

$$\begin{aligned} E &= \frac{I_{DA} - \beta I_{DD} - \alpha I_{AA}}{I_{DA} - \beta I_{DD} - \alpha I_{AA} + \gamma I_{DD}} \\ S &= \frac{I_{DA} - \beta I_{DD} - \alpha I_{AA} + \gamma I_{DD}}{I_{DA} - \beta I_{DD} - \alpha I_{AA} + \gamma I_{DD} + I_{AA}} \end{aligned} \quad (4.85)$$

Taking a close look at the above equation, it becomes clear that the value of  $S$  is not intrinsic to the molecules but depends on the intensity of the acceptor excitation light, because it directly depends on  $I_{AA}$ .<sup>11</sup>

<sup>11</sup>The direct excitation term  $\alpha I_{AA}$  also contains  $I_{AA}$  and therefore also seems to depend on the acceptor excitation intensity. However, this is not the case since the factor  $\alpha$  is determined in a measurement with the same acceptor excitation intensity and therefore the effect is canceled out.



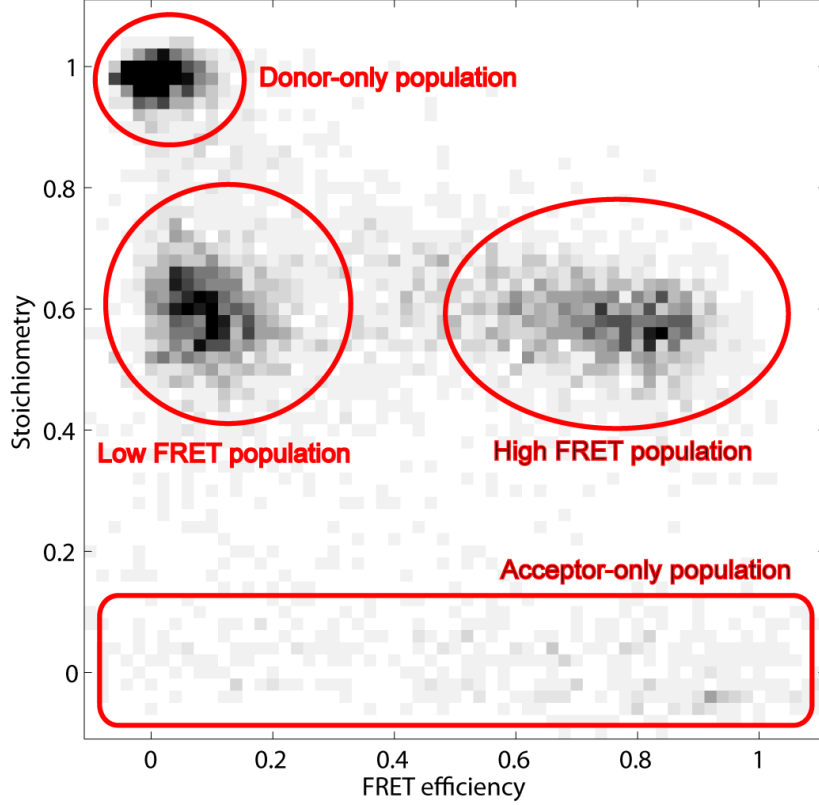


**Figure 4.13:** 2D histogram with FRET efficiency  $E$  and stoichiometry  $S$  of a mixture of two different FRET species: One DNA double strand with two fluorophores that are relatively close together, exhibiting high FRET, and another DNA double strand with two fluorophores that are relatively far apart, exhibiting low to zero FRET. Both species also include donor-only and acceptor-only fractions due to incomplete fluorescent labeling and/or photobleaching of individual fluorophores.

A typical two dimensional histogram is shown in Figure 4.13. The sample was a mixture containing two different FRET species: One DNA double strand with a FRET pair that is spaced relatively close together, exhibiting high FRET, and another DNA double strand with the same two fluorophores, but relatively far apart, exhibiting low to zero FRET. Both strands show the same stoichiometry  $S$ , because they have the same number and type of fluorophores. There are also populations of donor-only and acceptor-only molecules visible. These populations appear in almost every experiment, mostly because the labeling of biomolecules with fluorescent dyes is never 100% complete, so that a fraction of them is only labeled with one dye. Furthermore, some of the fluorophores may be inactive due to photobleaching or other photophysical effects. A histogram as shown in Figure 4.13 can be used to determine the correction factors  $\alpha$ ,  $\beta$ , and  $\gamma$ . The direct excitation  $\alpha$  has to be adjusted so that the acceptor-only species is centered around  $S = 0$ . Alternatively, a measurement of only the free acceptor fluorophore in absence of the donor can be performed, in that case  $\alpha = \frac{I_{DA}}{I_{AA}}$ . Analogously, the spectral crosstalk can be determined by adjusting  $\beta$  so that the donor-only species is centered around  $E = 0$  in the histogram, or it can be directly extracted by a measurement of the free donor fluorophore in absence of the acceptor, then  $\beta = \frac{I_{DA}}{I_{DD}}$ . Finally,  $\gamma$  can be obtained from the histogram in case there are two populations with equal stoichiometry but strongly different FRET efficiencies, as

shown in the example from Figure 4.13.  $\gamma$  then has to be adjusted so that both populations are centered around the exact same value of  $S$ . Alternatively, when  $\frac{1}{S}$  is plotted versus  $E$ , a straight line can be fitted through the two populations, and  $\gamma$  can be calculated from slope  $m$  and y-axis intercept  $y_0$  [41, 38]:  $\gamma = \frac{y_0 - 1}{y_0 + m - 1}$ . Frequently for calibration purposes, a mixture of two double-labeled DNA strands is used where one exhibits low FRET and the other high FRET. However, the determination of  $\gamma$  with such a calibration measurement may not be valid if the actual experiment is performed on a different type of biomolecule, or with different fluorescent labels, since the quantum yield  $\Phi$  of both donor and acceptor, and thereby also  $\gamma$ , heavily depend on the type of molecule they are attached to because of quenching effects. Even different labeling mutants of one and the same protein may have a different  $\gamma$  value.

## 4.11 Photon Distribution Analysis

Photon Distribution Analysis (PDA) was developed as a tool to interpret experimentally determined FRET histograms. Typically, in such a histogram, one or more FRET peaks appear that have a certain center and width. It is often unclear whether the width of those peaks originates from an actual underlying flexibility of the donor-acceptor distance, or just from the photon shot noise. With PDA it becomes possible to simulate the width of shot-noise limited FRET peaks under the experimental conditions in use. By comparing them to the actual data using nonlinear regression, a possible underlying donor-acceptor distance distribution can be discovered and quantified.

### 4.11.1 PDA theory

Since in Burst Analysis measurements, relatively few photons are counted in total due to the low concentration of fluorophores in the sample, the influence of the detector noise background has to be taken into account. The signal produced by a detector is thus  $S = I + B$ , where  $I$  is the signal originating from the fluorescence intensity at the detector, and  $B$  is the intrinsic noise of the detector. For a typical FRET experiment, two detectors are necessary, one for the donor and the other for the acceptor. Therefore, the total number of events counted is  $N_{total} = I_D + I_R + B_D + B_R$ . The physical quantity that can experimentally be observed is the *signal ratio*:

$$\frac{S_D}{S_A} = \frac{I_D + B_D}{I_A + B_A} \quad (4.86)$$

Obviously, multiple combinations of  $I_D$ ,  $I_R$ ,  $B_D$ , and  $B_R$  could lead to the same value of  $\frac{S_D}{S_A}$ . The probability of measuring a certain signal ratio,  $P\left(\frac{S_D}{S_A}\right)$ , is therefore the summation over all possible combinations of  $I_D$ ,  $I_R$ ,  $B_D$ , and  $B_R$  leading to  $\frac{S_D}{S_A}$ :

$$P\left(\frac{S_D}{S_A}\right) = \sum_{\substack{\text{all } I_D, I_A, B_D, B_A \\ \text{leading to } \left(\frac{S_D}{S_A}\right)}} P(I_D, I_A, B_D, B_A) \quad (4.87)$$

Equation 4.87 can be further developed by resolving the probability  $P(I_D, I_A, B_D, B_A)$  that the exact combination of  $I_D$ ,  $I_A$ ,  $B_D$ , and  $B_A$  occurs. The probability for a certain number of detector background counts is completely independent from the other contributions and can therefore be factored out. Furthermore,  $P(I_D, I_A)$  can be rewritten in terms of the total incident fluorescence intensity  $I = I_D + I_A$ :

$$P(I_D, I_A) = P(I)P(I_A|I) \quad (4.88)$$

Here,  $P(I_A|I)$  is the probability that exactly  $I_A$  out of  $I$  photons are coming from the acceptor. With these assumptions, Equation 4.87 reads:

$$P\left(\frac{S_D}{S_A}\right) = \sum_{\substack{\text{all } I, I_A, B_D, B_A \\ \text{leading to } \left(\frac{S_D}{S_A}\right)}} P(I)P(I_A|I)P(B_D)P(B_A) \quad (4.89)$$

Now each of the four terms has to be expressed in terms of physically relevant quantities. The probabilities to obtain  $B_D$  and  $B_A$  background counts, respectively, can be described by Poissonian distributions with average values  $\langle B_D \rangle$  and  $\langle B_A \rangle$ , respectively:

$$P_{\langle B_D \rangle}(B_D) = \frac{\langle B_D \rangle^{B_D} e^{-\langle B_D \rangle}}{B_D!} \quad P_{\langle B_A \rangle}(B_A) = \frac{\langle B_A \rangle^{B_A} e^{-\langle B_A \rangle}}{B_A!} \quad (4.90)$$

With the assumption of a fixed probability  $\epsilon$  that any given count is coming from the acceptor detector, and not from the donor detector, the probability of observing exactly  $I_A$  acceptor photons out of  $I$  total photons can be described by a binomial distribution.  $\epsilon$  can be regarded as an apparent FRET efficiency that has to be corrected for the quantum yields, detection efficiencies, crosstalk and direct excitation:

$$P(I_A|I) = \frac{I!}{I_A!(I-I_A)!} \epsilon^{I_A} (1-\epsilon)^{I-I_A} \quad (4.91)$$

The final term to consider in Equation 4.89 is the fluorescence intensity distribution  $P(I)$ . Although it can be described analytically as seen e.g. in section 4.3, this would be computationally very expensive. It is therefore advantageous to express it in terms of measurable quantities:  $F = N_{total} - B_D - B_A$ . With this substitution, Equation 4.89 reads:

$$P\left(\frac{S_D}{S_A}\right) = \sum_{\substack{\text{all } N, I_A, B_D, B_A \\ \text{leading to } \left(\frac{S_D}{S_A}\right)}} P(N_{total})P(I_A|N_{total} - B_D - B_A)P(B_D)P(B_A) \quad (4.92)$$

$P(N)$  can easily be determined from the measured distribution of photon counts by normalizing the latter to unity. The expressions for the other terms have been given in Equations 4.90 and 4.91. If the average background counts  $\langle B_D \rangle$  and  $\langle B_A \rangle$  are experimentally determined in a separate measurement, this leaves the apparent FRET efficiency  $\epsilon$  as the only free parameter of the problem, which can therefore be obtained by fitting Equation 4.92 to the measured FRET histograms.

The apparent FRET efficiency  $\epsilon$  can be transformed into the real efficiency  $E$ , which in turn can be expressed in terms of donor-acceptor distance  $R$  according to Equation 2.6:

$$\epsilon = 1 - \frac{1}{1 + \frac{\Phi_A \eta_A}{\Phi_D \eta_D} \frac{E}{1-E}} = 1 - \frac{1}{1 + \frac{\Phi_A \eta_A}{\Phi_D \eta_D} \frac{R_0^6}{R^6}} \quad (4.93)$$

In many cases, however, the molecular system in question does not exhibit one singular distance, resulting in a single fixed FRET efficiency, but rather one or multiple distribution of distances which can often be approximated as Gaussian. Possible causes for this phenomenon include

fluorophore linker flexibility or a non-rigid molecular structure. Therefore it is necessary to extend Equation 4.92 to the case of a distribution of efficiencies by integrating  $P\left(\frac{S_D}{S_A}\right)$  for all possible values of  $\epsilon$ , weighted with their probability  $P(\epsilon)$  to occur:

$$P\left(\frac{S_D}{S_A}\right) = \int_{\epsilon} P(\epsilon) \sum_{\substack{\text{all } N, I_A, B_D, B_A \\ \text{leading to } \left(\frac{S_D}{S_A}\right)}} P(N_{total})P(I_A|N_{total} - B_D - B_A)P(B_D)P(B_A) d\epsilon \quad (4.94)$$

Assuming a Gaussian distribution of efficiencies, an explicit expression for  $P(\epsilon)$  can be given (a complete derivation can be found in the supplementary material of [35]):

$$P(\epsilon) = \frac{R_0}{6\sigma_R\sqrt{2\pi}} \left(\frac{\Phi_A\eta_A}{\Phi_D\eta_D}\right)^{\frac{1}{6}} \frac{1}{(1-\epsilon)^2} \left(\frac{\epsilon}{1-\epsilon}\right)^{-\frac{7}{6}} \exp\left(-\frac{1}{2\sigma_R^2} \left[R_0 \left(\frac{\Phi_A\eta_A}{\Phi_D\eta_D}\right)^{\frac{1}{6}} \left(\frac{\epsilon}{1-\epsilon}\right)^{-\frac{1}{6}} - \bar{R}\right]^2\right) \quad (4.95)$$

In this equation,  $\bar{R}$  and  $\sigma_R$  are the mean value and standard deviation of the assumed Gaussian distribution of donor-acceptor distances, which then serve as PDA fit parameters.

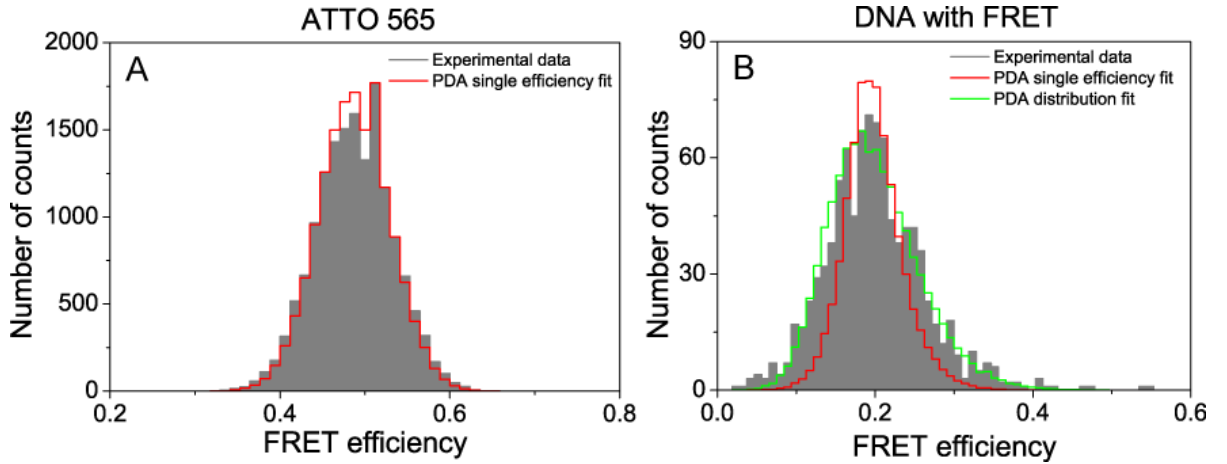


**Figure 4.14:** Comparison of two FRET measurements with PDA fit. (A) Measurement of single ATTO 565 fluorophores with an emission spectrum that overlaps with both detectors, thereby simulating a fake, but absolutely invariable, FRET efficiency, that can be fitted with a single FRET value. (B) Measurement of a DNA double strand with two fluorophores undergoing FRET. Due to fluorophore linker flexibility and the nonrigid DNA structure, the distribution cannot be fitted with a single FRET value, but only with an underlying distance distribution.

As mentioned before, with PDA, a statement can be made about the distribution of distances underlying a FRET histogram. Figure 4.14A shows an experimental measurement for an idealized case, where a fake "FRET" system was engineered by measuring a sample of freely diffusing ATTO 565 dye. This fluorophore can be excited with 532 nm, although with a relatively low absorption coefficient, and fractions of its fluorescence are detected in both detectors of the two-color PIE MFD setup introduced in Section 3.4.1. In principle, this system is a non-FRET system with extremely high spectral crosstalk, where the crosstalk is interpreted as "FRET" in order to simulate a FRET system with no underlying distance distribution. Figure 4.14A clearly demonstrates that the resulting distribution of experimental FRET values can be fitted with a single distance, hence the width of the experimental data results exclusively from shot

noise.

In Figure 4.14B, a real FRET experiment is shown. There, a DNA double strand labeled with the two fluorophores ATTO 532 and ATTO 647N is measured. The fluorophores have a distance small enough to allow for FRET. Trying to fit these data with a single distance fails (red curve), instead a distribution of distances is necessary (green curve).

## 5 Method Development with PIE

Pulsed Interleaved Excitation [5], introduced in Section 3.3, is a technique to precisely separate different fluorescent species and remove artifacts due to spectral crosstalk, or, if crosstalk is negligible, determine the FRET efficiency. PIE has already been used in many applications *in vitro*. It is of special advantage in live-cell measurements, where fluorescent proteins with a large spectral overlap are used, for example the widely used pair of GFP and RFP. Since photobleaching makes stationary FFS measurements in a living cell difficult, it is advantageous to combine PIE with spectroscopic techniques especially suited for *in vivo* measurements, such as Scanning FCS and RICS.

### 5.1 Scanning FCS with PIE

Scanning FCS is an enhancement of FCS where the confocal volume is repeatedly moved through the sample in a pattern such as, for example, a circle or a line. The scanning velocity is carefully adapted to the diffusion coefficient of the sample so that a fluorophore located on the scanning trajectory is illuminated with multiple scanning iterations before diffusing away. In this way, the total time the fluorophore is exposed to the excitation light is shortened, reducing photobleaching and other photophysical effects. This is especially useful for measurements in living cells, where diffusion is usually slow and fluorescent proteins with poor photostability are often used for labeling.

The scanning autocorrelation curve can be fitted with the model introduced in Section 4.8 to determine the diffusion coefficient and concentration of the sample. The scanning cross-correlation curve gives information about molecular binding between differently labeled binding partners.

However, as for stationary FCCS measurements, spectral crosstalk can cause artifacts yielding a non-zero scanning cross-correlation curve for a non-interacting sample. In the cellular context, an unambiguous decision whether two biomolecules interact with each other is often essential. Therefore, an important improvement of Scanning FCCS is its combination with PIE, which eliminates the effects introduced by spectral crosstalk and yields a non-zero scanning cross-correlation curve only in the case of an actual interaction.

## 5.2 PIE-Scanning FCS in aqueous solution

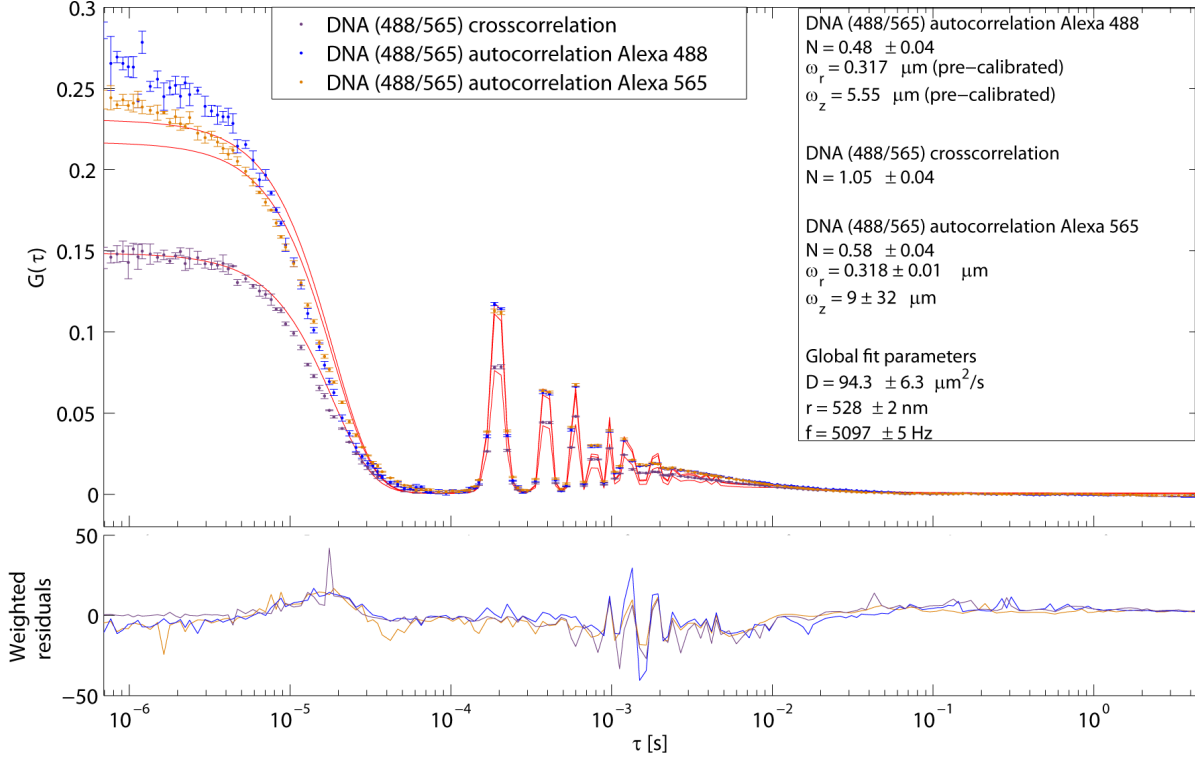


**Figure 5.1:** Scanning FCS curves and fits for a DNA double-stranded DNA labeled with Alexa 488 and Alexa 568 in aqueous solution. Blue curve: Alexa 488 autocorrelation. Yellow curve: Alexa 568 autocorrelation. Purple curve: Alexa 488/Alexa 568 cross-correlation. The two fluorophores always diffuse as a pair due to their colocalization on the DNA strand, causing a non-zero cross-correlation.

To demonstrate the principle of PIE-Scanning FCS, several model systems were tested in aqueous solution. A DNA double strand that was double labeled with Alexa 488 and Alexa 568 served as a positive cross-correlation control. The confocal volume for the 483 nm laser was pre-calibrated with a stationary FCS measurement of an ATTO 488 solution with a known diffusion coefficient of  $400 \frac{\mu\text{m}^2}{\text{s}}$  [42]. A circular Scanning FCS measurement with a scanning frequency of 5 kHz was taken in a 1 nM solution of the DNA sample and all three curves were globally fitted with a Scanning FCS fit model based on Equation 4.81 (Figure 5.1). The particle numbers  $N$  in the fit result are the population numbers of the two single-labeled and the double-labeled species, respectively. They can be transformed into concentrations using Equation 5.1 (using  $m^3$  as a unit for  $\omega_r$  and  $\omega_z$ ):

$$c \left[ \frac{\text{Mol}}{l} \right] = \frac{N}{1000 N_A \left( \frac{\pi}{2} \right)^{\frac{3}{2}} \omega_r^2 \omega_z} \quad (5.1)$$

For calculating the concentration of the double labeled species, an effective dual-color confocal volume is assumed that can be described by the volume parameters given in Equation 5.2.

$$\begin{aligned}\omega_{r,eff} &= \sqrt{\frac{\omega_{r,1}^2 + \omega_{r,2}^2}{2}} \\ \omega_{z,eff} &= \sqrt{\frac{\omega_{z,1}^2 + \omega_{z,2}^2}{2}}\end{aligned}\tag{5.2}$$

This yields a concentration of 0.73 nM of DNA strands labeled only with Alexa 488, of 0.54 nM for DNA strands labeled only with Alexa 565, and of 1.16 nM for the double labeled DNA strands. The diffusion coefficient of the DNA was globally determined to  $94.3 \frac{\mu\text{m}^2}{\text{s}}$ . The fit yielded an accurate result for the scanning frequency of 5.097 kHz and a scanning circle radius of  $0.528 \mu\text{m}$ . The presence of single-labeled species can be explained by the imperfect fluorescent labeling and by photobleaching. Analogous to Figure 4.10, all correlation curves including the cross-correlation followed an envelope curve constituted by the respective stationary FCS measurements.

As a negative control, a nanomolar mixture of two freely diffusing fluorophores, ATTO 488 and Alexa 555, was measured with a scanning frequency of 5 kHz and globally analyzed with the same Scanning FCS fit model, but without PIE (Figure 5.3). One advantage of PIE is, that with a single measurement and from a single dataset, a wealth of analysis options arises. For example, spectral crosstalk photons can be dismissed, or, as in this case, taken into account to emulate a measurement without PIE. Due to the significant overlap of the ATTO 488 emission spectrum with the optical filter used for the detection of Alexa 555, the amount of spectral crosstalk photons emitted by ATTO 488, but counted by the Alexa 555 detector, was relatively high compared to the number of photons emitted by the Alexa 555 fluorophore itself (Figure 5.2).

Since the diffusion coefficient of Alexa 555 was unknown, for the calibration of the confocal volume it was estimated to  $400 \frac{\mu\text{m}^2}{\text{s}}$ , the same value as ATTO 488, because most synthetic fluorophores are molecules of similar size and, therefore, have similar diffusion coefficients [42]. A scanning cross-correlation curve with a high amplitude was observed, although no interaction whatsoever took place between the two molecular species. This leads to false fit results shown in Figure 5.3, yielding a high population number of double labeled molecules and biased values for the single-labeled species. They result in concentration values of 0.44 nM for ATTO 488, of 0.93 nM for Alexa 555, and of 0.67 nM for the (nonexistent) double labeled species. The fit result for the scanning frequency is 5100 Hz and for the radius of the scanning circle  $0.575 \mu\text{m}$ .



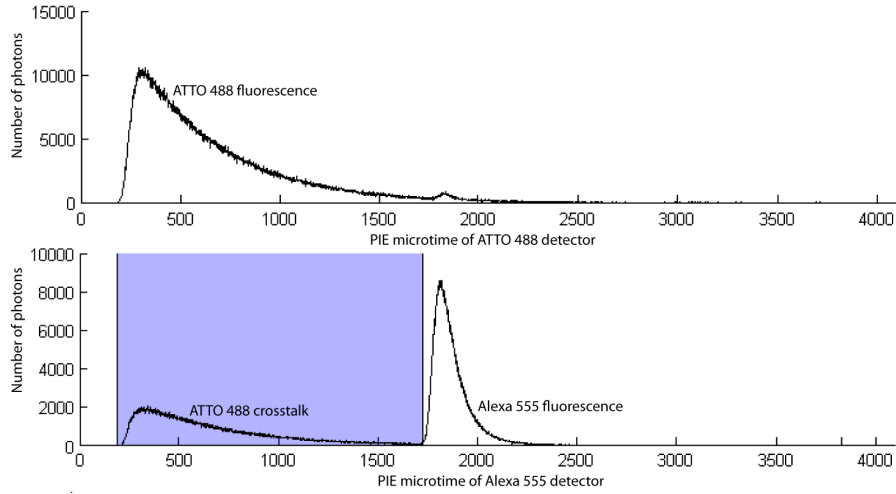


**Figure 5.2:** TCSPC diagram of the spectral crosstalk of ATTO 488 into the Alexa 555 detector (marked in blue). The relative amount of ATTO 488 crosstalk photons is high compared to the total amount of Alexa 555 fluorescence photons, therefore the effect of spectral crosstalk on the cross-correlation curve is very strong.

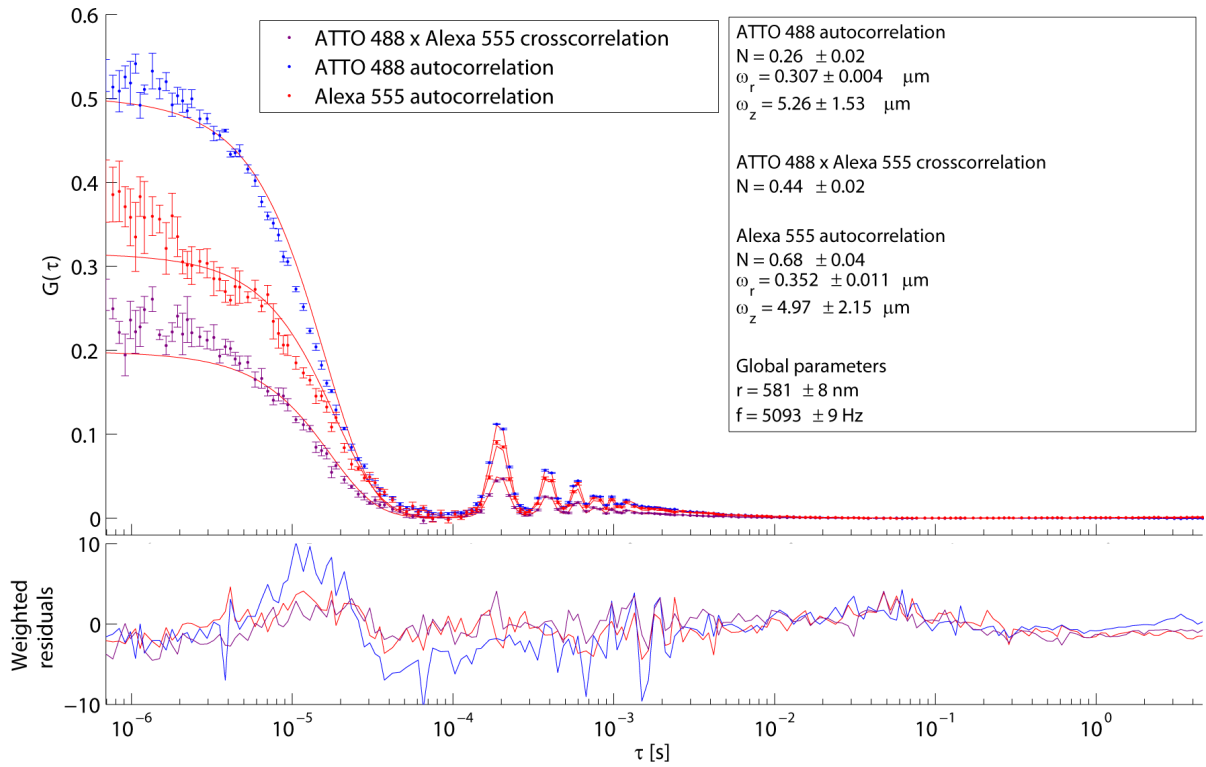


**Figure 5.3:** Scanning FCS curves and fits for a mixture of ATTO 488 and Alexa 555 in aqueous solution. Blue curve: ATTO 488 autocorrelation. Red curve: Alexa 555 autocorrelation. Purple curve: ATTO 488/Alexa 555 cross-correlation. All curves were analyzed without PIE. As a result, the cross-correlation curve has a non-zero amplitude.

The same negative control sample was analyzed with PIE, and all spectral crosstalk photons were dismissed. As a result, the scanning cross-correlation curve has zero amplitude (Figure 5.4). Furthermore, the amplitude of the Alexa 555 autocorrelation curve is corrected, now

yielding the true population numbers. The resulting concentrations are 1.16 nM for ATTO 488 and 0.37 nM for Alexa 555. Note that there is a dramatic change not only in the resulting concentration of Alexa 555 but also in that of ATTO 488, although the autocorrelation curve remains unchanged by PIE. This is caused by the global fit, which, in the case of analysis without PIE, distributed the ATTO 488 molecules into two different species, the single-labeled and the double-labeled ones.

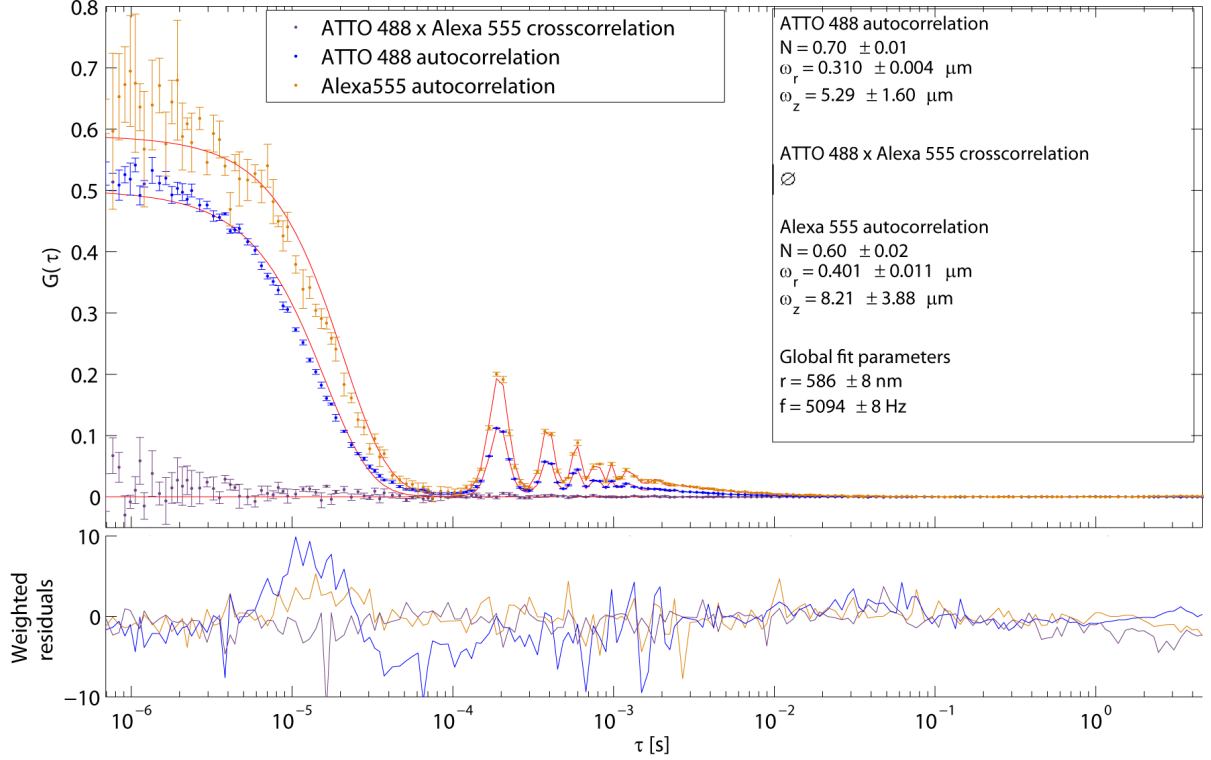


**Figure 5.4:** Scanning FCS curves and fits for a mixture of ATTO 488 and Alexa 555 in aqueous solution. Blue curve: ATTO 488 autocorrelation. Red curve: Alexa 555 autocorrelation. Purple curve: ATTO 488/Alexa 555 cross-correlation. All curves were analyzed with PIE. As a result, the cross-correlation curve has zero amplitude.

### 5.3 Raster Image Correlation Spectroscopy with PIE

The capabilities of PIE can be utilized in a similar way to improve RICS, another correlation technique especially suited for live-cell measurements. RICS, introduced in Section 4.9, is a technique that can be used to study the interaction of fluorescently labeled biomolecules under the experimental conditions present in a living cell, where photobleaching and the widely spread use of fluorescent proteins render stationary FFS measurements very challenging. In RICS, data from a relatively large area is collected, for example from a section within the cytosol or the nucleus of a cell, and data with high statistics can be obtained in a relatively short time. When two molecules with different labels interact, the RICS cross-correlation pattern will exhibit a distinct peak, otherwise it will theoretically consist purely of statistical noise. However, spectral crosstalk can lead to an artificial RICS cross-correlation appearing, although no molecular interaction took place. PIE can therefore contribute substantially to RICS by avoiding these artifacts, allowing a clear distinction whether two molecular species interact in

a cellular context or not. Because of the high sensitivity, weaker interactions can thus still be resolved with PIE.

## 5.4 PIE-RICS in aqueous solution

As a first proof-of-principle experiment, PIE-RICS was applied to different aqueous solutions containing two different fluorophores with either correlated or uncorrelated diffusion. A double-stranded DNA labeled at two different positions with Alexa 488 and Alexa 568 was used as a sample where the movement of the fluorophores was correlated. PIE-RICS was performed in a square  $5\text{ }\mu\text{m} \times 5\text{ }\mu\text{m}$  area within the sample. 20 image frames with  $128 \times 128$  pixels were recorded with a frame time of 3 s.<sup>1</sup> The resulting 20 RICS patterns were averaged, and the resulting auto- and cross-correlations as well as a global fit according to equation 4.83 are shown in Figure 5.6. Prominent peaks can be observed for all three correlation patterns, and especially the presence of a peak in the RICS cross-correlation shows directly the presence of an interaction between the two species.

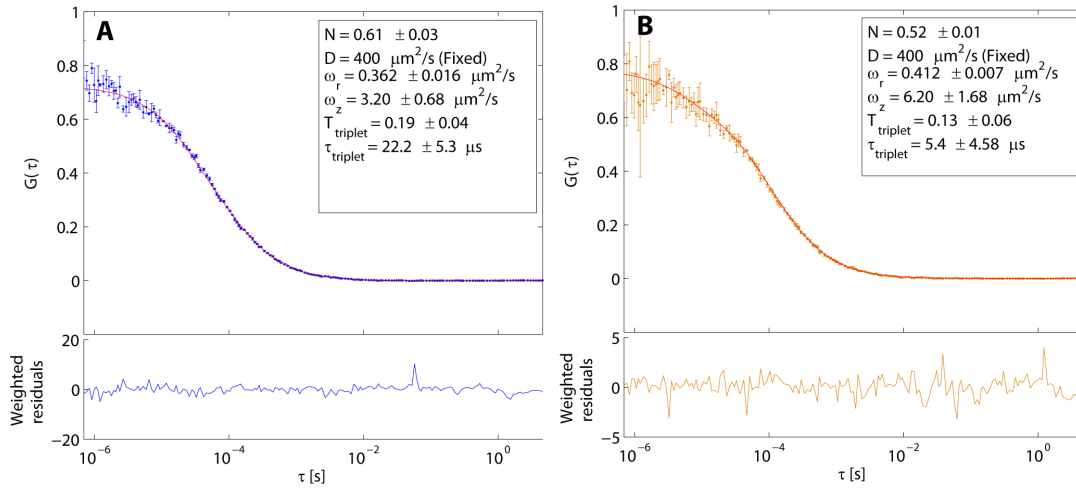


**Figure 5.5:** Stationary FCS measurement and fit of (A) Alexa 488 and (B) Alexa 555 in solution for calibration of the confocal volume parameters  $\omega_r$  and  $\omega_z$ .

The volume parameters for the fit were calibrated with two stationary FCS measurements on Alexa 488 and Alexa 555 in solution (Figure 5.5). As in Section 5.2, the diffusion coefficient of the freely diffusing fluorophores was assumed to be  $400\text{ }\frac{\mu\text{m}^2}{\text{s}}$ . The global RICS fit resulted in population numbers of  $N = 1.37$  for DNA labeled with only the Alexa 488 fluorophore,  $N = 1.58$  for DNA labeled with only the Alexa 565 fluorophore, and  $N = 0.62$  for the double labeled DNA. The diffusion coefficient was fitted to  $D = 57.7\text{ }\frac{\mu\text{m}^2}{\text{s}}$ .

<sup>1</sup>This led to a pixel size of  $s = 39.1\text{nm}$ , a line time of  $\tau_y = 23.4\text{ms}$ , and a pixel dwell time of  $\tau_x = 183.1\text{ }\mu\text{s}$ .

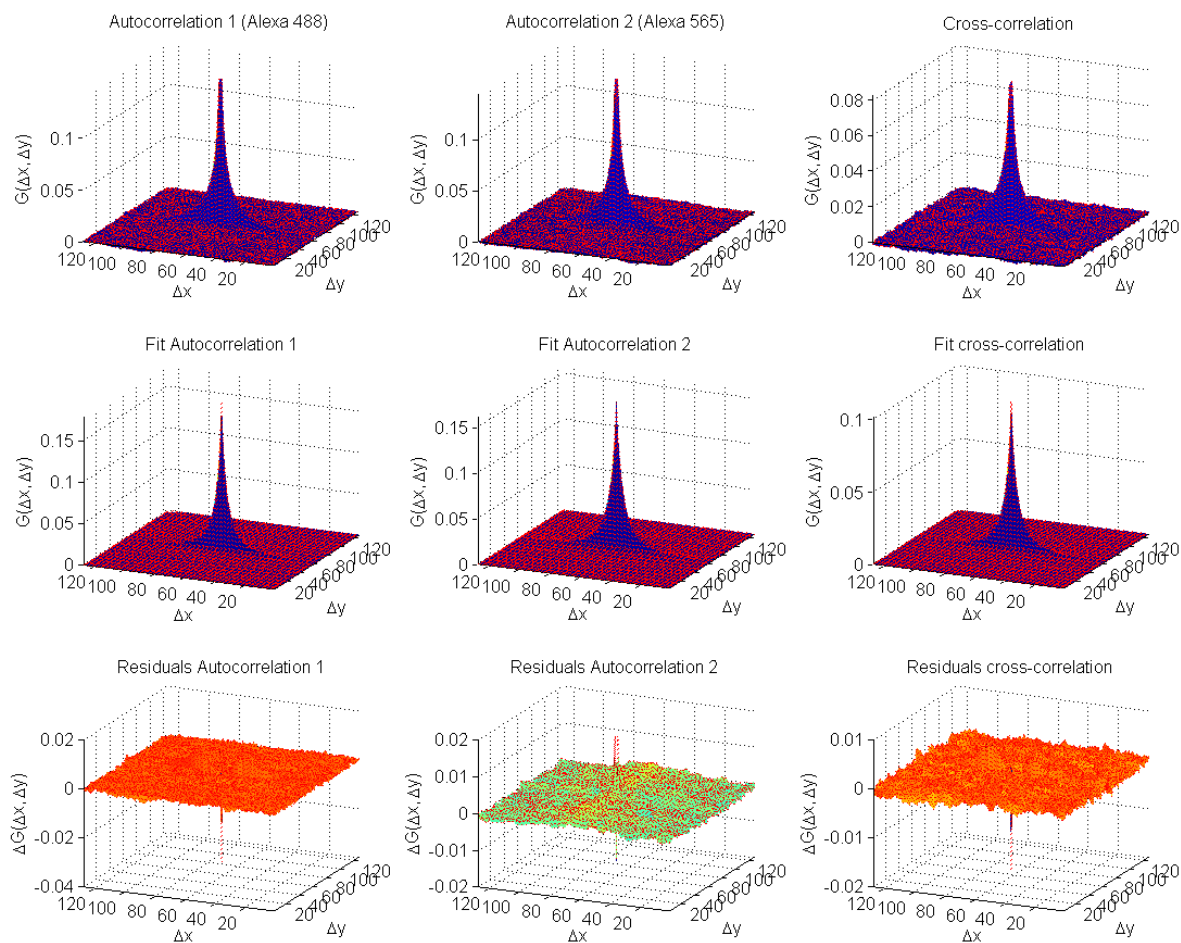


**Figure 5.6:** PIE-RICS analysis of a solution with a DNA cross-correlation construct that was labeled with Alexa 488 and Alexa 568. Both autocorrelations and the cross-correlation were globally fitted.

The experiment was repeated with a solution of two different non-interacting fluorophores, Alexa 488 and Alexa 555. These fluorophores diffuse independently from each other and consequently, zero RICS cross-correlation is expected. RICS was performed on 50 image frames and the resulting correlation patterns were averaged. The imaging parameters were identical with the previous experiment. When RICS is performed without PIE, a large and distinct cross-correlation peak can be observed due to spectral crosstalk (Figure 5.7). For a sample with unknown interaction properties, this observation would lead to the false assumption of interacting species, and hence this assumption was used for the global fit of the data with RICS to determine the extent of this artifact.

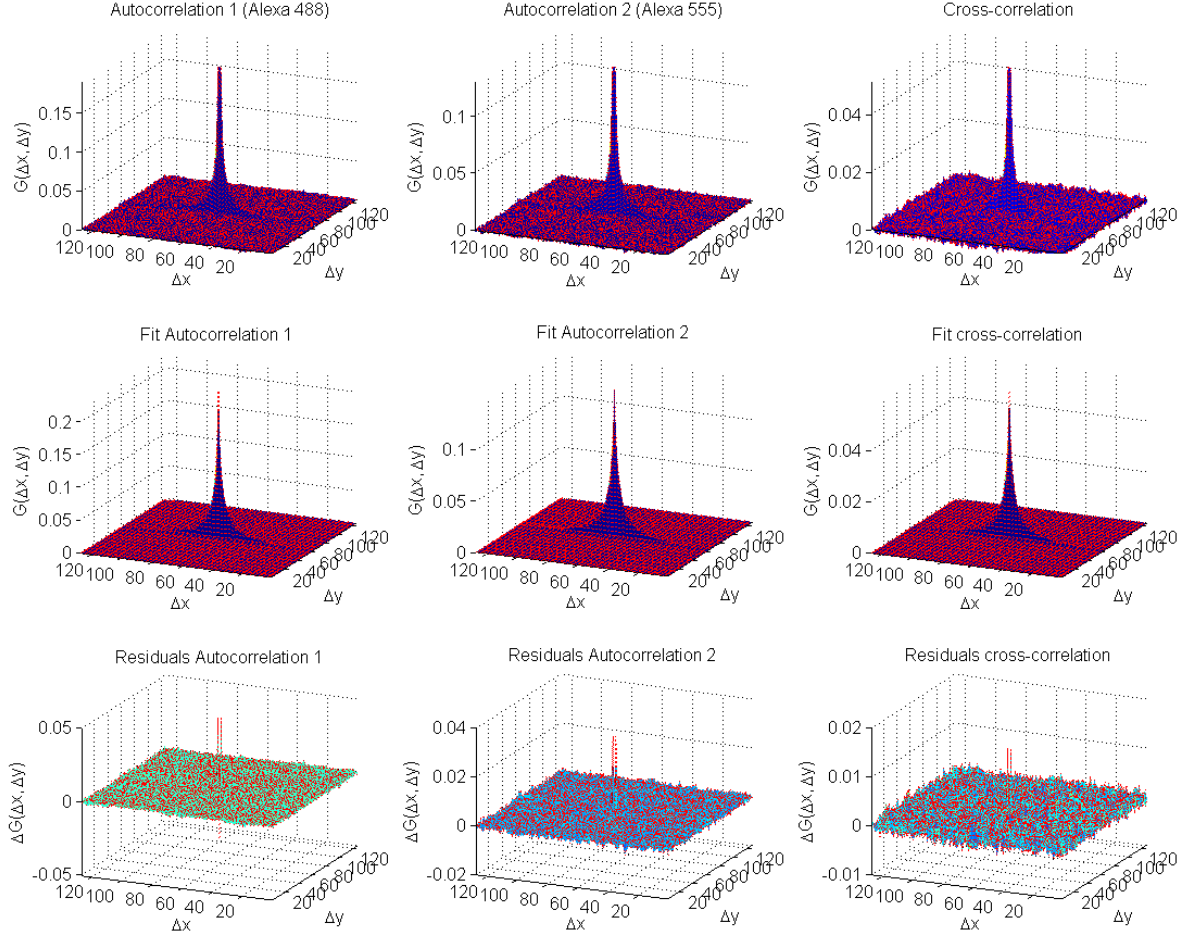


**Figure 5.7:** RICS analysis without PIE of a solution of two different non-interacting fluorophores, Alexa 488 and Alexa 555. The presence of a large cross-correlation amplitude would lead to the false assumption of interacting species, and this assumption was used for the global fit of the data with RICS.

The fit resulted in population numbers of  $N = 1.18$  for Alexa 488,  $N = 2.08$  for Alexa 555, and  $N = 0.40$  for the (nonexistent) interacting species. Given the fact that there are no interacting molecules in the samples, this very significant number is considerably misleading. The diffusion coefficient was fitted to  $D = 98.7 \frac{\mu\text{m}^2}{\text{s}}$ .

The same data was evaluated with PIE-RICS. Here, no cross-correlation photons were included for the correlation, and therefore the cross-correlation peak disappeared entirely (Figure 5.8). Furthermore, the population numbers can now be accurately determined. The fit results were  $N = 1.55$  for Alexa 488 and  $N = 1.48$  for Alexa 555, with a diffusion coefficient of  $D = 103.1 \frac{\mu\text{m}^2}{\text{s}}$ .

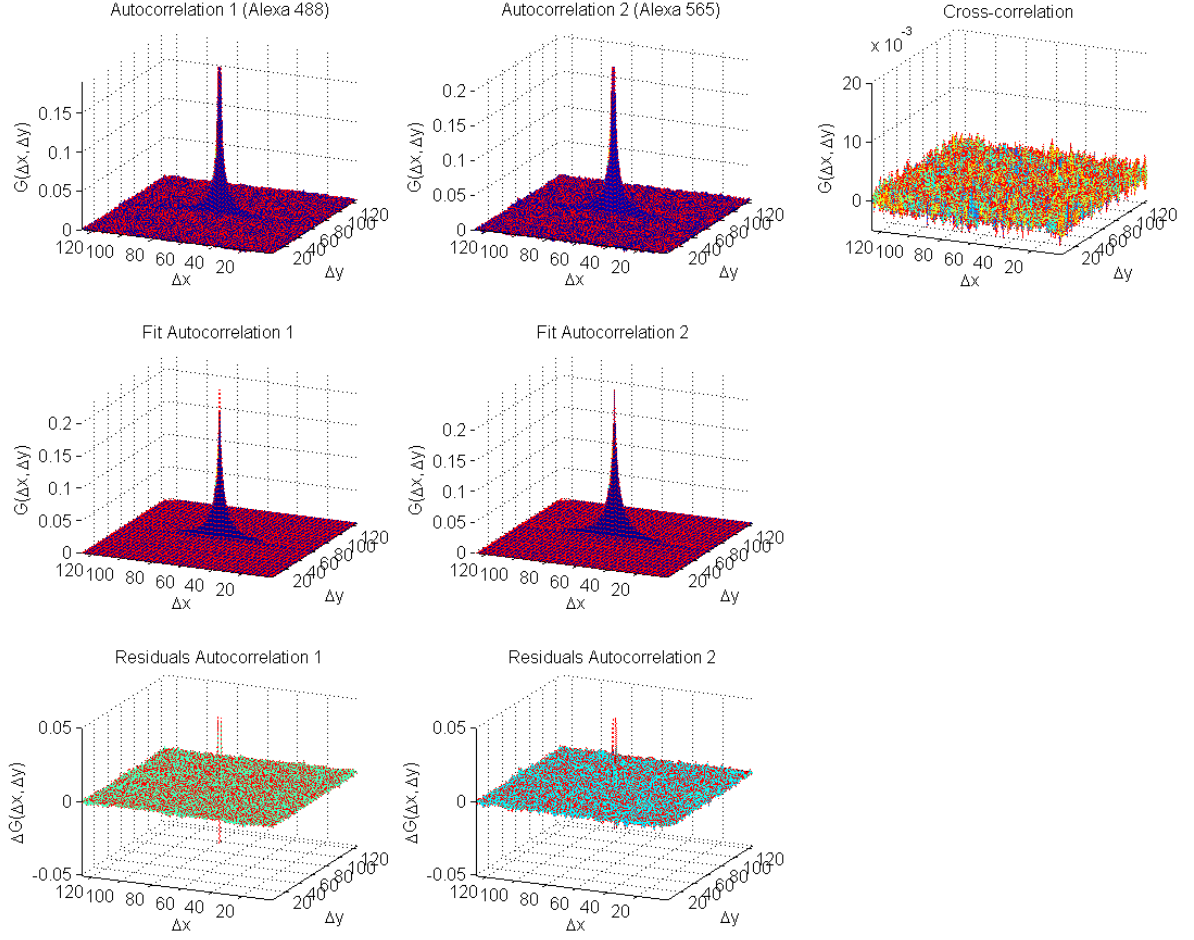


**Figure 5.8:** RICS analysis with PIE of a solution of Alexa 488 and Alexa 555. Here, the cross-correlation amplitude is perfectly zero. It is immediately visible that at the concentrations present in the sample solution, no interaction between the two species took place.

## 5.5 PIE-RICS in living cells

In the next step, PIE-RICS was tested on living cells that were transfected with two different fluorescent species. HEK293 cells [43], a cell line frequently used for biophysical experiments in a wide range of applications, were seeded in a chamber of an eight-well Lab-Tek chambered coverglass slide (NUNC A/S, Roskilde, Denmark) that had been coated with Poly-L-Lysine. After 24h incubation at 37°C in Dulbecco's Modified Eagle Medium (DMEM, Invitrogen, Darmstadt, Germany) with 10% fetal bovine serum and a Pen/Strep mix, the desired constructs were transfected into the cells using a FuGENE 6 kit (Roche Diagnostics, Mannheim, Germany) according to the manufacturer's instructions. After a second period of 24h incubation at 37°C, the medium was exchanged for DPBS buffer (incl. Ca and Mg, pH  $7.1 \pm 0.1$ , Invitrogen) prior to RICS measurements to reduce background fluorescence.



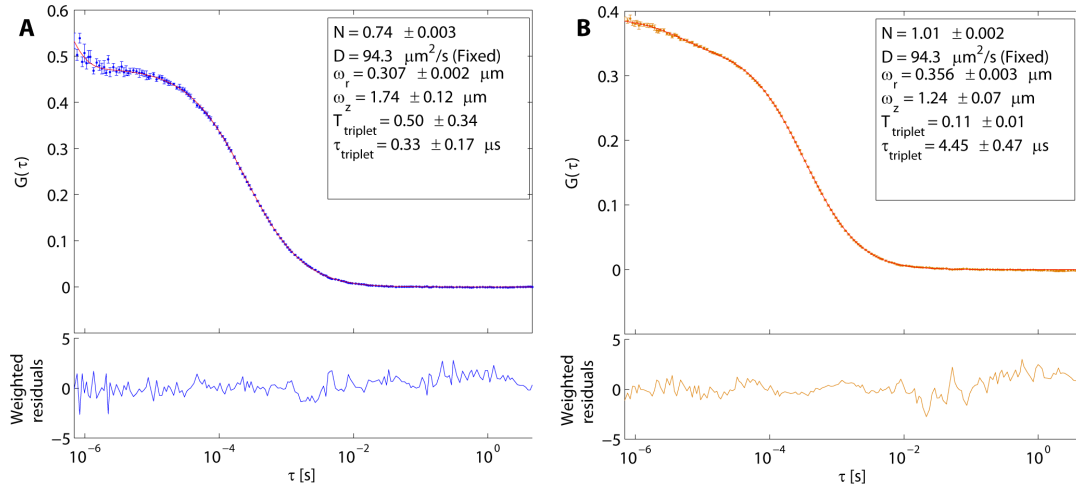


**Figure 5.9:** FCS volume calibration measurement and fit of a double-stranded DNA sample labeled with (A) Alexa 488 and (B) Alexa 565. The diffusion coefficient of the DNA was previously determined (Figure 5.1).

As a positive RICS cross-correlation control, the cells were transfected with a GFP/mCherry-construct where the two fluorescent proteins were covalently bound together by a short linker of three amino acids (glycine/serine/glycine).

PIE-RICS was performed in a square area within the cytosol of a HEK293 cell. 101 image frames with  $128 \times 128$  pixels, corresponding to  $6.8 \text{ } \mu\text{m} \times 6.8 \text{ } \mu\text{m}$ , were recorded with a frame time of  $1 \text{ s}$ .<sup>2</sup> A region of interest was selected, measuring  $100 \times 100$  pixels, which lay entirely within the cell. A running average of 10 frames was taken and subtracted prior to RICS analysis to remove stationary background fluorescence. In cells, autofluorescence is often a problem because it forms a slowly moving or stationary background causing artifacts in the RICS correlations. The resulting 92 RICS patterns were averaged, and the auto- and cross-correlations as well as a global fit according to equation 4.83 are shown in Figure 5.10.

Prominent peaks can be observed for all three correlation patterns, as expected. After calibration of the confocal volume parameters (Figure 5.9), global fitting yielded  $N = 86.2$  for GFP,  $N = 25.8$  for mCherry, and  $N = 8.0$  for the double-labeled species. The diffusion coefficients for the different molecules were determined to  $D = 13.6 \frac{\mu\text{m}^2}{\text{s}}$  for GFP,  $D = 13.1 \frac{\mu\text{m}^2}{\text{s}}$  for mCherry, and  $D = 6.71 \frac{\mu\text{m}^2}{\text{s}}$  for the fusion construct. The slower diffusion of the fusion construct is explained by its significantly larger size compared with the fluorescent proteins themselves.

<sup>2</sup>This led to a pixel size of  $s = 53.1 \text{ nm}$ , a line time of  $\tau_y = 7.8 \text{ ms}$ , and a pixel dwell time of  $\tau_x = 61.0 \text{ } \mu\text{s}$ .

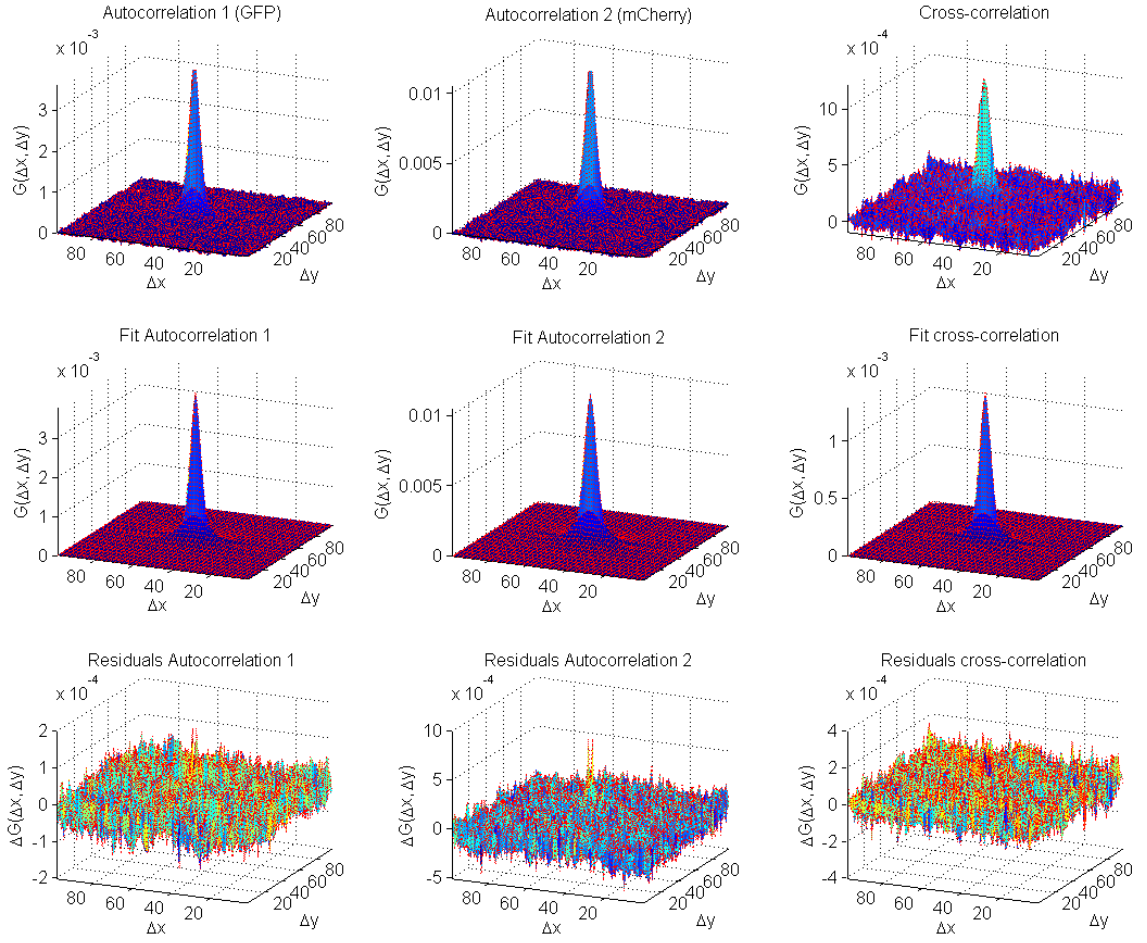


**Figure 5.10:** PIE-RICS analysis of a GFP/mCherry fusion construct in the cytosol of a HEK293 cell as a positive cross-correlation sample. Both autocorrelations and the cross-correlation were globally fitted.

The benefits of PIE-RICS have the greatest effect for systems with a weak interaction or none at all. Therefore, a second proof-of-principle system was designed. Using the same preparation procedure as described in Section 5.5, the HEK293 cells were transfected with two separate, non-interacting proteins: with freely diffusing GFP, and with a construct consisting of the ICDI-domain of the murine  $Ca_v1.4$   $Ca^{2+}$ -channel (presented in more detail in Section 5.7) that was labeled with mCherry. GFP could be found in the whole cell, whereas the labeled ICDI-domain remained in the cytosol due to its size (Figure 4.9).



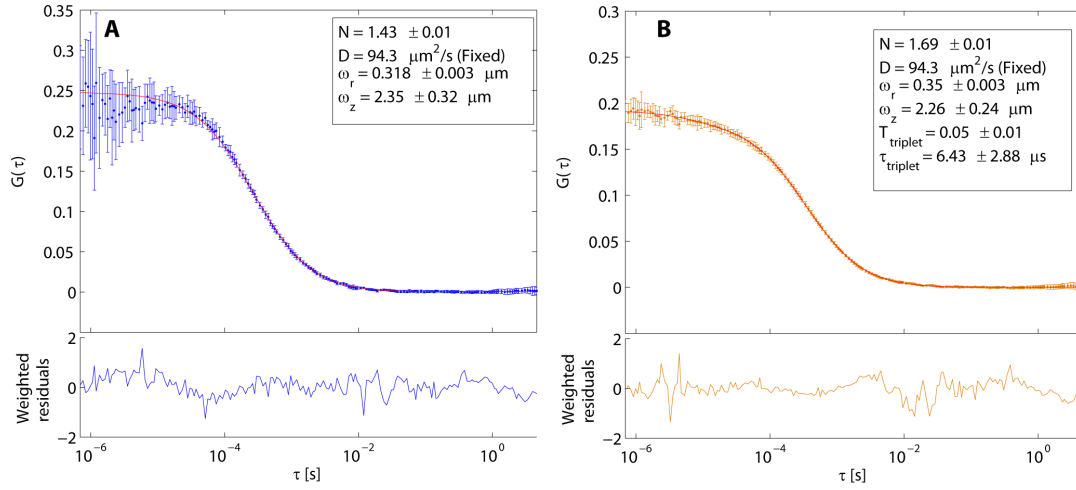


**Figure 5.11:** FCS volume calibration measurement and fit of a double-stranded DNA sample labeled with (A) Alexa 488 and (B) Alexa 565.

101 image frames with  $128 \times 128$  pixels, corresponding to  $3.9 \mu\text{m} \times 3.9 \mu\text{m}$ , were recorded with a frame time of 3 s.<sup>3</sup> A region of interest was selected, measuring  $40 \times 40$  pixels, which lay entirely within the cytosol of the cell, because the mCherry-labeled protein was absent in the nucleus. A running average background subtraction of 10 frames was applied prior to RICS analysis. The resulting 92 RICS patterns were averaged, and the calculated auto- and cross-correlations as well as fits for the autocorrelations are shown in Figure 5.12. A significant cross-correlation amplitude is visible due to spectral crosstalk. It was, however, too small to be reliably fitted, therefore fitting the cross-correlation was not included in the fit. The results were  $N = 297$  for GFP with a diffusion coefficient of  $D = 4.8 \frac{\mu\text{m}^2}{\text{s}}$ , and  $N = 83.3$  for mCherry with a diffusion coefficient of  $D = 4.8 \frac{\mu\text{m}^2}{\text{s}}$ .

<sup>3</sup>This led to a pixel size of  $s = 30.5\text{nm}$ , a line time of  $\tau_y = 23.4\text{ms}$ , and a pixel dwell time of  $\tau_x = 183.1\mu\text{s}$ .

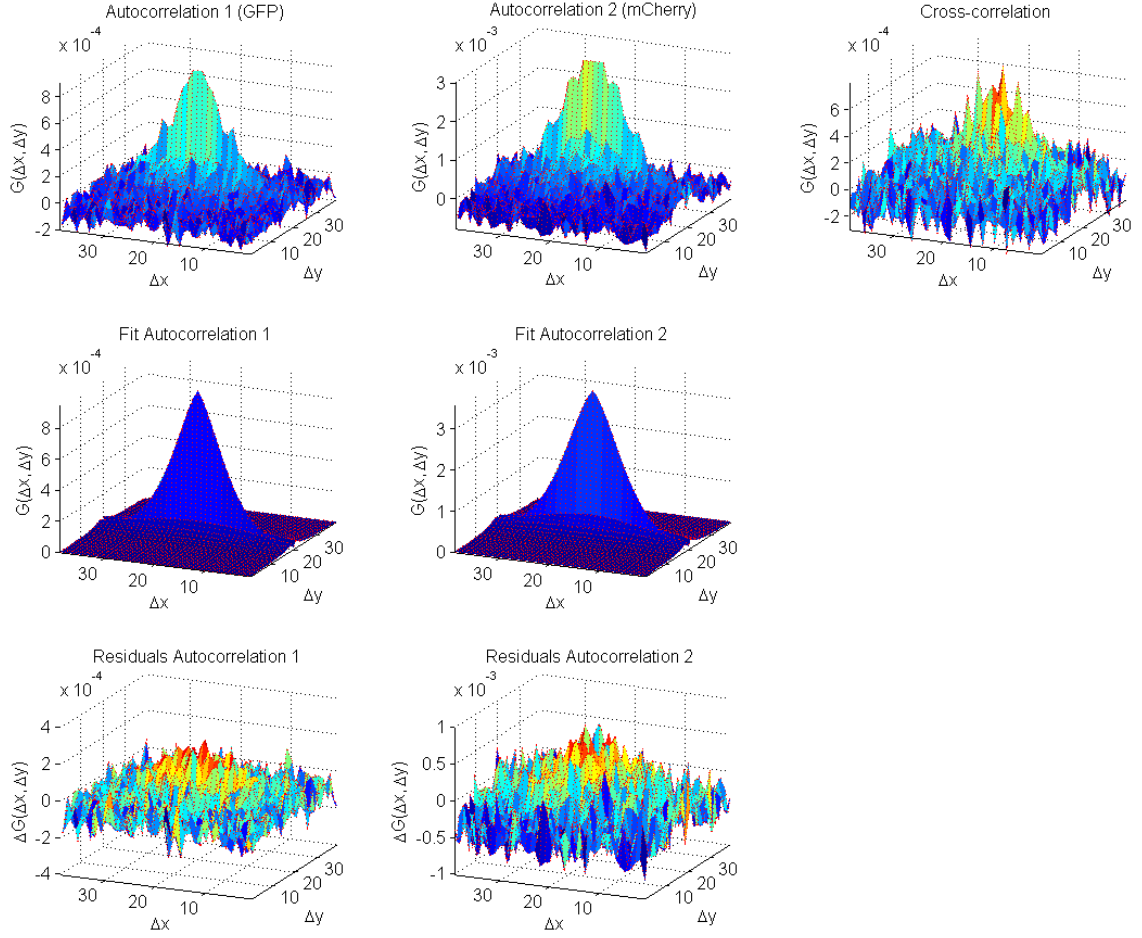


**Figure 5.12:** RICS without PIE in a cell expressing freely diffusing GFP as well as the mCherry-labeled ICDI domain of the  $\text{Ca}_v1.4 \text{ Ca}^{2+}$ -channel. No interaction takes place between those two species. Nonetheless, a significant cross-correlation amplitude is visible due to spectral crosstalk.

The same data was analyzed under identical conditions with PIE-RICS, excluding all crosstalk photons from the analysis. The resulting auto- and cross-correlations are shown in Figure 5.12. No cross-correlation amplitude is visible. The fit results were  $N = 399$  for GFP with a diffusion coefficient of  $D = 6.35 \frac{\mu\text{m}^2}{\text{s}}$ , and  $N = 47.9$  for mCherry with a diffusion coefficient of  $D = 10.5 \frac{\mu\text{m}^2}{\text{s}}$ . The determination of the diffusion coefficients both with and without PIE is not very accurate here, which is probably caused by the fact that the spatio-temporal decay of the RICS correlation curves can not be fitted very well due to photophysical effects of the fluorescent proteins, a problem that was also present in the FCS analysis of GFP-Dnmt1 (Chapter 6). However, the main power of this method, the accurate identification of molecular interactions, is not affected by this effect, because it does not rely on an exact determination of diffusion coefficients.

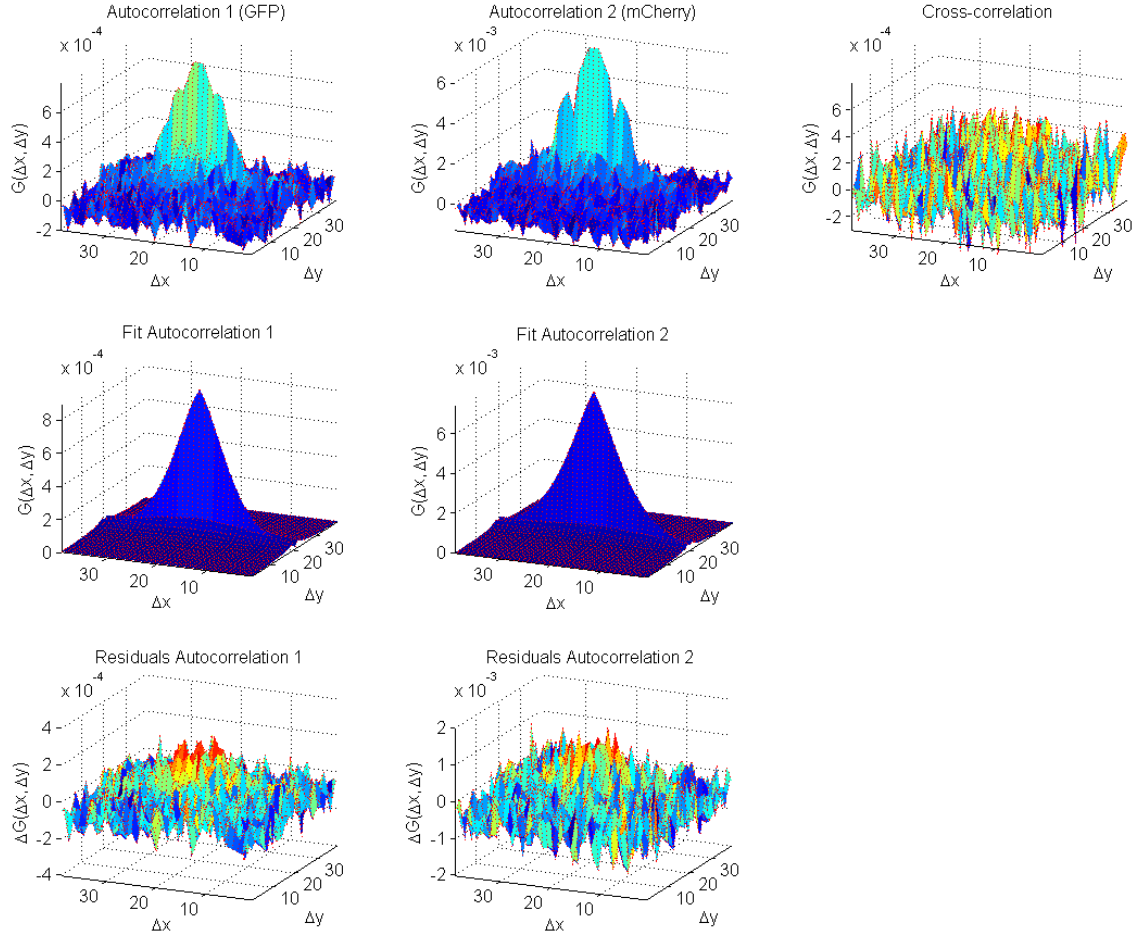


**Figure 5.13:** PIE-RICS in a cell expressing freely diffusing GFP as well as the mCherry-labeled ICDI domain of the  $\text{Ca}_v1.4 \text{ Ca}^{2+}$ -channel. No interaction takes place between those two species, and with the use of PIE, no artificial cross-correlation is measured.

## 5.6 Application to $\text{Ca}_v1.4$ channel domain

The  $\text{Ca}_v1.4 \text{ Ca}^{2+}$ -channel [44, 45] is a voltage dependent, L type calcium channel. It is of crucial importance in the ribbon synapses of retina photoreceptors, and  $\text{Ca}_v1.4$  dysfunction has been linked to night blindness in humans and mice.  $\text{Ca}_v1.4$  interacts with the calcium sensing messenger protein Calmodulin. To study the nature of the binding of Calmodulin to the  $\text{Ca}_v1.4$  channel, the soluble C-terminal part of murine  $\text{Ca}_v1.4$ , labeled twofold with the RFP derivative mCherry, and GFP-double-labeled murine Calmodulin were transfected into HEK293 cells according to the protocol introduced in Section 5.5. Two of each fluorescent proteins were used for labeling to make sure that a large percentage of the interacting molecules have at least one functioning label, because the folding efficiency of fluorescent proteins in cells lies only between 40 – 60 %.

50 image frames with  $256 \times 256$  pixels, corresponding to  $5.5 \mu\text{m} \times 5.5 \mu\text{m}$ , were recorded with a frame time of 1 s.<sup>4</sup> A region of interest was selected, measuring  $100 \times 100$  pixels, which lay entirely within the cytosol of the cell, because the  $\text{Ca}_v1.4$  channel fragment was absent in the

<sup>4</sup>This led to a pixel size of  $s = 21.5\text{nm}$ , a line time of  $\tau_y = 3.9\text{ms}$ , and a pixel dwell time of  $\tau_x = 15.3\mu\text{s}$ .

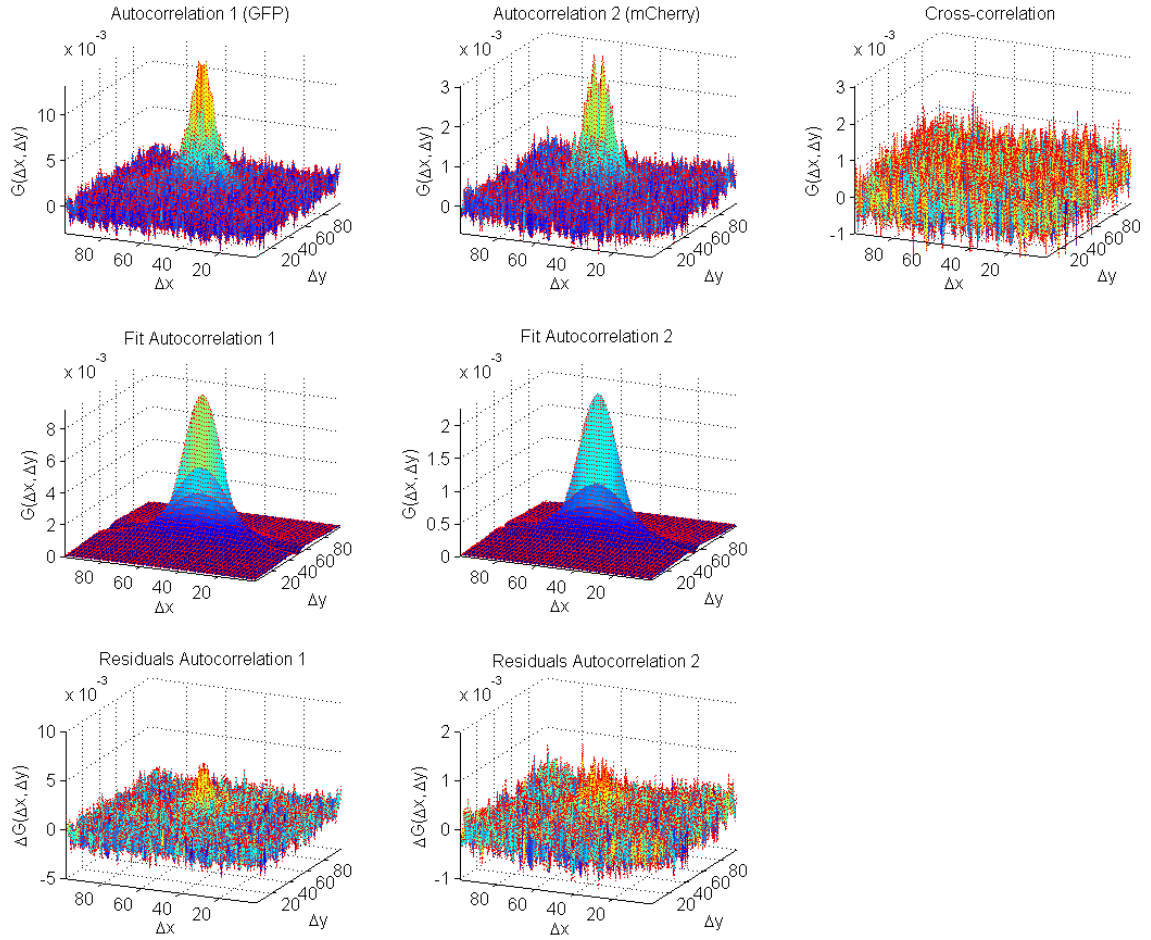


**Figure 5.14:** PIE-RICS in a HEK293 cell expressing the soluble C-terminal part of the  $\text{Ca}_v1.4 \text{ Ca}^{2+}$ -channel with a GFP label as well as mCherry-labeled Calmodulin in the cytosol. The PIE-RICS cross-correlation amplitude is zero, hence no interaction takes place between those two species. The confocal volume parameters for the fits were  $\omega_r = 0.426 \pm 0.009$  and  $\omega_z = 3.99 \pm 1.28$  for the GFP channel and  $\omega_r = 0.440 \pm 0.018$  and  $\omega_z = 6.72 \pm 3.41$  for mCherry.

nucleus due to its size. A running average background subtraction of 10 frames was applied prior to RICS analysis. The resulting 41 RICS patterns were averaged, and the calculated auto- and cross-correlations as well as fits for the autocorrelations are shown in Figure 5.14. No cross-correlation amplitude is visible, showing that there is no or only a very weak cytosolic interaction between the the  $\text{Ca}_v1.4$  channel and Calmodulin under the experimental conditions. The RICS autocorrelations were fitted with volume parameters that were previously calibrated with a stationary FCS measurement of a solution of double-labeled DNA. The fit results were  $N = 38.4$  for the GFP-labeled channel fragment with a diffusion coefficient of  $D = 2.0 \frac{\mu\text{m}^2}{\text{s}}$ , and  $N = 157.6$  for the mCherry-labeled Calmodulin with a diffusion coefficient of  $D = 3.5 \frac{\mu\text{m}^2}{\text{s}}$ .

## 5.7 Application to $\text{Ca}_v1.4$ channel ICDI subdomain

The ICDI domain is part of the soluble C-terminal part of the  $\text{Ca}_v1.4$   $\text{Ca}^{2+}$ -channel. It can block the Calmodulin binding pocket of the  $\text{Ca}_v1.4$  channel, thus influencing the regulation of the  $\text{Ca}_v1.4$  activity by Calmodulin. To stabilize the conformation in which the pocket is blocked, there is a relatively strong affinity between the ICDI domain and the binding pocket. With this knowledge in mind, a second experiment was designed. The GFP-double-labeled C-terminal part of the  $\text{Ca}_v1.4$  channel without its ICDI domain was expressed in HEK293 cells as described before, and additionally, the isolated ICDI-domain itself was labeled twofold with mCherry and equally expressed. If the affinity between the two domains is strong enough, a cross-correlation should be visible with PIE-RICS.

100 image frames with  $256 \times 256$  pixels, corresponding to  $2.4 \mu\text{m} \times 2.4 \mu\text{m}$ , were recorded with a frame time of 2 s.<sup>5</sup> A region of interest within the cytosol of the cell was selected, measuring  $100 \times 100$  pixels. A running average background subtraction of 10 frames was applied prior to RICS analysis. The resulting 91 RICS patterns were averaged, and the calculated auto- and cross-correlations as well as fits for the autocorrelations are shown in Figure 5.15. As in the previous experiment, the cross-correlation amplitude is zero, showing that there is no or only a very weak cytosolic interaction between the the  $\text{Ca}_v1.4$  channel and its separated ICDI domain under the experimental conditions. The RICS autocorrelations were fitted with the same volume parameters as used in Section 5.6. The fit results were  $N = 59.3$  for the GFP-labeled channel fragment with a diffusion coefficient of  $D = 2.6 \frac{\mu\text{m}^2}{\text{s}}$ , and  $N = 32.5$  for the mCherry-labeled ICDI-subdomain with a diffusion coefficient of  $D = 6.8 \frac{\mu\text{m}^2}{\text{s}}$ .

---

<sup>5</sup>This led to a pixel size of  $s = 9.4\text{nm}$ , a line time of  $\tau_y = 7.8\text{ms}$ , and a pixel dwell time of  $\tau_x = 30.5\mu\text{s}$ .

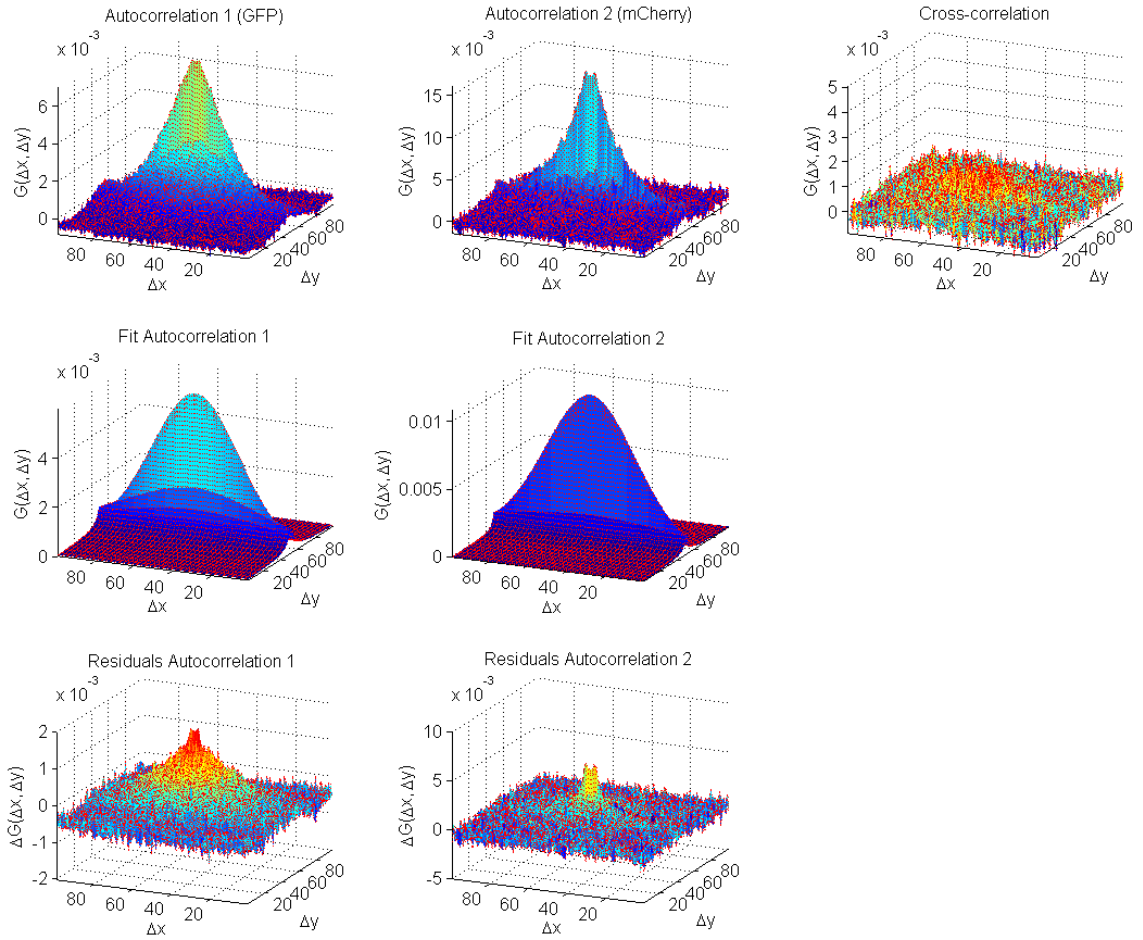


**Figure 5.15:** PIE-RICS in a HEK293 cell expressing the soluble, GFP-labeled, C-terminal part of the  $\text{Ca}_v1.4$   $\text{Ca}^{2+}$ -channel without its ICDI domain as well as the mCherry-labeled ICDI domain in the cytosol of the same cell. The PIE-RICS cross-correlation amplitude is zero, hence no interaction takes place between those two species. The confocal volume parameters for the fits were the same as in Figure 5.14.

## 5.8 Discussion

Scanning FCS and RICS are two potent techniques to collect information about diffusion and molecular binding from living cells. Perturbing effects such as photobleaching, which are often grave in live-cell measurements, can be greatly reduced by exposing the fluorophores to the excitation light for much shorter times. At the same time, the amount of statistics collected in a single experiment is increased by probing multiple locations within the cell. Even comparative studies between different cellular compartments are possible within a single measurement.

The combination of Scanning FCS and RICS with PIE improves the informative value of the methods greatly. Especially the question whether two differently labeled molecular species bind together in a cellular context, which is essential for the understanding of many biological processes, can in many cases not be unambiguously answered without PIE. Any artificial non-zero cross-correlation caused by spectral crosstalk obscures the interactions that really take place, and only comparative statements can be made with the help of additional negative-control measurements. Once the effects of spectral crosstalk are removed, however, the amplitude of the cross-correlation of both Scanning FCS and RICS is exactly zero for independent species, so in turn any non-zero cross-correlation is a direct proof of molecular interactions. In addition, without the influence of spectral crosstalk, the amplitudes of the Scanning FCS and RICS auto- and cross-correlations yield information about the fractions of molecules that are free and that are bound together, respectively.

One important limitation shared by both methods is their limitation to relatively low concentrations, with a limit typically between 100 nM and 1  $\mu$ M. This limit is mainly caused by the fact that the APDs used as fluorescence detectors start to show saturation effects for fluorescent count rates over approximately 100 kHz, which grow stronger for higher count rates. At count rates around 1 – 5 MHz, an APD is usually switched off automatically to prevent damage by overheating. Since the fluorescence count rate is directly proportional to the concentration of the sample, it is necessary to reduce the molecular brightness for high concentration, usually by using a lower excitation power. However, for low molecular brightnesses, typically below  $1 \frac{\text{kHz}}{\text{molecule}}$ , correlation curves of any type become very noisy due to the very low statistics per molecule in combination with the detector background noise. For measurements in cells, however, usually cells exhibiting a wide range of expression levels and thus concentrations are present that can be identified by the overall brightness of the respective cell. This makes it possible to select cells with an expression level corresponding to an adequate concentration.

In this work, PIE-Scanning FCS and PIE-RICS were established and proof-of-principle measurements in aqueous solutions of positive and negative cross-correlation samples were successfully performed. A double labeled DNA double strand served as a positive control and resulted in a non-zero cross-correlation with both methods. A mixture of two independently diffusing fluorophores was used as a negative control. Without PIE, both methods yielded a non-zero cross-correlation as well, whose amplitude depended strongly on the number of crosstalk photons emitted by the lower wavelength fluorophore relative to the photons emitted the longer wavelength fluorophore. Importantly, with PIE, the cross-correlation amplitude was completely zero for both methods, proving their capability to unambiguously decide about molecular interactions.

To prove the capabilities in live-cell measurements, one of the methods, PIE-RICS, was selected for further investigations. HEK293 cells were transfected with different controls: A GFP-mCherry fusion construct was designed as a positive cross-correlation control, and a HEK293 cell expressing both GFP and an mCherry-labeled protein, which were diffusing independently from each other, as a negative control. For the positive control cells, as expected, a non-zero RICS cross-correlation amplitude was observed. For the negative control cells, a non-zero cross-correlation amplitude was only present without PIE. With the application of PIE, the cross-correlation was zero for the negative control, proving that also for measurements on living cells, PIE allows unambiguous statements about molecular interactions.

As a biologically relevant application of PIE-RICS, the interaction of Calmodulin with the  $\text{Ca}_v1.4$  calcium channel was investigated. For this purpose, the cytoplasmic domain of the channel carrying the proposed binding site was cleaved from the membrane-bound part and labeled with mCherry. Calmodulin was labeled with GFP, and both proteins were expressed in HEK293 cells, freely diffusing in the cytoplasm. PIE-RICS experiments were performed at various concentrations. Although RICS autocorrelation was visible for both of the labels, no cross-correlation could be observed, leading to the statement that at least under the experimental conditions used here, no binding between Calmodulin and the  $\text{Ca}_v1.4$  domain takes place.

As an additional application, the autoinhibition of the ICDI subdomain of  $\text{Ca}_v1.4$  to the Calmodulin binding site of the  $\text{Ca}_v1.4$  channel was studied with PIE-RICS. For this purpose, the ICDI subdomain was cleaved from the  $\text{Ca}_v1.4$  domain and labeled with mCherry, and the  $\text{Ca}_v1.4$  domain itself was labeled with GFP. Both proteins were expressed freely diffusing in the cytoplasm of HEK293 cells, and PIE-RICS measurements were taken. Again, no cross-correlation was observed, leading to the result that under the present experimental conditions, no binding takes place between the ICDI domain and the  $\text{Ca}_v1.4$  domain.

In both cases, binding had been previously observed with a FRET assay [46] based on a direct analysis of the total fluorescence intensity emitted by a transfected cell in the donor- and acceptor-channels. One possible explanation for the differing results is the fact that for RICS, only cells with a low to medium fluorescence intensity, compared to the total range of available cells, were selected. These cells were expected to have a relatively low concentration of donor- and acceptor-labeled molecules, a prerequisite for RICS, which only functions up to a concentration of approximately 100 nM to 1  $\mu\text{M}$ . Binding between  $\text{Ca}_v1.4$  and either Calmodulin or the ICDI-domain, however, is concentration dependent, so their affinity may have been too low for the experimental conditions used here.



# 6 Dnmt1

## 6.1 Introduction

DNA methyltransferase 1 (Dnmt1) is a mammalian protein whose function is to copy DNA methylation patterns from parental do daughter strands during DNA replication to maintain this important epigenetic mark. With 183 kDa, it is a comparably large protein. It carries out complex interactions with DNA substrates and with a number of other proteins, particularly with the replication machinery [47]. Little is still known about its structural and dynamic properties, mechanistic function and the details of its interaction with the DNA strands. So far, only the structure of the *TS*-domain (Figure 6.1), which belongs to the N-terminal part of the protein, has been resolved. For the C-terminal part of Dnmt1, a homology model was proposed comprising approximately one third of its total length [48], based on a sequence comparison between Dnmt1 and procaryotic methyltransferases, who share the preserved motifs for the catalysis of the methyl transfer reaction. However, the C-terminal part of Dnmt1 by itself is catalytically inactive and is dependent on its N-terminal counterpart, indicating significant structural differences between the two pseudo-homologues.

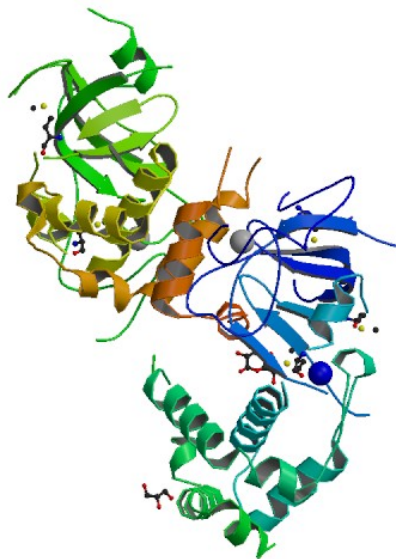


**Figure 6.1:** X-ray structure of the TS domain of Dnmt1. Image from the RCSB Protein Data Bank (<http://www.pdb.org>) of PDB-ID 3EPZ (Walker, J.R.; Avvakumov, G.V.; Xue, S.; Li, Y.; Bountra, C.; Weigelt, J.; Arrowsmith, C.H.; Edwards, A.M.; Bochkarev, A.; Dhe-Paganon, S.: Replication Foci-Targeting Sequence of Human DNMT1)

It was previously reported that Dnmt1 is able to dimerize [49], and it is an important and interesting question whether the formation of a dimer is necessary for catalysis of the methyl transfer reaction. An in vitro assay was designed together with the group of Prof. Heinrich Leonhardt, LMU München, to address this question. Dnmt1 was labeled with either GFP or

RFP as a fusion protein, and subsequently formed complexes with fluorescently labeled DNA substrates. Fluorescence fluctuation spectroscopy measurements were performed on Dnmt1 in the presence and absence of DNA substrates, and the data was evaluated with PCH, FIDA, FCA, FCS, and FCCS (Chapter 4).

## 6.2 Sample preparation

The proteins were expressed in HEK293T cells and purified in a one-step assay previously developed in the group of Prof. Leonhardt [50, 51]. The cells were lysed and the lysate was incubated with agarose beads that were functionalized via a Ni-NTA linker with his-tagged GFP binding proteins (GBP), or RFP binding proteins (RBP). These proteins act as antibodies against GFP and RFP, respectively, thus binding to any GFP- or RFP-labeled target proteins in the lysate. Due to the large weight of the beads, they could be separated from the lysate during several centrifugation and washing steps.

Covalent Dnmt1:DNA complexes were prepared and purified following a newly established protocol. Double-stranded DNA substrates of 42 base pair length were prepared, which contained a 5-aza-cytosine inhibitor at a central hemimethylated CpG site [50] (*trapping DNA*), and were labeled with either ATTO 550 or ATTO 700. The beads coated with GBP:GFP-Dnmt1 were incubated for 90 minutes at 37°C with the trapping DNA substrates in the presence of the cofactor S-adenosine-L-methionine, forming an irreversible covalent bond between Dnmt1 and trapping DNA. Notably, since the covalent GFP-Dnmt1:DNA bond is concentration-independent in contrast to reversible types of molecular binding, it renders these constructs ideally suited for FFS studies at nanomolar concentrations.

Samples with or without complexation with DNA were incubated with imidazole, an organic compound that competes for binding to the Ni-NTA beads' surface and as it is in high excess, leads to release of the target complexes, thereby eluting them from the beads. Note that after this purification method, GBP is still in complex with GFP. Directly prior to measurement the sample was centrifuged again to dispose of any residual beads in the solution.

In some cases, the sample underwent an additional purification step via size exclusion chromatography. For this purpose, an ÄKTA chromatograph with a Superose 6 PC 3.2/30 column (General Electric Healthcare, Munich, Germany) was used.

## 6.3 Excitation power analysis

To verify the validity of the different brightness analysis methods and to study the influence of photobleaching and other photophysical effects on the molecular brightness values obtained from these techniques, a set of measurements on the ATTO 565 fluorophore was taken with different laser excitation powers. Furthermore, the molecular brightness of a DNA strand with either one or two ATTO 565 labels was measured to study the characteristics of a fluorophore when used as a label on a biomolecule. Furthermore, since it was previously shown [14] that monomers can be distinguished from dimers with brightness analysis, the applicability under the given experimental conditions was verified.

Sample	PCH		FIDA		FCA		FCS	
	N	$\varepsilon$ [kHz]	N	$\varepsilon$ [kHz]	N	$\varepsilon$ [kHz]	N	$\varepsilon$ [kHz]
ATTO 565 (15 $\mu$ W)	0.42	43.7	0.36	51.8	0.36	51.3	0.31	60.2
ATTO 565 (25 $\mu$ W)	0.47	58.7	0.39	74.0	0.39	73.8	0.33	87.1
ATTO 565 (40 $\mu$ W)	0.55	81.5	0.41	110.8	0.42	111.0	0.36	128.7
ATTO 565 (60 $\mu$ W)	0.65	91.5	0.47	131.0	0.47	132.2	0.40	154.8
ATTO 565 (120 $\mu$ W)	0.88	103.9	0.61	156.5	0.60	161.2	0.51	189.2
DNA with ATTO565 (25 $\mu$ W)	0.81	36.0	0.72	40.5	0.72	41.3	0.73	40.5
DNA with 2 $\times$ ATTO565 (25 $\mu$ W)	0.58	55.3	0.43	77.0	0.44	76.7	0.43	77.8

**Table 6.1:** Influence of photobleaching and quenching on the molecular brightness of ATTO 565. FIDA volume parameters (Equation 4.35) were calibrated to  $a_1 = -0.51$  and  $a_2 = 0.16$  with a solution of ATTO 565.  $a_3$  was fixed to unity.

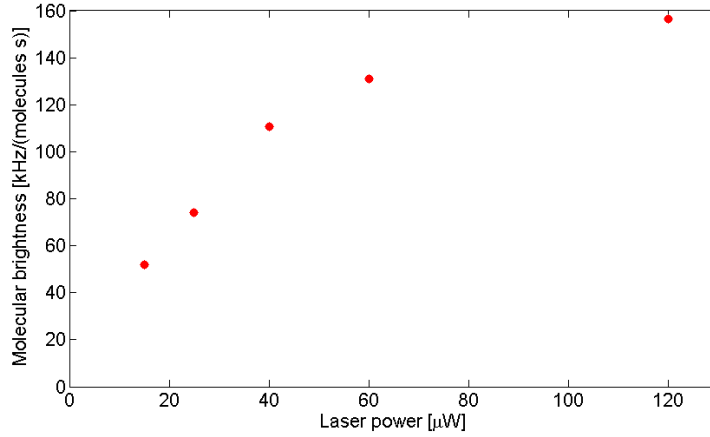


**Figure 6.2:** Molecular brightness of ATTO 565 as determined with FIDA versus laser excitation power. Relatively low photophysical effects are occurring up to 40  $\mu$ W, but for higher laser powers the proportionality between excitation power and molecular brightness vanishes.

From the experimental results shown in Table 6.1, it is visible that the PCH results show significant deviations from the values obtained with other methods. This is possibly caused by the assumption of a point spread function in the shape of a three dimensional Gaussian function that is made for PCH. Under actual experimental conditions however, this assumption is not very accurate [52]. In fact, the deviations of the actual PSF from the theoretical Gaussian profile increase with rising excitation power.

For laser powers up to approximately 40  $\mu$ W, the molecular brightness shows a relatively good proportionality with the excitation power, whereas for higher powers the two are no longer proportional (Figure 6.2). This value cannot be generalized to other fluorophores, because fluorophores can differ strongly in their photophysical properties. For example, it will be later shown that there are very strong photophysical effects for GFP at laser powers as low as 1  $\mu$ W. Interestingly, very similar values for  $N$  and  $\varepsilon$  were obtained by FIDA and FCA, whereas the results obtained by PCH and FCS differed quite strongly. This effect was increased even further for higher laser powers. Since it was apparent that the data could be fitted much better with FIDA than with PCH (data not shown), the FIDA and FCA results were assumed to be the

most accurate in this case.

When attached to a DNA strand, the fluorophore was quenched to about 50 % of its original molecular brightness (Table 6.1). This is a known effect, whose strength depends on the exact nature of compounds surrounding the fluorescent label. The quenching effect is also reflected in a reduced fluorescence lifetime for the DNA-bound fluorophore (Figure 6.3). A variation in quenching can appear already for a change as small as shifting the labeling position on the DNA strand to an adjacent nucleotide [53]. However, at least for the labeling positions used in this experiment, it is clearly possible to distinguish between DNA strands with a single fluorophore and those with two fluorophores with FIDA, FCS, and FCS (Table 6.1).

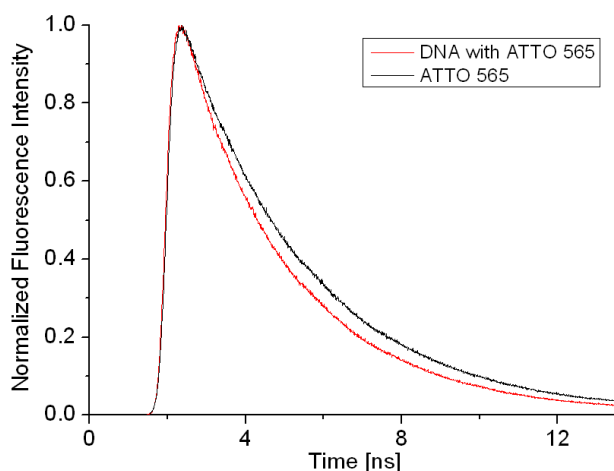


**Figure 6.3:** Fluorescence lifetimes of free ATTO 565 (black) and ATTO 565 bound to a DNA strand (red). The proximity to the DNA nucleotide causes fluorescence quenching, which is reflected in a faster lifetime decay.

## 6.4 GFP/GBP

Prior to applying FIDA in an experimental context, its volume parameters must be calibrated with a sample containing only a single fluorescent species of known properties. The parameters thus obtained can subsequently be used and kept fixed to fit data from other samples, possibly containing a higher number of fluorescent species. The calibration should ideally be performed with the same fluorophore that is subsequently used for the measurement. Since different fluorophores exhibit different photophysical imperfections such as photobleaching or blinking, the shape and size of the apparent confocal volume can vary. For synthetic fluorophores such as ATTO 488, the confocal volume will be close to a three dimensional Gaussian profile as assumed by PCH. For GFP/GBP, however, it was apparent from the FIDA volume parameters that the aberrations of the confocal volume were substantial. The parameters for a measurement of ATTO 488 and those for another measurement of pure GFP differed by more than 50% (Table 6.2, caption). Furthermore, it was apparent from the fitted curves, that fitting the GFP measurement with the volume parameters obtained from the ATTO 488 calibration measurement led to a less than optimal fit quality (Figure 6.4). Therefore, the volume parameters obtained from pure GFP were used for the subsequent measurements including GBP rather than those obtained with ATTO 488.

Previous data suggested that the binding of GBP enhanced the molecular brightness of GFP. To examine this brightness change of GFP caused by complex formation with GBP, a titration curve was recorded. For each level of GBP, the molecular brightness was calculated with the known set of FFS methods (6.2). The molecular brightness indeed depends on the relative GBP concentration. On the GBP saturation level, the molecular brightness of GFP is enhanced by approximately 25% (Figure 6.5).

Sample	PCH		FIDA		FCA		FCS	
	N	$\epsilon$ [kHz]	N	$\epsilon$ [kHz]	N	$\epsilon$ [kHz]	N	$\epsilon$ [kHz]
ATTO 488	0.82	12.5	0.80	13.0	0.83	12.7	0.66	16.5
GFP alone	0.72	16.1	0.68	17.1	0.70	16.8	0.66	17.9
GFP + GBP (4:1)	1.64	16.0	1.58	16.6	1.61	16.5	1.49	17.9
GFP + GBP (2:1)	1.10	17.4	1.04	18.4	1.06	18.2	1.00	19.5
GFP + GBP (3:2)	0.97	19.7	0.91	21.1	0.93	21.0	0.90	21.6
GFP + GBP (1:1)	1.26	19.8	1.19	20.9	1.21	20.8	1.16	21.8
GFP + GBP (1:2)	1.22	20.2	1.16	21.4	1.17	21.3	1.13	22.3

**Table 6.2:** Brightness enhancement of GFP by complex formation with GBP. Brightness values were determined with PCH, FIDA, FCA, and FCS. FIDA volume parameters (Equation 4.35) were equal to those presented in Figure 6.4. The volume parameters determined with GFP were used during the subsequent fits with GFP + GBP. Laser power was 25  $\mu$ W.

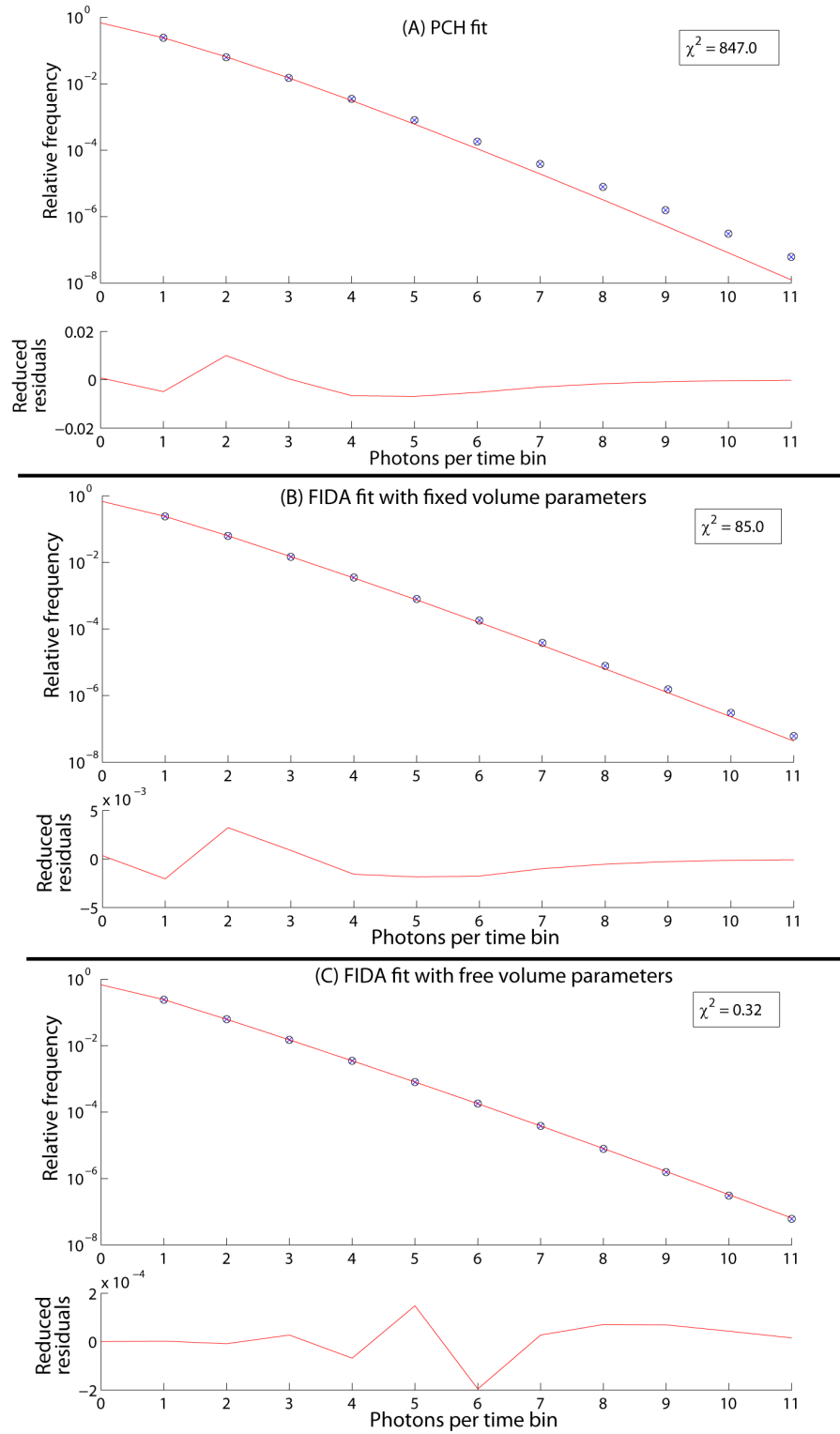


**Figure 6.4:** GFP brightness analysis with different fit methods: (A) with PCH, (B) with FIDA where the volume parameters (Equation 4.35) were fixed to values previously calibrated with a solution of ATTO 488 to  $a_1 = -0.47$  and  $a_2 = 0.15$ , (C) with FIDA where the volume parameters were used as additional fit parameters, resulting in  $a_1 = -0.65$  and  $a_2 = 0.20$ .  $a_3$  was always fixed to unity. PCH fit quality is very poor compared to FIDA, especially at the end of the curve. A small improvement in FIDA fit quality can be achieved by using the volume parameters as additional fit parameters.

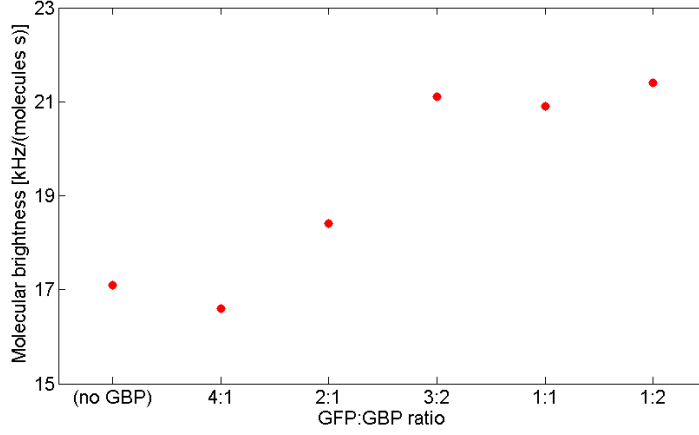


**Figure 6.5:** Brightness enhancement of GFP by complex formation with GBP as determined with FIDA. The molecular brightness increased by approximately 25% under GBP excess conditions.

As mentioned before, the strength of photophysical effects depending on the excitation power can vary strongly between different fluorophores. Since so far, only ATTO 565 has been investigated (Section 6.3), another detailed analysis was performed specifically for GFP in complex with GBP, which is the exact fluorophore used in the following sections to determine the dimerization state of Dnmt1. Both the molecular brightness and the diffusion times were monitored at various laser powers (Table 6.3).

Sample	PCH		FIDA		FCA		FCS		
	N	$\varepsilon$ [kHz]	N	$\varepsilon$ [kHz]	N	$\varepsilon$ [kHz]	N	$\varepsilon$ [kHz]	$\tau_D$ [ms]
GFP+GBP									
(5 $\mu$ W)	0.74	4.0	0.73	4.1	0.83	3.8	0.93	3.4	0.23
(10 $\mu$ W)	0.76	6.9	0.74	7.1	0.80	6.8	0.81	6.7	0.20
(20 $\mu$ W)	0.82	11.0	0.77	11.7	0.79	11.6	0.77	11.9	0.17
(50 $\mu$ W)	1.09	15.6	0.97	17.5	0.96	17.9	0.91	18.9	0.13
(100 $\mu$ W)	1.38	15.0	1.21	17.2	1.12	18.8	1.06	19.8	0.12
GFP-Dnmt1+GBP									
(5 $\mu$ W)	0.62	4.2	0.62	4.3	0.72	4.0	0.81	3.5	0.41
(10 $\mu$ W)	0.78	7.1	0.75	7.4	0.80	7.2	0.84	6.8	0.35
(20 $\mu$ W)	0.94	11.6	0.88	12.4	0.91	12.3	0.93	11.9	0.32
(50 $\mu$ W)	0.64	15.0	0.55	17.7	0.53	18.7	0.54	18.4	0.24
(100 $\mu$ W)	0.98	12.9	0.83	15.3	0.72	18.1	0.73	17.8	0.19

**Table 6.3:** Influence of the excitation power and of quenching on the molecular brightness and diffusion coefficient of GFP+GBP, both freely diffusing and bound to Dnmt1, a large and slowly diffusing protein. FIDA volume parameters (Equation 4.35) were determined with GFP+GBP calibration sample at 5  $\mu$ W to  $a_1 = -0.38$  and  $a_2 = 0.24$ .  $a_3$  was fixed to unity.

For higher laser powers it was evident that during the brightness analysis, the fitted curves did not match the experimental data very well any more. This effect was very strong for PCH, but also visible for FIDA. For FIDA, however, the situation could be improved when the volume parameters were used as fit parameters for each of the measurements.  $a_1$  and  $a_2$  would then obtain extremely unusual values, but the fit quality was better. Interestingly, in this case the

FIDA fit results approached those that were obtained with FCA, suggesting that FCA was able to determine the brightness more accurately than the other methods.

Similarly, for higher laser powers, the FCS curve could not be fitted very well anymore. Furthermore, the apparent diffusion times decreased, probably because the fluorophores went dark due to photobleaching or other effects before completing their way through the confocal volume. These observations lead to the decision that laser powers above 50  $\mu W$  should not be used for fluorescence fluctuation spectroscopy because of the strong deteriorations present.

Despite those photophysical effects, one very important statement could be made. For all laser powers and with all applied evaluation methods, the molecular brightness of GFP-Dnmt1 was always approximately equal to that of the GFP+GBP complexes, clearly showing that GFP-Dnmt1 was present in the monomeric state.

## 6.5 Dnmt1:DNA complexes

In order to investigate the possible formation of Dnmt1 dimers upon DNA binding, the molecular brightness of GFP-Dnmt1:DNA complexes was measured. For a dimer, a brightness twice as high as for a monomer is expected. However, first fluorescence measurements revealed a high tendency of the constructs to aggregate during or after the incubation with the DNA substrates (Section 6.2), possibly caused by the long exposure to a temperature of 37°C (Figure 6.6). A comparison of the size exclusion chromatograms of GFP-Dnmt1 and GFP-Dnmt1:DNA complexes later confirmed this finding, discovering a large amount of very heavy particles in the sample, very probably the aforementioned aggregates (Figure 6.11 A).

It is quite obvious that no reliable molecular brightnesses can be extracted from fluorescence data exhibiting such large and frequent bursts as present here. Therefore, from the size exclusion chromatography output, only those fractions were selected that had the same molecular size as the GFP-Dnmt1 constructs without DNA (The complexation with DNA is expected to change the molecular size only slightly).

Brightness analysis was subsequently applied to investigate the possibility of a dimerization of Dnmt1:DNA complexes. Both the molecular brightness of GFP-Dnmt1 and that of DNA:ATTO-700<sup>1</sup> were included into the analysis (Table 6.4).

---

<sup>1</sup>In the latter case, the size exclusion chromatography step was omitted due to a very low amount of bursts in the traces, indicating very few aggregates in the sample.



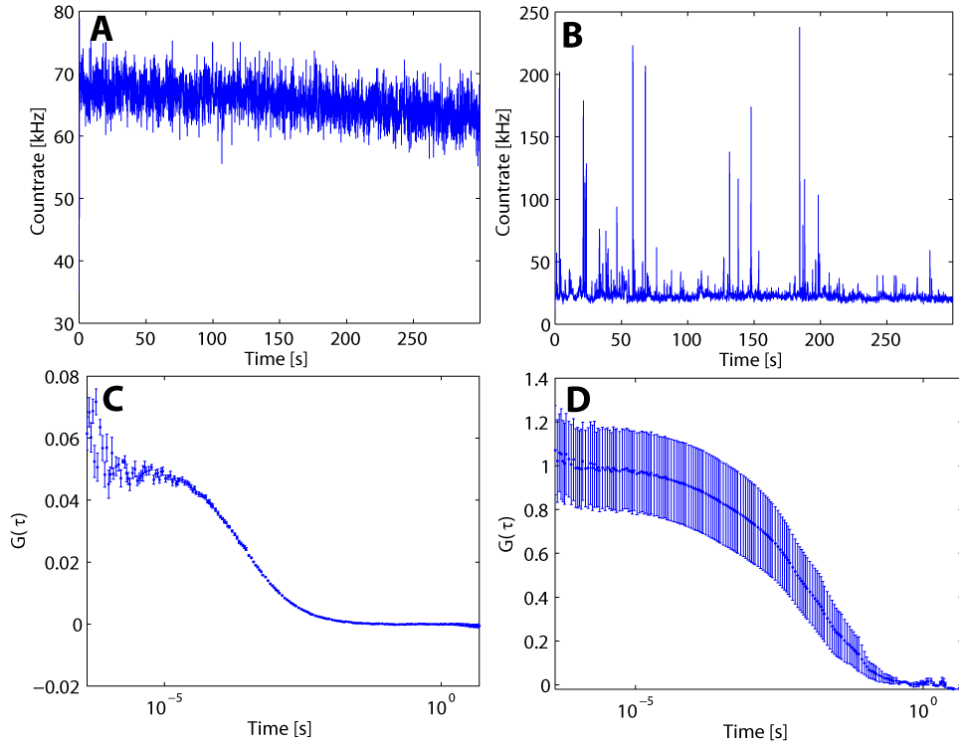


**Figure 6.6:** Aggregation of GFP-Dnmt1:DNA complexes after incubation at 37°C for 90 minutes. (A, B) Fluorescence intensity traces of GFP-Dnmt1 without and with the incubation step. Fluorescence bursts indicate a large aggregate diffusing through the confocal volume. (C, D) FCS curves of the measurements without and with the incubation step, respectively. The FCS curve of the GFP-Dnmt1:DNA measurement has very large error bars and shows relatively slow diffusion times, caused by the presence of large and thus very bright aggregates.

The brightness of GFP seems to decrease by approximately a third when attached to Dnmt1. Only a small variation in GFP brightness is visible upon complexation with DNA. The brightness of ATTO 700, however, increases by more than a factor of two after complex formation, at least when just one fluorescent species is assumed in the analysis. For an analysis incorporating two fluorescent species, the results show a strong variation depending on which method is chosen for the analysis. From the fit quality (Figure 6.7), it is apparent that the FIDA fit represents the data far better than the PCH fit and thus the fit results are somewhat more reliable. The fit quality could be improved even further by letting the FIDA volume parameters free even in the two species fit. The fit quality, assessed by the value of  $\chi^2 = 0.46$  is very good, although this approach is somewhat problematic due to the large number of six fit parameters. Furthermore, the mismatch between data and fit at the outer edge of Figure 6.7 (C) suggests that some very bright aggregates are still not accounted for in the fit.

The results of the brightness analysis indicate a complex with only one Dnmt1 molecule, but two or more DNA substrates. As a second, independent approach, this hypothesis is tested with FCCS analysis.

Sample	PCH		FIDA		FCA		FCS	
	N	$\varepsilon$ [kHz]	N	$\varepsilon$ [kHz]	N	$\varepsilon$ [kHz]	N	$\varepsilon$ [kHz] $\tau_D$ [ms]
GBP:GFP	1.09	15.6	0.97	17.5	0.96	17.9	0.91	18.9 0.13
GBP:GFP-Dnmt1	0.54	9.2	0.39	12.7	0.42	12.3	0.42	12.4 0.20
GBP:GFP-Dnmt1:DNA	0.45	11.7	0.34	15.7	0.37	15.1	0.37	15.1 0.25
DNA-ATTO700	10.1	8.2	10.0	8.2	10.1	8.2	8.85	9.4 0.46
Dnmt1:DNA-ATTO700	0.68	25.5	0.56	31.3	0.57	31.1	0.58	30.7 2.54
Dnmt1:DNA-ATTO700 (two species fit)	1.15	11.5	0.57	30.8	0.97	15.4		
Dnmt1:DNA-ATTO700 (free FIDA parameters)	0.05	91.0	0.002	98.4	0.02	114.4		
			0.58	26.7				
			0.03	64.6				

**Table 6.4:** Brightness analysis of Dnmt1:DNA complexes in comparison to the brightness of the respective monomeric fluorophore. For GFP, the FIDA volume parameters were used as fit parameters to improve the quality of the fit. For ATTO700, the FIDA volume parameters were determined with the DNA-ATTO700 sample to  $a_1 = -0.53$  and  $a_2 = 0.60$ .  $a_3$  was always fixed to unity. Laser power was set to 50  $\mu$ W. For GFP-Dnmt1, only a small increase in molecular brightness is measured upon complexation with DNA, whereas for ATTO700, the brightness is strongly increased.

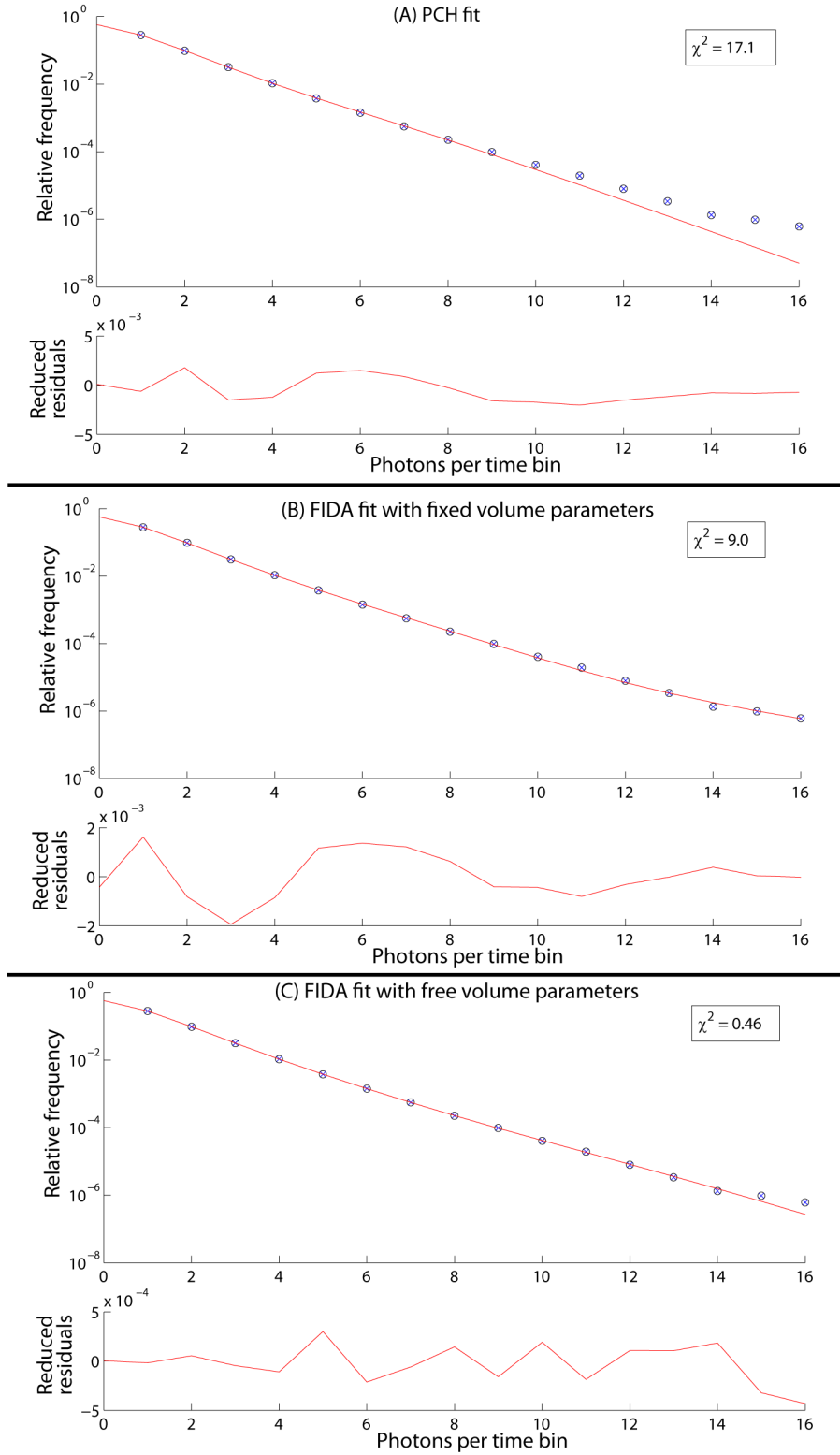


**Figure 6.7:** Two-component fits for brightness analysis, shown to assess the quality of the fits. (A) Two species PCH fit of Dnmt1:DNA-ATTO700 measurement. (B) Two species FIDA fit of the same data where the FIDA volume parameters were previously determined with a DNA-ATTO700 sample to  $a_1 = -0.53$  and  $a_2 = 0.60$ . (C) Two species FIDA fit where the volume parameters were used as additional fit parameters, resulting in  $a_1 = -0.33$  and  $a_2 = 0.36$ .  $a_3$  was always fixed to unity.

## 6.6 Dnmt1 cross-correlation

Two different mutants of Dnmt1 were co-expressed in HEK293 cells: Dnmt1, labeled with GFP as before, and additionally Dnmt1, labeled with monomeric RFP. Purification took place either with GBP or with RBP, as described in Section 6.2. In the case of a stable dimer of Dnmt1, approximately half of the complexes would stochastically be expected to carry one of each fluorescent label. In that case, a cross-correlation between GFP and RFP would be expected.

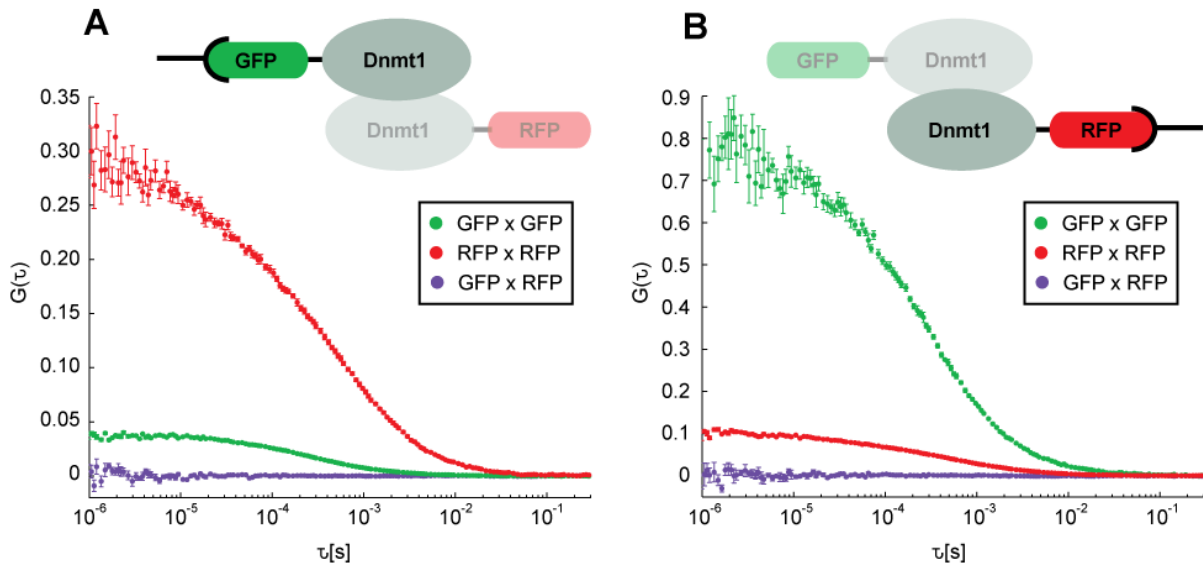


**Figure 6.8:** Fluorescence cross-correlation analysis of GFP-Dnmt1 and RFP-Dnmt1. (A) Purification via GBP antibodies. (B) Purification via RBP antibodies. The cross-correlation amplitude is zero in both cases. Furthermore, in both cases, the concentration of the respective fluorophore used for purification is much higher than that of the opposite fluorophore.

For both purification variants, GBP and RBP, the amplitude of the cross-correlation curve is zero, showing that there are no complexes with GFP and RFP, and thereby proving the absence of Dnmt1 dimers in the substrate-free state. Furthermore, for GBP purification, the concentration of GFP in the sample is much higher than that of RFP, and vice versa, proving that already during purification, where the overall sample concentration was much higher than during the fluorescence spectroscopy measurements, little to no dimers were present.

Moreover, in both cases, the much higher amplitude of the autocorrelation curve for the fluorophore that was not used for purification probably even originated at least partly from residual autofluorescent components of the sample solution, and not from the actual fluorescent proteins, because the respective fluorescent intensity, especially after size exclusion chromatography, was close to background level. Furthermore, the resulting autocorrelation could not be fitted with a one species FCS fit model, indicating a mixture of different background species.

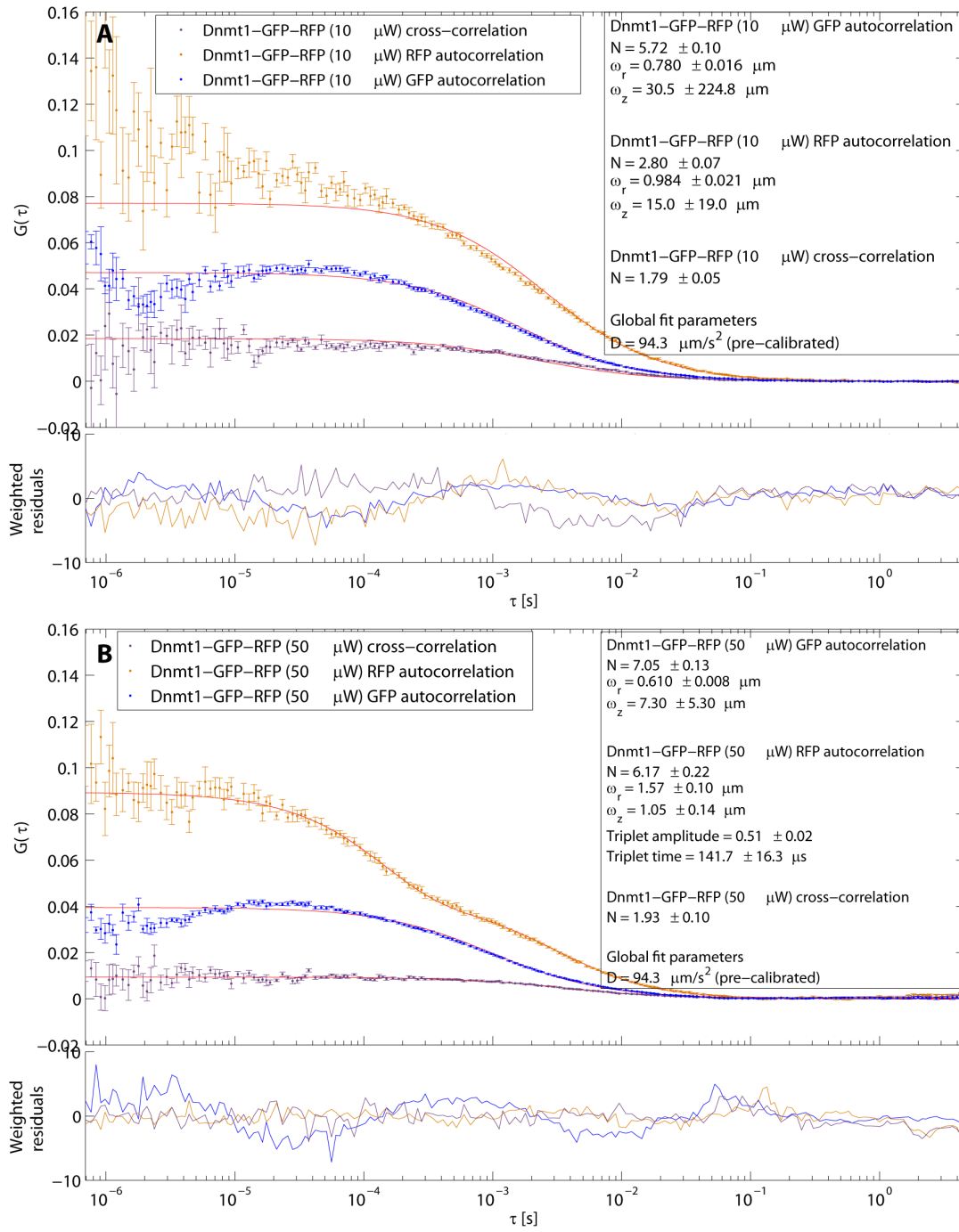


**Figure 6.9:** Fluorescence correlation curves of a Dnmt1-GFP-RFP construct at (A) 10  $\mu$ W and (B) 50  $\mu$ W laser excitation powers. Although significant changes in amplitude and shape both in the autocorrelation and cross-correlation curves are visible, a significant cross-correlation amplitude can be clearly observed even with an excitation power as high as 50  $\mu$ W.

Since photophysical effects such as observed with GFP are known to affect the cross-correlation amplitude, a control experiment was designed to exclude the possibility that GFP and RFP photophysics concealed a possible existing dimerization. A GFP-RFP-Dnmt1 construct was designed with the exact same labels as before, and analyzed with FCCS (Figure 6.9). A strong influence of the excitation power on the correlation curves could be observed. The apparent

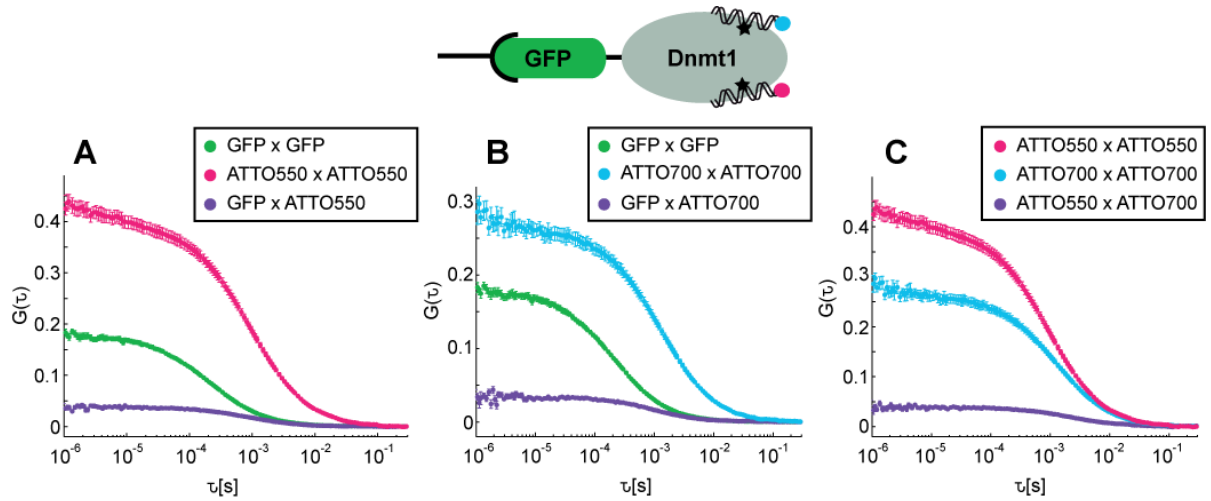


**Figure 6.10:** Fluorescence correlation curves of GFP-Dnmt1 that was incubated with DNA-ATTO550 and DNA-ATTO700. (A) Both autocorrelations and the cross-correlation between GFP and ATTO550, proving the binding between Dnmt1 and the ATTO550-labeled DNA substrates. (B) Auto- and cross-correlation curves for GFP and ATTO700, proving the same for DNA-ATTO700 substrates. (C) Auto- and cross-correlation curves for ATTO550 and ATTO700, proving unambiguously the presence of complexes with at least two different DNA substrates. Autocorrelation curves are shown for amplitude comparison.

size of the confocal volume varied significantly, and especially for RFP could only be fitted with very unusual volume parameters ( $\omega_r > \omega_z$ ). Furthermore, at  $50 \mu\text{W}$ , a very high triplet contribution could be observed for RFP. However, the experiment still clearly showed that even with  $50 \mu\text{W}$ , a relatively high laser excitation power for experiments with fluorescent proteins, a significant cross-correlation amplitude is detected for this GFP-RFP-construct. Hence, possible dimer formation would have also been detected in the previous experiment (Figure 6.8).

## 6.7 DNA cross-correlation

To examine the stoichiometry of DNA in Dnmt1:DNA complexes, GFP-Dnmt1 was simultaneously incubated with two differently labeled substrate DNA strands after purification: DNA-ATTO550 and DNA-ATTO700. If the complexes were formed with more than one DNA substrate, a cross-correlation between the ATTO550 and ATTO700 fluorophores would be visible, because for two or more substrates per complex, statistically at least 50 % of them would incorporate both fluorophores. To exclude artificial cross-correlation effects caused by aggregates or residual polystyrene beads, all samples were size exclusion purified in this and all following experiments prior to measurement and analysis.

Clearly, a significant cross-correlation amplitude can be seen for all three possible combinations of fluorophores (Figure 6.10). Since the formation of covalent complexes between Dnmt1 and DNA trapping substrates was expected, the cross-correlation between GFP and either of the DNA labels was not surprising (Figure 6.10 (A) and (B)). Additionally, a cross-correlation with significant amplitude was observed between the ATTO550 and ATTO700 labeled DNA substrates, proving that two different DNA strands are found within a complex, and together with the previous experiment, suggesting that at least two different DNA strands can be bound to the same GFP-Dnmt1 molecule.

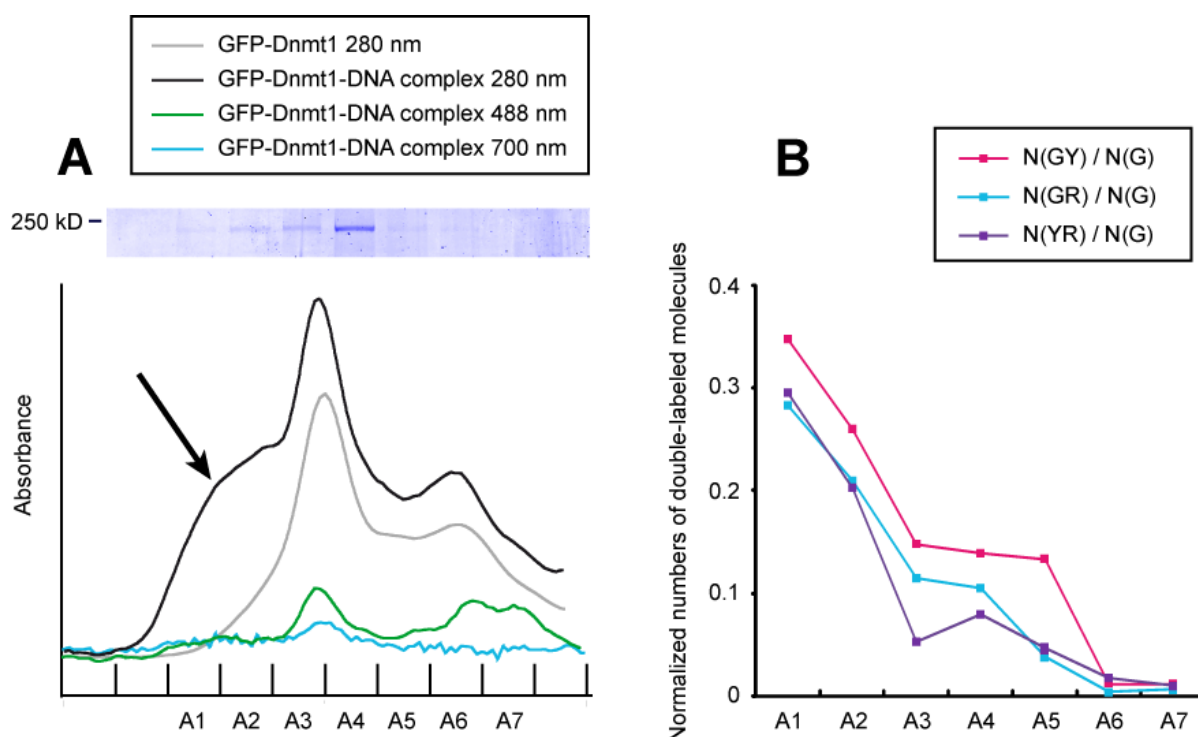


**Figure 6.11:** Assay to elucidate aggregation effects during the incubation of Dnmt1 with trapping DNA substrates. (A) size exclusion chromatogram at 280 nm of GFP-Dnmt1 (gray curve) and GFP-Dnmt1:DNA-ATTO550:DNA-ATTO700 complexes (black curve). Additional curves of the complexes were taken at GFP absorption (488 nm, green curve) and ATTO700 absorption (700 nm, blue curve), confirming the presence of GFP and ATTO700 in the peak between fractions A3-A4, presumably the location of the complexes. A broad shoulder arose on the heavy flank of the GFP-Dnmt1 peak after incubation (arrow), presumably caused by aggregates. The sample solution was separated into aliquots (A1-A7). (B) Normalized fluorescence cross-correlation amplitude of the different aliquots. A very high cross-correlation is observed for aliquots containing aggregates. A significant and relatively constant cross-correlation amplitude is observed for all aliquots containing GFP-Dnmt1:DNA constructs. The cross-correlation drops to zero for aliquots containing light components such as protein or DNA fragments.

The diffusion times in the GFP channel were significantly shorter than for the two synthetic fluorophores. This phenomenon was repeatedly observed for GFP and is probably caused by photophysical effects of GFP, changing the apparent confocal volume for this fluorophore.

To gain additional information about the issue of aggregation, an extensive assay combining chromatography and spectroscopy was designed.

GFP-Dnmt1:DNA-ATTO550:DNA-ATTO700 complexes were prepared as before, and underwent size exclusion chromatography (Figure 6.11 (A)). Subsequently, chromatography output fractions of different size ranges were investigated with FCCS. Global FCS fits were applied to all three possible triplets of two autocorrelations and the corresponding cross-correlation. The resulting concentrations were normalized to the respective concentration of GFP-Dnmt1 (Figure 6.11 (B)).

Chromatograms of both GFP-Dnmt1 and GFP-Dnmt1:DNA-ATTO550:DNA-ATTO700 were taken at 280 nm, the peak absorption wavelength of aromatic amino acids and therefore of proteins in general. A large peak emerged between fractions A3-A5, indicating that this

were the fractions containing the complexes. Additional chromatograms of GFP-Dnmt1:DNA-ATTO550:DNA-ATTO700 were taken at 488 nm, the absorption wavelength of GFP, and at 700 nm, that of ATTO700. In both curves, a peak emerged at the very same position as in the 280 nm peak, confirming the presence of both fluorophores in these fractions, as expected. An SDS-PAGE analysis of the fractions (performed by Carina Frauer in the lab of H. Leonhardt, LMU München) is also shown in Figure 6.11 (A), confirming the correct molecular weight of the complexes in this specific chromatogram peak.

By comparing the size exclusion chromatogram to that of a GFP-Dnmt1 sample that was not incubated with DNA substrates, the formation of aggregates became apparent. A large shoulder (Figure 6.11 (A), arrow) is only visible on the heavy flank of the sample after the trapping DNA incubation step. This is in good agreement with earlier observations (Figure 6.6). Furthermore, the central peak position of the GFP-Dnmt1:DNA sample was found at a slightly heavier position in the chromatogram, as would be expected due to the higher molecular weight of the GFP-Dnmt1:DNA complex compared to pure GFP-Dnmt1.

By separately analyzing a number of small fractions of the chromatogram (A1-A7) with FCCS (Figure 6.11 (B)), an unambiguous picture emerged: For fractions containing mainly large aggregates (A1, A2), a very large cross-correlation amplitude was measured for all three possible fluorophore combinations. For the fractions containing only the GFP-Dnmt1:DNA complexes (A3-A5), a relatively constant cross-correlation of significant amplitude was measured, confirming the observation of the presence of at least two different DNA substrates in the complex. For the fractions containing lighter components such as protein degradation products or DNA fragments (A6, A7), the cross-correlation amplitude approached zero, as expected.

To exclude the possibility that complexes might aggregate subsequent to the enzymatic reaction, which could lead to an artificial cross-correlation amplitude, a control experiment was designed. GFP-Dnmt1:DNA-ATTO550 and GFP-Dnmt1:DNA-ATTO700 complexes were prepared separately according to the established protocol. The two components were then pooled and analyzed with fluorescence cross-correlation (Figure 6.12).

In this experiment, cross-correlation was observed between GFP-Dnmt1 and each of the two different labeled DNA strands, which was expected. However, no significant cross-correlation amplitude was observed between the different DNA labels, ruling out aggregation subsequent to the enzymatic reaction. Furthermore, the formed complexes are sufficiently stable that no DNA substrates are exchanged after the reaction, a strong indication that both of the DNA strands form a very strong bond with Dnmt1.



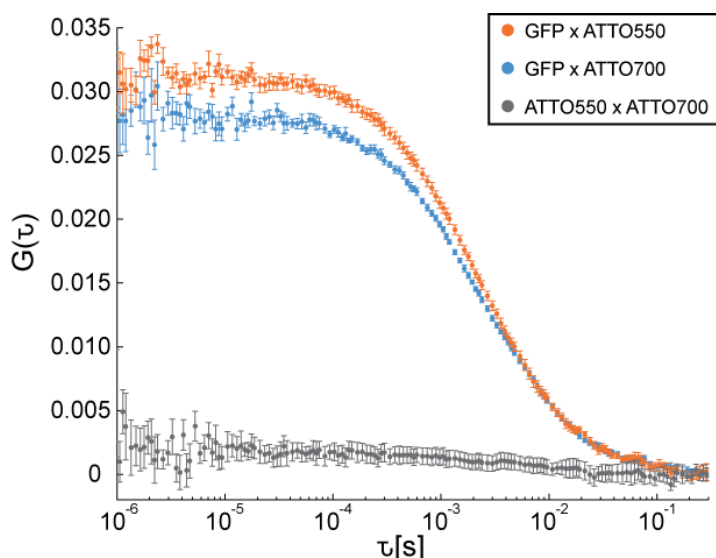


**Figure 6.12:** Fluorescence cross-correlation analysis of a solution of GFP-Dnmt1 that was incubated with DNA-ATTO550, and GFP-Dnmt1 that was incubated with DNA-ATTO700. Due to the enzymatic reaction, cross-correlation is clearly visible between GFP and either of the ATTO labels. No significant cross-correlation could be observed between DNA-ATTO550 and DNA-ATTO700, though.

## 6.8 Further investigation of the Dnmt1:DNA bonds

From the observation that a single Dnmt1 molecule forms a very strong bond with more than one DNA substrate, the question arises whether both of these bonds are covalent, or if one bond is reversible. An experimental artifact caused by fluorescent labeling could also be the present, since electrostatic adhesion of synthetic fluorophores to biomolecules is known to occur and is a quite common problem. Therefore, an assay was designed to distinguish between covalent and non-covalent bonds. GFP-Dnmt1 was incubated with a trapping DNA-ATTO700 substrate and an unmodified DNA strand, labeled with ATTO 550, called binding substrate because Dnmt1 forms a reversible, non-covalent bond with it. The binding DNA substrate was otherwise identical to the trapping DNA with the exception of having a canonical cytosine instead of the 5-aza-cytosine used for the trapping reaction (Figure 6.13 (B)). As a control, the experiment was also performed with two different trapping DNA strands as in the previous section (Figure 6.13 (A)).

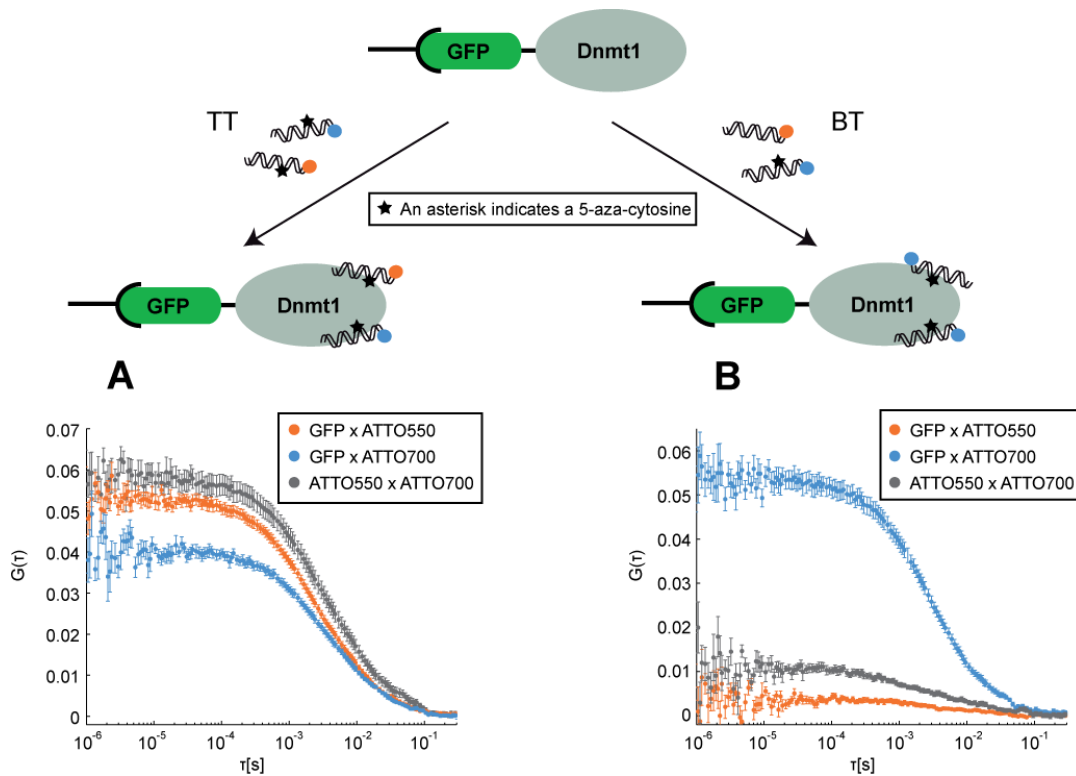


**Figure 6.13:** Binding/trapping DNA assay. To determine whether Dnmt1 can form more than one covalent bond with different DNA substrates, it was incubated either with two trapping DNA substrates with different labels (A), or with one trapping DNA substrate and one binding DNA substrate, which does not have the 5-aza-cytosine modification responsible for the formation of a covalent bond (B). FCCS analysis showed a significant cross-correlation between the two DNA labels only in case (A), revealing that Dnmt1 can indeed form covalent bonds with at least two different DNA substrates.

FCCS analysis of the two experiments showed a large cross-correlation between all three possible labels in case (A), where both DNA-ATTO550 and DNA-ATTO700 contained the 5-aza-cytosine. In case (B), however, a significant cross-correlation was only observed between GFP-Dnmt1 and DNA-ATTO700, which was the only trapping DNA strand in this experiment. Only a very small, residual cross-correlation could be observed between GFP-Dnmt1 and the binding DNA-ATTO550 strand or between the two DNA labels, possibly caused by a small, remaining contamination with aggregated proteins. However, the great difference between the two experiments leads to the conclusion that Dnmt1 indeed binds covalently to both DNA strands. To further solidify this surprising result, the previous experiments were repeated with an additional Guanidinium chloride (*GdCl*) denaturation step, which is expected to break any non-covalent bonds (Table 6.5)

Protein	DNA Substrates	CC pairing	FCCS (before <i>GdCl</i> )	FCCS (after <i>GdCl</i> )
GFP-Dnmt1	binding + trapping	GFP/ATTO550	-	-
		GFP/ATTO700	+	+
		ATTO550/ATTO700	-	-
GFP-Dnmt1	2× trapping	GFP/ATTO550	+	+
		GFP/ATTO700	+	+
		ATTO550/ATTO700	+	+
GFP-Dnmt1 (C1229W)	binding + trapping	GFP/ATTO550	(-)	-
		GFP/ATTO700	(-)	-
		ATTO550/ATTO700	(-)	-
GFP-Dnmt1 (C1229W)	2× trapping	GFP/ATTO550	(-)	-
		GFP/ATTO700	(-)	-
		ATTO550/ATTO700	(-)	-

**Table 6.5:** Summary of the assays performed to identify the nature and location of the bond between Dnmt1 and the two DNA strands. Dnmt1 was incubated either with differently labeled trapping and binding DNA strands, or with two differently labeled trapping DNA strands. FCCS analysis was performed before and after denaturation of the complexes by 6 M *GdCl*. "+" indicates the presence and "-" the absence of a non-zero cross-correlation amplitude. A "(-)" with brackets marks results where a small cross-correlation amplitude could be observed, probably caused by residual aggregation effects. Denaturation did not affect the bond in any case. The complete set of experiments was repeated with the catalytically inactive GFP-Dnmt1<sup>C1229W</sup> mutant. Here, no cross-correlation whatsoever could be observed.

*GdCl* denaturation did not change the previous results in any case, consistent with the formation of two covalent bonds between Dnmt1 and the DNA substrates. The experiments were also performed with the catalytic site mutant GFP-Dnmt1<sup>C1229W</sup> [47] in order to search for a possible second covalent binding site. In contrast to the previous results, this mutant did not form any covalent bonds, not even with one DNA strand, suggesting that both covalent bonds are formed at the site of the enzymatic reaction.

## 6.9 Discussion

In this study, the interaction of Dnmt1 with trapping DNA substrates was investigated with various fluorescence fluctuation spectroscopy methods.

Considerable efforts were undertaken to carefully select the analysis method best suited for the experimental situation. For the synthetic ATTO 565 fluorophore and for the fluorescent protein GFP, a quantitative comparison between PCH, FIDA, FCA, and FCS brightness analysis was undertaken. In every experiment, FIDA proved far superior to PCH and FCS both in terms of how well the data were fitted and regarding the accuracy of the resulting brightness values. Furthermore, the worse the data quality, for example due to photophysical effects, the greater the difference between the methods (Figures 6.4 and 6.7, Table 6.3).

FCA, the only method that does not involve a nonlinear regression algorithm, in general yielded very accurate results as well, that were in most cases very similar to those determined with FIDA. This appears somewhat surprising, since the method is so simple and easy to use. However, when more than one fluorescence species was analyzed, the FIDA results were the most reliable, especially when the volume parameters were left free during the two component fit

(Table 6.4 and Figure 6.7).

The impact of photophysical effects such as photobleaching were studied for GFP. An adequate laser excitation power of 40 – 50  $\mu$ W was carefully selected, finding a compromise between the need to minimize photophysical effects and at the same time collecting enough fluorescent photons to gain sufficient statistics for the different analysis methods in a reasonable time (Figure 6.2, Table 6.3). Furthermore, the possibility that photophysical effects or a poor folding efficiency of the fluorescent proteins prevent FCCS measurements with GFP and RFP was excluded by measuring a GFP-RFP-Dnmt1 construct, although a considerable influence of the laser excitation power on the amplitude of the cross-correlation function was observed (Figure 6.9).

The question whether Dnmt1 is present in monomeric or dimeric form during the enzymatic reaction was addressed with different brightness analysis methods and fluorescence cross-correlation spectroscopy. Brightness analysis results with GFP-labeled Dnmt1:DNA constructs indicated monomeric Dnmt1 (Table 6.4), although the results remained somewhat ambiguous. Therefore an FCCS assay was designed to answer this question unambiguously. GFP-Dnmt1 and RFP-Dnmt1 were co-expressed, purified via either GBP or RBP, and analyzed with FCS and FCCS. No cross-correlation could be observed, showing that Dnmt1 is monomeric at least in the absence of DNA substrates. Furthermore, when purified via GBP, almost no RFP-Dnmt1 was present and vice versa, indicating that the monomeric state was not a consequence of the low sample concentrations during the spectroscopic experiments (Figure 6.8).

During the brightness analysis experiments, it became apparent from the brightness of the DNA labels that more than one DNA strand was present in the Dnmt1:DNA complexes (Table 6.4). To test this hypothesis, another FCCS assay was performed. GFP-Dnmt1 was simultaneously incubated with two differently labeled DNA strands, DNA-ATTO550 and DNA-ATTO700. A significant cross-correlation was present between GFP and either of the ATTO labels, verifying the successful enzymatic reaction between Dnmt1 and both DNA strands. More importantly, a significant cross-correlation was also present between the two ATTO labels, showing that at least two DNA strands were present in the Dnmt1:DNA complexes (Figure 6.10).

Since the finding of complexes from monomeric Dnmt1 and multiple DNA substrates was somewhat unexpected, aggregation had to be ruled out as a possible cause of measurement artifacts both in brightness analysis and FCCS. Therefore, an extensive assay was designed, where the complexes were purified by size exclusion chromatography, and several of the resulting sample fractions were analyzed with FCCS separately from each other (Figure 6.11). These experiments yielded two important results. First, a large amount of molecular aggregates was found in the sample, possibly caused by the relatively long incubation at 37°C. This result is backed up by earlier observations of the fluorescent trace (Figure 6.6), which exhibited unusually large fluorescence fluctuations on extreme time scales and very bright fluorescence peaks. Second, in the purified, aggregation free sample, the cross-correlation between the two DNA labels ATTO 550 and ATTO 700 was persistent and hence not caused by aggregation.

The somewhat implausible suspicion that new aggregates were formed in the short time span between size exclusion chromatography and the fluorescence spectroscopy experiments, a control experiment was performed where Dnmt1:DNA-ATTO550 and Dnmt1:DNA-ATTO700 complexes were incubated after separate purification via size exclusion chromatography. In this case, no cross-correlation was observed between ATTO 550 and ATTO 700 (Figure 6.12).

To further investigate the nature of the two bonds between Dnmt1 and the DNA substrates, GFP-Dnmt1 was incubated with two different types of substrate DNA: a trapping DNA sample, labeled with ATTO 700, and a binding DNA sample, labeled with ATTO 550, that lacked the 5-aza-cytosine modification responsible for the trapping reaction forming the covalent bond. This assay resulted in the finding that only GFP-Dnmt1:DNA-ATTO700 complexes were formed. Cross-correlation could be observed neither between ATTO550 and GFP, nor between ATTO550 and ATTO700, which provided evidence that all bonds were of covalent nature (Figure 6.13). To confirm these findings, the samples were exposed to 6 M *GdCl*, a strong denaturant, and none of the results were altered (Table 6.5).

To identify a possible second reaction site within the Dnmt1 structure, the above experiment was repeated with the catalytically inactive Dnmt1<sup>C1229W</sup> mutant. However, this mutant did not bind to any of the DNA substrates, neither binding nor trapping, suggesting that only a single residue within the protein is responsible for the enzymatic reaction. This is, on the one hand, not surprising, since one catalytic site is known for Dnmt1 that can form a covalent bond with the trapping DNA substrates. On the other hand, the formation of two covalent bonds at the catalytic site is unexpected and a solid biochemical explanation of the underlying mechanisms is still necessary.

In conclusion, in this study, evidence was found that monomeric Dnmt1 forms covalent bonds with two trapping DNA substrates simultaneously. These results are very surprising and, since their impact on the view of Dnmt1 function would be dramatic, have to be confirmed and further investigated.

## 7 Burst Analysis study of conformational changes of BiP

The contents of this chapter have been published in [54].

### 7.1 BiP

Molecular chaperones play an important role in the cellular cycle by aiding protein folding, transport, and quality control. One important group of molecular chaperones are the heat shock proteins (Hsp), which are overexpressed under conditions of cellular stress (hence their name), and particularly the family of the Hsp70 chaperones, named after their molecular weight. Hsp70s are ATPases that are present in all domains of life such as archaea, eubacteria, and eukaryotes, and even in some organelles such as mitochondria and chloroplasts [55]. The *immunoglobulin heavy chain binding protein* (BiP) is the only Hsp70 present in the endoplasmic reticulum (ER) [56], where it interacts with a variety of substrate proteins. It supports their folding and assembly and plays a key role in the ER stress adaptability [57]. BiP is translocated into the ER via an N-terminal import sequence which is cleaved upon arrival. It interacts with its substrates both during their translocation into the ER and in the lumen of the ER. Due to the wide range of substrate proteins, it has to recognize a highly diverse set of substrate proteins in the unfolded or non-native state. One of its most important substrates is the unassembled immunoglobulin heavy chain, whose major binding site is located within the C<sub>H</sub>1 domain, which is an intrinsically disordered protein and unfolded in the absence of the immunoglobulin light chain [58, 59]. The main binding motif could be identified as a stretch of seven amino acids (HTFPAVL) forming a group of hydrophobic residues [60, 61]. The interaction of BiP with both the entire C<sub>H</sub>1 domain as a representative substrate and the isolated HTFPAVL peptide chain as the isolated binding motif are promising subjects of investigation.

A crystal structure of BiP has not yet been determined. However, there are several close homologue proteins whose structure has been resolved such as Sse1 (Figure 7.1). Like all Hsp70 proteins, BiP exhibits a two-domain structure consisting of an N-terminal nucleotide binding domain (NBD), connected by a flexible hydrophobic linker to the substrate binding domain (SBD). The SBD consists of a compact  $\beta$ -sandwich domain with a hydrophobic cleft for substrate binding, and the  $\alpha$ -helical *lid* at the C-terminal end [62].

In this chapter, the conformational transitions underlying the function of BiP are analyzed by single molecule FRET experiments. Conformational changes in the presence or absence of different nucleotides, the discrimination between different types of substrates such as the entire C<sub>H</sub>1 domain and the isolated HTFPAVL peptide chain, and the influence of the co-chaperone ERdj3 [63] on the BiP conformation are monitored.

## 7.2 Sample preparation

Expression and purification of BiP, C<sub>H</sub>1, and ERdj3, in *Escherichia Coli* cells (BL21 star, Invitrogen, Darmstadt, Germany), and the labeling of BiP were performed by M. Marcinowski in the lab of J. Buchner at the TU München. A short summary of the methodology will be given here; for a more detailed description, refer to [54].

Murine BiP and ERdj3 with an N-terminal 6x-His tag and a TEV protease cleavage site were expressed in inclusion bodies. After lysis, the supernatant was purified with a Ni-NTA FF column. In the case of ERdj3, purification was performed under denaturing conditions followed by refolding, because ERdj3 misfolds in *Escherichia coli* due to the lack of a redox system which is present in the ER, the natural environment for this protein. Elution from the Ni-NTA beads was performed by a buffer carrying 1 M imidazole, followed by a second purification step via size-exclusion chromatography and cleavage of the His-tag with TEV-protease in *HKM-buffer* (50 mM Hepes/KOH pH 7.5, 150 mM KCl, 10 mM MgCl<sub>2</sub>)<sup>1</sup>. The TEV-protease and the uncleaved remainders were filtered out by a Ni-NTA FF column, leaving the protein in HKM buffer for labeling and storage. For BiP labeling (Figure 7.1), double Cys mutants were incubated for 1 h at room temperature with equal amounts of ATTO 532 and ATTO 647 with a tenfold excess of label in total, followed by purification via size exclusion chromatography.

C<sub>H</sub>1 was expressed in inclusion bodies. After lysis in a denaturing Tris/HCl buffer with 10 mM  $\beta$ -mercaptoethanol, 10 mM EDTA, and 8 M urea, the solution was purified in an ion exchange column (Q-Sepharose, GE Healthcare, München, Germany). After partial refolding (C<sub>H</sub>1 remains intrinsically disordered in absence of its binding partner C<sub>L</sub>, but its internal disulfide bridge is formed) by dialysis [64], a second purification step by a Superdex 75pg gel filtration column (GE Healthcare) was applied. For further details on C<sub>H</sub>1 production, refer to [59]. The HTFPAVL peptide was purchased from Biomatik (Wilmington, USA).

The labeled proteins were incubated in micromolar concentrations at 37°C in the respective environments: HKM buffer with or without 1 mM of ADP or AMP-PNP (15 min), HKM buffer with 1 mM ADP and either  $> 14\mu\text{M}$  C<sub>H</sub>1 or  $> 70\mu\text{M}$  HTFPAVL binding peptide (120 min), or HKM buffer with  $5\mu\text{M}$  ERdj3 and 1 mM of different nucleotides (15 min). The respective dissociation constants were determined to be well below those concentrations, and in particular they were similar for C<sub>H</sub>1 ( $K_d = 7.4 \pm 0.2\mu\text{M}$ ) and the HTFPAVL peptide ( $K_d = 11.6 \pm 0.6\mu\text{M}$ ) [54]. For single molecule experiments, the labeled protein was diluted with HKM buffer to a final concentration that was carefully adjusted in several iterations by repeatedly diluting it and observing the frequency of fluorescence bursts on the confocal system, until a number of only a few bursts per second was achieved to ensure a minimal probability of multimolecular events. The respective concentrations of nucleotides, substrates, and ERdj3 were held constant during dilution. A volume of approximately 200  $\mu\text{l}$  was filled into a chamber of an eight-well Lab-Tek chambered coverglass slide (NUNC A/S, Roskilde, Denmark). These containers have proven to be free of contamination with fluorescent material and their lid effectively prevents sample evaporation during the measurement time, which often lasted an hour or more. To avoid adhesion of the sample to the glass surface of the container, it was coated beforehand with bovine serum albumin when necessary. All measurements were performed with the two-color PIE multi-parameter setup introduced in Section 3.4.1.

---

<sup>1</sup>A HEPES based buffer was chosen because experiments showed that Tris leads to BiP aggregation. The use of PBS was precluded because the phosphate would intervene with BiP as an ATPase. The composition and concentration of the different salts were chosen as close as possible to native conditions while still keeping BiP stable.

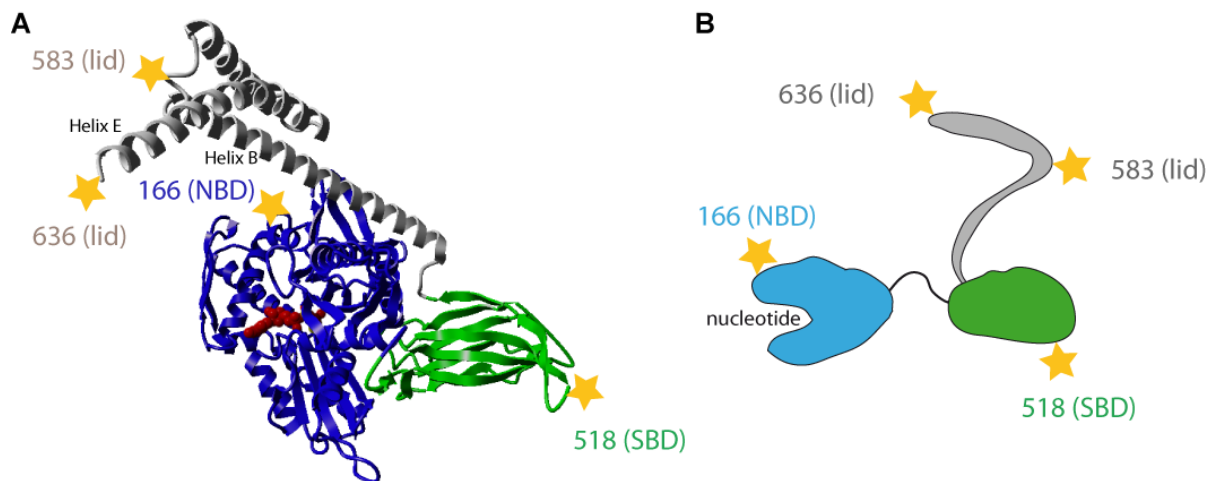


**Figure 7.1:** (A) Crystal structure of the BiP homologue protein Sse1 and (B) a schematic representation of BiP. The two-domain structure (shown in blue and green) and the  $\alpha$ -helical lid (in gray) are visible. The sites of the cysteine mutations used for labeling are indicated by stars.

All recorded events were sorted into two-dimensional histograms of FRET efficiency  $E$  versus stoichiometry  $S$  (Section 4.10.1). Complexes that were labeled with either donor only ( $S = 1$ ) or acceptor only ( $S = 0$ ) fluorophores were discarded. From the remaining events, another fraction was discarded when there was a large difference in burst duration between donor fluorescence and acceptor fluorescence, which is a strong indication of photobleaching of a fluorophore. For each individual experiment, a minimum of 1000 events after this preselection process was collected. One dimensional FRET histograms of the remaining events were further analyzed with PDA (Section 4.11).



### 7.3 Monitoring BiP conformations

Four different double-cysteine mutants were engineered to gain insight into the functionally relevant conformational changes of BiP (Figure 7.1):

- (166/518): The labeling position 166 is located on the NBD, and 518 on the  $\beta$ -sheet of the SBD. Therefore, with this mutant the inter-domain distance can be monitored.
- (518/583) and (518/636): The labeling positions 583 and 636 are both located on different positions of the lid and thus capable to yield information on the lid position relative to the SBD.
- (166/636): The lid position relative to the NBD could be observed.

The anisotropy of neither donor nor acceptor changed significantly upon binding of nucleotides, substrates, and/or ERdj3 (Table 7.1), showing that the rotational freedom of the fluorescent labels was not affected by any of the binding partners. The observed changes in the FRET efficiency are therefore solely based on changes in donor-acceptor distance.

		<b>ATTO 532</b>		<b>ATTO 647</b>	
		$r_\infty$	$\langle r \rangle$	$r_\infty$	$\langle r \rangle$
(166/518)	apo	0.06	0.10	0.19	0.21
(166/518)	ADP	0.04	0.10	0.18	0.21
(166/518)	AMP-PNP	0.04	0.08	0.19	0.22
(166/518)	Peptide/ADP	0.04	0.08	0.20	0.21
(166/518)	CH1/ADP	0.04	0.09	0.18	0.21
(166/518)	ERdJ3/apo	0.07	0.12	0.21	0.24
(166/518)	ERdJ3/ADP	0.07	0.12	0.22	0.25
(166/518)	ERdJ3/AMP-PNP	0.07	0.12	0.22	0.24
(166/518)	ERdJ3/ATP	0.10	0.13	0.22	0.25
(518/636)	apo	0.09	0.14	0.20	0.23
(518/636)	ADP	0.07	0.12	0.19	0.23
(518/636)	AMP-PNP	0.05	0.09	0.20	0.23
(518/636)	Peptide/ADP	0.06	0.11	0.19	0.23
(518/636)	CH1/ADP	0.06	0.10	0.20	0.24
(518/636)	ERdJ3/apo	0.06	0.12	0.23	0.25
(518/636)	ERdJ3/ADP	0.04	0.07	0.22	0.25
(518/636)	ERdJ3/AMP-PNP	0.04	0.08	0.20	0.24
(518/636)	ERdJ3/ATP	0.04	0.08	0.21	0.25
(166/636)	apo	0.05	0.08	0.27	0.28
(166/636)	ADP	0.04	0.07	0.23	0.28
(166/636)	AMP-PNP	0.01	0.04	0.21	0.27
(166/636)	Peptide/ADP	0.03	0.07	0.26	0.29
(166/636)	CH1/ADP	0.02	0.07	0.22	0.28
(518/583)	apo	0.06	0.11	0.18	0.21
(518/583)	ADP	0.05	0.10	0.19	0.21
(518/583)	AMP-PNP	0.02	0.06	0.18	0.21
(518/583)	Peptide/ADP	0.01	0.09	0.19	0.22
(518/583)	CH1/ADP	0.03	0.07	0.19	0.22

**Table 7.1:** The time-resolved fluorescence anisotropy was measured in the presence and absence of nucleotides, substrates, and/or ERdJ3 for both donor and acceptor. The time-resolved anisotropy was numerically integrated to calculate the steady-state anisotropy  $\langle r \rangle$ . An exponential function was fitted to determine the residual anisotropy  $r_\infty$  that represents the rotation of the protein complex, which is much slower than the fluorescence lifetime  $\tau$  of the ATTO fluorophores.

### 7.3.1 Inter-domain communication

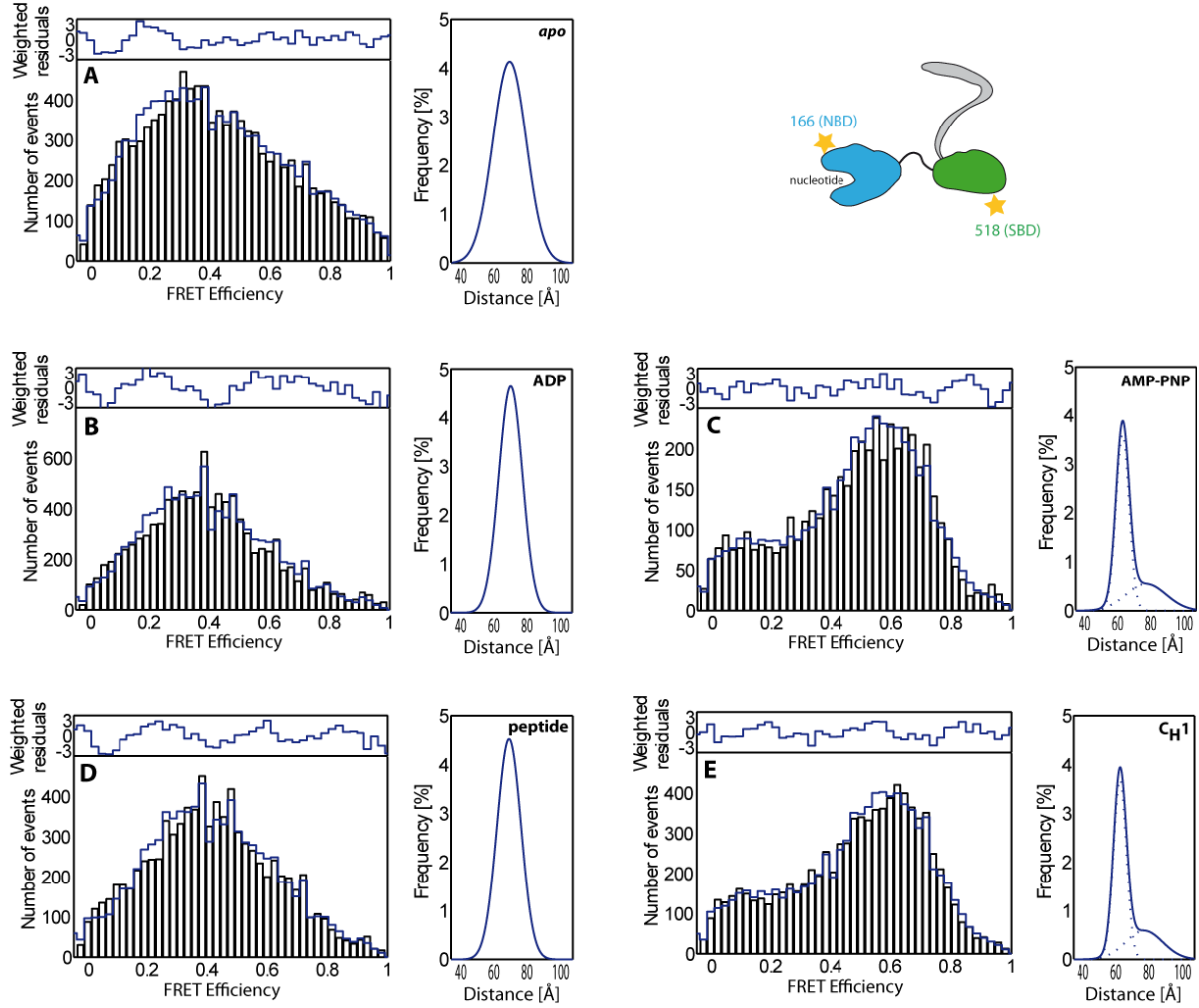


**Figure 7.2:** Single molecule FRET distributions and PDA distance fit results for the (166/518) mutant in the absence of nucleotides (A), in the presence of ADP (B), in the presence of AMP-PNP (C), in the presence of the HTFPAVL peptide substrate and ADP (D), and in the presence of the  $C_H1$  substrate and ADP (E). A domain schematic of BiP is given with the labeling positions indicated.

The distance distribution between the NBD and SBD was observed using the (166/518) mutant. Both the nucleotide-free (apo) state and the ADP state showed a broad distribution of FRET efficiencies centered around  $d \approx 66\text{Å}$  with a width of  $\sigma = 12\text{Å}$  and  $\sigma = 8\text{Å}$  for the apo and ADP-bound states, respectively (Table 7.2, Figure 7.2). Distance distributions with a width on this order are very broad for single molecule FRET experiments, indicating that BiP is highly heterogeneous in these states and adopts multiple conformational substates. In the presence of the non-hydrolyzable ATP analogue AMP-PNP, two distinct populations emerge, indicating a partitioning of BiP between two population with lower and higher inter-domain distances, respectively. The predominant population has a peak donor-acceptor distance of  $d \approx 58\text{Å}$  with a width of  $\sigma = 5\text{Å}$ , which is consistent with a tighter coupling between the domains and less variability compared with the apo and ADP-states. Both findings are in excellent agreement with previous studies on BiP [65]. A second population with a broad distance distribution centered around  $d = 75\text{Å}$  with a width of  $\sigma = 14\text{Å}$  was also present.

In the presence of ADP and the HTFPAVL peptide as a substrate, the center and width of the distance distribution were almost identical to the ADP state. However, when C<sub>H</sub>1 was chosen as substrate in the presence of ADP, a striking difference could be observed. The NBD and SBD come into close contact to each other, and the distance distributions were practically identical to those observed in the ATP-bound state. These findings suggest a so far unknown influence of the substrate on the relative orientation of the NBD and SBD domains.

### 7.3.2 Conformation of the lid

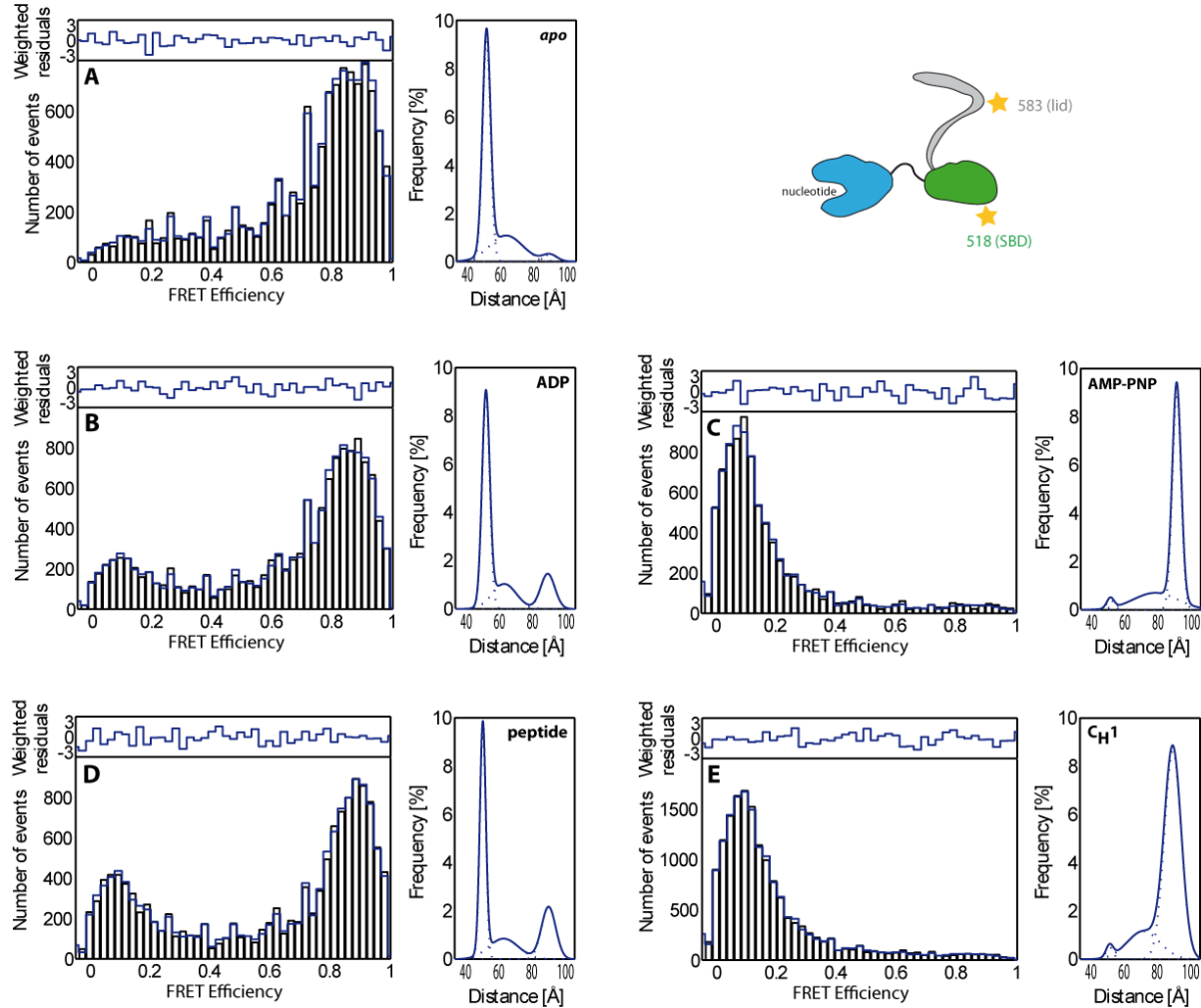


**Figure 7.3:** Single molecule FRET distributions and PDA distance fit results for the (518/583) mutant in the absence of nucleotides (A), in the presence of ADP (B), in the presence of AMP-PNP (C), in the presence of the HTFPAVL peptide substrate and ADP (D), and in the presence of the C<sub>H</sub>1 domain and ADP (E). A domain schematic of BiP is given with the labeling positions indicated.

Both lid-mutants (518/583 and 518/636) showed similar behavior under all investigated conditions (Tables 7.3 and 7.4, Figures 7.3 and 7.4). In the apo-state, there was a broad variety of conformations that could be divided into three main conformational substates: First, one narrow "closed" state with a mean distance of  $d = 47\text{\AA}$ ,  $\sigma = 4\text{\AA}$  and  $d = 48\text{\AA}$ ,  $\sigma = 3\text{\AA}$  for (518/583) and (518/636), respectively, was observed and was significantly populated in both mutants (64.1% and 41.0%, respectively); second, a very broad intermediate state with dis-

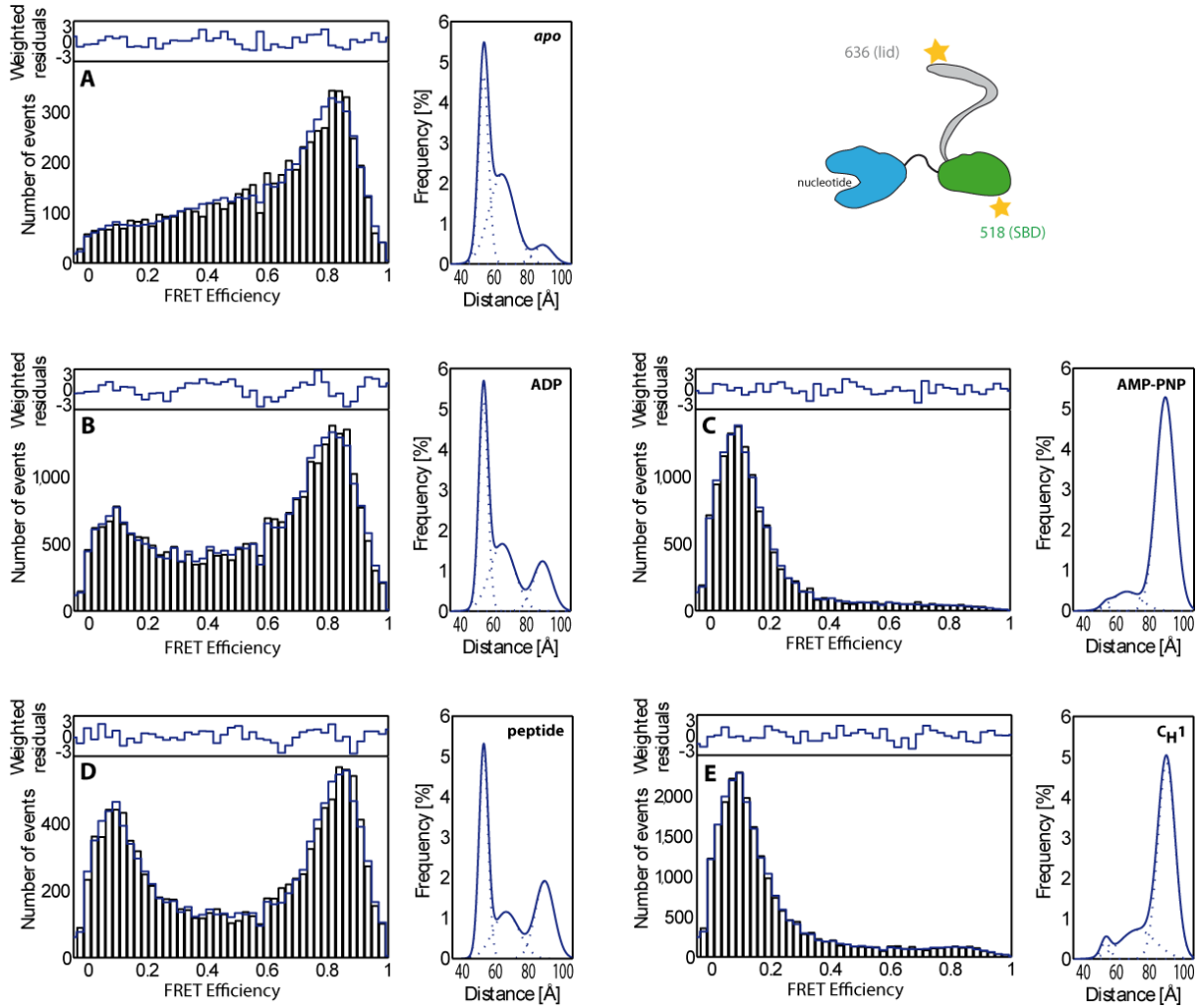


**Figure 7.4:** Single molecule FRET distributions and PDA distance fit results for the (518/636) mutant in the absence of nucleotides (A), in the presence of ADP (B), in the presence of AMP-PNP (C), in the presence of the HTFPAVL peptide substrate and ADP (D), and in the presence of the C<sub>H</sub>1 domain and ADP (E). A domain schematic of BiP is given with the labeling positions indicated.

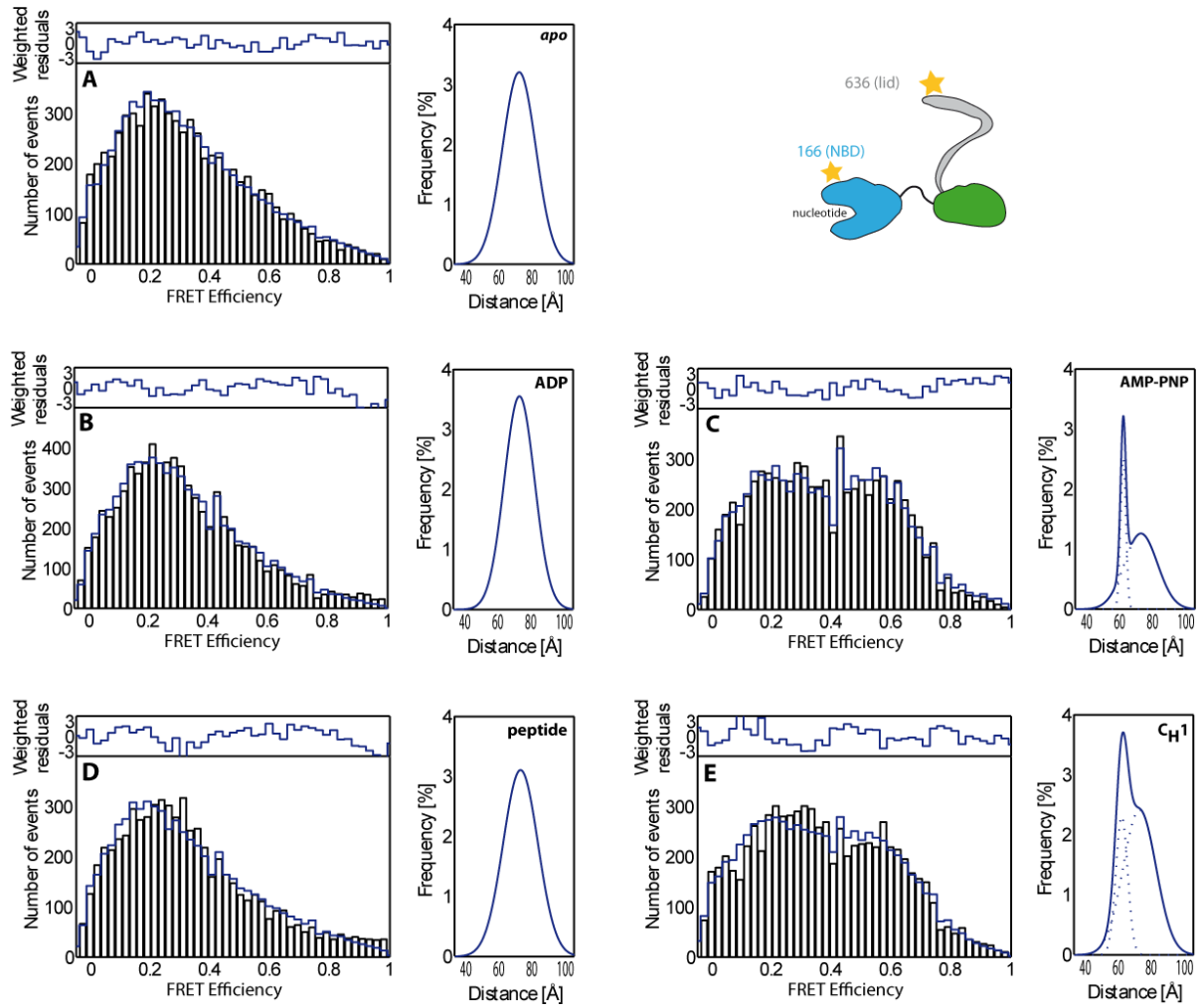


**Figure 7.5:** Single molecule FRET distributions and PDA distance fit results for the (166/636) mutant in the absence of nucleotides (A), in the presence of ADP (B), in the presence of AMP-PNP (C), in the presence of the HTFPAVL peptide substrate and ADP (D), and in the presence of the  $C_H1$  domain and ADP (E). A domain schematic of BiP is given with the labeling positions indicated.

tances around  $d = 60\text{\AA}$ ,  $\sigma = 12\text{\AA}$  and  $d = 61\text{\AA}$ ,  $\sigma = 9\text{\AA}$ , was also significantly populated (31.5% and 50.0%, respectively); and a third, "open" conformation with distances centered around  $d = 91\text{\AA}$ ,  $\sigma = 5\text{\AA}$  and  $d = 90\text{\AA}$ ,  $\sigma = 7\text{\AA}$  was observed that was sparsely populated (3.6% and 7.7%, respectively). The observation of three substates is in agreement with what was found for the bacterial Hsp70 member DnaK in [66] using fixation of lid elements to the  $\beta$ -sheet and electron paramagnetic resonance spectroscopy with spin labels in lid and  $\beta$ -sheet. The very broad distribution observed for the intermediate state suggests dynamic fluctuations between the open and closed conformations. However, on the millisecond timescale that is accessible by burst analysis measurements, no evidence for dynamics could be found using a technique introduced in [36].

The addition of ADP led to only minor changes, as was already the case for the inter-domain conformation (Section 7.3.1). The binding of AMP-PNP however, shifts the majority of molecules into the open-lid state, leaving only a minor fraction in the closed-lid conformation.

Additionally, the position of the lid relative to the NBD was monitored using the (166/636) mutant (Table 7.4, Figure 7.5). Again, a nearly identical, broad distribution was measured for the apo and ADP states, centered around  $d \approx 72\text{\AA}$  with a width of  $\sigma \approx 12\text{\AA}$ , indicating a high heterogeneity under these conditions. In the AMP-PNP bound state, a second narrow population could be observed that was centered around  $d = 59\text{\AA}$  and  $\sigma = 2\text{\AA}$ .

In the presence of the HTFPAVL peptide and ADP, the same results were observed for the lid mutants (518/583 and 518/636) as in the ADP-only state: For the majority of the molecules, the lid was closed. A second population with a broad intermediate state comprised approximately a third of the molecules. When the C<sub>H</sub>1 domain was added, however, the open state became the predominant population, just as in the AMP-PNP-bound state. Similarly, for the NBD/lid mutant (166/636), the peptide-bound state showed no significant differences to the ADP state, whereas with C<sub>H</sub>1, a second, narrow population emerged similar to what was observed with AMP-PNP.

In summary, a very consistent picture emerged for all mutants. The nucleotide state of the NBD regulates both the relative position of the NBD to the SBD and the conformation of the lid in a concerted way. The NBD and SBD are in relatively loose contact in the ADP bound state, and the lid is closed. Binding of AMP-PNP leads to a compaction of the NBD and SBD and, in a concerted movement, the lid is opened. When a short polypeptide is bound, the protein stays in the ADP-bound conformation, whereas upon binding of C<sub>H</sub>1, the AMP-PNP-bound state is observed.

## 7.4 The co-chaperone ERdJ3

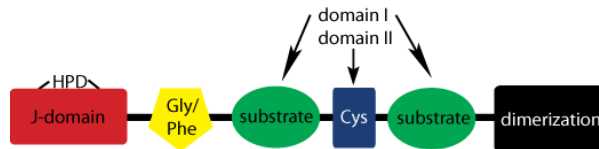


**Figure 7.6:** Domain schematic of the Hsp40 co-chaperone ERdJ3.

An important aspect for understanding the mechanism of BiP and other Hsp70 proteins is the influence of the major class of co-chaperones, the Hsp40/J-proteins. The BiP co-chaperone ERdJ3 is an important component of the BiP/Ig folding complex in the ER [67]. It is highly abundant in the ER lumen and is up-regulated under ER-stress conditions. It consists of four domains (Figure 7.6), of which the N-terminal *J-domain* binds to the interface between the BiP NBD and SBD in the presence of ADP with a dissociation constant of  $k_d = 0.9 \pm 0.1\mu M$ . Furthermore, hydrophobic residues in domains I and II are responsible for ERdJ3 binding to C<sub>H</sub>1 with a  $k_d = 0.2\mu M$ . It is known that ERdJ3 transfers substrate proteins to BiP [63], but the underlying mechanism for this transfer reaction is currently not clearly understood. ATPase assays showed that the binding of ERdJ3 to BiP leads to an increase in ATP hydrolysis [68]. To elucidate and monitor the influence of ERdJ3 on the conformation of BiP, two of the FRET mutants described in the previous sections were chosen: the inter-domain mutant (166/518) and one of the lid mutants (518/636).

		Subpopulation 1			Subpopulation 2			Subpopulation 3			Donor only	$\chi^2$
		%	$d[\text{\AA}]$	$\sigma[\text{\AA}]$	%	$d[\text{\AA}]$	$\sigma[\text{\AA}]$	%	$d[\text{\AA}]$	$\sigma[\text{\AA}]$	%	
(166/518)	apo	97.0	66	12	-	-	-	-	-	-	3	2
(166/518)	ADP	96.4	67	8	-	-	-	-	-	-	3.6	4.8
(166/518)	AMP-PNP	30.9	75	14	66.5	58	5	-	-	-	2.6	2.29
(166/518)	ADP/Peptide	95.3	66	8	-	-	-	-	-	-	4.7	2.59
(166/518)	ADP/CH1	30.5	75	13	66.7	58	5	-	-	-	2.7	1.59
(166/518)	ERdJ3/apo	95.5	69	11	-	-	-	-	-	-	4.5	1.87
(166/518)	ERdJ3/ADP	46.9	70	13	48.9	57	5	-	-	-	4.2	1.06
(166/518)	ERdJ3/AMP-PNP	42.4	73	11	55.7	58	5	-	-	-	1.9	0.92
(166/518)	ERdJ3/ATP	26.2	73	14	72.4	57	5	-	-	-	1.4	1.52
(166/518)	ERdJ3 domain/ADP	96.1	68	8	-	-	-	-	-	-	3.9	6.35
(166/518)	ERdJ3 QPD / ADP	37.3	72	11	60.8	58	4	-	-	-	1.9	1.5
(166/518)	ERdJ3/CH1/ATP	58.8	70	11	36.9	56	3	-	-	-	4.3	0.72

**Table 7.2:** PDA fit results for the inter-domain mutant (166/518) in the presence and absence of nucleotides, substrates, and/or ERdJ3. For each distribution, the percentage of molecules occupying it is given (%) as well as its peak distance  $d$  and width  $\sigma$ .



		Subpopulation 1			Subpopulation 2			Subpopulation 3			Donor only	$\chi^2$
		%	$d[\text{\AA}]$	$\sigma[\text{\AA}]$	%	$d[\text{\AA}]$	$\sigma[\text{\AA}]$	%	$d[\text{\AA}]$	$\sigma[\text{\AA}]$	%	
(518/636)	apo	7.7	90*	7*	41.0	48	4	50.0	61	9	1.3	1.36
(518/636)	ADP	20.4	90*	7*	41.4	49	3	36.7	62	9	1.5	2.77
(518/636)	AMP-PNP	87.3	90	7	0.9	48*	3*	11.8	63	10	0	1.03
(518/636)	ADP/Peptide	31.8	90*	7*	40.6	47	3	26.4	63	9	1.1	1.85
(518/636)	ADP/CH1	74.1	91	6	3.4	48*	3*	22.5	71	13	0	1.78
(518/636)	ERdJ3/apo	9.0	94*	8*	47.6	49	4	42.7	63	9	0.8	2.26
(518/636)	ERdJ3/ADP	78.5	93	8	4.5	49*	4*	17.0	64	9	0	1.77
(518/636)	ERdJ3/AMP-PNP	74.9	95	9	3.7	49*	4*	21.4	68	11	0	1.82
(518/636)	ERdJ3/ATP	78.8	94	8	2.3	49*	4*	18.9	67	12	0	1.26
(518/636)	ERdJ3 domain/ADP	12.6	90*	8	50.5	49	3	36.2	64	10	0.7	3
(518/636)	ERdJ3 QPD / ADP	75.6	93	6	3.4	48*	3	21.0	68	11	0	8.85
(518/636)	ERdJ3/CH1/ADP	67.6	87	6	5.5	48*	5	26.9	66	10	0	4.07

**Table 7.3:** PDA fit results for the lid mutant (518/636) in the presence and absence of nucleotides, substrates, and/or ERdJ3. For each distribution, the percentage of molecules occupying it is given (%) as well as its peak distance  $d$  and width  $\sigma$ . Values marked with an asterisk (\*) were fixed during the fit. Parameters were fixed when it was apparent that the data could be fit consistently with the same set of distributions as in a different measurement with comparable label positions, but the relative population of the distribution was insufficient for determining them unambiguously. A small fraction of donor-only molecules was sometimes necessary to fit the data accurately. The third subpopulation that was necessary to fit this mutant was difficult to determine, probably due to the high mobility of the lid, and is therefore shown in gray.

		Subpopulation 1			Subpopulation 2			Subpopulation 3			Donor only	$\chi^2$
		%	$d[\text{\AA}]$	$\sigma[\text{\AA}]$	%	$d[\text{\AA}]$	$\sigma[\text{\AA}]$	%	$d[\text{\AA}]$	$\sigma[\text{\AA}]$	%	
(166/636)	apo	95.5	71	12	-	-	-	-	-	-	4.5	1.33
(166/636)	ADP	96.2	72	11	-	-	-	-	-	-	3.8	2.09
(166/636)	AMP-PNP	74.0	72*	12*	23.9	59	2	-	-	-	2.1	2.29
(166/636)	ADP/Peptide	96.6	72	12	-	-	-	-	-	-	3.4	2.63
(166/636)	ADP/CH1	70.9	72*	12*	24.3	59	4	-	-	-	4.9	2.9
(518/583)	apo	3.6	91*	5*	64.1	47	3	31.5	60	12	0.7	1.03
(518/583)	ADP	18.4	90	5*	59.2	47	3	22.3	60	9	0.1	1.05
(518/583)	AMP-PNP	69.9	93	3	2.7	46*	3*	27.4	78	16	0	1.77
(518/583)	ADP/Peptide	27.4	92	5*	50.3	45	2	22.4	60	11	0	1.85
(518/583)	ADP/CH1	77.9	91	6	1.9	46*	3*	20.3	70	12	0	1.49

**Table 7.4:** PDA fit results for the mutants (166/636) and (518/583) in the presence and absence of nucleotides and substrates. For each distribution, the percentage of molecules occupying it is given (%) as well as its peak distance  $d$  and width  $\sigma$ . Values marked with an asterisk (\*) were fixed during the fit. Parameters were fixed when it was apparent that the data could be fit consistently with the same set of distributions as in a different measurement with comparable label positions, but the relative population of the distribution was insufficient for determining them unambiguously. A small fraction of donor-only molecules was sometimes necessary to fit the data accurately. The third subpopulation that was necessary to fit the lid mutant (518/583) was difficult to determine, probably due to the high mobility of the lid, and is therefore shown in gray.

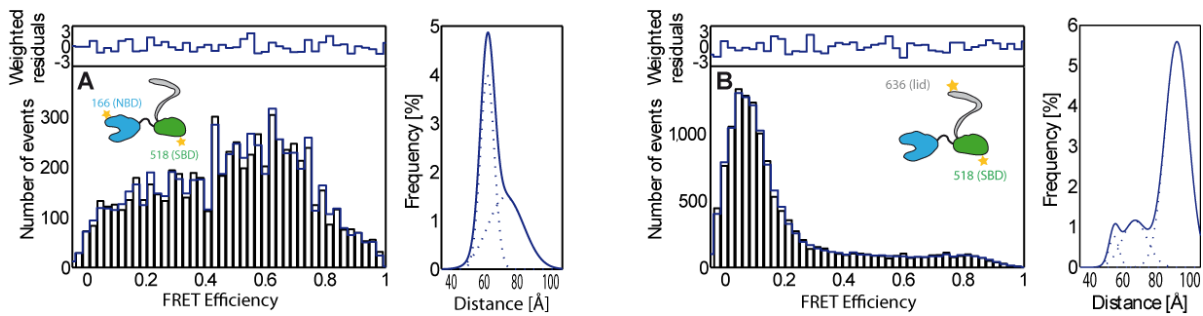


**Figure 7.7:** Single molecule FRET distributions and PDA distance fit results for the (166/518, A) and (518/636, B) mutants in the presence of ERdJ3 and ADP.

In the nucleotide-free state and in the presence of AMP-PNP, the addition of ERdJ3 had no significant effect on the conformation of BiP. In the ADP-state, however, the presence of ERdJ3 caused both mutants to also adopt the states that were observed in the presence of AMP-PNP: for a large population, the inter-domain distance was increased, and the lid was predominantly in the open position (Figure 7.7).

ERdJ3 binds to the NBD/SBD-interface of BiP via an HPD motif in its J-domain. The complete ERdJ3 protein can be replaced by the isolated J-domain, which will also bind to BiP and even induce the same increase in ATP hydrolysis. However, it no longer induced a change in the ADP-state conformation of the protein (Tables 7.2 and 7.3), indicating that the BiP conformations induced by the wild type ERdJ3 are not only due to the binding of the J-domain to the NBD/SBD interface. A second, complementary result was the observation that the QPD mutant of the full length ERdJ3, which does not stimulate the ATPase activity of BiP [54], influenced the BiP conformation the same way as the wild type ERdJ3 (Tables 7.2 and 7.3). ERdJ3 might thus stabilize the BiP- $C_H1$  complex by inducing a conformation potent for protein-substrate binding.

## 7.5 Discussion

The conformational states of the Hsp70 chaperone BiP were analyzed upon nucleotide, substrate, and co-chaperone binding with a single molecule FRET Burst Analysis assay. A strong communication between the NBD and the SBD is characteristic for Hsp70 proteins. Concerted changes between the separation of the NBD and SBD and the conformation of the lid could be observed, leading to two conformational profiles: In the nucleotide-free and the ADP-state, the NBD and SBD are in loose contact and simultaneously the lid adopts a broad variety of conformations that could be divided into three subpopulations. Generally, in the nucleotide-free and the ADP state, the observed FRET distributions tended to be broader, indicating a more heterogeneous structure. In the ATP-state, the NBD and SBD domains come into closer contact, an observation that was previously reported [65], and the lid is wide open (Figure 7.8A). The lid appears to be moving as a single entity as no significant differences could be observed between the mutants (518/583) and (518/636), which had labeling positions in the middle or at the end of the lid.

From these observations, BiP can be characterized as a tripartite molecular machine in which conformational changes are transmitted across the domains, coupling the nucleotide state of the NBD to the opening state of the lid and vice versa. These correlated conformational changes might serve as a relay mechanism for the coupling of the ATPase activity of the NBD to sub-

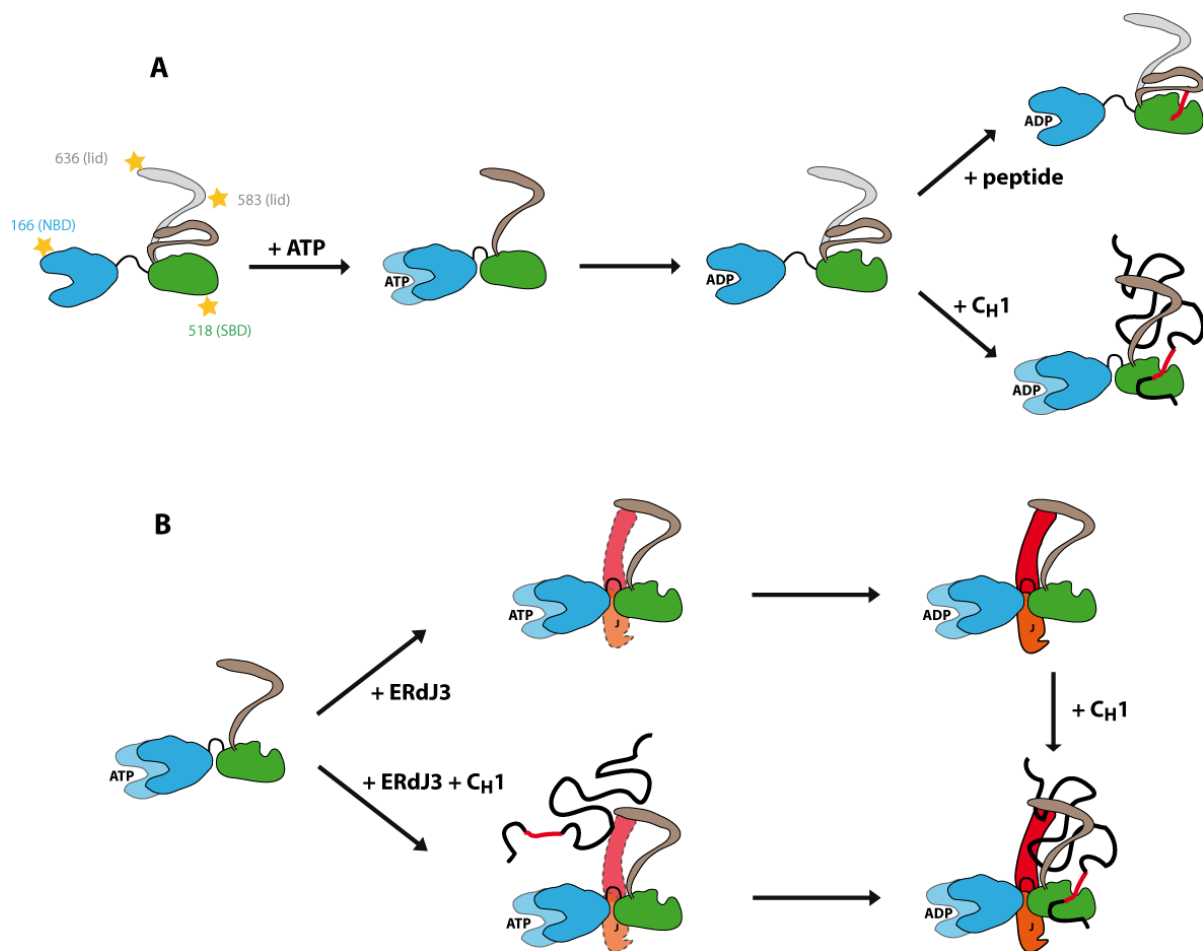


**Figure 7.8:** (A) Conformational changes of BiP for different nucleotide states and substrates. (B) Influence of the co-chaperone ERdj3 on the conformation of BiP in absence or presence of the substrate protein CH1

strate binding in the SBD and the chaperone function.

BiP-substrate interactions were analyzed using either the authentic substrate protein CH1, or a short polypeptide derived from this domain. Although the biochemical parameters such as dissociation constants and the stimulation of the BiP ATPase rates are similar for these two, the conformation of BiP shows a clear discrimination between the substrates (Figure 7.8A). When the peptide is bound, the lid is predominantly in the closed conformation, and accordingly the inter-domain distance increases. In contrast, when CH1 is bound, the lid is found in an open position and the domains are in closer proximity to each other. BiP appears to monitor the nature of the bound substrate, indicating that the open conformation of the lid in the presence of a substrate protein may not only be due to steric hindrance but may also be of functional nature, supporting the substrate binding cleft of the SBD with the chaperone function.

Consistent with the importance of the lid conformation, the conformational changes are regulated by two different mechanisms: First, by the nucleotide binding state of the NBD, and second, by the interaction with the co-chaperone ERdj3. ERdj3 is the predominant Hsp40

co-chaperone in Immunoglobuline folding and is known to bind and transfer substrates to BiP [63]. Analogous to other J-proteins [69], ERdj3 forms a stable complex with the ADP-bound BiP, and strongly influences BiP conformation. ERdj3 induces the open-lid conformation that is also observed when C<sub>H</sub>1 is bound as a substrate. This is in contrast to the mitochondrial Hsp70, where binding of the J-protein does the opposite, inducing in the ATP-bound state a conformation that is normally adopted with ADP [69]. In the ATP-state of BiP, the binding of ERdj3 appeared to have no influence on the conformation (Figure 7.8B). Interestingly, binding of the isolated J-domain of ERdj3 did not induce the described change in the conformation of BiP. A possible explanation is that domain I or II of ERdj3 (Figure 7.6) interacts with BiP in addition to the J-domain, presumably directly with the lid, to keep it in an open conformation (Figure 7.8B). The functional consequence of this hypothesis is that ERdj3 primes ADP-bound BiP for substrate binding by opening the lid. Accordingly, the C<sub>H</sub>1 domain binds faster and stronger to BiP in the presence of ERdj3 while peptide binding is impeded (results not shown). Hence, a mechanistic description of the function of ERdj3 in the BiP chaperone cycle becomes possible (Figure 7.8B): ERdj3 transports substrate proteins to BiP in the ATP-state. During or after stimulated ATP hydrolysis, the substrate protein is transferred to BiP, and in addition to its transfer function, ERdj3 supports the binding between BiP and its substrate by stabilizing the open-lid conformation. The chaperone cycle is completed by the exchange of ADP against ATP and the release of ERdj3 and the bound substrate.

## 8 Summary and Outlook

In this work, a wide spectrum of Fluorescence Fluctuation Spectroscopy (FFS) methods was implemented, optimized, and applied to relevant biophysical systems. Scanning FCS and RICS, two FFS techniques specially suited for live-cell measurements, were combined with Pulsed Interleaved Excitation. The selective crosstalk-free cross-correlation removes the inherent flaw of these methods that showed a non-zero cross-correlation even for non-interacting species. The necessity for an argumentation based on different cross-correlation amplitudes to show molecular binding is omitted, and an immediate, unambiguous statement becomes possible without the need for a binding-free reference measurement. Successful proof-of-principle experiments were performed both in aqueous solutions and in living cells. Fluorophores with correlated and with uncorrelated motion served as positive and negative controls, respectively. The new capabilities of PIE-RICS were then applied by investigating the binding characteristics of Calmodulin to the CaV1.4 calcium channel. The cytosolic part of the channel, labeled with mCherry, was expressed in HEK293 cells together with GFP-labeled Calmodulin. Under the chosen experimental conditions, no binding could be observed. Without PIE, such a clear statement would have been impossible. In a second assay, the inhibitory function of the ICDI domain of the CaV1.4 channel was studied. The GFP-labeled C-terminal part of the CaV1.4 channel without its ICDI domain and the isolated ICDI-domain itself, labeled with mCherry, were expressed in HEK293 cells. Again, no binding could be observed between those two species under the present conditions.

In addition to these correlation-based methods, there are a variety of fluorescence brightness analysis methods: The Photon Counting Histogram (PCH), Fluorescence Intensity Distribution Analysis (FIDA), and Fluorescence Cumulant Analysis (FCA). These methods were carefully evaluated with regard to their reliability and accuracy. FIDA proved to be the best method for brightness analysis, with FCA also delivering accurate results for experiments with only one fluorescent species. Brightness analysis was then applied to the interaction of DNA methyl transferase 1 (Dnmt1) with substrate DNA strands. Dnmt1 was previously suspected to form dimers in the active state. With all brightness analysis methods, however, no dimers were found. Furthermore, brightness analysis indicated multiple DNA substrates per Dnmt1 molecule. This surprising result was further investigated with Fluorescence Cross-Correlation Spectroscopy (FCCS) in combination with PIE. Both the monomeric state of Dnmt1 and the complexation with multiple DNA strands could be confirmed with PIE-FCCS.

As a third application, the conformational changes of the Hsp70 chaperone BiP were investigated using single molecule FRET experiments. BiP consists of the nucleotide binding domain (NBD) and the substrate binding domain (SBD) that includes an alpha-helical lid structure. The distance between the SBD and the NBD was monitored as well as the lid conformation. The influence of different nucleotides, different types of substrates and of the co-chaperone ERdj3 was analyzed. In all cases, a concerted motion between the inter-domain-distance and the lid conformation was observed, indicating a functional relation between the two. BiP assumed two different conformational states upon binding of a large substrate protein ( $C_{H1}$ ) or a short polypeptide chain comprising the binding sequence of the  $C_{H1}$ , enabling it to recognize the nature of a bound substrate. Finally, the co-chaperone ERdj3 was found to prime the conformation of BiP for substrate binding.

To further develop the capabilities of the Fluorescence Fluctuation Spectroscopy methods applied here, a fusion of the the two setups used for this work would be a logical next step. With a three-color multi-parameter setup, FRET experiments as used for this work will become even more powerful, allowing the accurate determination of multiple intra-molecular distances. Furthermore, the extension to four or more different colors would equip the experimentator with the possibility to monitor very closely complex molecular interactions, for example by measuring via FRET the conformational changes of two different proteins binding to each other. The consequence of these developments is, of course, a spectrally resolved confocal setup, one of which is currently built in our group.

Another important trend will be the convergence of different evaluation methods into a powerful multi-parameter analysis. Already now, properties like anisotropy, fluorescence lifetime, dynamic FRET, and the stoichiometry can be extracted from a single molecule burst analysis measurement. Extracting the maximum possible information content from just one measurement should be the goal of further methodical refinements.

# A Spectra

Selecting the right optical interference filters and dichroic mirrors is a key factor in the design of multicolor confocal microscopes. Bringing together aims like an optimal detection efficiency for fluorescence photons and blocking as large portion of the laser light as possible from reaching the detectors is often a difficult task due to overlapping emission spectra and laser lines. Therefore, the transmission spectra of the filters chosen for this work are specified in this appendix.



## A.1 Two-color PIE multi-parameter setup

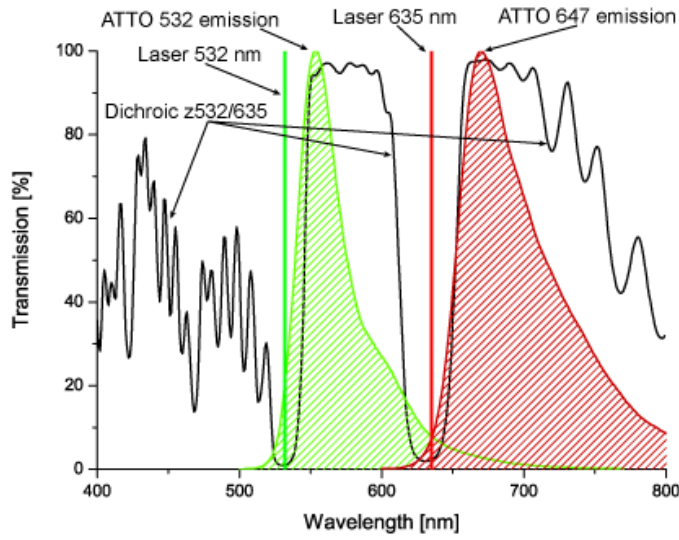


**Figure A.1:** Transmission spectrum for the dichroic mirror DualLine z532/635 (Figure 3.3, D1) that was used to separate excitation from emission light.

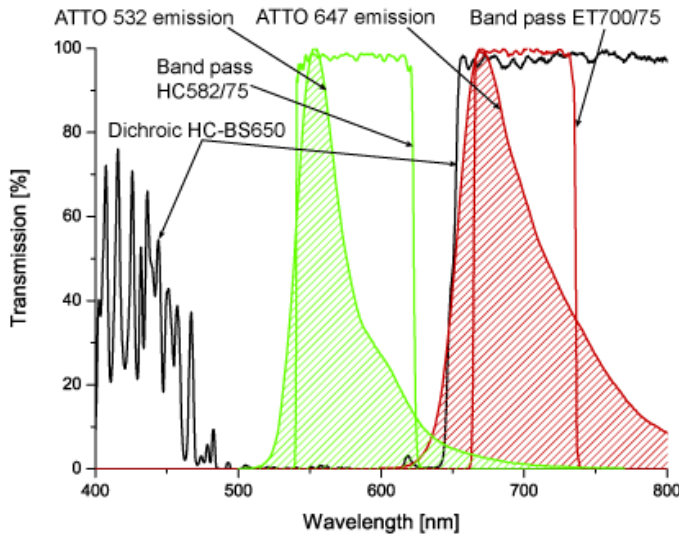


**Figure A.2:** Transmission spectrum for the dichroic mirror HC-Beamsplitter BS650 (Figure 3.3, D2) that was used to separate the fluorescence of the different fluorophores, and of the band pass filters HC582/75 and ET700/75 (Figure 3.3, F1 and F2) used to spectrally select the fluorescence from ATTO 532 and ATTO 647, respectively.

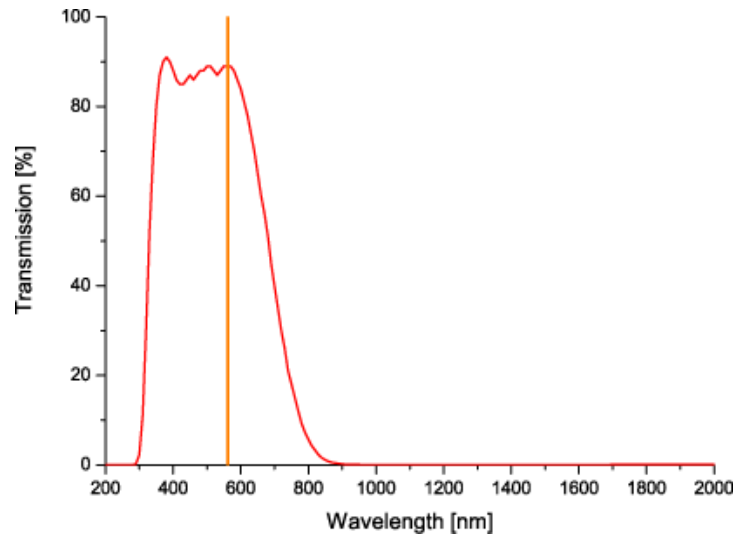


**Figure A.3:** Transmission spectrum for the Schott KG5 infrared short pass filter used to spectrally clean up the 561 nm laser beam, which is contaminated with the infrared supercontinuum.

## A.2 Three-color PIE scanning setup

### A.2.1 Dnmt1 configuration

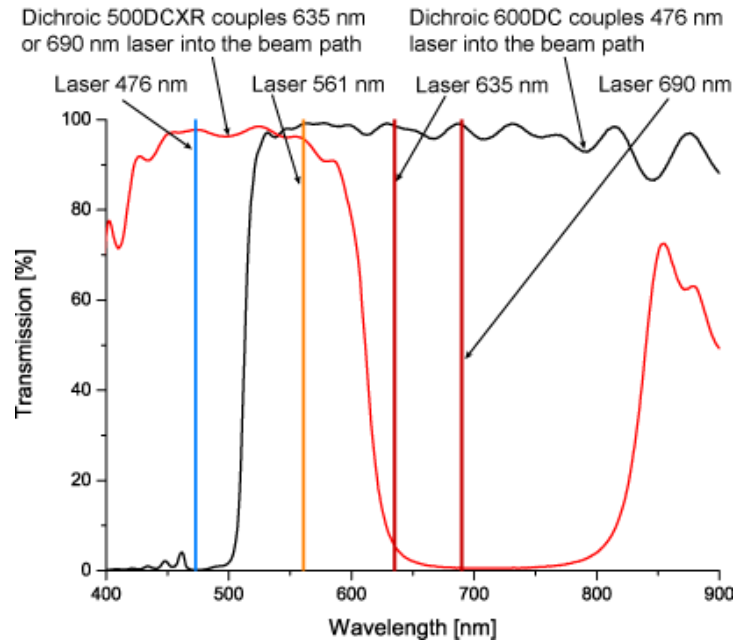


**Figure A.4:** Transmission spectra of the dichroic mirrors 500DCXR and 600DC (Figure 3.4, D1 and D2) that were used to superimpose the laser beams of different wavelengths in both the Dnmt1 and the RICS configuration. The 561 nm laser passes through both dichroic mirrors, each of which reflects one additional wavelength, thereby superimposing it onto the transmitted beam.

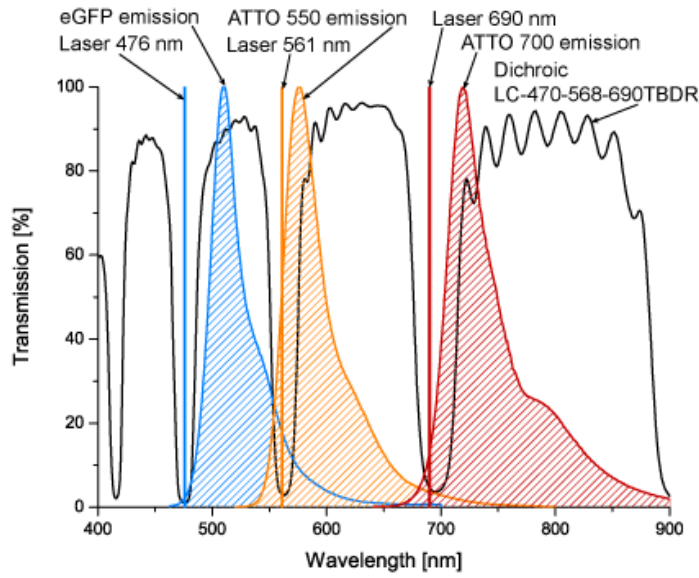


**Figure A.5:** Transmission spectrum of the dichroic mirror LC-470-568-690TBDR (Figure 3.4, D3) that was used to separate excitation from emission light in the Dnmt1 configuration.

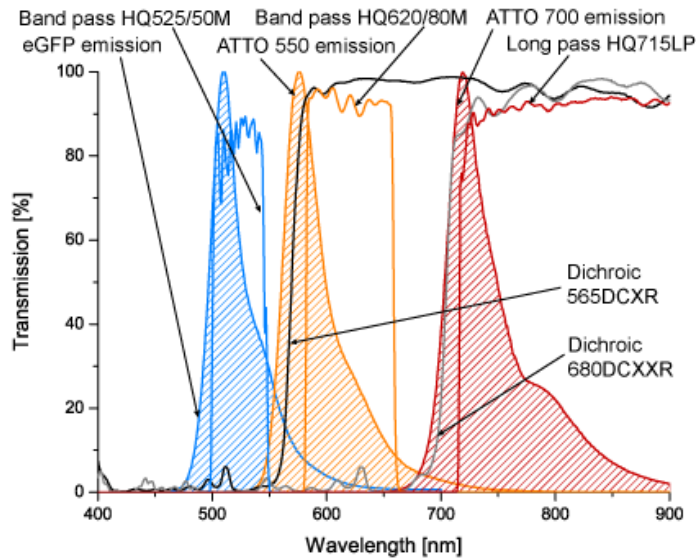


**Figure A.6:** Transmission spectra of the dichroic mirrors 565DCXR and 680DCXXR (Figure 3.4, D4 and D5) that were used to separate the fluorescence of the different fluorophores in the Dnmt1 configuration, and of the band pass filters HQ 525/50 M, HQ 620/80 M, and HQ 715LP, (Figure 3.4, F1, F2, and F3) used to spectrally select the fluorescence from eGFP, ATTO 550, and ATTO 700, respectively.

### A.2.2 RICS configuration

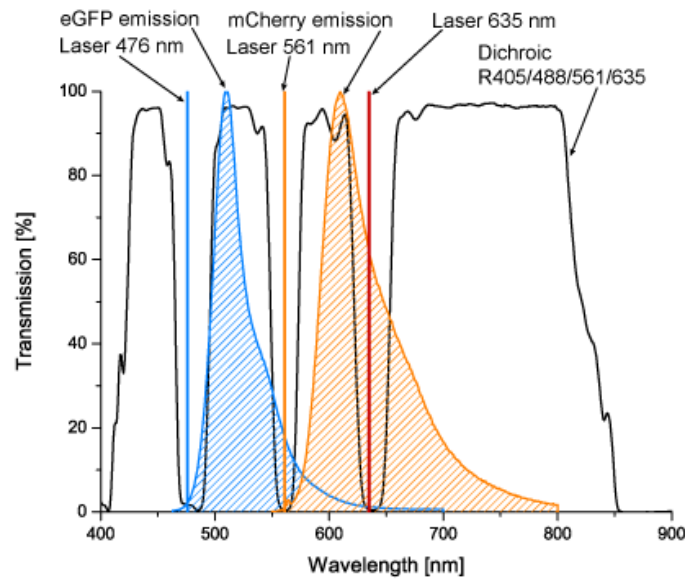


**Figure A.7:** Transmission spectrum of the dichroic mirror R405/488/561/635 (Figure 3.4, D3) that was used to separate excitation from emission light in the RICS configuration.

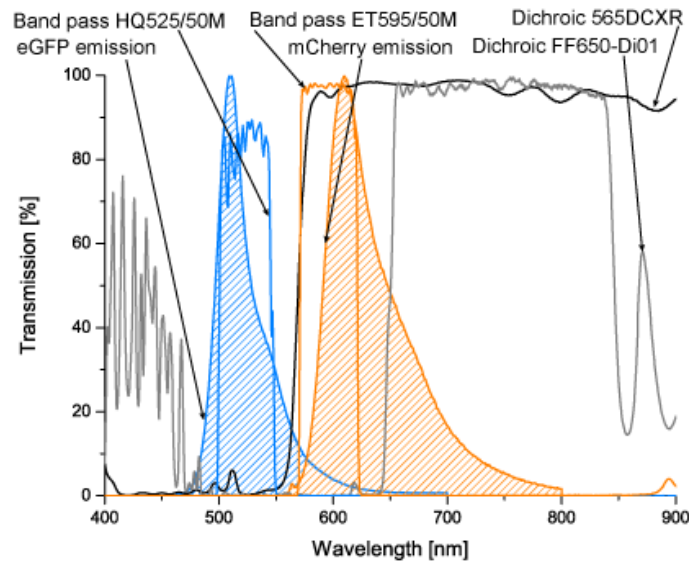


**Figure A.8:** Transmission spectra of the dichroic mirrors 565DCXR and FF650-Di01 (Figure 3.4, D4 and D5) that were used to separate the fluorescence of the different fluorophores in the RICS configuration, and of the band pass filters HQ 525/50 M and ET 595/50 M, (Figure 3.4, F1 and F2) used to spectrally select the fluorescence from eGFP and mCherry, respectively. Note that the second dichroic FF650-Di01 only functions as a mirror in this case due to the lack of use of a third wavelength in the RICS experiments.

## B Computer code

### B.1 Number & Brightness

```
% y contains the fluorescence intensity trace
% averaging_time sets the size of the pieces that are evaluated
% TcspcData.Header.ClockRate/binsize transforms from TCSPC clock tics to seconds

for i = 1:numel(y)/averaging_time
    m = mean(y(averaging_time*(i-1)+1:averaging_time*i));
    v = var(y(averaging_time*(i-1)+1:averaging_time*i));
    number(i) = 2(-3/2)*m2/(v-m);
    brightness(i) = ((v-m)/m*(TcspcData.Header.ClockRate/binsize));
end
```

## B.2 Fast correlation algorithm [1]

```
// determine max macro time
if (t1[np1-1]>t2[np2-1])
{maxmat=t1[np1-1];}
else {maxmat=t2[np2-1];}

// correlate
for (k=0;k<nb;k++) {
  p=0;
  for (i=0;i<np1;i++) {
    if (photons1[i]!=0) {
      if (k==0) {pw=1;}
      else {pw=pow(2, k-1);};
      limit_l= (__int64)(xdat[k*nc]/pw+t1[i]); //left border of the block
      limit_r= limit_l+nc;                    // right border of the block
      j=p;
      while ((j<np2) && (t2[j]<=limit_r)) {
        if (photons2[j]!=0) {
          if (t2[j]>limit_l)                //if correlation time positive
          {
            index=t2[j]-limit_l+(__int64)(k*nc);
            corrl[index]+=(double) (photons1[i]*photons2[j]);
          }
          else {p++;}
        }
        j++;
      };
    };
  };
  if (k>0) {
    for(im=0;im<np1;im++) {t1[im]=t1[im]>>1;};
    for(im=1;im<np1;im++) {
      if (t1[im]==t1[im-1])
        {photons1[im]+=photons1[im-1]; photons1[im-1]=0;};
    };

    for(im=0;im<np2;im++) {t2[im]=t2[im]>>1;};
    for(im=1;im<np2;im++) {
      if (t2[im]==t2[im-1])
        {photons2[im]+=photons2[im-1]; photons2[im-1]=0;};
    };
  };
};
```

### B.3 Fit algorithm for PCH and FIDA

```
[result,resnorm,residual] = lsqcurvefit(@delta,x0,x,y_experimental_normiert);

function y = delta(x0, xdata)
% {extract C1, e1, C2, e2, A0, a1, a2, a3, binwidth from x0}
if strcmp(FitMethod, 'PCH')
    y_complex=PCH_GF_3DGauss(C1, epsilon1, C2, epsilon2, binwidth);
elseif strcmp(FitMethod, 'FIDA')
    y_complex=FIDA_GF(C1, epsilon1, C2, epsilon2, a1, a2, a3, binwidth);
end
y = [real(y_complex); imag(y_complex)];

% Fit in real, not Fourier space
fitresult = y(1:number_of_fft_points) +...
    1i * y(number_of_fft_points+1:2*number_of_fft_points);
y = real(fft(fitresult)/number_of_fft_points);
% Use statistical weighting
y = y./sqrt(y_experimental_normiert.*(1-y_experimental_normiert));
end

function GenFunc_PCH = PCH_GF_3DGauss(C1, epsilon1, C2, epsilon2, binwidth)
GenFunc_PCH=zeros(numel(PchFitData.xi_array),1);
for i=1:numel(PchFitData.xi_array)
    GenFunc_PCH(i)=exp(C1*2/sqrt(pi) * quadgk(@(u)...
        sqrt(u).*(exp(epsilon1.*exp(-u).*binwidth.*...
            (exp(complex(0,2.*pi.*PchFitData.xi_array(i)))-1))-1), 0, inf)...
        +C2*2/sqrt(pi) * quadgk(@(u)...
        sqrt(u).*(exp(epsilon2.*exp(-u).*binwidth.*...
            (exp(complex(0,2.*pi.*PchFitData.xi_array(i)))-1))-1), 0, inf));
end
end
```

```

function GenFunc_FIDA = FIDA_GF(C1, epsilon1, C2, epsilon2, a1, a2, a3, binwidth)
    GenFunc_FIDA=zeros(numel(PchFitData.xi_array),1);
    gamma = 2^(-3/2);
    C1 = C1 / gamma;
    C2 = C2 / gamma;
    epsilon1 = epsilon1 * gamma;
    epsilon2 = epsilon2 * gamma;
    u = 2*a1 + 6*a2 + 1;
    v = 2*a1 + 3*a2 + 2;
    B0 = 8*u/v;
    A0 = v/(8*u^2);
    C1 = C1 * A0;
    C2 = C2 * A0;
    epsilon1 = epsilon1 * B0;
    epsilon2 = epsilon2 * B0;
    number_of_distribution_points = 200;
    for i=1:numel(PchFitData.xi_array)
        GenFunc_FIDA(i)=exp(C1* quadgk(@(u)...
            (1+a1*u+a2*u.^2).*(u.^a3).*(exp(epsilon1.*exp(-u).*binwidth.*...
            (exp(complex(0,2.*pi.*PchFitData.xi_array(i)))-1))-1), 0, inf)...
            +C2* quadgk(@(u)...
            (1+a1*u+a2*u.^2).*(u.^a3).*(exp(epsilon2.*exp(-u).*binwidth.*...
            (exp(complex(0,2.*pi.*PchFitData.xi_array(i)))-1))-1), 0, inf));
    end
end

function y = Exponential_Distribution(lambda, x)
    for i = 1:numel(x)
        if x(i) >= 0
            y(i) = lambda*exp(-lambda*x(i));
        end
    end
end

```



## B.4 Cumulant Analysis

```
function CumulantAnalysis()
[y,x] = hist(ListOfMacroTimes,...
            [binning/2:binning:(max(ListOfMacroTimes)-binning/2)]);
for i = 2:8
    % MATLAB 'moment()' command gives the central moments
    centralmoment(i) = moment(y,i);
end
clockrate = TcspcData.Header.ClockRate;
mittelwert = mean(y);

% ki are the cumulants (NOT factorial cumulants!)
k(1) = 0;
k(2) = centralmoment(2);
k(3) = centralmoment(3);
k(4) = centralmoment(4) - 3*centralmoment(2)^2;
k(5) = centralmoment(5) - 10*centralmoment(3)*centralmoment(2);
k(6) = centralmoment(6) - 15*centralmoment(4)*centralmoment(2)...
      - 10*centralmoment(3)^2 + 30*centralmoment(2)^3;
k(7) = centralmoment(7) - 21*centralmoment(5)*centralmoment(2)...
      - 35*centralmoment(4)*centralmoment(3)...
      + 210*centralmoment(3)*centralmoment(2)^2;
k(8) = centralmoment(8) - 28*centralmoment(6)*centralmoment(2)...
      - 56*centralmoment(5)*centralmoment(3) - 35*centralmoment(4)^2...
      + 420*centralmoment(4)*centralmoment(2)^2 + 560*centralmoment(3)^2*...
      centralmoment(2) - 630*centralmoment(2)^4;

% k_(i) are the factorial cumulants
k_(1) = mittelwert;
k_(2) = k(2) - mittelwert;
k_(3) = k(3) - 3*k(2) + 2*mittelwert;
k_(4) = k(4) - 6*k(3) + 11*k(2) - 6*mittelwert;
```

```

% The following equations are the solutions of the equation system:
% (See J. Müller, BiophysJ 2004, 86: 3981-3992)
% k(1) =      e1  *N1 + e2  *N2
% k(2) = g2*(e1^2*N1 + e2^2*N2)
% k(3) = g3*(e1^3*N1 + e2^3*N2)
% k(4) = g4*(e1^4*N1 + e2^4*N2)
% The system has to been solved with MAPLE and the resulting equations
% have to be copy&pasted below.
% g2, g3, g4 are gamma factors that have also been solved with MAPLE
% assuming a 3D gaussian PSF

g(1) = 1;
g(2) = sqrt(2)/4;
g(3) = sqrt(12)/18;
g(4) = 1/8;

Cumulants.e_1species = k_(2)/(g(2)*k_(1));
Cumulants.N_1species = k_(1)^2*g(2)/k_(2);

% Cumulants.e1_2species = {Insert lengthy results from MAPLE calculations here}
% Cumulants.N1_2species = {Insert lengthy results from MAPLE calculations here}
% Cumulants.e2_2species = {Insert lengthy results from MAPLE calculations here}
% Cumulants.N2_2species = {Insert lengthy results from MAPLE calculations here}

Cumulants.e_1species = Cumulants.e_1species/UserValues.PCH.binning*clockrate;
Cumulants.e1_2species = Cumulants.e1_2species/UserValues.PCH.binning*clockrate;
Cumulants.e2_2species = Cumulants.e2_2species/UserValues.PCH.binning*clockrate;
end

```

# Bibliography

- [1] S. Felekyan, R. Kuhnemuth, V. Kudryavtsev, C. Sandhagen, W. Becker, and C. A. M. Seidel. Full correlation from picoseconds to seconds by time-resolved and time-correlated single photon detection. *Review of Scientific Instruments*, 76(8), 2005.
- [2] T. Förster. Zwischenmolekulare energiewanderung und fluoreszenz. *Annalen der Physik*, 437(1-2):55–75, 1948.
- [3] John D. Jackson. *Classical Electrodynamics*. John Wiley & Sons, New York, USA, 1975.
- [4] Marvin Minsky. Patent no. 3013467: Microscopy apparatus. Patent, December 1961.
- [5] Barbara K. Müller, Evgeny Zaychikov, Christoph Bräuchle, and Don C. Lamb. Pulsed interleaved excitation. *Biophysical Journal*, 89(5):3508–3522, 2005.
- [6] C. Eggeling, S. Berger, L. Brand, J. R. Fries, J. Schaffer, A. Volkmer, and C. A. M. Seidel. Data registration and selective single-molecule analysis using multi-parameter fluorescence detection. *Journal of Biotechnology*, 86(3):163–180, 2001.
- [7] Michelle A. Digman, Rooshin Dalal, Alan F. Horwitz, and Enrico Gratton. Mapping the number of molecules and brightness in the laser scanning microscope. *Biophysical Journal*, 94(6):2320–2332, 2008.
- [8] Alan Stuart and J. Keith Ord. *Kendall’s Advanced Theory of Statistics*, volume 1: Distribution Theory. Hodder Education, London, UK, 1994.
- [9] Yan Chen, Joachim D. Mueller, Peter T.C. So, and Enrico Gratton. The photon counting histogram in fluorescence fluctuation spectroscopy. *Biophysical Journal*, 77(1):553 – 567, 1999.
- [10] Bahaa Saleh and David L. MacAdam, editors. *Photoelectron Statistics: With Applications to Spectroscopy and Optical Communication*. Springer, New York, USA, 1978.
- [11] Leonard Mandel. Fluctuations of photon beams and their correlations. *Proceedings of the Physical Society*, 72(6):1037 – 1048, 1958.
- [12] Joseph R. Lakowicz. *Principles of Fluorescence Spectroscopy*. Springer, New York, USA, third edition, 2006.
- [13] S. Chandrasekhar. Stochastic problems in physics and astronomy. *Rev. Mod. Phys.*, 15(1):1 – 89, 1943.
- [14] Peet Kask, Kaupo Palo, Dirk Ullmann, and Karsten Gall. Fluorescence-intensity distribution analysis and its application in biomolecular detection technology. *Proceedings of the National Academy of Sciences of the United States of America*, 96(24):13756–13761, 1999.

- [15] Andreas Schenk. *Fluorescence Fluctuation Spectroscopy: Theoretical Basis, Experimental Realization, and Applications to Biomolecular Systems*. PhD thesis, Fakultät für Naturwissenschaften der Universität Ulm, 2003.
- [16] Rudolf Rigler and Elliot L. Elson, editors. *Fluorescence Correlation Spectroscopy: Theory and Applications*. Springer, New York, USA, first edition, 2001.
- [17] Kaupo Palo, Leif Brand, Christian Eggeling, Stefan Jäger, Peet Kask, and Karsten Gall. Fluorescence intensity and lifetime distribution analysis: Toward higher accuracy in fluorescence fluctuation spectroscopy. *Biophysical Journal*, 83(2):605 – 618, 2002.
- [18] Joachim D. Mueller. Cumulant analysis in fluorescence fluctuation spectroscopy. *Biophysical Journal*, 86(6):3981 – 3992, 2004.
- [19] Douglas Magde, Elliot Elson, and W. W. Webb. Thermodynamic fluctuations in a reacting system—measurement by fluorescence correlation spectroscopy. *Phys. Rev. Lett.*, 29(11):705–708, 1972.
- [20] Elliot Elson and Douglas Magde. Fluorescence correlation spectroscopy. I. conceptual basis and theory. *Biopolymers*, 13(1):1–27, 1974.
- [21] Douglas Magde, Elliot Elson, and W. W. Webb. Fluorescence correlation spectroscopy. II. an experimental realization. *Biopolymers*, 13(1):29–61, 1974.
- [22] Adolph Fick. V. on liquid diffusion. *Philosophical Magazine Series 4 (1851-1875)*, 10(63):30–39, 1855.
- [23] Michael Wahl, Ingo Gregor, Mattias Patting, and Jörg Enderlein. Fast calculation of fluorescence correlation data with asynchronous time-correlated single-photon counting. *Optics Express*, 11(26):3583–3591, 2003.
- [24] Jerker Widengren, Rudolf Rigler, and Ülo Mets. Triplet-state monitoring by fluorescence correlation spectroscopy. *Journal of Fluorescence*, 4:255–258, 1994.
- [25] Jerker Widengren, Rudolf Rigler, and Ülo Mets. Fluorescence correlation spectroscopy of triplet states in solution: a theoretical and experimental study. *Journal of Physical Chemistry*, 99:13368–13379, 1995.
- [26] Petra Schwille, Franz-Josef Meyer-Almes, and Rudolf Rigler. Dual-color fluorescence cross-correlation spectroscopy for multicomponent diffusional analysis in solution. *Biophysical Journal*, 72(4):1878–1886, 1996.
- [27] Katrin G. Heinze, Michael Jahnz, and Petra Schwille. Triple-color coincidence analysis: One step further in following higher order molecular complex formation. *Biophysical Journal*, 86(1):506–516, 2004.
- [28] N.O. Petersen. Scanning fluorescence correlation spectroscopy. I. theory and simulation of aggregation measurements. *Biophysical Journal*, 49(4):809 – 815, 1986.
- [29] N.O. Petersen, D.C. Johnson, and M.J. Schlesinger. Scanning fluorescence correlation spectroscopy. II. application to virus glycoprotein aggregation. *Biophysical Journal*, 49(4):817 – 820, 1986.

- [30] Michelle A. Digman, Claire M. Brown, Parijat Sengupta, Paul W. Wiseman, Alan R. Horwitz, and Enrico Gratton. Measuring fast dynamics in solutions and cells with a laser scanning microscope. *Biophysical Journal*, 89(2):1317 – 1327, 2005.
- [31] Michelle A. Digman, Parijat Sengupta, Paul W. Wiseman, Claire M. Brown, Alan R. Horwitz, and Enrico Gratton. Fluctuation correlation spectroscopy with a laser-scanning microscope: Exploiting the hidden time structure. *Biophysical Journal*, 88(5):L33 – L36, 2005.
- [32] Michelle A. Digman and Enrico Gratton. Analysis of diffusion and binding in cells using the RICS approach. *Microscopy Research and Technique*, 72(4):323 – 332, 2009.
- [33] C. Zander, M. Sauer, K. H. Drexhage, D.-S. Ko, A. Schulz, J. Wolfrum, L. Brand, C. Eggeling, and C. A. M. Seidel. Detection and characterization of single molecules in aqueous solution. *Applied Physics B: Lasers and Optics*, 63:517–523, 1996.
- [34] Ashok A. Deniz, Maxime Dahan, Jocelyn R. Grunwell, Taekjip Ha, Ann E. Faulhaber, Daniel S. Chemla, Shimon Weiss, and Peter G. Schultz. Single-pair fluorescence resonance energy transfer on freely diffusing molecules: Observation of Förster distance dependence and subpopulations. *Proceedings of the National Academy of Sciences of the United States of America*, 96(7):3670–3675, 1999.
- [35] Matthew Antonik, Suren Felekyan, Alexander Gaiduk, and Claus A. M. Seidel. Separating structural heterogeneities from stochastic variations in fluorescence resonance energy transfer distributions via photon distribution analysis. *The Journal of Physical Chemistry B*, 110(1):6970–6978, 2006.
- [36] Stanislav Kalinin, Suren Felekyan, Matthew Antonik, and Claus A. M. Seidel. Probability distribution analysis of single-molecule fluorescence anisotropy and resonance energy transfer. *The Journal of Physical Chemistry B*, 111(34):10253–10262, 2007.
- [37] Stanislav Kalinin, Suren Felekyan, Alessandro Valeri, and Claus A. M. Seidel. Characterizing multiple molecular states in single-molecule multiparameter fluorescence detection by probability distribution analysis. *The Journal of Physical Chemistry B*, 112(28):8361–8374, 2008.
- [38] Barbara K. Müller. *Die gepulste alternierende Anregung in der konfokalen Fluoreszenzspektroskopie*. PhD thesis, Fakultät für Chemie und Pharmazie der Ludwig-Maximilians-Universität München, 2006.
- [39] Eyal Nir, Xavier Michalet, Kambiz M. Hamadani, Ted A. Laurence, Daniel Neuhauser, Yevgeniy Kovchegov, and Shimon Weiss. Shot-noise limited single-molecule FRET histograms: Comparison between theory and experiments. *The Journal of Physical Chemistry B*, 110(44):22103–22124, 2006.
- [40] Achillefs N. Kapanidis, Nam Ki Lee, Ted A. Laurence, Sören Doose, Emmanuel Margeat, and Shimon Weiss. Fluorescence-aided molecule sorting: Analysis of structure and interactions by alternating-laser excitation of single molecules. *Proceedings of the National Academy of Sciences of the United States of America*, 101(24):8936–8941, 2004.
- [41] Nam Ki Lee, Achillefs N. Kapanidis, You Wang, Xavier Michalet, Jayanta Mukhopadhyay, Richard H. Ebright, and Shimon Weiss. Accurate FRET measurements within single

- p diffusing biomolecules using alternating-laser excitation.
- Biophysical Journal*
- , 88(4):2939–2953, 2005.
- [42] Technical report.
- [43] F. L. Graham, J. Smiley, W. C. Russell, and R. Nairn. Characteristics of a human cell line transformed by DNA from human adenovirus type 5. *J Gen Virol*, 36(1):59–72, 1977.
- [44] Christian Wahl-Schott, Ludwig Baumann, Hartmut Cuny, Christian Eckert, Kristina Griessmeier, and Martin Biel. Switching off calcium-dependent inactivation in l-type calcium channels by an autoinhibitory domain. *Proceedings of the National Academy of Sciences*, 103(42):15657–15662, 2006.
- [45] Kristina Griessmeier, Hartmut Cuny, Katrin Rötzer, Oliver Griesbeck, Hartmann Harz, Martin Biel, and Christian Wahl-Schott. Calmodulin is a functional regulator of Cav1.4 L-type Ca<sup>2+</sup> channels. *Journal of Biological Chemistry*, 284(43):29809–29816, 2009.
- [46] Kristina Griebmeier. *Untersuchungen zur Regulation des L-Typ Calciumkanals Cav1.4 durch Calcium / Calmodulin*. PhD thesis, Fakultät für Chemie und Pharmazie der Ludwig-Maximilians-Universität München, 2009.
- [47] Lothar Schermelleh, Fabio Spada, Hariharan Easwaran, Kourosh Zolghadr, Jean Margot, Cristina Cardoso, and Heinrich Leonhardt. Trapped in action: direct visualization of DNA methyltransferase activity in living cells. *Nature Methods*, 2(10):751 – 756, 2005.
- [48] Pawel Siedlecki, Regine Garcia Boy, Slobodan Comagic, Ralf Schirrmacher, Manfred Wiessler, Piotr Zielenkiewicz, Sandor Suhai, and Frank Lyko. Establishment and functional validation of a structural homology model for human DNA methyltransferase 1. *Biochemical and Biophysical Research Communications*, 306(2):558–563, 2003.
- [49] K. Fellingner, U. Rothbauer, M. Felle, G. Längst, and H. Leonhardt. Dimerization of dna methyltransferase 1 is mediated by its regulatory domain. *Journal of Cellular Biochemistry*, 106(4):521–528, 2009.
- [50] Carina Frauer and Heinrich Leonhardt. A versatile non-radioactive assay for DNA methyltransferase activity and DNA binding. *Nucleic Acids Research*, 37(3):e22, 2009.
- [51] Carina Frauer. *Studies of Mechanisms Controlling DNA methyltransferase 1*. PhD thesis, Fakultät für Biologie der Ludwig-Maximilians-Universität München, 2010.
- [52] Bo Huang, Thomas D. Perroud, and Richard N. Zare. Photon counting histogram: One-photon excitation. *ChemPhysChem*, 5(10):1523 – 1531, 2004.
- [53] M. Torimura, S. Kurata, K. Yamada, T. Yokomaku, Y. Kamagata, T. Kanagawa, and R. Kurane. Fluorescence-quenching phenomenon by photoinduced electron transfer between a fluorescent dye and a nucleotide base. *Analytical Sciences*, 17(1):155–160, 2001.
- [54] Moritz Marcinowski, Matthias Höller, Matthias J. Feige, Danae Baerend, Don C. Lamb, and Johannes Buchner. Substrate discrimination of the chaperone BiP by autonomous and cochaperone regulated conformational transitions. *Nature: Structural and Molecular Biology*, (This article is currently available as an advance online publication on <http://www.nature.com/nsmb/>)(-):-, 2011.

- [55] Samuel Karlin and Luciano Brocchieri. Heat shock protein 70 family: Multiple sequence comparisons, function, and evolution. *Journal of Molecular Evolution*, 47:565–577, 1998.
- [56] Sean Munro and Hugh R. B. Pelham. An hsp70-like protein in the ER: Identity with the 78 kd glucose-regulated protein and immunoglobulin heavy chain binding protein. *Cell*, 46(2):291–300, 1986.
- [57] Ingrid G. Haas and Matthias Wabl. Immunoglobulin heavy-chain binding-protein. *Nature*, 306(5941):387–389, 1983.
- [58] Young-Kwang Lee, Joseph W. Brewer, Rachel Hellman, and Linda M. Hendershot. BiP and immunoglobulin light chain cooperate to control the folding of heavy chain and ensure the fidelity of immunoglobulin assembly. *Mol. Biol. Cell*, 10(7):2209–2219, 1999.
- [59] Matthias J. Feige, Sandra Groscurth, Moritz Marcinowski, Yuichiro Shimizu, Horst Kessler, Linda M. Hendershot, and Johannes Buchner. An unfolded C<sub>H</sub>1 domain controls the assembly and secretion of IgG antibodies. *Molecular Cell*, 34(5):569–579, 2009.
- [60] Sylvie Blond-Elguindi, Steven E. Cwirla, William J. Dower, Robert J. Lipshutz, Stephen R. Sprang, Joseph F. Sambrook, and Mary-Jane H. Gething. Affinity panning of a library of peptides displayed on bacteriophages reveals the binding specificity of BiP. *Cell*, 75(4):717–728, 1993.
- [61] M.-J. Gething, S. Blond-Elguindi, J. Buchner, A. Fourie, G. Knarr, S. Modrow, L. Nanu, M. Segal, and J. Sambrook. Binding sites for Hsp70 molecular chaperones in natural proteins. *Cold Spring Harbor Symposia on Quantitative Biology*, 60:417–428, 1995.
- [62] Xiaotian Zhu, Xun Zhao, William F. Burkholder, Alexander Gragerov, Craig M. Ogata, Max E. Gottesman, and Wayne A. Hendrickson. Structural analysis of substrate binding by the molecular chaperone DnaK. *Science*, 272(5268):1606–1614, 1996.
- [63] Ying Shen and Linda M. Hendershot. ERdj3, a stress-inducible endoplasmic reticulum DnaJ homologue, serves as a CoFactor for BiP’s interactions with unfolded substrates. *Mol. Biol. Cell*, 16(1):40–50, 2005.
- [64] Matthias J. Feige, Franz Hagn, Julia Esser, Horst Kessler, and Johannes Buchner. Influence of the internal disulfide bridge on the folding pathway of the CL antibody domain. *Journal of Molecular Biology*, 365(4):1232–1244, 2007.
- [65] Jueyang Wei and Linda M. Hendershot. Characterization of the nucleotide binding properties and ATPase activity of recombinant hamster BiP purified from bacteria. *Journal of Biological Chemistry*, 270(44):26670–26676, 1995.
- [66] Rainer Schlecht, Annette H. Erbse, Bernd Bukau, and Matthias P. Mayer. Mechanics of the substrate binding pocket of Hsp70 chaperones enables differential interaction with client proteins. *Nature: Structural and Molecular Biology*, -(–):–, 2011.
- [67] Laurent Meunier, Young-Kwang Usherwood, Kyung Tae Chung, and Linda M. Hendershot. A subset of chaperones and folding enzymes form multiprotein complexes in endoplasmic reticulum to bind nascent proteins. *Mol. Biol. Cell*, 13(12):4456–4469, 2002.

- [68] Ying Shen, Laurent Meunier, and Linda M. Hendershot. Identification and characterization of a novel endoplasmic reticulum (ER) DnaJ homologue, which stimulates ATPase activity of BiP in vitro and is induced by ER stress. *Journal of Biological Chemistry*, 277(18):15947–15956, 2002.
- [69] Koyeli Mapa, Martin Sikor, Volodymyr Kudryavtsev, Karin Waegemann, Stanislav Kalinin, Claus A.M. Seidel, Walter Neupert, Don C. Lamb, and Dejana Mokranjac. The conformational dynamics of the mitochondrial Hsp70 chaperone. *Molecular Cell*, 38(1):89–100, 2010.



# List of abbreviations

ADP	Adenosine Diphosphate
AMP-PNP	Adenylyl Imidodiphosphate
APBS	All-Photon-Burst-Search
APD	Avalanche Photodiode
ATP	Adenosine Triphosphate
BiP	Immunoglobulin Binding Protein
CaV	Voltage-Gated Calcium Channel
CGF	Cumulant Generating Function
C <sub>H</sub> 1	Immunoglobulin heavy chain domain 1
DCBS	Dual-Channel-Burst-Search
DPBS	Dulbecco's Phosphate Buffered Saline
DNA	Deoxyribonucleic Acid
Dnmt1	DNA Methyltransferase 1
eGFP	Enhanced Green Fluorescent Protein
ER	Endoplasmic Reticulum
ERdJ3	ER DnaJ Homologue 3
FCA	Fluorescence Cumulant Analysis
FCGF	Factorial Cumulant Generating Function
FCCS	Fluorescence Cross-Correlation Spectroscopy
FCS	Fluorescence Correlation Spectroscopy
FFS	Fluorescence Fluctuation Spectroscopy
FIDA	Fluorescence Intensity Distribution Analysis
FMGF	Factorial Moment Generating Function
FRET	Förster Resonance Energy Transfer
GBP	GFP Binding Protein
GdCl	Guadinium Chloride
GFP	Green Fluorescent Protein
HEK293	Human embryonic Kidney 293 cells
HEPES	(4-(2-Hydroxyethyl)-1-Piperazineethanesulfonic Acid
HKM	HEPES with Potassium and Magnesium
Hsp	Heat Shock Protein
ICDI	Inactivator of Calcium Dependent Inactivation
Ig	Immunoglobulin
MFD	Multiparameter Fluorescence Detection
MGF	Moment Generating Function
N&B	Number & Brightness Analysis

NBD	Nucleotide Binding domain
Ni-NTA	Nickel-Nitrilotriacetic Acid
p.c.h.	Experimentally measured photon counting histogram
PCH	Photon Counting Histogram Analysis
PCI	Peripheral Component Interconnect
PDA	Photon Distribution Analysis
PGF	Probability Generating Function
PIE	Pulsed Interleaved Excitation
PSF	Point Spread Function
RBP	RFP Binding Protein
RFP	Red Fluorescent Protein
RICS	Raster Image Correlation Spectroscopy
SBD	Substrate Binding Domain
SDS-PAGE	Sodium Dodecyl Sulfate Polyacrylamide Gel Electrophoresis
Sse1	Structure-Specific Endonuclease 1
TCSPC	Time-Correlated Single Photon Counting
TEV	Tobacco Etch Virus
TTL	Transistor-Transistor Logic

# Acknowledgements

I thank Prof. Don Lamb, my thesis advisor, for giving me the opportunity to do my PhD thesis in your group. I very much appreciate the high competence of your scientific advice and the fact that your door was always open for me and my questions. The most important encouragement during the difficult periods of my thesis was the knowledge that the progress of your students is important to you and that you care about us. Thank you also for the opportunity to attend many exciting conferences, particularly the Biophysical Society Meetings.

I thank my second advisor, Prof. Christoph Bräuchle, for his support within the IDK-NBT and the CeNS, and for providing an outstanding infrastructure for excellent research in this institute.

I gratefully acknowledge the SFB 749, the Nanosystems Initiative Munich (NIM), the Center for NanoScience (CeNS), and the Elite Network of Bavaria (ENB) for funding and support, and for many exciting events, particularly within the International Doctorate Program NanoBioTechnology.

I thank Moritz Marcinowski, Dr. Matthias Feige, and Prof. Johannes Buchner for our very successful and equally pleasurable collaboration on BiP. Moritz, without your skillful and tireless effort, such a great publication would not have been possible. In particular, I gratefully acknowledge Moritz for providing the schematics of BiP and ERdJ3 and the crystal structure of Sse1 for this work.

I thank Dr. Carina Frauer and Prof. Heinrich Leonhardt for our collaboration on Dnmt1. I very much enjoyed working with you and discovering such extraordinary results. I gratefully acknowledge Carina for providing many of the Dnmt1 schematics and the SDS-PAGE analysis of the size purification fractions shown in this work.

I thank Christos Pappas and Prof. Christian Wahl for our fruitful and enjoyable collaboration on the CaV1.4 channel. Christos, I cannot yet thank you for letting me score a goal against you, but I will keep trying.

I thank my wonderful colleagues from AK Lamb, AK Bräuchle, and AK Michaelis. It was never hard for me to drive to work in the mornings, no matter how bad the science was currently working out - you would always make my day! Furthermore, having outstanding experts like you around on virtually every subject makes life so much easier. Although it is impossible to name all that helped me at some point, I would like to give special thanks to some of you. Thank you, Martin, for being the most amazing colleague, and for always being right. Thank you, Niko, for being the most awesome office mate. Thank you, Gregor, for listening to my worries when science didn't work out as it should. Thank you, Adam, for many discussions of enormous scientific and mathematic depth, I profited from them and I enjoyed them. And thank you, Vova, for countless hours of programming, discussing, bugfixing, and football.

I thank Monika Franke and Dr. Moritz Ehrl for all the entertaining discussions we had in our office and in the kitchen, and I thank you, Moritz, for your profound advice on all kinds of questions, reaching from scientific over administrative to private.

I thank my parents for their lifelong support, and for the feeling that whatever happens, you are always there for me. And finally, I thank you, Astrid, for being the anchor in my life and for taking me as I am.

## Publications

- Moritz Marcinowski, Matthias Höller, Matthias J. Feige, Danae Baerend, Don C. Lamb, and Johannes Buchner. Substrate discrimination of the chaperone BiP by autonomous and cochaperone regulated conformational transitions. *Nature: Structural and Molecular Biology* (This article is currently available as an advance online publication on <http://www.nature.com/nsmb/> and will be published in print in 2011)
- Günter Wrobel, Matthias Höller, Sven Ingebrandt, Sabine Dieluweit, Frank Sommerhage, Hans-Peter Bochem, Andreas Offenhäusser. Transmission Electron Microscopy study of the Cell-Sensor Interface. *Journal of the Royal Society Interface* (2008), 5:213-222.

## Posters

- 53th Annual Meeting of the Biophysical Society, February 28 - March 04, 2009, Boston, USA: Investigation of Dnmt1-DNA Interaction using Fluorescence Fluctuation Spectroscopy
- 54th Annual Meeting of the Biophysical Society, February 20-24, 2010, San Francisco, USA: Applications of Pulsed Interleaved Excitation in Live Cell Experiments

# CURRICULUM VITAE

## Education:

08/2006 - 02/2011	PhD thesis, LMU München, Institut für physikalische Chemie, group of Prof. Don C. Lamb <i>Topic: Advanced Fluorescence Fluctuation Spectroscopy with Pulsed Interleaved Excitation</i>
10/1999 - 07/2005	Studies of Physics, RWTH Aachen ( <i>Diplom, Overall grade: 1.2</i> )
06/2004 - 05/2005	Diploma thesis, Forschungszentrum Jülich ( <i>Overall grade: 1.0</i> )
09/2001 - 07/2002	Academic exchange year, Université Paris-Sud XI, Frankreich
08/1998 - 08/1999	Civilian service at Caritas Pflegedienste, Bergisch Gladbach
08/1989 - 06/1998	Secondary School: Erzbischöfliches St.-Angela-Gymnasium, Wipperfürth ( <i>Abitur, Overall grade: 1.5</i> )

## Scholarships:

seit 10/2006	Scholarship within the international Doctorate Program NanoBioTechnology of the Center for NanoScience, München
--------------	--